Technische Universität München

Kinetic Monte Carlo Simulations of Organic Solar Cells

Tim Albes

Vollständiger Abdruck der von der Fakultät für Elektrotechnik und Informationstechnik der Technischen Universität München zur Erlangung des akademischen Grades eines

Doktors der Naturwissenschaften (Dr. rer. nat.)

genehmigten Dissertation.

Vorsitzender:		Prof. Dr. Rolf Witzmann
Prüfer der Dissertation:	1.	Prof. Dr. Alessio Gagliardi
	2.	Prof. Dr. Peter Müller-Buschbaum

Die Dissertation wurde am 20.06.2018 bei der Technischen Universität München eingereicht und durch die Fakultät für Elektrotechnik und Informationstechnik am 30.12.2018 angenommen.

Für meinen Vater, meine Mutter und meinen Bruder.

Abstract

Harnessing sunlight to cover humankind's relentlessly increasing energy demand in a cost-efficient and scalable way is one of the most desirable future developments on Earth. In this regard, organic solar cells – photovoltaic cells comprised of organic semiconductors – offer the prospect of cheap light-harvesting devices that are compatible with large-scale fabrication processes. Due to a generally disordered molecular arrangement and a substantially lower permittivity of organic semiconductors, the processes controlling the charge generation, transport and loss mechanisms in organic solar cells differ considerably from those of inorganic solar cells.

The need for a deeper understanding of the physics of devices based on organic semiconductors has driven the development of microscopic numerical models in order to complement experimental research. Especially simulations based on the kinetic Monte Carlo method represent a powerful tool because they allow to explicitly model the disordered configuration of organic molecules and track the dynamic behavior of single particles. This is a particular advantage over experiments or continuum-based models in which the underlying single-particle effects are often concealed within effective quantities.

In this thesis, a 3D kinetic Monte Carlo model of organic solar cells is presented and used to obtain a comprehensive picture about the charge carrier distribution, the charge pair separation dynamics and charge recombination in the active layer. These microscopic quantities can be linked to the macroscopic solar cell performance which allows to identify the origin of loss mechanisms.

At first, bulk-heterojunction cells are studied. The necessity of a 3D particle-based model is highlighted by showing that the reduction of a bulk-heterojunction to an effective medium cannot capture the morphological effects appropriately.

Next, the effects arising from the key differences of organic (compared to inorganic) semiconductors, namely the low permittivity and the energetic disorder, are investigated. It was found that in case of low permittivity and large disorder insufficient charge pair separation from the heterojunction interface leads to a strongly inhomogeneous charge carrier distribution in the active layer with charges accumulating along the heterojunction interface, thus leading to increased recombination. However, even slight changes in disorder or permittivity can affect the interface density and charge separation time drastically and can outweigh orders of magnitude of recombination rates.

At last, in a joint modeling and experimental study, an explanation for the so far not understood origin of photocurrent in fullerene-based systems with low donor content is provided. The effect of a hole-transfer from the dispersed donor to the fullerene phase is proposed and the fullerene phase is identified as the ambipolar charge transport layer.

Kurzfassung

Die Umwandlung von Strahlungsenergie der Sonne in elektrische Energie ist einer der erstrebenswertesten Wege, um den stetig wachsenden Energiebedarf der Menschheit zu decken. Insbesondere organische Solarzellen, Photovoltaik-Zellen basierend auf organischen Materialien, erlauben es kostengünstig und großflächig hergestellt zu werden.

Die vorherrschenden Mechanismen in organischen Halbleitern, sowie Bauteilen bestehend aus diesen, sind bisher jedoch nicht ins Detail verstanden. Numerische Simulationen basierend auf dem kinetischen Monte Carlo Algorithmus stellen eine hilfreiche Methode dar, um virtuelle Modelle von organischen Solarzellen nachzubilden und tiefgehende Einblicke in deren Funktionsweise zu bekommen. Solche Modelle erlauben es explizit die in organischen Materialien vorherrschende ungeordnete Struktur zu implementieren und bieten gleichzeitig Zugriff auf die zeitliche Entwicklung einzelner Teilchen. Somit ermöglichen sie eine genauere Modellierung von organischen Solarzellen im Vergleich zu etablierten Modellen basierend auf Kontinuums-Beschreibungen und bieten Zugriff auf Größen, die in Experimenten oftmals verborgen bleiben.

In vorliegender Arbeit wird die Implementierung eines 3D kinetischen Monte Carlo Modells für organische Solarzellen vorgestellt. Das entwickelte Modell wird angewandt um ein umfassendes Bild der Ladungsträgerverteilung, der zeitlichen Entwicklung der Trennung von positiven und negativen Ladungen und deren Rekombination zu erhalten. Das Verhalten einzelner Teilchen kann zur Ableitung der makroskopischen Kennzahlen der Solarzelle verwendet werden und dazu beitragen, den Ursprung von Verlusten auf mikroskopischer Ebene zu identifizieren.

Zunächst werden Mischphasen-Zellen untersucht. Das entwickelte 3D Modell wird mit einem makroskopischen 1D Modell verglichen, um seine Notwendigkeit hervorzuheben.

Nachfolgend wird gezeigt, dass die niedrige Permittivität und die ungeordnete Struktur der organischen Materialien für eine stark inhomogene Ladungsträgerverteilung innerhalb der Zelle verantwortlich sind, was zu erhöhten Verlusten führt. Schon kleine Änderungen in Permittivität und dem Grad der Unordnung können einen bedeutsamen Einfluss auf diesen Effekt haben und erhebliche Rekombinationszeiten aufwiegen.

Zuletzt wird das Modell angewendet, um das bisher nicht verstandene Funktionsprinzip von organischen Solarzellen mit sehr niedrigem Donator-Anteil zu erklären. Der Effekt eines Loch-Transfers von den Donator-Molekülen auf die Akzeptor-Phase wird vorgeschlagen, wonach die Akzeptor-Phase die ambipolare Transportschicht für Ladungen darstellt. Der Effekt wird durch eine kollaborative Studie aus Modell und Experiment verifiziert.

List of Own Publications and Contributions

This thesis is based on the author's work carried out at the Department of Electrical and Computer Engineering, Technical University of Munich, Germany. Parts of this work correspond to or are in parts identical to the following publications or contributions of the author.

Peer-reviewed journals

T. Albes, L. Xu, J. Wang, J. W. P. Hsu, and A. Gagliardi, "Origin of Photocurrent in Fullerene-Based Solar Cells", *The Journal of Physical Chemistry C*, vol. 122, no. 27, pp. 15 140–15 148, 2018

T. Albes and A. Gagliardi, "Charge Pair Separation Dynamics in Organic Bulk-Heterojunction Solar Cells", *Advanced Theory and Simulations*, vol. 1, no. 7, p. 1 800 032, 2018

A. Gagliardi, S. Wang, and T. Albes, "Simulation of Charge Carrier Mobility Unbalance in Organic Solar Cells", *Organic Electronics*, vol. 59, pp. 171–176, 2018

W. Kaiser, J. Popp, M. Rinderle, T. Albes, and A. Gagliardi, "Generalized Kinetic Monte Carlo Framework for Organic Electronics", *Algorithms*, vol. 11, no. 4, p. 37, 2018

W. Kaiser, T. Albes, and A. Gagliardi, "Charge Carrier Mobility of Disordered Organic Semiconductors with Correlated Energetic and Spatial Disorder", *Physical Chemistry Chemical Physics*, vol. 20, no. 13, pp. 8897–8908, 2018

T. Albes and A. Gagliardi, "Influence of Permittivity and Energetic Disorder on the Spatial Charge Carrier Distribution and Recombination in Organic Bulk-Heterojunctions", *Physical Chemistry Chemical Physics*, vol. 19, no. 31, pp. 20 974–20 983, 2017

T. Albes, P. Lugli, and A. Gagliardi, "Investigation of the Blend Morphology in Bulk-Heterojunction Organic Solar Cells", *IEEE Transactions on Nanotechnology*, vol. 15, no. 2, pp. 281–288, 2016

B. Weiler, R. Nagel, T. Albes, T. Haeberle, A. Gagliardi, and P. Lugli, "Electrical and Morphological Characterization of Transfer-Trinted Au/Ti/TiOx/p+-Si Nano-and Microstructures with Plasma-Grown Titanium Oxide Layers", *Journal of Applied Physics*, vol. 119, no. 14, p. 145 106, 2016

Book chapter

M. Auf der Maur, T. Albes, and A. Gagliardi, "Thin-Film Solar Cells", in *Handbook of Optoelectronic Device Modeling and Simulation: Lasers, Modulators, Photodetectors, Solar Cells, and Numerical Methods*, J. Piprek, Ed., Taylor & Francis, Boca Raton, 2017

Conference proceedings

T. Albes, P. Lugli, and A. Gagliardi, "Kinetic Monte Carlo Simulations to Investigate the Effects of Interfaces in Organic Photovoltaic Cells Including a Realistic Blend Morphology", in *International Conference on Simulation of Semiconductor Processes and Devices (SISPAD)*, Washington, DC, USA, 2015, pp. 450–453

T. Albes, B. Popescu, D. Popescu, F. Arca, and P. Lugli, "Optimization of Organic Solar Cells by kinetic Monte Carlo Simulations", in *14th IEEE International Conference on Nanotechnology (IEEE-NANO)*, Toronto, ON, Canada, 2014, pp. 1023–1028

T. Albes, B. Popescu, D. Popescu, M. Loch, F. Arca, and P. Lugli, "Kinetic Monte Carlo Modeling of Low-Bandgap Polymer Solar Cells", in *40th IEEE Photovoltaic Specialist Conference (PVSC)*, Denver, CO, USA, 2014, pp. 0057–0062

Conference presentations

L. Xu, T. Albes, J. Wang, M. De Anda Villa, T. Daunis, Y.-J. Lee, A. V. Malko, A. Gagliardi, and J. W. P. Hsu, "Charge Photo-Generation and Transport in High Photovoltage Fullerene-Based Organic Photovoltaics", in *SPIE Photonics West OPTO, Oral Presentation*, San Francisco, CA, USA, Jan. 2017

T. Albes and A. Gagliardi, "Investigating Interface Effects in Bulk Heterojunction Organic Solar Cells by Kinetic Monte Carlo Simulations", in *Materials Research Foundation (MRS) Fall Meeting, Oral Presentation*, Boston, MA, USA, Nov. 2016

A. Gagliardi and T. Albes, "Investigation of the Blend Morphology in Bulk-Heterojunction Organic Solar Cells", in *15th IEEE International Conference on Nanotechnology (IEEE-NANO), Oral Presentation*, Rome, Italy, Jul. 2015

T. Albes, P. Lugli, and A. Gagliardi, "Establishing an Interface between Kinetic Monte Carlo and Drift Diffusion Simulations of Organic Bulk-Heterojunction Solar Cells to Investigate the Effect of the Effective Medium Approach", in *International Conference on Hybrid and Organic Photovoltaics (HOPV), Oral Presentation*, Rome, Italy, May 2015

A. Gagliardi, T. Albes, and P. Lugli, "Kinetic Monte Carlo Simulations to Investigate Interface Effects in Organic Photovoltaic Cells Including a Realistic Blend Morphology", in *International Conference on Hybrid and Organic Photovoltaics (HOPV), Poster Presentation*, Rome, Italy, May 2015

Diploma thesis

T. Albes, "Kinetic Monte Carlo Modelling of Bulk-Heterojunction Organic Solar Cells", Diplomarbeit, Department of Physics, Technical University of Munich, Munich, Germany, 2014

Contents

Abstract i

Kurzfassung ii

List of Own Publications and Contributions iii

Contents vii

1. Introduction 1
- 1.1. Motivation . . . 1
- 1.2. Outline and context of publications . . . 5
- 1.3. Preliminary work . . . 6

2. Organic Solar Cells 9
- 2.1. Basic principles of photovoltaics . . . 9
- 2.2. Characterization of solar cell performance . . . 12
- 2.3. Solar cell technologies . . . 15
- 2.4. Organic semiconductors . . . 17
  - 2.4.1. Energetic structure . . . 18
  - 2.4.2. Charge transport . . . 23
  - 2.4.3. Excitons . . . 25
- 2.5. Organic solar cells . . . 26
  - 2.5.1. Working principle and design . . . 26
  - 2.5.2. Active layer morphology . . . 29
  - 2.5.3. Pathways to improve the efficiency . . . 30

3. The Kinetic Monte Carlo Algorithm 33
- 3.1. Historical development . . . 33
- 3.2. Classification and advantages . . . 35
- 3.3. Kinetic Monte Carlo algorithm . . . 37
  - 3.3.1. Probability density function . . . 38
  - 3.3.2. Choosing time and transition in the direct method . . . 41
- 3.4. Algorithm procedure . . . 44

4. Kinetic Monte Carlo Model of Organic Solar Cells 47
- 4.1. State-of-the-art implementations . . . 47

4.2. System Setup . . . 49
4.2.1. Lattice discretization . . . 49
4.2.2. Morphology generation . . . 52
4.2.3. Energy distribution . . . 57
4.2.4. Treatment of Coulomb interaction . . . 62
4.3. Implementation of processes . . . 67
4.3.1. Exciton generation . . . 68
4.3.2. Exciton diffusion . . . 71
4.3.3. Exciton decay . . . 71
4.3.4. Exciton separation . . . 71
4.3.5. Charge carrier hopping . . . 72
4.3.6. Charge carrier recombination . . . 74
4.3.7. Collection at electrodes . . . 76
4.3.8. Injection from electrodes . . . 77
4.4. Simulation input parameters . . . 78
4.5. Evaluation details . . . 80
4.5.1. Particle trajectories . . . 80
4.5.2. Charge mobilities . . . 81
4.5.3. Charge carrier densities . . . 81
4.5.4. Charge pair displacement . . . 82
4.5.5. Counter-based evaluation . . . 82
4.5.6. Local Coulomb potential . . . 84

5. Investigation of Blend Effects in Bulk-Heterojunction Organic Solar Cells 85
5.1. Background . . . 86
5.2. Model specifics . . . 87
5.2.1. Drift-Diffusion model . . . 88
5.2.2. Kinetic Monte Carlo model . . . 89
5.2.3. Establishing a common basis . . . 89
5.3. Results and discussion . . . 91
5.3.1. Mobility fit . . . 91
5.3.2. Mobility extraction . . . 92
5.3.3. Re-fit with extracted mobilities . . . 93
5.3.4. Charge density evaluation . . . 94
5.4. Conclusion . . . 95

6. Influence of Permittivity and Energetic Disorder on the Spatial Charge Carrier Distribution in Organic Bulk-Heterojunction Solar Cells 97
6.1. Background . . . 98
6.2. Model specifics . . . 99
6.3. Results and discussion . . . 101
6.3.1. Charge accumulation and operation regimes . . . 101

6.3.2. Influence on recombination . . . 105
6.4. Conclusion . . . 109

7. Charge Pair Separation Dynamics in Organic Bulk-Heterojunction Solar Cells 111
7.1. Background . . . 112
7.2. Model specifics and evaluation details . . . 114
7.3. Results and discussion . . . 119
7.3.1. Charge pair separation dynamics: absolute times . . . 119
7.3.2. Charge pair separation dynamics: relative times . . . 122
7.3.3. Relation of transport to mobility . . . 123
7.3.4. Relation of separation to geminate recombination . . . 124
7.4. Conclusion . . . 126

8. The Origin of Photocurrent in Fullerene-Based Solar Cells 127
8.1. Background . . . 128
8.2. Methods . . . 131
8.2.1. Model specifics . . . 131
8.2.2. Experimental details . . . 133
8.3. Results and discussion . . . 133
8.3.1. The origin of hole-escape . . . 133
8.3.2. Energy barrier lowering . . . 140
8.3.3. Comparison of model and measurements . . . 140
8.4. Conclusion . . . 141

9. Summary and Conclusion 143

A. Appendix 145
A.1. Generation profiles . . . 145
A.2. Densities and potential in fullerene-based solar cells . . . 147

List of Figures 149

List of Tables 151

Bibliography 153

Acronyms 175

Acknowledgment 177

1. Introduction

1.1. Motivation

Solar irradiation is by far the largest, on human timescales inexhaustible source of energy on Earth. A vast 10^{18} kWh of energy reach the Earth's surface during the course of a year in form of sunlight [1]. Compared to mankind's total annual energy supply of roughly 1.6×10^{14} kWh as of 2015 [2], harvesting a fraction of 0.016 % of the available sunlight would be sufficient to cover the worldwide energy demand. After all, also the majority of fossil fuels in the Earth's mantle, i.e. crude oil, natural gas and coal (*not* fissile elements which originate from supernovae), are a product of sunlight that has been converted by photosynthesis of plants and algae and stored in form of chemical energy in carbohydrates. The dwindling amount of fossil fuels and the abundant availability of sunlight make the usage of solar power inevitable on future perspectives. According to an outlook by the Energy Information Administration [3], solar energy could provide one third of the global energy demand by 2060.

The direct conversion of radiation into electrical energy by solar cells, officially termed photovoltaic cells because they utilize incident photons to create an electrical voltage, is arguably one of the most elegant ways to harness sunlight. Solar cells require no mechanical components (such as turbines or generators), do not emit physically or environmentally harmful waste products (such as CO_x, NO_x, SO_2, particulate matter, which are either toxic or green-house gases) during their operation and the resulting electrical energy can easily be converted into other forms of energy.

A downside of sunlight is that it is not particularly concentrated: on a sunny day, the maximal solar irradiance is around $1\,\mathrm{kW\,m^{-2}}$ at sea level. Thus, on an area of $1\,\mathrm{m^2}$ and during 10 h of sunshine around 10 kWh are deposited, which is equal to the chemical energy stored in 1 L of gasoline. The irradiance is even lower on cloudy days and in regions of larger latitudinal coordinates. In order to obtain the equivalent energy contained in the gas tank of a car of 50 L (i.e. 500 kWh) during average weather conditions in middle latitude regions ($250\,\mathrm{W\,m^{-2}}$) with a solar cell with 20 % efficiency from a solar rooftop with $10\,\mathrm{m^2}$ area, one would need 1000 h, or several months. Therefore, large-area solar modules are required to make up for the low concentration of sunlight and collect a sufficient amount of energy for practical applications.

Currently established solar cells are mainly based on Silicon (Si). Si is abundantly available and the knowledge about its physical properties and processing techniques has benefited from decades of research in the chip industry. While solar cells based on monocrystalline Si reach efficiencies of up to 26.7 % nowadays [4], the processing of Si to

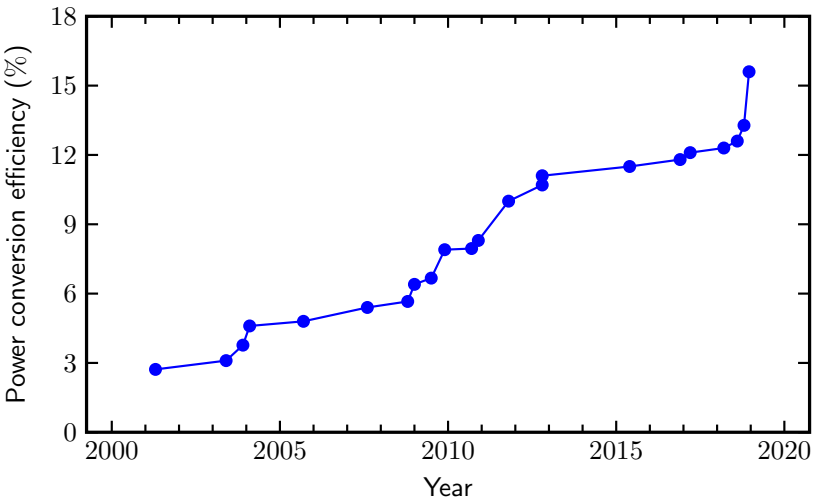

Figure 1.1. – Record power conversion efficiencies of single junction organic solar cells. Data from: Solar cell efficiency tables 2001 to 2019 (latest version [4])[1].

highly pure crystals is generally expensive because it requires high-temperature processing conditions. Furthermore, the complex manufacturing process often involves harmful chemicals and is not easily scalable. These drawbacks have prevented the large-scale adoption of Si solar cells, in particular for residential, private installations.

Next-generation solar cells are technologies that offer the prospect to overcome these restrictions and allow for a cost-efficient, large-scale adaption of photovoltaic technology.

During recent years, especially solar cells comprised of organic materials, so called Organic Solar Cells (OSCs), have become serious contenders to emerge as next-generation solar cells and have been subject of intense research [5]–[9]. OSCs exhibit a wide range of favorable features such as the compatibility to low-temperature manufacturing processes with high throughput (e.g. roll-to-roll printing) [10], [11], a low energy payback time [12], [13] and sustainability (i.e. abundant availability and recyclability) [14]. Additional unique features such as mechanical flexibility, low weight and semi-transparency open up the possibility for a variety of novel applications, for example small, mobile/wearable power units or the integration of light harvesting devices in building facades.

One of the main reasons for the absent prevalence of OSCs is their lack in Power Conversion Efficiency (PCE), i.e. the ratio by which a solar cell can convert the incident radiant power to electrical power, in comparison to their inorganic counterparts. Figure 1.1 shows the trend in the PCE of OSCs between 2001–2019. Intense research has led to a steady increase in efficiency and the PCE of pioneering devices reaches 13 %-14 % [15]–[18] for single junction cells by now. A PCE of 15 % is generally considered as the threshold for successful commercialization [19]. In combination with a 20-year lifetime this is estimated to allow OSCs to produce electricity at a price of less than 0.07 $/kWh

[1]Data confirmed by National Renewable Energy Laboratory (http://www.nrel.gov/).

(= 0.06 €/kWh) which is roughly the current cost of production (without taxes and other charges) for electricity in the U.S. (or Germany) [12].

Just recently and for the first time, the milestone efficiency of 15 % was reported both in a single junction [20] as well as in a multi-junction OSC [21]. While this is a truly promising and motivating development from a commercial point-of-view, from a scientific standpoint there is much more room for improvement as the theoretical limitation for OSCs is estimated to be around 27 % for single junction cells [22], and consequently even higher for multi-junction cells. Further optimization therefore requires a deeper understanding of the physical processes and loss mechanisms in OSCs.

OSCs are based on organic semiconductors, for whose discovery in the late 1970s Heeger, MacDiarmid and Shirakawa were awarded with The Nobel Prize in Chemistry in 2000 [23]. The vast amount of organic compounds available and the ability to tune the optical and electrical properties of organic semiconductors, e.g. their bandgap or their response to electric fields, by chemical engineering allows to adapt the organic semiconductors to the desired needs of the application. This has not only been beneficial for OSCs [24]–[28], but has also led to the development of a variety of electronic components such as organic light-emitting diodes [29], organic field-effect transistors [30], and organic thermoelectric generators [31], which were derived in analogy to the corresponding inorganic devices.

Compared to the extensive experimental, analytical and numerical research on inorganic semiconductors performed during the 20th century, the understanding of the physics of organic semiconductors is still in its infancy. There are two fundamental differences of organic semiconductors compared to their inorganic counterparts:

(1) For one, organic materials generally lack a periodic arrangement of their constituents, which leads to a spatially varying distribution of their energy levels.

(2) Furthermore, electric charges are only weakly screened in organics due to their substantially lower permittivity with values around $\varepsilon_r = 3 - 4$ (compared to silicon $\varepsilon_r = 11.7$).

These differences have two important implications for the physics of organic semiconductors and OSCs:

(i) Due to the spatial disorder, charges tend to be spatially confined to certain molecules or sub-units of molecules. Charge motion in organic semiconductors takes place by a thermally activated “hopping” process between such localized states instead of delocalized band transport as present in inorganic semiconductors.

(ii) The absorption of light in organic materials leads to the generation of strongly bound charge pairs/excited states (excitons) instead of free charges. In order to obtain free charges that can be extracted, an additional separation mechanism is required, which makes the introduction of a two-component donor/acceptor heterojunction necessary. In order to understand the charge separation process from the heterojunction, the dynamics of the charge pairs needs to be considered explicitly and on a single particle level.

A further difficulty in gaining a comprehensive picture of the functionality of OSCs arises from the fact that the mechanisms responsible for photocurrent generation can range over both large spatial dimensions (from charge localization at the (sub-)nm scale to hundreds of nm of absorption layer size) and timescales (between tens of fs for charge transfer and several µs for non-geminate recombination).

So far, optimizations in device performance have largely been achieved by experiments, yet they often rely on "trial-and-error" approaches. Resolving charge behavior spatially and temporally by experimental techniques is challenging due to the disordered structure and effects on a single particle level. Furthermore, due to the complex geometry of its constituents, closed-form analytic models of full-device OSCs are hard to formulate and quickly become impossible to solve. Design and optimization of OSCs must therefore be complemented by the 'third pillar' of research: numerical simulations based on virtual device models are valuable tools to gain insights into the charge generation, transport and loss mechanisms in OSCs and to guide the further development and the improvement of such.

In order to meet the mentioned complexities in OSCs by a numerical model, especially simulations based on the kinetic Monte Carlo (kMC) method are a suitable tool to investigate the processes governing the operation of OSCs. The kMC method shows several advantages that make it the preferred choice to model OSCs:

(a) due to its event-based, stochastic nature it is well suited to model the thermally activated hopping transport between localized states (as well as diffusive processes);

(b) it allows to explicitly consider single particles and evaluate their time-dependent behavior;

(c) it is able to resolve processes on the nm/fs scale while still being able to model entire device geometries (hundreds of nm) and slow processes (µs);

(d) it does not struggle with convergence problems, not even for disordered geometries as existent in OSCs.

The kMC method is a mesoscopic simulation model since it bridges the gap between macroscopic continuum models and microscopic atomistic models. Continuum-based models are well-established in inorganic semiconductor research. They are the suitable choice for systems in which collections of particles can be approximated by continuous quantities, as generally the case in inorganic semiconductors with high symmetries. However, for complex geometries on small scales and large local variations of quantities, e.g. charge densities, they can suffer from convergence problems. Furthermore, the implementation of single-particle effects and their time-dependency is not generally possible. Atomistic models, on the other hand, are not capable of modelling entire devices. While being more accurate, their computational demand quickly becomes unfeasible for even slightly larger physical structures (several nm).

In this work, a sophisticated, state-of-the-art 3D kMC model for OSC solar cells is described which is utilized to perform simulations of a full solar cell device under real operation conditions, while considering morphological and particle-based effects on the nanoscale. The spatially and energetically disordered morphology as well as the set of the major dynamic processes responsible for the time-dependent behavior of particles are implemented. A particular emphasis is laid on an elaborate treatment of the electrostatic interaction between all individual charges and the correlation effects arising herefrom. The developed model is able reproduce the solar cell characteristics and allows to evaluate quantities that are only accessible through microscopic modelling. Using this model, we evaluate the spatially resolved charge carrier distributions, charge mobilities, the time-dependent charge pair separation and recombination in OSCs as well as establish their link to the solar cell performance and identify the major loss mechanisms. A particular focus of the investigations is put on the influence of the two key factors permittivity and the energetic disorder, as well as the active layer morphology.

1.2. Outline and context of publications

At first, in Chapter 2, the fundamentals of solar cells – with the focus on organic materials as constituents – are presented. After a review of the operation principle of photovoltaic devices and an overview of established and emerging solar cell technologies in general, the specific properties of organic semiconductors, which differ significantly from inorganic semiconductors (in particular in terms of the energetic disorder and the permittivity), are introduced. The herefrom resulting implications for energy and charge transport in OSCs, as well as the role of the active layer morphology, are presented in the following in order to introduce the necessary theoretical background to understand the model implementations. Lastly, pathways how to improve the efficiency of OSCs are described briefly.

Chapter 3 presents the essence of the kMC algorithm. A brief historical review of the development of kMC simulations and its versatile applicability gives the reader an impression of the scope of kMC simulations. It follows a mathematical derivation of the algorithm and a blueprint of the general flow of the application of a sequential kMC algorithm. Parts of Chapter 3 have been published in [32].

Chapter 4 merges the two preceding chapters and shows the specific implementation of the fundamental processes in OSCs into an event-based kMC framework to form a comprehensive, three dimensional model for OSCs. The beginning of the chapter provides a literature survey of state-of-the art modelling approaches for OSCs and highlights the specific advantages of the implementation that is used within this thesis. Then, the setup of the device and the implementation of all processes is described in detail. The input parameters and evaluation details are presented and their applicability is discussed.

After the theoretical background and the description of the model, the following four chapters present different applications of the kMC model to address current issues in

OSC research.

In Chapter 5, the need for a 3D model of the active layer morphology is highlighted by comparing the kMC model to a Drift-Diffusion (DD) implementation. This is particularly important in Bulk-Heterojunction (BHJ) OSCs because the important processes for the generation of photo-current, i.e. the transition from optical excitation to free charges, occur at the heterojunction interface. We show that these processes cannot be captured by reducing the active layer to an effective medium with effective solar cell parameters. The differences between the models are elucidated by comparing the device characteristics and the charge carrier distributions within the active layer. The content of this chapter has been published in [33].

In continuation to the drawbacks of the 1D model, which concern mainly interface effects, it follows in Chapter 6 a demonstration of what can be achieved with the 3D kMC model: the distribution of charge carriers within a bulk-heterojunction organic solar cell and its performance are investigated with respect to the energetic disorder and the permittivity. It was found that charges in low-permittivity and highly disordered organic blends accumulate at the heterojunction interface, which has a considerable effect on charge recombination, which we quantify in turn. The results presented in this chapter are based on [34].

Next to the analysis of steady state quantities, Chapter 7 demonstrates the power of a time-dependent kMC model: the separation dynamics of exciton-generated electron-hole pairs from the BHJ interface are explicitly extracted, statistically analyzed over a large set of charge pairs and separation times are quantified. The separation times in dependence of the permittivity and the disorder are put into relation to the recombination times as the loss mechanism competing with separation. This exceeds the capabilities of continuum models, which lack the consideration of the underlying behavior of single charges. It is shown that even small changes in permittivity and disorder can outweigh orders of magnitude of recombination rates, which allows to formulate guidelines for optimization of the separation process. The results presented in this chapter are based on [35].

Chapter 8 shows that the kMC model is not only able to help understand effects in BHJs but also in newly arising OSC device architectures. In a joint experimental and numerical study, we present a model explaining the origin of photocurrent in fullerene-based solar cells with low donor concentrations. The results provide a theory for the not yet understood working mechanism of OSCs at low donor concentrations below the percolation threshold. The content of this chapter has been published in [36].

In the end, Chapter 9 provides a summary and a conclusion.

1.3. Preliminary work

Preliminary work carried out within T. Albes, “Kinetic Monte Carlo Modelling of Bulk-Heterojunction Organic Solar Cells”, Diplomarbeit (unpublished), submitted to the Department of Physics, Technical University of Munich, Munich, Germany (quoted [37]

in the following), in May 2014 by me, Tim Albes, has been incorporated into this thesis in agreement with the doctoral supervisor Prof. Dr. Alessio Gagliardi.

During the preliminary work, the foundation for this work was laid and the core of the kMC model was set up. The theoretical background (Chapter 2 and Chapter 3) and the implementation of the model (Chapter 4) of the thesis at hand are based on [37] and are in parts identical to it. Chapter 2 and Chapter 3 are a summary of knowledge about OSCs and the kMC algorithm; they have been adapted from [37]. Chapter 4 is an updated version of the implementation described in [37].

Prior studies carried out within [37] include the validation of the model by comparison to experimentally fabricated solar cells as well as first investigations concerning the influence of the permittivity on device performance [38], [39].

The novel research results are presented in Chapters 5-8 and have been published in [33]–[36]. Parts of [33]–[36] have also been incorporated into Chapters 1-4.

2. Organic Solar Cells

This chapter aims to give an introduction into the field of solar cells and OSCs in particular. In the beginning, the basic working principles of solar cells and the figures of merit to characterize their performance are covered. A brief overview of existing solar cell technologies bridges the gap to novel device concepts, such as active layers based on organic materials. Organic materials exhibit fundamentally different properties in terms of charge carrier generation and transport than their inorganic counterparts. The concept of charge transport based on hopping between localized states in spatially and energetically disordered semiconductors and the implications of low permittivities, as inherent in organic semiconductors, on charge generation is explained. It follows a description of the key working processes that take place in OSCs from light absorption to power extraction. At last, the influence of different active layer morphologies is described and possible pathways to improve the efficiency of OSC are presented.

Some content of this chapter is based on [37] and is in parts identical with it.

2.1. Basic principles of photovoltaics

The underlying principle for the direct conversion of radiative energy to electrical energy is the photovoltaic effect, discovered by E. Bequerel in 1839 [40] and first explained by A. Einstein in 1905 [41]. It can be observed in semiconductors that are exposed to photons with energies larger than their bandgap energy. An incident photon can deposit its energy in the semiconductor and excite an electron from a bound state over the bandgap in an unoccupied state. This leaves a hole state behind. The charges can then be extracted to obtain an electric current.

Specifically, three essential steps are required to convert radiation energy into electrical energy:

1. Absorption of light and generation of electron-hole pairs
2. Separation of electron-hole pairs into free charges
3. Transport of free charges to opposite electrodes

Each device that is able to perform steps (1) to (3) is a solar cell. Therefore every solar cell consists of a structure to account for all of these processes.

At first, to make use of the incident light an appropriate absorber material as active layer must be used. Semiconductors are a suitable choice as active materials because their bandgap energy usually is in the energy range of photons from sunlight and allows

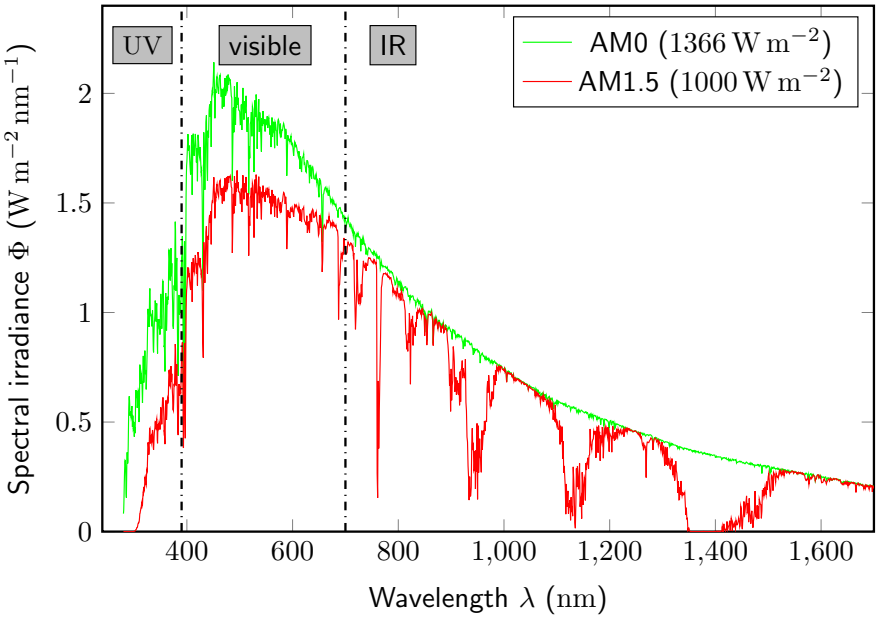

Figure 2.1. – Spectral solar irradiance. The AM0 spectrum corresponds to extraterrestrial conditions without absorption in the atmosphere. The AM1.5 standard with an integrated power of 1000 W m^{-2} resembles irradiance under an incident light angle of 48.19° on earth.[1]

excitation by the photovoltaic effect. The solar spectrum is shown in Figure 2.1. The AM0 condition is the measured spectral irradiance $\Phi(\lambda)$ of the sun outside of the Earth's atmosphere. Different absorption bands from gaseous H_2O in the Infra-Red (IR) and ozone (O_3) in the Ultra-Violet (UV), as well as scattering by dust and aerosols lower the effective radiation that reaches the Earth's surface and can be used by terrestrial solar cells (AM1.5 spectrum). As can be seen, the peak irradiance is in the visible range. A semiconductor with a bandgap E_g can only absorb photons with energies that are at least larger than its bandgap. Materials with a larger bandgap absorb less sunlight and are transparent to wider parts of the solar spectrum. For example, silicon has a bandgap of $E_g^{\mathrm{Si}} = 1.12\,\mathrm{eV}$ at room temperature. This corresponds to a wavelength of $\lambda = 1100\,\mathrm{nm}$. Silicon can therefore make use of photons that have wavelengths smaller than 1100 nm, i.e. the entire UV and visible spectrum, as well as a large part of the IR spectrum.

After the absorption, an electron-hole pair is formed. The electron is lifted to a higher, excited state and leaves an unoccupied hole-state behind. An excited state in a semiconductor can be imagined as a Coulomb-bound pair of electron and hole, called exciton. The binding energy of an exciton is inversely proportional to the permittivity ε_r (or: dielectric constant) of the absorbing material. In silicon, exciton binding energies are of the order of 10 meV and therefore less than the thermal energy $k_B T \approx 25\,\mathrm{meV}$.

[1] Data from National Renewable Energy Laboratory (http://rredc.nrel.gov/solar/spectra/am1.5/)

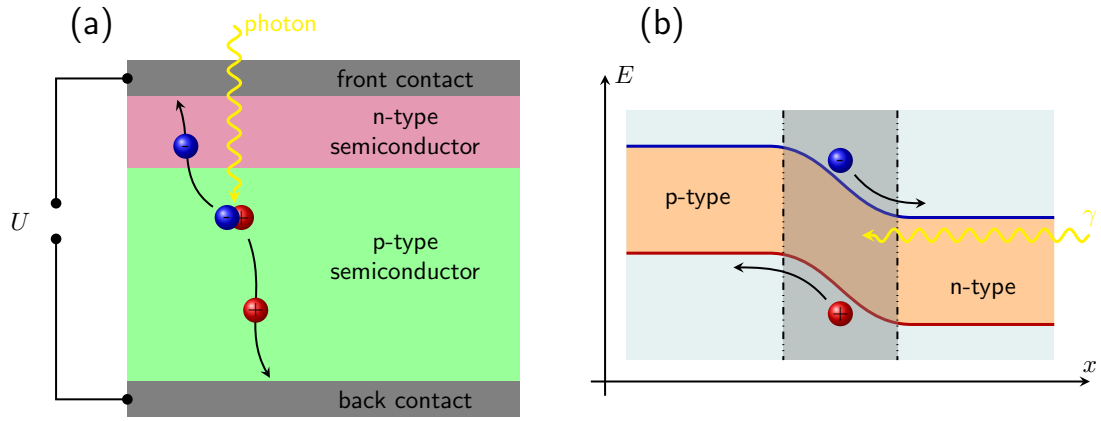

Figure 2.2. – Generic solar cell working principle. (a) The basic structure of a solar cell consists of an active layer in between two metallic contacts. A photon is absorbed in the active layer and generates an electron-hole pair. The pair must be separated and electron and hole driven towards opposite electrodes where they can be extracted and contribute to an external current. (b) A junction between n-type conductive and p-type conductive materials supports the separation of opposite charges and directs the current to obtain a direct current.

Excitons are either directly dissociated by the energy of the incident photon or by thermal fluctuations. For materials with low dielectric constants the introduction of special heterojunctions of a donor and acceptor material is needed to overcome the high binding energy. This is a crucial factor for the design of OSCs as will be discussed in Section 2.5.

Electrons and holes must be spatially separated and their flow directed to opposite electrodes in order to obtain a direct current. The desired transport is schematically indicated in Figure 2.2a. To direct electrons to one end of the cell and holes to the opposite side, the active layer is formed from a junction between an electron-conducting (n-type) and a hole-conducting (p-type) material. The energetic distribution of states in such a junction drives electrons into the n-type material and holes in the p-type semiconductor and restrains them inside the respective material as shown schematically in Figure 2.2b.

Electrons and holes can, depending on the specific material properties and the design of the cell, approach each other and recombine after a characteristic lifetime. The distance they diffuse during their lifetime is called the diffusion length. Classification into two different classes of solar cells is possible: if the diffusion length is sufficiently larger than the thickness of the active layer the cell can be operated as a diffusion cell where charges motion towards the contacts is driven alone by the concentration gradient of photoinduced charges; otherwise, an additional internal electric field is necessary to efficiently drive

electrons and holes towards the contacts and lower recombination. Diffusion cells are only applicable for materials with large charge mobilities, e.g. crystalline silicon. For low-mobility materials it is necessary to generate an internal electric field for example by controlling the size of the pn-junction by specific doping concentrations or using the potential drop over the active layer induced by a difference in the work functions of the electrodes.

Finally, charges arriving at an electrode contact need to be transferred to the metal. A charge carrier concentration gradient builds up a potential difference (the photo-voltage) that can be tapped to power an external load. Upon connecting the solar cell to an external circuit, the photo-voltage generated by the illumination leads to a photo-current through the connected load.

For each photon absorbed by the cell, only one electron-hole pair can be generated, which limits the achievable photo-generated electrical current that can be extracted from the cell. It would therefore seem plausible to use only low-bandgap semiconductors in order to absorb photons from a wide part of the solar spectrum. However, for photon energies that are larger than the bandgap the excess energy is lost by thermal relaxation to the edges of the bandgap. This limits the maximum achievable photo-voltage and hence the efficiency. On the other hand, large bandgaps reduce the amount of photons that can be absorbed by the semiconductor and therefore reduce the photo-current. The ideal configuration is therefore a tradeoff between current and voltage. Based on this principle, a theoretical limit for the performance of single-junction solar cells has been derived by Shockley and Queisser [42]. The so-called Shockley-Queisser-limit states the maximum PCE for a single-junction solar cell under standard AM1.5 illumination condition in dependence of the bandgap of the semiconductor. The ideal bandgap is derived to be approximately 1.34 eV, for which a maximum PCE of 33.7 % can be achieved [1]. In OSCs, the intermediate step of exciton separation and the lower charge mobility decreases the maximum achievable PCE. The limit was extended to OSCs with maximum PCEs of 23 %-27 % [22], [43].

2.2. Characterization of solar cell performance

The relationship between current density output (j) and contact potential drop (U) of a solar cell device under illumination and load provides the important Current Density-Voltage (j-U) characteristic. It is used to evaluate the performance of a solar cell and to extract figures of merit. The current density is defined by $j = \frac{I}{A}$, where I is the absolute current through the surface area A of the cell.

The typical j-U-output characteristic of a solar cell with and without illumination is illustrated in Figure 2.3. Depending on the operation regime (i.e. the applied load), the cell exhibits different current outputs and potential drops:

- At negative bias ($U < 0\,\mathrm{V}$) the current saturates asymptotically against the so called generation current (j_g) and is determined by the illumination and electron-hole pair

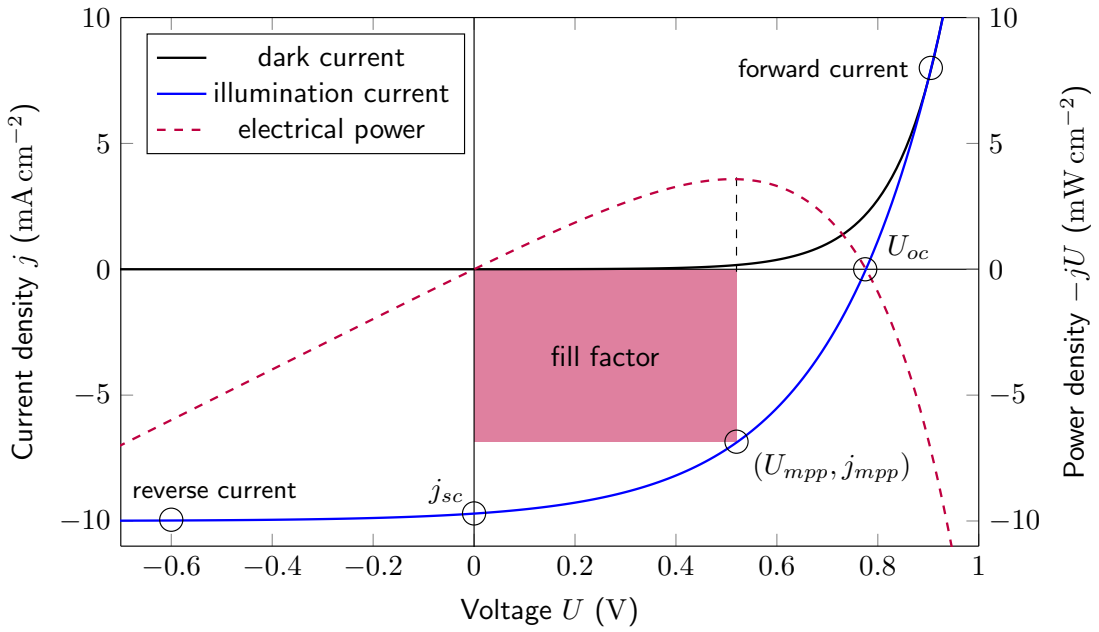

Figure 2.3. – Typical j-U behavior of a solar cell with important figures of merit. Illumination shifts the dark current characteristic by the generation current in reverse current direction. The short circuit current j_{sc}, open circuit voltage U_{oc}, and fill factor FF are the important quantities to characterize the solar cell performance.

generation. Separated electrons and holes are transported to the cathode and anode, respectively, defining the reverse current direction. The charge migration is more efficient for larger (negative) voltages and the saturation current is reached when all electrons and holes from dissociated excitons are collected and none recombine on their way. The cell dissipates power in this regime (photodetector regime).

- At no potential drop ($U = 0\,\mathrm{V}$), the short-circuit current (j_{sc}) is defined. Usually $|j_{sc}| \leq |j_g|$, because at short-circuit condition a finite amount of recombination occurs.

- Voltages between $U = 0\,\mathrm{V}$ and $U = U_{oc}$ are the regime in which a photovoltaic device is operated because power can be extracted from the device here. The electrical power throughput of a cell is $P_{cell} = I \cdot U = j \cdot A \cdot U$. By definition, a negative P_{cell} means that electrical power is released by the cell, while a positive value stands for power dissipation. To extract the highest possible power from the solar cell it has to be operated at the Maximum Power Point (MPP) (U_{mpp}, j_{mpp}) where P_{cell} is maximized: $P_{mpp} = j_{mpp} \cdot A \cdot U_{mpp}$. The shape of the j-U curve in this regime is crucial for the solar cell performance. This can be visualized by observing

the fill factor

$$FF = \frac{P_{mpp}}{j_{sc}\, A\, U_{oc}} = \frac{j_{mpp} U_{mpp}}{j_{sc} U_{oc}} \tag{2.1}$$

which represents the relation of the extracted power to the maximum possible power given by the product of short-circuit current and open circuit voltage. With increasing applied voltage charge carriers experience a decreasing driving force towards those electrodes at which they need to be extracted for a negative current. Consequently, recombination as well as extraction at the wrong electrodes increases which lowers the extracted power.

- At the open-circuit voltage U_{oc}, the net driving force for charge carriers to either electrode is zero. Such a balanced transport in positive and negative current direction yields no net current, which is the definition of the open circuit voltage $j(U_{oc}) = 0$. Large recombination of free charge carriers can be observed here, because the Coulomb interaction is the only force acting and driving electrons and holes to approach each other.

- For even larger voltages $U > U_{oc}$, generated charge carriers are mostly extracted at the wrong electrodes – in terms of solar cell operation. The cell exhibits an exponentially increasing current behavior in forward direction, generated by charges that were injected at electrodes and made their way through the active layer.

If no illumination is present, normal diode behavior is observed: a small current due to thermally activated charge carriers at voltages smaller than the open circuit-voltage and an exponential increase afterwards.

A large fill factor is obtained when j rises abruptly as U approaches U_{oc}. The overall PCE of a solar cell, η, is given by the relation of the highest extracted electric power P_{mpp} to the incident spectral power P_γ

$$\eta \;=\; \frac{P_{mpp}}{P_\gamma} \;=\; \frac{j_{sc}\, A\, U_{oc}\, FF}{P_\gamma}, \tag{2.2}$$

and is characterized by the quantities j_{sc}, U_{oc}, and FF. The incident spectral power is the integral of the spectral irradiance (Figure 2.1) over all incident wavelengths λ and the area of the cell A, $P_\gamma = \int d\lambda\, \Phi(\lambda) \cdot A$. Increasing any of j_{sc}, U_{oc}, FF (and not decreasing one of the others at the same time) increases the overall efficiency.

From a more microscopic point-of-view, η can alternatively be expressed by

$$\eta \;=\; \eta_{abs}\, \eta_{exs}\, \eta_{col} \;=\; \eta_{abs}\, \eta_{exs}\, (1 - \eta_{ehr}) \tag{2.3}$$

as the product of efficiencies of all contributing internal processes, namely the light absorption efficiency η_{abs}, the efficiency of exciton separation η_{exs}, and efficiency of the charge migration to and collection by the electrodes η_{col}. The latter can also be expressed by its complementary process, the charge recombination efficiency η_{ehr} as $(1 - \eta_{ehr})$. These quantities are important when it comes to relating the internal charge processes to the macroscopic figures of merit of an OSC.

2.3. Solar cell technologies

The discovery of the first solar cell dates back to the 1880s [44]. It was based on selenium and had a PCE of around 1 %. Further research on photovoltaic technology was then suspended for a long time due to the reliance on fossil fuels during the proceeding industrialization. More than 70 years later, in 1954 at Bell Laboratories, a silicon solar cell with an efficiency of 6 % was developed [45]. Since then, a variety of different solar cell technologies have emerged and can roughly be categorized into three different generations, based on the materials used as absorber and their device architecture.

First generation solar cells are based on crystalline silicon (c-Si) and they account for more than 90 % of the worldwide solar cell share in terms of production [46]. The efficiency of monocrystalline silicon cells (mono-Si) has been improved to 26.7 % [47] and is approaching its theoretical efficiency limit of 29.4 %, based on the Shockley-Queisser limit for its bandgap of 1.12 eV [48]. The large efficiency is a result of the high purity of mono-Si and its favorable bandgap energy. Despite its advantages of being abundantly available and non-toxic and although the manufacturing process has received great benefit through the semiconductor industry, the fabrication of mono-Si is expensive due to the high-temperature processes required to grow the highly purified crystals. Furthermore, due to the indirect bandgap of Si and the resulting low absorption coefficient, silicon solar cells need to have thicknesses of several hundreds of µm in order to efficiently absorb incident light, thus requiring large amounts of material. Poly-crystalline (poly-Si) wafers are only partially crystalline with grain boundaries between the crystalline regions. Poly-Si is easier to process and solar cells made from poly-Si absorption layers are a tradeoff between lower production cost and decreased efficiency of about 22.3 % [47].

According to the price learning curve [46], for a doubling in cumulative solar cell production, the module price has dropped by an average of 24 % since the 1980s. However, since the efficiency of pure silicon solar cells is slowly reaching the theoretical maximum and a minimum thickness (i.e. a minimum amount of material) is required in order to efficiently absorb light, this will eventually lead to a power-to-cost ratio for mono-Si based solar cells that cannot be improved any further. Thus, different solar cell technologies have gained research interest.

Second generation solar cells are so-called Thin-Film (TF) solar cells. These are made of thin films of semiconductor materials such as amorphous Si (a-Si), microcrystalline Si (µc-Si), Copper Indium Gallium Selenide (CIGS) or Cadmium Telluride (CdTe). TF solar cells emerged due to expectations for low production costs and minimal material consumption, which make these cells more attractive for industrial applications.

a-Si and µc-Si differ from c-Si as they generally lack a long-range order in the arrangement of the Si atoms. While a-Si is completely disordered, µc-Si (better called nc-Si) forms partially crystalline regions (nanocrystals, nc). The disordered arrangement leads to many defect states in the form of dangling bonds (a hybrid silicon orbital without a bond). These defects act as recombination centers and lower the effective charge mobility which has a negative influence on device performance. The dangling bonds are

commonly passivated by hydrogen atoms which yields a-Si:H or nc-Si:H with improved electronic properties. Due to their (partially) amorphous structure both a-Si and nc-Si effectively exhibit a direct bandgap and show better absorption coefficients than c-Si. Therefore, smaller thicknesses are sufficient to absorb the solar spectrum. The record PCEs of a-Si cells is 10.2 % while nc-Si based cells achieve an efficiency of 11.9 % [47]. Due to lower processing temperatures the fabrication of a-Si or µc-Si is cheaper. However, the biggest disadvantage of disordered Si cells is their degradation due to illumination (Wronski-Staebler effect).

CIGS and CdTe TF cells were developed because of their high stability and good efficiencies. These cells are also much less expensive to produce than c-Si cells. CIGS cells have the highest efficiencies of TF cells with 21.7 % [47]; CdTe cells have an efficiency of 20.0 % [47].

Although these TF solar cells are competitive to the first generation solar cells because of lower costs and good efficiencies, they have some drawbacks. Except for a-Si, most of the materials that these cells are made of are either becoming increasingly rare and more expensive (In) or are toxic (Cd). Mass production of these solar cells would also require new facilities which increases the total production cost. Because of these drawbacks, another generation of solar cells has been inspired.

Third generation solar cells refer to a broad class of novel approaches for solar cells. The focus is laid on devices that combine the advantages of the first generation cells with those of the 2nd generation, namely a reasonably high efficiency for thin-films with large absorption, minimal material consumption, and the possibility for low-cost production on large scales. Some of the most notable concepts for third generation cells are Dye-Sensitized Solar Cells (DSSCs), perovskite solar cells, and OSCs.

DSSCs, also called Grätzel cells after their developer M. Grätzel, separate the absorption of photons from the transport of charge carriers [49]. A DSSC consists of a photosensitive dye that covers a porous wide bandgap titanium dioxide (TiO_2) anode and is immersed in an electrolyte. Solely the dye is responsible for light absorption. Dyes show good light incoupling and allow for a TF structure. After excitation, the electron is transferred from the dye to the TiO_2 which transports the charge out of the cell to an external circuit. The electrolyte is used to close the circuit and refill the dye with electrons. Grätzel cells are inexpensive to produce and reach efficiencies of 11.9 % [47]. However, the major challenge of DSSCs is their long-term stability. The electrolyte can leak from the cell if it is not properly encapsulated or it can lead to corrosion of the metal electrode. Another DSSC device architecture based on a substitution of the liquid electrolyte by a solid, organic semiconductors, solid state DSSC [50], can help resolve these problems.

Another notable material for solar cell application is the methylammonium lead halide perovskite $CH_3NH_3PbX_3$, where X can be either of the halides Cl, Br, or I. Perovskites have received great attention since they were found to be an effective absorber in mesoporous TiO_2 (just like the dye in DSSCs) in 2009 [51]. It was found that the mesoporous structure is not required for an effective solar cell and stable, TF absorbing

layers could be formed from planar perovskite layers alone, acting both as electron and hole transporter [52]. Both mesoporous and TF perovskite devices are intensely researched and achieve record efficiencies 20.9 % to 22.1 % [47], [53]. Problems with perovskite-based solar cells include long-term stability, a hysteresis effect attributed to migrating ions, and the toxicity of lead on which the best-performing devices depend (lead-free devices show lower performances).

Finally, OSCs based on semiconducting polymers and small organic molecules have emerged as candidates for next-generation solar cell applications. OSCs are classified as such because their absorption and transport layer consists entirely of organic materials. A major advantage of polymer based devices is the possibility to process them by roll-to-roll printing, spin-coating or spray-coating techniques at low temperatures. Thus they hold the possibility for a substantially lower manufacturing cost due to the compatibility to fabrications techniques that are highly scalable and require little energy. The large absorption coefficient of the order of $\alpha = 10^5\,\mathrm{cm}^{-1}$ allows for very thin (50 nm-200 nm) active layers with good light incoupling and low material usage. Additional interesting features are the mechanical flexibility and the low weight: many applications from small, mobile power units to charge smartphones or power wearable electronic devices up to the integration in architectural designs are imaginable. On the downside, OSCs still struggle with long-term stability and lack in PCEs.

The PCE of OSCs is not yet competitive with the efficiencies of 1st and 2nd generation solar cells. This is due to the fact that the charge generation, transport and loss mechanisms in organic semiconductors and devices build from them are, due to their low permittivity and disordered structure, fundamentally different from those of inorganic semiconductors and are not as well understood. The efficiencies for single junction OSCs to date are around 13 %-14 % [16]–[18]. Thus, optimization and a better understanding of the internal processes by experiment and theory is needed to further improve their efficiency. The following chapters are aimed to give a basic introduction into the theory of organic materials and the working principles of OSCs.

2.4. Organic semiconductors

Semiconducting organic molecules are the basis for organic optoelectronic devices such as OSCs. In contrast to conventional inorganic semiconductors, in which either single elements (e.g. Si, Ge) or atomic compounds (e.g. GaAs, InGaAs) in a periodic arrangement represent the building blocks of a crystal, organic semiconductors are a composition of organic (i.e. Carbon-based) molecules. These are typically conjugated polymers or polycyclic aromatic compounds, which exhibit the necessary energetic configuration for charge conduction. However, in organic solids, much weaker inter-molecular forces are present which leads to fundamentally different electrical and optical properties compared to conventional semiconductors. The basics of the energetics of organic semiconductors as well as their electrical and optical properties shall briefly be introduced here. More

details about the properties of organic semiconductors can be found in [54], [55].

2.4.1. Energetic structure

The chemical element carbon (C) is the basis for all organic matter. Carbon is extremely versatile and can form bonds with almost every element of the periodic table. Thus, a vast number of organic compounds is known and they can be classified into several major material classes. Among these, polymers and small molecules that contain conjugated π-systems are the most important for OSCs. A brief description of how conjugated systems and their energetic structure originate from single carbon atoms is given here.

Molecules are comprised of a set of nuclei and electrons. Such a multi-particle system can, in principle, be fully described by the Hamilton operator considering the kinetic and potential energy terms of all constituents. However, for more than two particles the Schrödinger equation cannot be solved analytically and one must rely on different concepts in order to obtain the wave functions (representing the Molecular Orbitals (MOs)) and the eigenenergies (representing the MO energy levels) of the Hamiltonian (representing the molecule). There exist several different approaches to construct suitable wave functions for molecules in quantum chemistry; the focus here is laid on the MO theory and the concept of hybridization. While the former provides a good understanding of the spectroscopic properties of a molecule, the latter is more useful when it comes to the spatial arrangement of atoms in a molecule (bonding angles and interatomic distances).

In MO theory, electrons are not seen to be associated to a single nucleus but rather to the molecule as a whole. Charge carriers are distributed over the dimensions of the entire molecule. In a Linear Combination of Atomic Orbitals (LCAO) approach MOs are formed from the atomic orbitals of atoms in their ground state. In general, the combination of n atomic orbitals yields n MOs. Charges reside in the MO energy levels instead in distinct atomic orbitals. But how do MO energy levels originate from single atoms? The underlying mechanism is that the Coulomb interaction of multiple nuclei acting on charge carriers lifts the degeneracy of the identical energetic states of single carbon atoms. This leads to a splitting of the degenerate energetic states when they are brought together so close that their atomic orbitals overlap. In the case of just two atomic orbitals with one electron participating in the bonding process one so-called bonding and one antibonding state are formed. This is indicated schematically in Figure 2.4. As one can see in the MO-diagram (Figure 2.4, right hand side), the bonding state is energetically lower than the single atomic states, which makes it the favorable state to occupy. When two electrons, one of each of the two atoms, lower their energy by sharing a bonding state, the atoms form a bond. The resulting antibonding state would lead to an increase in energy and is not occupied in the ground state.

Carbon atoms can adopt different energetic configurations depending on the environment they are surrounded with. Figure 2.5 illustrates different configurations of carbon. In its ground state, a single carbon atom has an electronic configuration of $1s^2 2s^2 2p^2$

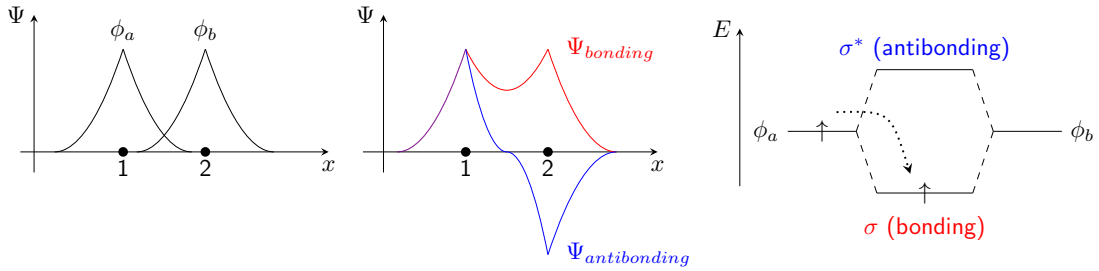

Figure 2.4. – Overlap of atomic wave functions ϕ leads to formation of bonding and antibonding states.

with two localized electrons in the inner $1s$ shell, two electrons in the fully occupied $2s$ shell, and the two remaining electrons in two different outer orthogonal $2p$ orbitals, e.g. p_x and p_y (Figure 2.5a). For a chemical bond usually only the valence electrons are considered since the inner orbitals are strongly localized around the nucleus (indicated as yellow sphere in Figure 2.5a). For the concept of hybridization, in contrast to MO theory, only the interaction between two individual atomic orbitals is considered instead of orbitals from all atoms. An at first glance energetically unfavorable configuration is the promotion of one inner $2s$ electron to the third unoccupied p_z orbital. This sets the carbon atom in an excited configuration $1s^2\,2s^1\,2p_x^1\,2p_y^1\,2p_z^1$. By a linear combination of the four now singly occupied orbitals four tetragonal sp^3 *hybrid atomic orbitals* can be formed (see Figure 2.5b) which are occupied with one electron each. Such hybrid atomic orbitals can now interfere with another, also hybridized atomic orbital of a neighboring atom and can split the degenerate energy level into a bonding and anti-bonding state. The bonding configuration can be favorable when the energy gained from the two atoms sharing their electrons in the respective orbital is larger than the promotion energy for the hybridization. The bond between two hybrid orbitals is aligned along the axis through the nuclei of the corresponding atoms, which is called a σ-bond. Because one sp^3 orbital can form exactly one bond with another atom, they are called *single bonds* in chemical terms. This bond is predominant in classical inorganic semiconductors like silicon and germanium, or organic molecules where the C atom has four equivalent bonds like in methane.

Alternatively, instead of four tetrahedrally aligned hybridization orbitals, the formation of three trigonal-planar sp^2 orbitals separated from each other by an angle of 120° is possible following the same principle as described above. In this case, only two $2p$ orbitals and the $2s$ orbital form hybrid orbitals while the third p_z orbital remains unaffected and is aligned orthogonally to the sp^2 orbital plane (Figure 2.5c).

The sp^2 configuration is of special importance for the concept of conjugated systems in organic materials. Figure 2.6 illustrates the bonding mechanism and its effect on the electronic configuration of the MOs in sp^2-systems. The sp^2 orbitals can form σ-bonds with neighboring orbitals by splitting in a bonding and a antibonding state. The crucial

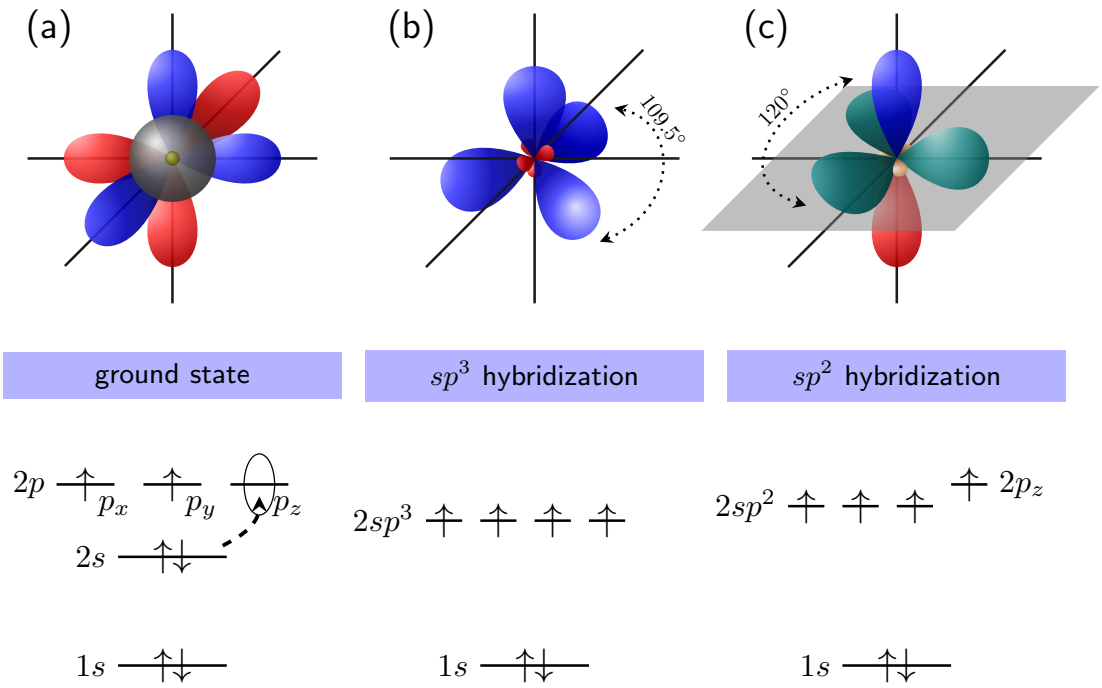

Figure 2.5. – Atomic orbitals of carbon in the ground state (a) have fully occupied $1s$ and $2s$ shells, while the remaining p_x and p_y orbitals are partially filled with one electron each. In the sp^3 configuration (b), four equal hybrid orbitals, separated by an angle of 109.5°, are formed from intermixing of the $2s$ and $2p$ atomic orbitals. Each of the orbitals is occupied by one electron and is able to bond to a neighboring atom by a single σ-bond. Alternatively, three sp^2 orbitals can be formed (c) which are separated by 120° in a plane perpendicular to the unaltered p_z orbital.

difference in this configuration is that the unhybridized p_z orbitals (reaching vertically out of the plane) also overlap, although to a smaller extent, and form an additional, weaker bond which is called a π-bond. The combination of σ- and π-bond is known as a *double bond*. Because the overlap and therefore the bonding energy of π-bonds is weaker, electrons are not as strongly localized in between the nuclei and are extended over the participating atoms. The consecutive alternation between single and double bonds in a molecule consisting of more than just two carbon atoms is called *conjugation*.

The overlap of multiple (degenerate) p_z-orbitals in polymers or aromatic rings leads to a division into further energy levels. The weaker binding energy of a π-bond as compared to a σ-bond reflects in the energy levels of the MO: the energy level splitting due to the degeneracy lifting of the p_z orbitals $E(\pi \rightarrow \pi^*)$ is smaller than $E(\sigma \rightarrow \sigma^*)$, therefore the π/π^* states represent the frontier orbitals of the molecule, which in turn determine its electronic and optical properties. Electrons successively fill the resulting MOs from the ground state up under consideration of the Pauli exclusion principle. The energetic

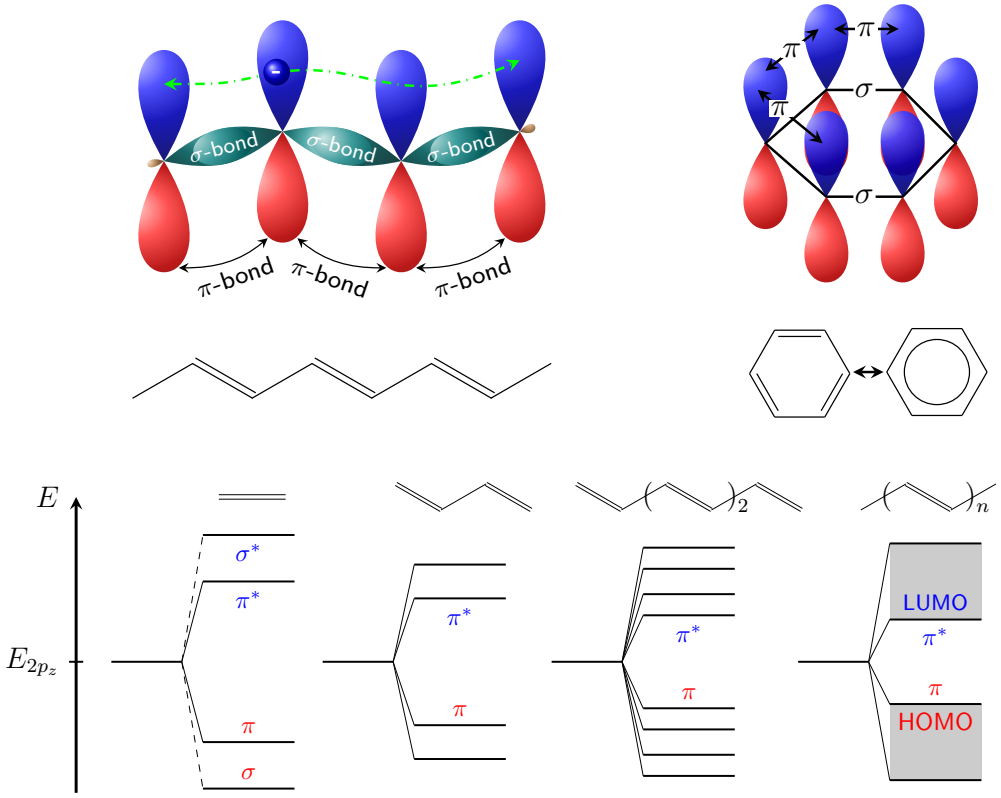

Figure 2.6. – Overlap of frontier p_z orbitals determines the electronic properties of organic molecules. (top) Overlap along a chain segment of polyacetylene (polymer) and the benzene (aromatic small molecule) leads to charge delocalization over the molecule. A combination of these linear and ring shaped systems forms the basis for many important conductive polymers. (bottom) Lifting of the degeneracy of π-states forms MO states including the HOMO and LUMO.

states of the Highest Occupied Molecular Orbital (HOMO) and the Lowest Unoccupied Molecular Orbital (LUMO) can be introduced in analogy to the valence and conduction band in inorganic semiconductor physics. The bonding state π with the highest energy is the HOMO energy level, while the anti-bonding state π^* with the lowest energy level is the LUMO level. HOMO and LUMO are separated by an energetic bandgap E_g which is typically between 1.5 eV and 3 eV [55].

In case of a widely extended periodic arrangement the band-structure theory of semiconductors applies and the frontier orbitals exhibit sharp edges in form of the conduction and valence band edges. A periodic overlap of the p_z orbitals can then lead to charge conduction, which is is the case in highly ordered organic crystals. However, generally in organic solids the structural configuration can differ strongly from a periodic arrangement. As shown in Figure 2.7, the backbones of aromatic rings and conjugated

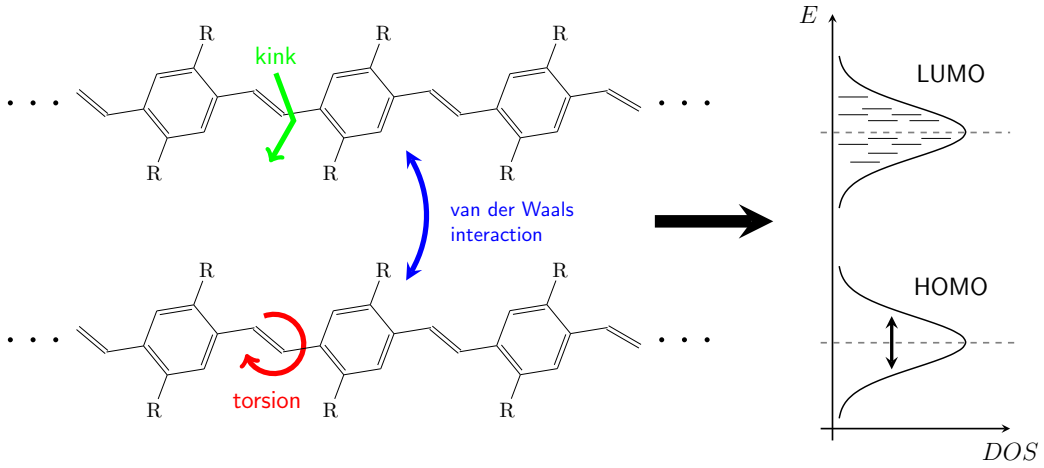

Figure 2.7. – Structural disorder in the form of torsion and kinks induced by weak inter-molecular interactions broadens the MO energy levels.

chains are covalent (σ) bonds between carbon atoms in sp^2 hybridization – they form the basic structure of the molecules. However, the inter-molecular forces between organic molecules are dominated by much weaker and locally varying van der Waals-interactions, dipole-dipole interactions and hydrogen-bonds. This leads to kinks and twists of the molecules, as well as different inter-molecular distances. Thus, the periodic arrangement is disrupted and with it the p_z overlap, which affects charge delocalization and therefore alters charge conduction. Together with different side-chains, finite and different molecules sizes as well as impurities, the energetic structure of organic molecules is often strongly disordered. No bandstructure can generally be defined for solids from such disordered constituents and one must rely on the more general concept of a Density of States (DOS) in order to describe their energetic configuration. The effect of structural disorder on the broadening of the frontier energy levels is illustrated in Figure 2.7. The sharp band edges are broadened by the *energetic disorder* around the intrinsic HOMO and LUMO energy levels.

One should distinguish between the intrinsic DOS as a broadening induced by the structural disorder of the material (around HOMO/LUMO energy levels, of the order of 100 meV) and the extrinsic DOS, introduced by defects usually deep within the bandgap and of the order of several hundreds meV. In this work, we only consider intrinsic disorder.

Due to the disorder, charges tend to get confined in local potential valleys of the DOS. They are therefore not delocalized but rather localized to certain units or sub-units (e.g. monomers of a polymer) of a molecule. This has important implications on charge transport, as will be discussed next, which takes place by a hopping mechanism between localized states instead of by delocalized band transport.

To quantitatively describe the distribution of the localized states around the respective

HOMO and LUMO energies a Gaussian DOS or an exponential DOS is commonly used to describe the disorder. During this work, we will only consider a Gaussian DOS of the form

$$g(E) = \frac{N}{\sqrt{2\pi\sigma^2}} \exp\left(-\frac{(E-E_0)^2}{2\sigma^2}\right) \tag{2.4}$$

where N is the available density of localized states, E_0 is the center of the HOMO or LUMO level, and σ is the energetic disorder. Such a DOS has been introduced by Bässler [56] and was confirmed to be a suitable description of the disorder in organic semiconductors.[57], [58]

Semiconductivity in organic materials

Semiconductivity is not narrowly defined and the distinction from insulators is somewhat fluent. One of the common definitions is that the conductivity of a semiconductor can be modified over several orders of magnitude by introduction of impurity states via dopants. In the ground state, organic materials are usually insulators due to their high bandgap of 1.5 eV to 3 eV. Their HOMO states are all occupied and full bands cannot contribute to charge transport. To exhibit intrinsic conductivity at room temperature there must be a sufficient number of electrons thermally excited into LUMO states because here free states are available for transport. However, the valleys of the energetic disorder act as defect states that compensate any thermally excited charge carriers by trapping them. An introduction of a certain amount of external charges is necessary to observe a measurable conductivity in organic materials. This was first observed by introducing additional charges by doping organic molecules: in 1976 Shirakawa, MacDiarmid and Heeger showed that the conductivity of the polymer polyacetylene could be modified over a wide range by doping it with large amounts of iodine. They were awarded with the Nobel Prize in Chemistry in 2000 [59] for this discovery. In terms of the definition given above this makes polyacetylene doped with iodine a semiconductor. In general, to make organic materials semiconducting, additional charges must be introduced, be it from dopants, by injection from an adjacent metal, or by illumination. Depending on which charge types are introduced the terms n-type and p-type organic semiconductor can be applied. Additional charges first successively fill the defect states. If a sufficient amount of charges to fill the low levels in the DOS is introduced, charge conduction is possible.

2.4.2. Charge transport

In crystalline inorganic semiconductors, electrons under the influence of a periodic lattice potential are described by Bloch-waves, i.e. a free wave with a modification factor due to the periodic lattice. Scattering and deviations from the otherwise ballistic transport only occurs due to impurities. For low impurity concentrations, the mean free path of charges

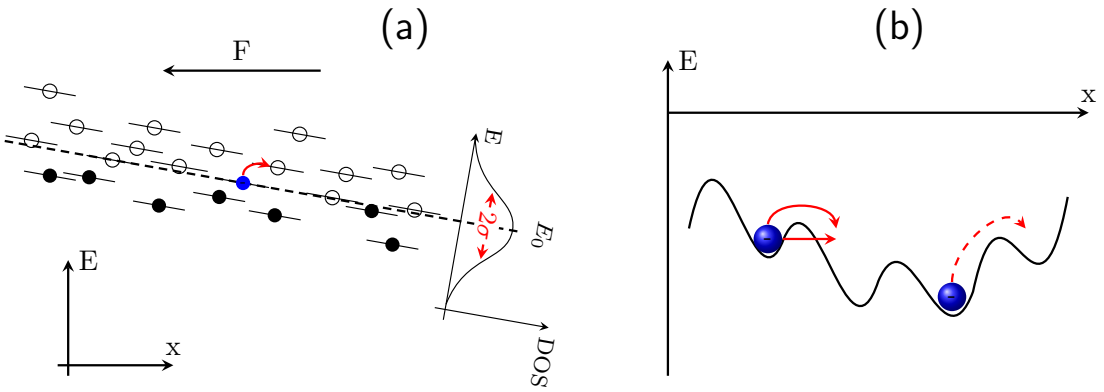

Figure 2.8. – (a) Hopping transport in disordered organic systems can be described by a Gaussian distributed modification of localized state energies around the MO energy levels. Driving forces for hopping processes are thermal activation and the influence of an electric field. (b) Hopping transport as a combination of tunneling and thermal activation.

is large and extends over many atoms in the solid. This leads to mobilities of the order of e.g. $10^3\,\mathrm{cm^2\,V^{-1}\,s}$ in Si.

In organic disordered systems, due to the lack of a long-range order, the mean-free path before charges find a deviation from the periodic arrangement is small. Charges are confined to localized states with a localization length of the order of $\alpha = 0.1\,\mathrm{nm} - 1\,\mathrm{nm}$ [60], [61]. Charge carrier transport is described as an incoherent tunneling process from one localized state to another, commonly called a *hopping* transport process. Hopping transport as the dominant transport mechanism in organic disordered systems and OSCs has been generally agreed on [54], [55], [62]. An illustration of the hopping transport in a Gaussian DOS is depicted in Figure 2.8a. Consequently, a reduction in mobility is observed for hopping transport, the charge mobility in organic semiconductors is limited by the hopping mechanism. Typically, charge mobilities in disordered organic systems can be as low as $10^{-5}\,\mathrm{cm^2\,V^{-1}\,s^{-1}} - 10^{-3}\,\mathrm{cm^2\,V^{-1}\,s^{-1}}$ [8] and therefore many orders of magnitude lower than in crystalline inorganic semiconductors.

A model to describe hopping processes in disordered systems is the Miller and Abrahams model [63] (see also Section 4.3.5):

$$a_{hop} = a_0 \cdot \exp(-2\gamma r) \begin{cases} \exp\left(-\frac{\Delta E}{k_B T}\right) & \text{for} \quad \Delta E > 0 \\ 1 & \text{for} \quad \Delta E \leq 0 \end{cases} \tag{2.5}$$

The hopping rate a_{hop} is given in s^{-1} and depends on the so called attempt-to-hop frequency (or maximum hopping rate) a_0 which is of the order of the typical phonon oscillation frequency at room temperature (about $10^{12}\,\mathrm{s^{-1}}$), the inverse localization constant $\gamma = \alpha^{-1}$, the distance between localized states r, and the energy level difference

between initial and final localized state with respect to the thermal energy $\Delta E/k_BT$. The Miller-Abrahams model is divided in a tunneling part and a thermal activation part. The potential energy landscape of an electron in a disordered material is indicated in Figure 2.8b. A tunneling process is more likely if the tunneling distance (or hopping distance) r is smaller and if the overlapping integral which is inversely proportional to γ is larger. On the other hand, a carrier can gain energy by absorbing a phonon and get thermally activated. This process is dependent on the energetic difference ΔE of the initial and final localized state and is described by the Boltzmann factor $\exp(-\Delta E/(k_B\,T))$.

Bässler utilized the Miller-Abrahams model to investigate charge mobility in a Gaussian density of states in dependence of the disorder σ, temperature, and applied electrostatic field by kMC simulations [56]. At larger disorder, the energy distribution of localized states around the HOMO/LUMO levels is widened. This can be imagined by the energy landscape in Figure 2.8b. On the one hand it is more unlikely to hop out of an energy valley with large disorder and on the other hand the states with increased energy are much harder to surmount. Thus, charge carriers get either trapped in a state with deep energy or have a hard time finding a subsequent pathway around energy peaks they can follow. This lowers the effective mobility. Excess charges introduced into the DOS first thermally relax into the lowest energy levels. Charge transport then takes place not around the intrinsic MO level but around a deeper transport energy $E_t = E_0 - \frac{\sigma^2}{k_BT}$. This relaxation is implicitly considered in the kMC simulations employed in this study.

Another commonly used model to describe charge transport by means of a charge transfer process between molecules is the Marcus model [64]. Additional charges on organic molecules can lead to a distortion of the molecule due to the charge. The complex of a charge and its deformation on the molecule is known as a quasi-particle called polaron. Polarons are basically lattice shifts within the molecule in order to compensate for the additional charge. This can lead to a "self-trapping" of the charge, which lowers their effective mobility. Marcus theory considers this effect by introducing a reorganization energy of the molecule due to the charge transfer process. The Marcus theory for charge transport is not used within this work, but shall be mentioned at this point for the sake of completeness.

2.4.3. Excitons

Upon illumination, organic molecules can be excited to a higher energetic state. Excitation corresponds to the interaction of an incident electromagnetic wave with the MO system (usually a π-π^*-transition) and can be represented in an MO diagram as the lifting of an electron from a HOMO to a LUMO state. This leaves an unoccupied hole state in the HOMO. When such an electron-hole pair is generated, the charges interact with each other via Coulomb force and are spatially localized. Because organic materials have a much lower permittivity ε_r than common inorganic semiconductors, electromagnetic forces are not well screened. With ε_r around 3 to 5 [65], the electron hole pair forms a bonding state with energies of the order of several 100 meV [8]. Bound electron-hole pairs

are know as *excitons* from inorganic semiconductor physics. In silicon, with $\varepsilon_r = 11.7$ excitons are weakly bound with energies of the order of 25 meV [66] and are termed Wannier-Mott excitons. For excitons with a sufficiently larger dissociation energy, as in the case of the discussed excitonic electron-hole pairs, the term Frenkel exciton is common.

Due to the strong bonding between electron and hole, the exciton is localized on e.g. one monomer of a polymer chain or on a small molecule. Excitons have a net charge of zero and do not contribute to an electric charge transport. By interaction with thermal oscillations (phonons) excitons can diffuse through the material. This can be seen as a hopping process from one localized state to another. Exciton motion represents an energy transport through the solid with no net charge transport. The excited state can decay after a characteristic lifetime of the order of ns by relaxation to the ground state by emission of a photon (radiative decay) or by releasing its energy in form of phonons (non-radiative decay).

In order to obtain a photo-current in OSCs, an additional design concept, namely the introduction of a donor/acceptor heterojunction, is required in order to provide the necessary energy to overcome the binding energy between the electron and the hole. This is a peculiarity of the operation principle in OSCs and will be discussed in the next section.

2.5. Organic solar cells

The essential steps taking place in an OSC from incident light to the extraction of a photo-current are briefly introduced in this section. For further details, many reviews about the physics behind organic solar cells can be found in literature [6]–[9], [67], [68].

2.5.1. Working principle and design

The geometrical structure of an OSC as well as its energetic configuration and a schematic representation of the working principle is illustrated in Figure 2.9.

In Figure 2.9a, a typical OSC device architecture is shown. The solar cell is fabricated on a transparent substrate, e.g. glass, representing the front side where the light incides. On top of the substrate, a transparent conductive oxide such as Indium Tin Oxide (ITO) forms the anode. The anode can be modified by a hole-transport (or electron-blocking) layer such as Poly(3,4-ethylenedioxythiophene)-poly(styrenesulfonate) (PEDOT:PSS), in order to provide a filter for charge carriers and alter the contact work function. Next, the active layer comprised of organic materials is the part which makes use of the incident photons in order to generate charge carriers. On top of the active layer, the cathode (e.g. Al) is deposited as the back-contact. Similarly to the anode, the cathode can optionally be modified by an electron-transport (or hole-blocking) layer. The internal processes of the OSC should direct positive charges to the anode and vice versa electrons to the cathode in order to generate a direct current that can be tapped by connecting the cell

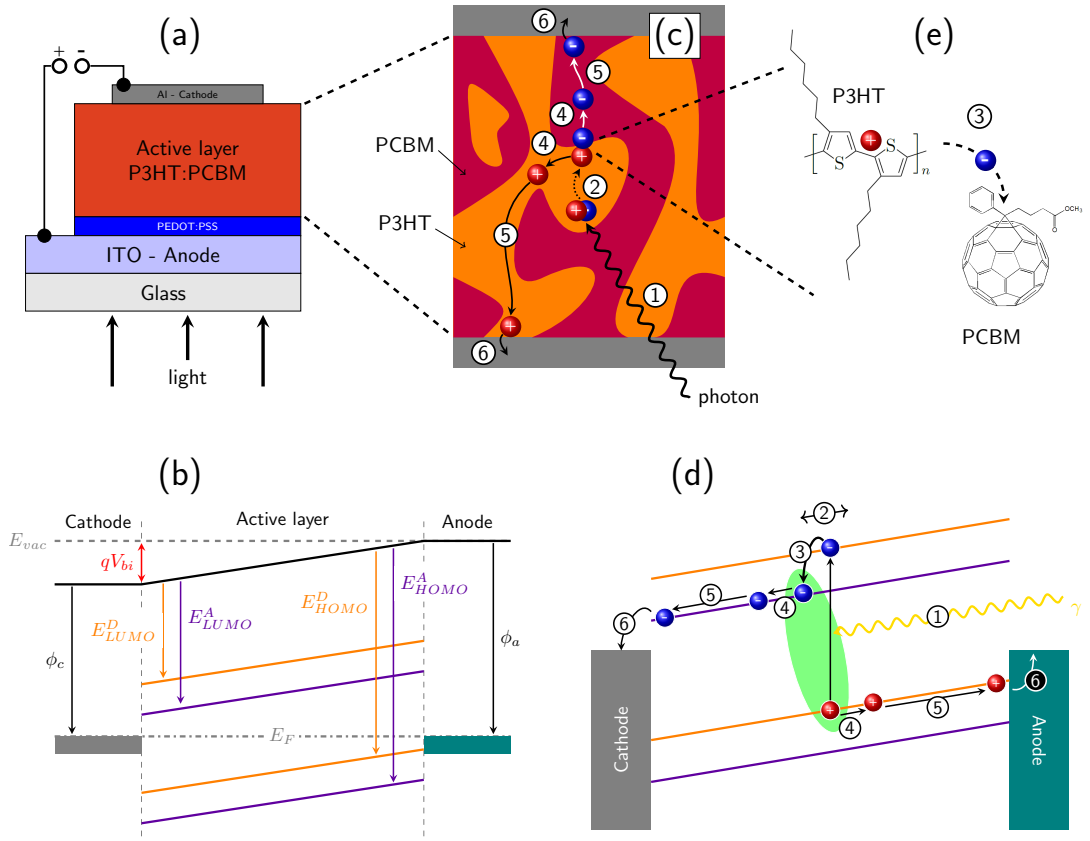

Figure 2.9. – Geometrical structure (a,c,e) and energetic configuration (b,d) of an OSC. On top: typical device architecture of an OSC (a), its active layer morphology (c), and an illustration of the charge transfer process (e) from donor to acceptor. At the bottom: energetic configuration (b) and working principle of an OSC in a schematic energy diagram (d). The key steps are indicated by numbers in the geometrical (c) and energetical picture (d): Incident light generates a strongly bound exciton (1). After diffusion of the exciton (2) to a donor/acceptor heterojunction, the exciton can dissociate into an electron and a hole by a charge transfer process (3). The electron-hole pair needs to separate against the mutual interaction of electron and hole (4), then the charges can percolate to the electrodes (5) and be collected (6).

to an external circuit.

In Figure 2.9b, the energetic configuration of the solar cell structure is shown. When forming a junction between the contacts and the active layer materials, the Fermi level E_F aligns across the entire device in the equilibrium state. In order to help direct positive and negative charges towards separate contacts, contacts with different work functions are utilized. Typically, the cathode is chosen to have a lower work function ϕ_c than the anode work function ϕ_a. Upon alignment of E_F, the difference in intrinsic work

functions of the metals $\Delta\phi = \phi_c - \phi_a$ induces a potential drop across the active layer. This built-in potential modifies the HOMO/LUMO energy levels of the organic materials in the active layer in a way that a driving force for electrons towards the cathode and vice versa for holes towards the anode is induced. The HOMO and LUMO energy levels of the donor and acceptor and their bending due to the built-in potential are indicated in Figure 2.9b: the donor HOMO and LUMO is denoted by E^D_{HOMO} and E^D_{LUMO}, the HOMO and LUMO energy level of the acceptor by E^A_{HOMO} and E^A_{LUMO}. The MO energy levels of the acceptor are deeper in energy than those of the acceptor in order to provide for the necessary energy difference to dissociate the strongly bound excitons.

Figure 2.9c and Figure 2.9d illustrate the key steps of photo-current generation from incident light in a spatial and energetical picture, respectively. At first, (1) a photon absorbed in the active layer can generate a strongly bound exciton. The exciton can then diffuse through the material (2). In order to generate charge carriers, the exciton needs to be dissociated into electron and hole. Due to their high binding energy of several hundreds of meV excitons cannot be dissociated at room temperature ($k_BT \approx 25\,\text{meV}$) or by excess energy of the photon and an additional process is required. For this purpose, the concept of a heterojunction comprised of two organic materials with a large difference in MO energy offset was introduced. The energy difference of the corresponding HOMO and LUMO states of the material must be larger than the dissociation energy of an excitonic state. When an exciton diffuses towards a donor/acceptor heterojunction a charge-transfer process is performed (3) that separates charges onto molecules of different species. Hence, materials that electrons are transferred to are called (electron-) acceptor materials, while those where the electron originated and in which the remaining hole resides are called (electron-) donor materials. The most prominent acceptor materials are derivatives of the Buckminster fullerene, Phenyl-C61/C71-butyric acid methyl ester (PCBM), because their large electronegativity has shown major improvement in exciton dissociation [69]. However, nowadays also non-fullerene acceptors are increasingly studied [70] on which the current record devices are based on [18]. For the donor molecules, one of the most widely studied materials is the polymer Poly(3-hexylthiophen-2,5-diyl) (P3HT), but also here many new molecules are actively being engineered [9]. The charge transfer process is indicated by (3), together with the molecular skeletal formulas of P3HT and PCBM in Figure 2.9e. Heterojunctions comprised of P3HT and PCBM are some of the most extensively studied compositions today and act as a benchmark device for comparison of novel devices. They are easy to process and show reasonably high efficiency of up to 5 % [71], [72].

After excitons have become dissociated at a heterojunction interface, the electron resides in the acceptor material and the hole stays in the donor phase. However, the charges are not free yet, as the electron-hole pair is Coulombically bound to each other. This state is often called a Charge Transfer (CT) state. In order to obtain free charges, the electron-hole pair needs to separate against their mutual interaction (4). The driving forces for this process are the internal electric field and thermal activation. Once the

charges have been separated, they can be transported in their respective transport phases (electrons in the acceptor, hole in the donor), driven by the electric field, towards the contacts. At the contacts, charges can be collected (6) and contribute to an external current.

Several loss mechanisms can occur in OSCs after the photon absorption that reduce the amount of generated photo-current: in case no junction between donor and acceptor is in range of the exciton diffusion length from the location where the exciton was generated (2), the exciton decays before it can be separated. In such a case the energy deposited by the incident photon is lost. Furthermore, charge recombination between electrons and holes can take place. If, during the initial charge separation process of electron and hole (4), the electron-hole pair does not manage to overcome their mutual attraction, it can recombine (geminately). After exciton dissociation and during the transport to the metal contacts (5), charge carriers can meet a charge of opposite type and recombine (non-geminately). Since electrons are transported in the acceptor material and holes in the donor material, recombination generally takes place at a heterojunction interface. Because of the low dielectric constant in organic materials, electrostatic interactions can have a considerably larger influence on the attraction between electrons and holes than in inorganics. Charges transported in their respective phases are attracted by the Coulomb interaction of opposite charges, driven towards each other at a heterojunction interface, and have an increased probability to recombine. Electrons and holes generated from exciton dissociation can either recombine with other exciton-generated charges or with charges injected from the electrodes. Experimentally, it is not possible to distinguish where a charge originated. If at all, only the absolute number of recombination processes can be investigated. With kMC simulations however, one is able to track every single charge and store its origin. It can be specifically distinguished which charges were involved and allows for an accurate determination of the recombination ratio.

2.5.2. Active layer morphology

The first OSCs were comprised of a single layer of an organic material in between two contacts [73]. These cells showed very low PCEs because the internal electric field is not sufficient to separate excitons and they had to rely on the dissociation of excitons at the contacts instead.

OSCs based on a heterojunction between two materials at first consisted of a planar structure of donor on acceptor material stacked on top of each other. This was realized by Tang [74] and led to OSCs of 1 % PCEs. In such a bilayer configuration free charges can only face charges of opposite type at the planar heterojunction. In their respective phase and on the way to an electrode, few to no opposite charge carriers are present. Therefore, this setup provides an efficient migration to the electrodes and minimizes recombination which can only take place at the donor/acceptor interface. The exciton dissociation efficiency was improved a lot by the introduction of fullerenes as acceptor materials [69], since then research focused on donor:fullerene systems. Nowadays, the

field of non-fullerene acceptors is emerging [70].

A major disadvantage of the planar heterojunction is the low exciton separation rate. An exciton can only diffuse a distance of the order of 10 nm through the material from the origin of its generation [6]. If it was generated further away from a heterojunction than the mean diffusion length, then it will decay and the excitation energy is lost. To resolve this issue, Heeger and Yu [75] introduced the concept of a BHJ. Donor and acceptor material are mixed together in a blend to form a BHJ blend. The concept is illustrated in Figure 2.9c. Due to a fine intermixing the exciton separation efficiency can be improved drastically, because the mean distance to a junction is lowered. In contrast, for too fine intermixing there are no subsequent pathways for charges from their position of generation towards the electrodes. Charge migration is disturbed and recombination of free charges increased. It has been shown that the morphology can be controlled in a certain manner e.g. by a thermal annealing process [72]. The heating process leads to a clustering of donor and acceptor material and an increased cluster size. A tradeoff between small distances to a heterojunction (small exciton decay) and large free pathways in the respective phases (small electron-hole recombination) has to be found for optimal performance. Ideally, the cluster size should be of the order of the exciton diffusion length to provide an efficient exciton separation. The charge recombination is then increased due to lack of pathways to electrodes, but the overall efficiency improves drastically compared to a planar heterojunction. The exact internal structure of a BHJ is still a subject of debate. Effective (bottom-down) experimental methods to gain direct insight in a BHJ are difficult to perform. This is one of the reasons for the development of kMC methods because one can control the appearance of the donor/acceptor phase intermixing in a model (see Section 4.2.2) and track the dynamic movement of single particles within the blend.

Recently, a novel active layer morphology has been subject of study: donor/fullerene systems with very low concentrations of donor have been shown to yield good short-circuit currents [76]–[78]. In such devices, the low amount of donor is fully dispersed within the fullerene matrix and consecutive percolation pathways for holes are missing because the donor forms isolated domains. This gives rise to the question whether the prevalent BHJ morphology, including transport pathways for charges within separate phases is a necessity for the operation of OSCs and, in particular, shows that the processes controlling the photo-current generation in OSC still lack understanding and that further insight is required. Investigating the functionality of this particular system is the topic of Chapter 8.

2.5.3. Pathways to improve the efficiency

Many problems responsible for the lack in efficiency of OSCs can be attributed to the two key differences of organic semiconductors with respect to their inorganic counterparts, namely their substantially lower permittivity ε_r as well as the spatially varying energetic disorder σ. These fundamental differences have to two important implications for the

operation principle of OSCs: For one, upon light absorption, the low permittivity leads to the generation of strongly bound electron-hole pairs (excitons) instead of free charges. In order to separate the charge pair, the utilization of a two-component donor/acceptor active layer is necessary. Thus, charge generation takes place at the donor/acceptor heterojunction interface. At the same time, the low exciton diffusion length must be accounted for, which has led to the intermixed BHJ morphology, a tradeoff between efficient exciton separation and sufficiently good charge transport. Furthermore, due to the disorder, charge transport takes place by a thermally activated hopping process between localized states, i.e. between monomers of a polymer or between small organic molecules, instead of delocalized band transport. Once a charge transfer at a heterojunction has taken place, the electron-hole pair is subject to their mutual Coulomb interaction and sees a disordered potential landscape in a spatially disordered BHJ, which can lead to insufficient separation of charges from the interface and, in turn, local charge accumulation and concomitant space-charge effects. It is therefore evident that the behavior of charges, after they originate at the interface, is subject to an interplay between spatial and energetic disorder, thermal activation, mutual Coulomb interaction, and internal electric fields – and is much more complex than in structured inorganic solar cell.

Understanding and gaining control over the properties of electron-hole pairs, in particular their separation from the heterojunction and their recombination dynamics is a key factor in the photogeneration process in OSC blends [79]–[82]. A focus of the present work is dedicated to study the influence of permittivity and energetic disorder on charge behavior within the donor/acceptor morphology, in particular the charge distribution and dynamics, and their relation to loss processes, i.e. recombination.

The separation dynamics are often described by the Onsager-Braun (OB) [83], [84] model, in which kinetic rates are used to describe separation, re-formation, and (geminate) recombination of the bound state. These rates do not contain effects that are based on spatial variations and are therefore not appropriate to describe the influence of the blend morphology, local variation of energetic disorder, or different Coulomb energies for different electron-hole distances [79], [85]. The kMC method is a suitable tool to include the spatial variations as well as the time-dependency of the charge separation process and is therefore the superior tool to model the occurring proccesses responsible for the operation of OSCs.

Koster et al. have emphasized that the permittivity is one of the key quantities to overcome the current drawbacks of OSCs by tackling a number of negative effects induced by strong Coulomb interaction at the same time: the high exciton binding energy in order to dissociate excitons more efficiently, geminate and non-geminate recombination as well as all overall space-charge induced effects [86], [87]. For relative permittivities larger than approx. 8 to 10, the exciton binding energy becomes negligible and thermal fluctuations or excess energy of the photon are sufficient to generate free charges [86], [87]. There has since been an increasing number of studies demonstrating the positive effect of materials with high permittivity on device performance, e.g. refs. [82], [88]–[92].

However, it is a demanding task to synthesize high-ε_r organic materials and it is not obvious if such materials can ever be successfully utilized for OSCs. Until this is not possible, the donor/acceptor concept will be the preferred device configuration. A large part of this work is attributed to show that even slight increases in permittivity can strongly affect charge separation times and recombination times and can nevertheless be very beneficial for organic solar cells even if values around 8 to 10 cannot be reached.

3. The Kinetic Monte Carlo Algorithm

The light induced generation and successive transport of excitons and charge carriers in disordered organic systems is a complex interplay between many factors. No closed analytical model has been derived so far and it is doubtful if it is even possible to develop a general model to cover the vast number of disordered solids. Numerical simulations provide a viable tool to gain insight into the behavior at the nanoscale. Especially kMC simulations hold advantages over other numerical models that make them a proper choice to model disordered organic systems, namely the access to time-dependent single-particle trajectories and the possibility to incorporate 3D morphologies on device scales.

In this chapter, the fundamental ideas of the kMC method are covered. At first, a brief survey of the historical development is given and the classification of the kMC method in comparison to competing simulation models is described. Thereafter, the mathematical framework of the algorithm is derived. The typical execution steps for the implementation of the algorithm are highlighted and give insight into the application of the procedure before the specific implementation for OSCs is covered in Chapter 4.

The content of this chapter is based on [37] and is in parts identical with it. Parts of this chapter have been published in M. Auf der Maur, T. Albes, and A. Gagliardi, "Thin-Film Solar Cells", in *Handbook of Optoelectronic Device Modeling and Simulation: Lasers, Modulators, Photodetectors, Solar Cells, and Numerical Methods*, J. Piprek, Ed., Taylor & Francis, Boca Raton, Sep. 2017.

3.1. Historical development

The term *Monte Carlo method* refers to a broad class of numerical algorithms that offer a simple yet powerful tool to solve real world problems by utilizing random numbers. The expression originated from the famous Monte Carlo Casino located in Monte Carlo, the municipality of the Principality of Monaco, where allegedly an uncle of S. Ulam, (Ulam is often referred to as the inventor of the Monte Carlo method), used to utilize random numbers to gamble away his money [93].

The idea for the use of random numbers in an algorithm came from E. Fermi [94] and was further pursued by S. Ulam and N. Metropolis in the 1940s studying neutron diffusion in fissionable materials at the Los Alamos National Laboratory. At the same institute one of the most popular Monte Carlo methods of this kind, the Metropolis algorithm [95], was developed in a study about the calculation of state equations for a

system of interacting particles described by a hard sphere cutoff potential. At roughly the same time and also for the Manhattan project, a group around J. v. Neumann was first to program the ENIAC computer to carry out Monte Carlo simulations for the study of thermonuclear reactions [96].

In the following decades, Monte Carlo methods have proven to be a versatile tool in a variety of areas, ranging from the evaluation of multidimensional integrals [97], via surface adsorption processes, radiation damage annealing, statistical physics [98]–[100], through to applications in computational biology [101] and many more. Especially the development of a Monte Carlo algorithm class that models physical systems as dynamically evolving from state to state by a certain set of transition rates obtained large interest as it allowed to study time-dependent properties of physical systems. This class of algorithms is today commonly known as *kinetic Monte Carlo (kMC)*. It has received great benefit in the growing computational power of modern processors and still provides one of the major tools to simulate the dynamical behavior of physical systems, e.g. transport processes in inorganic semiconductor devices [102] or leakage currents through high-permittivity materials [103].

Major contributions to the modern kMC algorithm, as it is used in this work, have been made by A. Bortz, M. Kalos and J. Lebowitz in 1975 [100] and D. Gillespie in 1976 [104] and 1977 [105].

Bortz, Kalos and Lebowitz developed a model to describe the formation of domains in ferromagnetic materials below their critical temperature. With regard to the Ising model [106], they stated that the arrangement of next neighbors to a randomly chosen spin from a magnetic material can be reduced to a small number of equivalent configurations with different multiplicities. Instead of choosing one spin, looking at its surroundings, calculating the probability for a spin exchange, and executing or rejecting the swap with a certain probability, they proposed a new algorithm. By not choosing a single random spin but rather one of the equivalent configurations, weighted by their multiplicity, they found an improvement in efficiency to solve the Ising model and laid the foundations of the modern kMC method.

Gillespie published his famous work about a new method to examine chemical reactions near instabilities where deterministic approaches are invalid. For complex systems with many molecules and a set of reactions between them involved, such as solutions of distinct reactants, analytical solutions in both a deterministic or stochastic framework soon become unfeasible. He proposed a simple and efficient numerical method to offer a systematic approach in simulating the chain of processes that, strung together, describe the time evolution of the system based on only one fundamental assumption. Gillespie and his work made a great contribution in popularizing the method and are often referred to today as the kMC method. More detail on the Gillespie algorithm is given in Section 3.3. For the scope of this work, the ideas of Gillespie are followed closely but the approach by Bortz, Kalos and Lebowitz and the Gillespie algorithm are similar and the treatment of system time evolution is essentially the same.

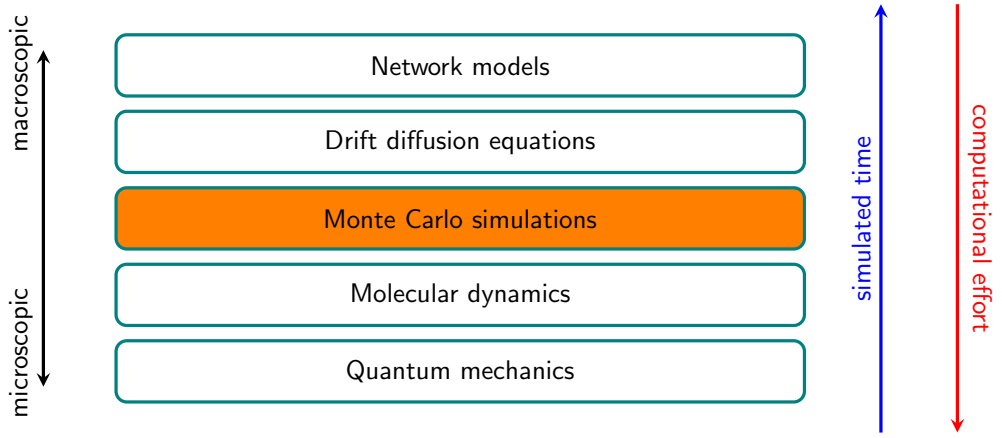

Figure 3.1. – Different model approaches for different scales in time and dimension. Kinetic Monte Carlo simulations bridge the gap between macroscopic and microscopic modelling techniques.

3.2. Classification and advantages

To model a physical system, one needs to identify the spatial dimensions and the time scales on which the underlying processes determining the properties of the system occur. Depending on the time and length scales, there are several different modelling approaches. The choice of the appropriate model comes along with a tradeoff between the simulated time (i.e. the time span that the model can predict the system's functionality) and the computational effort (i.e. the real-world time that the model prediction needs to run on the computing machine). Figure 3.1 shows an overview of the different levels of simulation models. A full quantum mechanical treatment is the most accurate approach, but is highly unfeasible for any larger system. On the other hand, network models hide all underlying device properties and cannot be used to predict device functionality. Among the models that can be suited to model physical components are:

- Molecular dynamics (MD): microscopic, discrete
- kinetic Monte Carlo (kMC): mesoscopic, discrete
- Drift-diffusion (DD): macroscopic, continuous

Molecular Dynamics (MD) is the preferred tool for the dynamical behavior of microscopic systems at the molecular level (nm scale) [107], such as for example the folding of a protein. Within MD, the classical equations of motion are integrated forward in time for an ensemble of particles. Hence, MD provides access to the time-dependent evolution of all particles in the system. It is commonly used to model the interaction of single atoms with all spatial movements such as vibrations that occur on time scales of the order of 10^{-15} s (= femtoseconds). Therefore, the total time interval that can be calculated in a reasonable amount of real time are less than µs. Many interesting molecular processes in

devices happen on longer time scales, e.g. diffusion, phase transitions or a steady state in OSCs, and can therefore not be investigated using MD. This is known as the time-scaling problem of MD and an approach to overcome this limitation is needed for a full device model.

Another common and macroscopic approach are continuum models such as the DD model. In continuum models, instead of being based on single particles, the system is characterized by continuous quantities like the local charge carrier distribution and the local current densities and differential equations between them. This not only allows to model larger structures but can also lead to a strongly reduced computational demand. The differential equations are self-consistently solved until convergence is reached: an initial distribution of the charge carrier densities and the electrostatic potential is guessed and the current density for this guess calculated. The obtained solution is used to calculate a new distribution of charge carriers and potential. This process is iteratively repeated until a steady state is reached, defined by a certain difference in the current between two iterations. The downside of this method is that the information about the dynamics of single particles is concealed within the continuous quantities. Furthermore, it is difficult to incorporate more complex morphologies, especially in 3D. For spatially disordered systems, such as BHJ OSCs, the DD equations become highly nonlinear and it may not be possible to obtain a converging solution. This is why in DD models, complex structures are often reduced to an effective medium of lower dimensionality with effective physical parameters. This approximation is in many cases a strong simplification of the functionality and comes with physical inaccuracy. Chapter 5 contains a comparison between the DD model and the kMC model for OSCs.

To overcome the time-scaling problem on the one hand, and on the other hand be able to implement the desired nanoscale morphology, the kMC method offers a suitable tool. In comparison to MD, kMC is based on the concept of *coarse-graining* the system dynamics (illustrated in Figure 3.2a). The system is characterized by a set of long-term states with discrete transitions between them (so-called infrequent events). Motions on smaller timescales, like fast vibrational modes, can be neglected as long as the current state can still be assigned to a long-term state. Coarse-graining allows to neglect a sufficient amount of (fast) processes and thus, reach much longer overall simulation times up to seconds without the loss of important system dynamics. Only transitions between long-term states determine the dynamic evolution of the system. It needs to be carefully considered which processes are implemented in the model and which ones are combined to long-term states in order not to lose essential parts of the system dynamics. This way the kMC method can accomplish a tradeoff between accuracy and simulated time and bridges the gap between MD and continuum approaches. An illustrative description of coarse graining for kMC can be found in [108].

For the processes in OSCs, particles like excitons, electrons and holes reside in localized states. Their motions can consist of processes on smaller timescales, but as long as they do not perform a hopping process from one localized state to another, the particles are

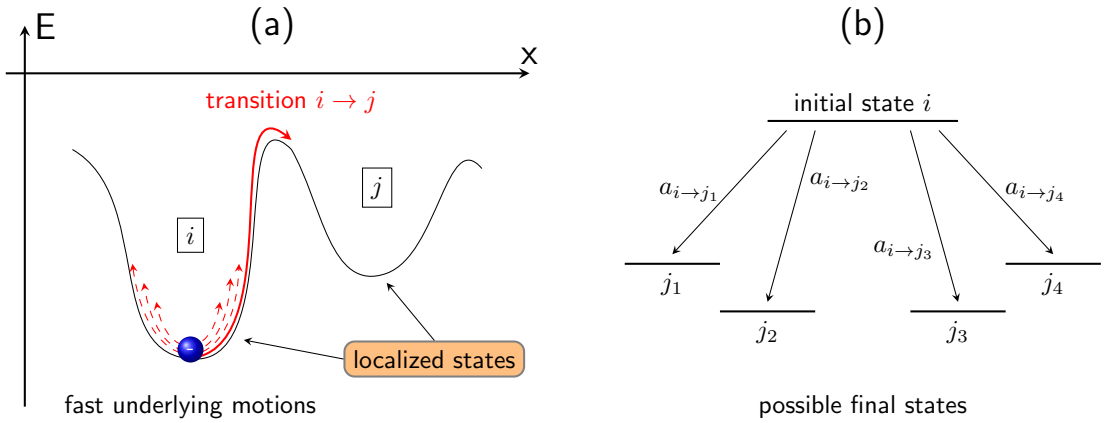

Figure 3.2. – (a) Transitions from long-time state to long-time state with underlying fast modes in an infrequent-event system. (b) State-to-state transitions reduced to the needs for kMC.

spatially assigned to that state. The overall dynamical behavior is only determined by jumps to another localized state. This makes the concept of an infrequent event system applicable.

To consider the morphology on the nanoscale, the whole photoactive layer comprised of donor and acceptor molecules will be discretized into a grid of localized states between which hopping processes can take place. This allows on the one hand to include a more accurate picture of the donor acceptor morphology. On the other hand, one is able to account for dynamical processes of individual particles at the nanoscale.

3.3. Kinetic Monte Carlo algorithm

The essential concept of the kMC method is, as stated above, the characterization of the considered system by a set of system specific long-time states. A state is for example defined by the position of all particles in the system at a certain time. Under dynamical evolution, it is possible for the system to change its state by certain system-specific transitions, e.g. the motion of particles from one state to another. It needs to be noted that all physics describing the system dynamics is contained in the transition rates. Since the kMC method is not an ab-inito method, it is not able to predict transition rates. The rates are input to the simulation and can either be based on underlying physical models or on experimental measurements. The task for an accurate kMC model is to identify all the important processes that take place in the system by considering processes that happen on long time scales and neglecting those which act on very small time scales. For these processes, rate expressions must then be obtained. Under the assumption that the rates are chosen well, kMC provides the correct dynamical evolution of the system.

Let the physical system considered be in a certain system state i. Depending on the

current system setup, a set of M distinct states $\{j\} = \{j_1, \dots j_M\}$ exists to which a transition (or: event) can take place. This is indicated in Figure 3.2b. The transitions from an initial state i to the possible final states $\{j\}$ can be characterized by at corresponding set of transition rates $\{a_{ij}\} = \{a_{ij_1}, \dots a_{ij_M}\}$ given in units of s^{-1}. Transition rates are a measure for the probability of the corresponding transition from $i \to j$. An important property of the physical system must be that the rates are memoryless, meaning that they are only dependent on the setup of the current state and are not dependent on how the system evolved into it. This property is known from the theory of Markov chains [109] and it allows, if the set of rate constants is known, to determine the dynamical evolution of the system.

As known from statistical physics [110], stochastical processes characterized by discrete transitions from state to state under temporal evolution can phenomenologically be described by the master equation

$$\frac{dp_i(t)}{dt} = -\sum_{j=1}^{M} a_{ij}\, p_i(t) + \sum_{j=1}^{M} a_{ji}\, p_j(t). \tag{3.1}$$

The probability $p_i(t)$ to find the system in state i at a certain time t changes in a way that is determined by the rate constants a_{ij} and the probabilities of only the initial state $p_i(t)$ and the possible final states $p_j(t)$. Finding solutions of the master equation, be it by analytical or numerical methods, is often complex and not feasible. The kMC method does not try to solve the master equation. It is based on a stochastical framework and provides a numerical approach to obtain the dynamic system evolution based on the time dependent propagations from state to state. By choosing a transition pathway through a chain of subsequent states, one possible dynamical evolution evolution of a system through its phase-space is obtained. The kMC method can therefore be imagined as a direct execution of the Master equation. Such a walk through a pathway of transitions forms a Markov chain. Averaging over a large number of such Markov chains provides an equivalent system behavior as described by the master equation.

In order to derive the associated mathematical framework, the concept of the Gillespie algorithm [104] is adapted in the following.

3.3.1. Probability density function

The algorithm as proposed by Gillespie is reliant on the ability to characterize the system events by a set of transitions

$$\{R_\mu\} \text{ with } \mu = 1, 2, \dots, M \tag{3.2}$$

where each R_μ corresponds to a transition $i \to \{j_\mu\}$ from above and M is the total number of possible transitions. All transitions must describe distinct processes and their number can vary over time, depending on which events are enabled at a certain step in the system evolution. As stated before, it is essential to consider all important processes

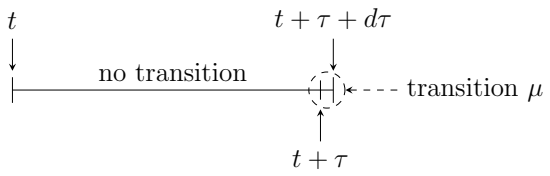

Figure 3.3. – Illustration of the probability density function interpretation: after a time τ of inactivity, a transition μ occurs in an infinitesimal time interval $d\tau$.

between long-time states in order to be able to accurately reproduce the behavior of the system. The main task is now to develop a procedure to simulate the time dependent evolution of the system under consideration of the given transitions. This makes it necessary to derive an algorithm that is able to choose which transition will be carried out and (for the time dependency) at what time span, all based on the drawing of random numbers.

In order to quantify the transitions, a transition probability rate a_μ corresponding to each transition is introduced. The set of transition rates are defined as

$$\begin{aligned} a_\mu \delta t = {} & \text{probability for a transition } R_\mu \text{ to} \\ & \text{occur in the next time interval } \delta t. \end{aligned} \tag{3.3}$$

At any given time, the set of $\{a_\mu\}$ characterizes the possible transitions. They are usually functions of the current system setup and will change over time. Determining their specific values for an organic solar cell is the focus of Section 4.3.

Instead of finding a solution to the master equation, the kMC method is based on a function called the Probability Density Function (PDF). The PDF is the suitable function to select a transition and its corresponding time step based on random numbers. The PDF is defined as

$$\begin{aligned} P(\tau,\mu)\, d\tau = {} & \text{probability at time } t \text{ for the next transition} \\ & \text{to occur in time interval } (t+\tau\,,\, t+\tau+d\tau) \\ & \textit{and} \text{ being a transition of type } R_\mu, \end{aligned} \tag{3.4}$$

where $P(\tau,\mu)$ is the PDF. This function can be interpreted as follows: it is a joint probability density function of the continuous time variable τ ($0 \leq \tau < \infty$) and the integer variable μ ($\mu = 1, 2, \ldots, M$) characterizing the transition. At a certain time t, the PDF represents the probability for transition μ to occur within an infinitesimal time span of $d\tau$ after no other event has taken place for a time interval τ (cf. Figure 3.3). Hence, $P(\mu,\tau)$ can be seen as the independent probabilities to have no transition in the time interval $(t\,,\, t+\tau)$ *and* to have a transition of type R_μ immediately afterwards in the infinitesimal interval $(t+\tau\,,\, t+\tau+d\tau)$. The latter is precisely the definition of a transition probability given by Equation (3.3). Mathematically, the joint probability of

two independent probabilities equals their product:

$$P(\tau, \mu)\, d\tau = (P_0(\tau) \cdot a_\mu)\, d\tau. \tag{3.5}$$

In order to calculate the probability for no occurring event $P_0(\tau)$, the interval $(t, t+\tau)$ is divided into K parts of equal length $\varepsilon = \frac{\tau}{K}$. The probability for no event μ in a time interval of length ε is $(1 - a_\mu \varepsilon)$. The combined probability for no transition at all in each of the intervals ε, separately, is then

$$\prod_{\nu=1}^{M} (1 - a_\nu \varepsilon) = 1 - \sum_{\nu=1}^{M} a_\nu \varepsilon + o(\varepsilon).$$

For the entire time interval τ, no reaction must occur in any of the K subintervals. $P_0(\tau)$ is therefore the product of probabilities for no transition occurring in each of the subintervals combined,

$$P_0(\tau) = \left[1 - \sum_{\nu=1}^{M} a_\nu \varepsilon + o(\varepsilon)\right]^K = \left[1 - \sum_{\nu=1}^{M} a_\nu \frac{\tau}{K} + o\left(\frac{\tau}{K}\right)\right]^K,$$

where $o(\varepsilon)$ is an error term of the order of ε. The expression above must be true for any number of subintervals K. For $K \to \infty$, the error term $o(K^{-1})$ approaches zero. Exploiting the representation of the exponential function as the limit of a sequence[1], one obtains

$$P_0(\tau) = \lim_{K\to\infty} \left[1 - \frac{1}{K} \sum_{\nu=1}^{M} a_\nu \tau\right]^K = \exp\left(-\sum_{\nu=1}^{M} a_\nu \tau\right). \tag{3.6}$$

Using the abbreviation

$$a = \sum_{\nu=1}^{M} a_\nu \tag{3.7}$$

as the total transition probability per unit time, where $a\,\delta t$ stands for the probability that *any* transition will occur in the next time interval δt, the final expression for the PDF is given by

$$P(\tau, \mu) = a_\mu \cdot \exp\left(-\sum_{\nu=1}^{M} a_\nu \tau\right) = a_\mu \exp(-a\tau). \tag{3.8}$$

This function, only dependent on the set of events a_μ, is the starting point to choose a random number pair (τ, μ) that characterizes the next transition and time step in the dynamic evolution of the system. The PDF is properly normalized, meaning that every pair (τ, μ) with $\tau \in (0 \leq \tau < \infty)$ and $\mu = 1, 2, \ldots, M$ has its weighted contribution to the

[1] $\exp(x) = \lim_{n\to\infty} (1 + \frac{x}{n})^n$

PDF and that it is guaranteed to obtain an associated value for the PDF by randomly choosing one pair:

$$\int_{t=0}^{\infty} d\tau \sum_{\nu=1}^{M} P(\tau,\nu) = \sum_{\nu=1}^{M} a_\nu \int_{t=0}^{\infty} d\tau \exp(-a\tau) = 1. \tag{3.9}$$

Now, the crucial *Monte Carlo* step can be defined: by choosing a random pair of the variables (τ,μ) according to the PDF $P(\tau,\mu)$ after Equation (3.8), a weighting based on the magnitude of the various transitions and the exponential decrease in time is performed. For the execution of this step, two approaches were suggested by Gillespie: the *direct method* and the *first reaction method*. In this context, the *direct method* is used. The direct method is most efficient in the way it utilizes random numbers to determine a pair of transition and a time step. There will be a brief comment on the differences of the methods at the end of the section.

3.3.2. Choosing time and transition in the direct method

In the direct method, the PDF is divided into two separate PDFs, each of which is itself normalized and only dependent on either the time τ or the transition μ, respectively:

$$P(\tau,\mu) = P_1(\tau) \cdot P_2(\mu|\tau). \tag{3.10}$$

Here, the first factor represents the probability density that any of the possible transitions takes place in the time interval $(t+\tau, t+\tau+d\tau)$, irrespective of which one. Thus, $P_1(\tau)$ is the sum over all transitions. With Equation (3.8) it follows

$$P_1(\tau) = \sum_{\nu=1}^{M} P(\tau,\nu) = \sum_{\nu=1}^{M} a_\nu \exp(-a\tau) = a \cdot \exp(-a\tau). \tag{3.11}$$

From this and Equation (3.10), $P_2(\mu|\tau)$ is easily derived as

$$P_2(\mu|\tau) = \frac{P(\tau,\mu)}{P_1(\tau)} = \frac{a_\mu}{a}, \tag{3.12}$$

and $P_2(\mu|\tau)\, d\tau$ represents the probability that a reaction μ occurs, given the condition that a time step of τ has been chosen before.

Both P_1 and P_2 are properly normalized PDFs on their own. Generating two random numbers according to these PDFs yields a pair (τ,μ), distributed with the total PDF $P(\tau,\mu)$[2].

Random number generation and the inversion method

All modern programming languages offer the possibility to generate (pseudo-) random numbers. Pseudorandom numbers are sufficient for the Monte Carlo method, although

[2] for an extended proof, see [111]

the sequence after which they repeat should be large and the algorithm after which they are generated should be fast. For the Monte Carlo step, the generated random numbers need to be distributed according to the PDFs (3.11) and (3.12). Since these are specific functions, a procedure is needed to generate them from simpler distributions, such as a uniform distribution in the unit interval.

Random numbers in a uniform distribution over the unit interval $(0, 1)$ can be defined as follows: the probability for a random number r to be in an arbitrary subinterval $r \in (\alpha, \beta)$ with $(0 \leq \alpha < \beta \leq 1)$ is given by the length of the subinterval:

$$p(\alpha \leq r \leq \beta) = \beta - \alpha. \tag{3.13}$$

Every normalized PDF $P(x)$ has an associated cumulative distribution function, defined by

$$F_1(x) = \int_{-\infty}^{x} P_1(x')\, dx' \qquad \text{for a continuous } P_1(x), \tag{3.14}$$

$$F_2(i) = \sum_{i'=1}^{i} P_2(i') \qquad \text{for a discrete } P_2(i). \tag{3.15}$$

Because $\lim\limits_{x \to -\infty} F_1(x) = 0$ and $\lim\limits_{x \to \infty} F_1(x) = 1$ for the continuous case, and $F_2(0) = 0$ and $F_2(M) = 1$ for the discrete case, both functions are monotone and limited. Thus, there exists an inverse function F^{-1} for each of them. It is made sure that every value from the output range has a corresponding value x or i in the domain range. The concept of the inversion method is to draw two uniform random numbers $r_1, r_2 \in (0, 1)$, and calculate $x = F_1^{-1}(r)$ and i from $F_2^{-1}(i)$. This way the obtained values for x and i are distributed according to the PDF from which F is derived.

Continuous time step

Using the inversion method and the PDF $P_1(\tau) = a \cdot \exp(-a\tau)$, the corresponding cumulative probability function is[3]

$$F_1(\tau) = \int_0^{\tau} a \cdot \exp(-a\tau')\, d\tau' = 1 - \exp(-a\tau). \tag{3.16}$$

The continuous and exponentially distributed time variable τ, which describes the time passed before one transition (or, for a more vivid interpretation: the time "needed" for one transition), is then given by the inverse function of F_1. Hence[4],

$$\tau = F_1^{-1}(r_1) = \frac{1}{a} \ln\left(\frac{1}{r_1}\right) \qquad \text{with } a = \sum_{\nu=1}^{M} a_\nu \text{ and } r_1 \in (0, 1) \tag{3.17}$$

[3] note that $P_1(t)$ is only defined for $t \geq 0$

[4] The term $1 - r$ has been replaced by r. Since we are dealing with probabilities, this is valid for uniform random numbers in the unit interval.

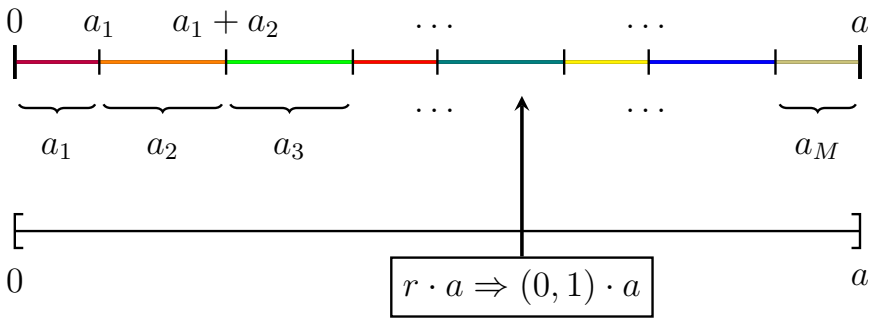

Figure 3.4. – Drawing a discrete transition by a continuous random variable $r \in (0,1)$. All enabled rate constants are added to yield the total rate a. Multiplication of a random number in the unit interval with the total rate corresponds to one specific rate process, weighted by its magnitude. Rates are added until the next addition will exceed $r \cdot a$. The last rate in the addition is chosen.

Discrete transition

To choose a transition μ from the set of events $\{a_\mu\}$ $(\mu = 1, 2, ..., M)$ by a random number r_2, the cumulative probability must satisfy

$$F_2(\mu - 1) < r_2 \leq F_2(\mu) \tag{3.18}$$

That is, $r_2 \in (0,1)$ corresponds to one plateau in the discrete histogram of F_2. Substituting Equation (3.12) in Equation (3.15) yields an expression for $F_2(\tau|\mu)$:

$$F_2(\tau|\mu) = \sum_{\nu=1}^{\mu} \frac{a_\nu}{a} \tag{3.19}$$

With this, the above condition reads

$$\sum_{\nu=1}^{\mu-1} \frac{a_\nu}{a} < r_2 \leq \sum_{\nu=1}^{\mu} \frac{a_\nu}{a} \tag{3.20}$$

or, multiplying by a,

$$\sum_{\nu=1}^{\mu-1} a_\nu < r_2 \cdot a \leq \sum_{\nu=1}^{\mu} a_\nu \quad \text{with } a = \sum_{\nu=1}^{M} a_\nu \text{ and } r_2 \in (0,1). \tag{3.21}$$

This represents a sum of all transition probabilities, up to an index for which the sum is larger than the random variable r_2. This index is set to be the chosen transition μ. The process to derive μ computationally from a random number is illustrated in Figure 3.4.

Remarks on the first reaction method

In the first reaction method after Gillespie [104], a random number is generated for every transition that can take place separately. A time step is assigned to every event and they are sequentially queued by ascending time. The transition with the smallest time is chosen to be executed, it's rate is re-calculated and the transition is re-entered in the waiting queue. However, the other rates remain unchanged with the changes that the executed transition brings to the system. This method is faster in execution than the direct method but, by neglecting the changes of the executed transition to the system, it leads to physical incorrectness. Because the severity of the physical error that the first reaction method makes is hard to estimate, the direct method is applied in our model for the sake of physical correctness.

3.4. Algorithm procedure

After the mathematical derivation, which condenses to only two equations (3.17) and (3.21) to calculate a pair of random numbers (τ, μ), the rest of the kMC method is fairly straightforward and can be reduced to only a few, simple steps. The whole procedure is depicted in a flowchart in Figure 3.5.

0. Initialization

Right after the start, system specific parameters are read in by the program. This includes all parameters that must be known in order to set up the system and to calculate the transition rates. Variables to store the occurrence of relevant processes during the simulation are set up here. A crucial variable is the simulation time t_{stop}. It determines how long the dynamic evolution of one run should be simulated. The starting time is set to $t = 0$. Specific initialization for the organic solar cell model is shown in Section 4.2 and includes the lattice discretization into nodes, the assignment of energy levels to every node and the pre-calculation of Coulomb energy values for a specific treatment of the electrostatic interaction. A list of all input parameters can be found in Section 4.4.

1. Calculate transition rates

The kMC method is reliant on physical models for all processes that can occur in the system. All physics enters the model in terms of the transition rates which are calculated in this step. Depending on the current state only some transitions may be activated. Conditions must be met in order to make sure that rates for processes that cannot occur in a certain system state are deactivated. This is realized by setting the value for a deactivated rate $a_\mu = 0$ so that it is not considered in the selection a transition after Equation (3.21). After all rates have been calculated and stored, they are summed up to provide the total rate a. The calculation of transition rates is the topic of Section 4.3.

2. Monte Carlo step

As described in the preceding section, a random pair (τ, μ) is generated according to the PDF $P(\tau, \mu)$. Two uniform random numbers r_1 and r_2 are drawn; from these, the time step τ is calculated after Equation (3.17) and the transition is calculated after Equation (3.21). This accounts for the stochastically correct time step τ for the selection of a transition μ.

3. Update system

To update the system the time t is advanced by τ. Based on which transition μ has been chosen, the system configuration needs to be updated accordingly. How every update is specifically performed is also covered Section 4.3.

After updating the system, a check is performed whether the simulation time has reached the specified stopping time t_{stop}. If $t < t_{stop}$, the simulation will continue by jumping back to step 1 and recalculate the event rates. This way, the system update on the behavior of other processes is reflected. The steps 1-3 represent the so called *Monte Carlo loop*. They will be executed as long as termination condition is not yet fulfilled.

4. Termination and data output

Through the successive time advance t eventually becomes larger than the stopping time and the Monte Carlo loop is terminated. At last the variables tracking selected events are printed out and can be evaluated. Details about the evaluation of physical quantities are given in Section 4.5

Overall, the kMC method offers a straightforward algorithm to simulate the time-dependent evolution of a system. It is only reliant on (i) the assumption that all physical processes can be determined by rate expressions (3.3), and (ii) that a (pseudo-)random number generator with a sufficiently small correlation between two subsequent numbers and a large period is provided.

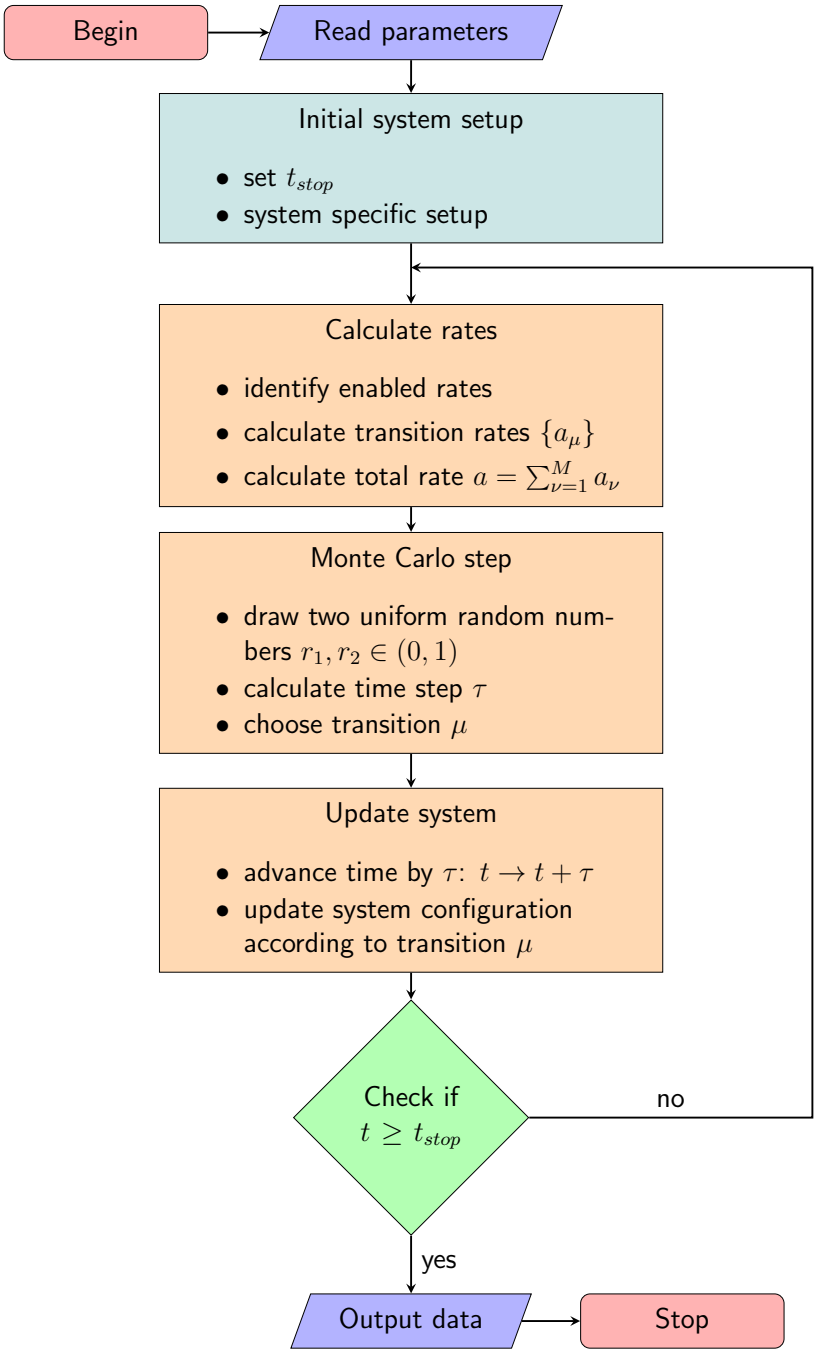

Figure 3.5. – Flowchart of a general kinetic Monte Carlo algorithm.

4. Kinetic Monte Carlo Model of Organic Solar Cells

With the fundamental working principle of OSCs and the framework of the kMC method being introduced, the specific implementation is shown in this chapter. The physical processes governing the operation of OSCs are merged with the kMC framework to obtain a simulation tool that is able to reproduce the characteristics of OSC devices under illumination, while giving insight to the internal dynamics at the level of single particles. At first, a literature survey of past and current kMC models for OSCs is given and the specific advantages of the model described herein are highlighted. After that, the consecutive steps of the Monte Carlo procedure are described. The initial system setup including the discretization of the photoactive layer and the generation of the morphology is described. An essential part of the model is the treatment of Coulomb interaction. A method based on the evaluation of the Ewald summation is implemented. By making use of the discrete nature of the lattice, a considerable amount of processing time can be outsourced to the initial setup process. It follows the derivation of the specific models for each process considered and a description of how the system is updated after every single transition. The equations to calculate event rates resemble the core of the simulator, since the underlying physics enters the model with them. In order to prepare for the results, an overview of the input parameters and further information on the evaluation of the data output is given.

The content of this chapter is an updated version to the implementation described in [37] and is in parts identical to it.

4.1. State-of-the-art implementations

The first applications of the kMC method to model charge transport in disordered systems date back to the late 1980's [112]. In his pioneering work [56] Bässler showed that the kMC method is a convenient tool to simulate charge carrier dynamics in terms of a discrete hopping process between localized states in disordered organic materials described by a Gaussian DOS. Since then, the method has been utilized to investigate (unipolar) charge transport in disordered organic semiconductors [113]–[116].

The concept of photoactive layers consisting of donor and acceptor materials for exciton dissociation gave rise to the kMC studies of two-phase (bilayer) systems including excitons, their separation, ambipolar electron and hole conduction as well as their recombination

[117]–[119].

After the introduction of the BHJ [75] to overcome the large exciton decay in bilayer structures, models were developed to reproduce the intermixed structure of the donor acceptor blend [120]. Watkins et al. included both charge carrier and exciton dynamics in a kMC framework to study the dependence of the morphology on device performance at short circuit conditions [121]. They showed that the internal quantum efficiency strongly depends on the the interfacial area between donor and acceptor material and developed an algorithm to control the phase separation in a BHJ. In order to simulate full j-U-characteristics of BHJ devices, Marsh et al. [122] used a BHJ model together with a charge injection process from the electrodes into the organic materials, based on a thermionic emission process according to Wolf et al. [123]. They used their model to study recombination and collection efficiencies over typical voltage ranges and for different illumination intensities. However, they did not include exciton dynamics and restricted their studies to charge carrier effects. To combine all previous models in one, Meng et al. took account of all processes concerning exciton and charge carrier transitions including injection from the electrodes [124]. Because they implemented all major processes, their model allowed them to compare their results to an experimentally fabricated device with two polymers acting as donor and acceptor materials and make predictions about its optimization.

Further applications of the kMC method to OSCs have been performed to study for example the effect of morphology [125], exciton dynamics [126], [127], charge transport and mobility [33], [128], [129], charge separation [35], [130]–[133], geminate [134], [135] and nongeminate recombination [136]–[138], space charge effects [34] and charge trapping [135]. More information about the kMC method and its applicability to disordered systems can be found in e.g. [115], [139], [140].

A group around Casalegno has tackled a two approximations that had been made in many kMC models but had never been tested to extent [118]. (1) The first approximation is the use of a cutoff radius to calculate the Coulomb interaction instead of an exact treatment of the long-range electrostatic forces. A cutoff seems especially inappropriate in organic materials where the dielectric screening length is much larger than in inorganic semiconductors. Casalegno et al. introduced a treatment known from MD to calculate the long-range electrostatic interactions, the Ewald sum [141], and showed that the device performance is underestimated by the use of a cutoff. (2) Secondly, many previous implementations relied on the First Reaction Method (FRM) method as proposed by Gillespie [104], where events are sorted by waiting times in a queue and the transition with the smallest time is executed first. In the FRM used in former kMC models only the rate corresponding to the one executed (the fastest) transition is updated. Therefore, the system update is not reflected on the remaining processes that might be affected by the executed transition. Groves et al. noticed this problem and performed a study about the difference of this modified FRM approach and the direct method [142]. They came to the conclusion that, in terms of charge separation after the dissociation of an

exciton into electron and hole, both methods differ by less than two percent. However, their study is mainly focused on bilayer devices. Since the effects in other active layer structures, such as a BHJ or dilute donor systems, could be quite different, a Monte Carlo algorithm using the direct method seems to be more appropriate.

In this work, a comprehensive kMC model based on the most advanced methods by Meng et al. is described but without the approximations mentioned by Casalegno. The core of the model follows the implementation described in [118], but is adapted to BHJ cells and its capabilities are largely extended as described in detail throughout this chapter. A full treatment of the electrostatic interactions via evaluation of the Ewald sum and the use of the direct method as derived in Chapter 3 are implemented. The simulator is used to model state-of-the-art OSC devices like the extensively studied P3HT:PCBM composition in both a BHJ configuration or a diluted donor configuration. However, the model can be applied to other material configurations if their material specific parameters such as the HOMO and LUMO levels, disorder and the hopping prefactors are known.

A focus of this study is the treatment of full-device simulations during operation of the solar cell with all major dynamical processes implemented, including charge injection from the contacts and the consideration of the correlation between all charges in the system. Full-device simulations while considering effects on the nanoscale is a particular advantage of the kMC method: the physical processes controlling the operation of OSCs range over large spatial dimensions from charge localization at the (sub-)nm scale [61] up to hundreds of nm of absorption layer size as well as large timescales between tens of fs for charge pair separation and several µs for non-geminate recombination [81]. Therefore, a sufficiently large number of simulation steps need to be executed in a kMC simulation in order to sample the slowest processes to a sufficient extent with respect to the fast processes and hence make valid statements about their occurrence and their steady-state values. This comes at the cost of computational demand and makes kMC simulations generally slower than continuum-based simulations or numerically solving the Master equation [143], [144]. On the contrary, the kMC method does not suffer from convergence problems for complex geometries and allows to investigate the transient evolution of a system, which makes it the preferred choice for dynamical analyses of disordered semiconductors and BHJs.

4.2. System Setup

4.2.1. Lattice discretization

To represent the spatial nanoscale structure of the solar cell in the simulation model, at the beginning of each simulation the photoactive layer and the electrodes are divided into a 3D lattice consisting of a discrete set of nodes. Each node in the photoactive layer is aimed to represent a localized state at which a particle can reside, i.e. a node can be seen as either a monomer in a polymer chain or small molecule. An equidistant node spacing of $l = 1\,\mathrm{nm}$ is chosen as lattice constant. This resembles a typical hopping

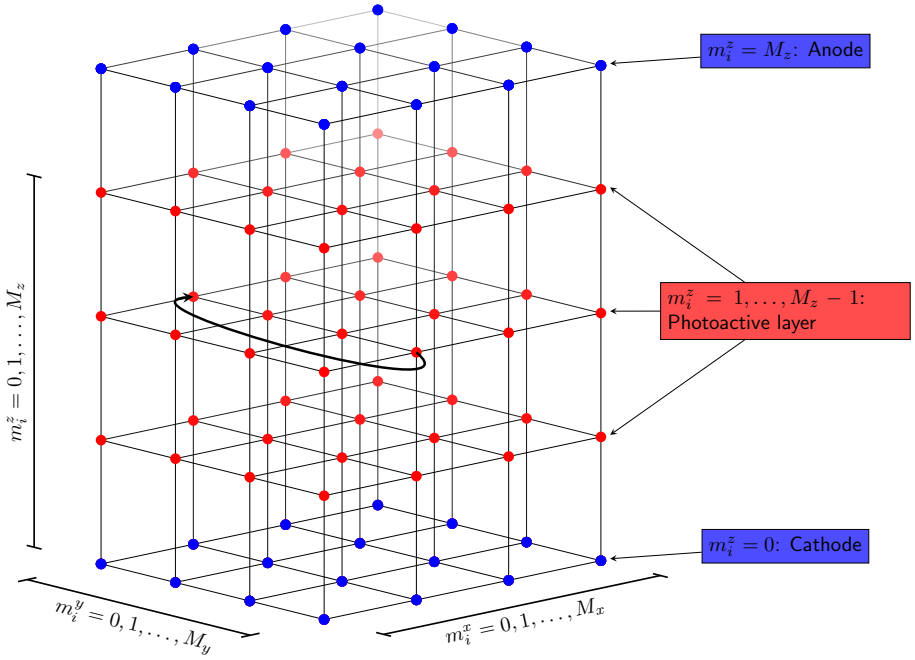

Figure 4.1. – Grid representation of the solar cell. Bottom and top nodes are cathode and anode, respectively. The nodes in between represent localized states of either a polymer monomer or a small molecule. Every node stores information about the current system state. The arrow indicates the periodic boundary conditions applied in x- and y-direction.

distance along a polymer chain or between two small molecules. Also, it allows to account for the fine phase segregation of donor and acceptor materials in a bulk-heterojunction and to consider local effects on the scale of nm.

A typical grid representation is shown in Figure 4.1. The total number of grid sites in the three spatial dimensions is denoted by M_x, M_y and M_z, respectively. Due to $l = 1\,\text{nm}$, the magnitude of the M's is equal to the solar cell dimensions in nm. While $M_z \cdot l$ corresponds to the actual thickness of the device, periodic boundary conditions are applied in x- and y-direction. If the entire area of a typically $1\,\text{cm}^2$ large device would be considered with a lattice spacing of 1 nm, the number of nodes would be of the order of $10^7 \times 10^7 \times 100 = 10^{16}$. Such an amount of sites would make the simulation unfeasible in terms of computational effort. Considering a box segment with the full height ($M_z \cdot l = 50\,\text{nm}$ to $200\,\text{nm}$, device thickness) but reduced planar dimensions of the order of $M_x \cdot l = M_y \cdot l \approx 50\,\text{nm}$ as a periodic simulation box to represent a larger, extended photoactive layer is aimed to be a sufficient tradeoff between simulation time and accurate representation of morphology. This assumption is valid as long as the size of typical features of the morphology does not get as coarse as the dimensions of the bulk volume $V = M_x\, M_y\, M_z\, l^3$. A justification for this assumption was performed in [37].

Periodic boundary conditions for all particles transitions and interactions have to be applied in x- and y-direction in this approach. For example, it must be assured that the neighboring site in positive y-direction of a particle at $y = M_y\, l$ is the node at $y = 0$, as indicated in Figure 4.1.

To take account of the electrodes, the nodes at the bottom $z = 0$ and at the top $z = M_z\, l$ represent the cathode and anode, respectively. Correspondingly, all nodes with $z/l \in 1, 2, ..., M_z - 1$ are either donor or acceptor sites. Every node in the photoactive layer has a certain set of fixed and variable properties assigned, and the total set of nodes including their current properties is a full representation current system state of the layer. The properties of a node are:

Node position: In the initial setup, every node gets its coordinates in the grid assigned. The coordinates remain fixed for each node throughout the simulation. The position is used to find the neighboring localized states, to check their properties in order to see if certain events are enabled, and to calculate the corresponding rates. To quantify the discrete lattice, the position of a node i can be described as

$$r_i = (x_i,\, y_i,\, z_i) = (m_i^x\, l,\, m_i^y\, l,\, m_i^z\, l)$$

with the set of integer variables $m_i^x \in [0, M_x - 1]$, $m_i^y \in [0, M_y - 1]$, and $m_i^z \in [0, M_z]$. Periodic boundary conditions in x- and y-direction require that $n \cdot M_x + m_i^x = m_i^x$ and $n \cdot M_y + m_i^y = m_i^y$, with $n \in \mathbb{N}$. This way, all processes can be reduced to a simulation box of $[0, M_x - 1] \times [0, M_y - 1] \times [0, M_z]$, with a total number of nodes $M_x \times M_y \times (M_z + 1)$. In z-direction the electrodes at $m_i^z = 0$ and $m_i^z = M_z$ represent real boundaries of the system.

Node occupation: The node occupation variable stores whether a particle resides at a particular node at the current simulation time and, if so, which kind of particle. During the dynamic time evolution nodes can become occupied with excitons, electrons or holes. A node is not allowed to be occupied by more than one particle at a time. This has an effect on some transitions:

Hopping transitions to occupied nodes are deactivated which must be considered by setting the hopping rate to occupied nodes to zero. If two neighboring nodes are occupied by an electron and a hole, respectively, recombination is activated, i.e. the rate becomes non-zero. Additionally, no excitons can be generated at already occupied nodes.

Node material: Every node in the photoactive layer is either of donor or acceptor type. This information is stored in a node material variable. To generate the intermixed distribution of a BHJ morphology, a special algorithm is applied (cf. Section 4.2.2). It shall be stressed that in all results, the morphology is generated once per simulation in the initial setup and remains constant throughout the execution, if not stated otherwise.

Node interfaces: Each node has the information assigned if, and in which direction, an interface to another material is present. Interfaces are crucial for the locations where and how excitons get separated and where charges can recombine. Analyzing the size of the interfacial area between donor and acceptor phase are is almost impossible by experiments. In the simulation, the number of neighboring nodes with a donor/acceptor junction can easily be counted and be used to determine such as the average cluster size and the recombination current density of the phases.

Node energy levels: Two distinct energy values, E_i^{HOMO} and E_i^{LUMO}, are assigned to each node, representing the energetic states affecting holes and electrons, respectively. Depending on whether a node represents an acceptor or a donor material, its molecular orbital energy differs. After the morphology has been generated, a fixed HOMO (E_A^{HOMO} or E_D^{HOMO}) and a fixed LUMO (E_A^{LUMO} or E_D^{LUMO}) level are assigned to each node to account for the distribution of the two phases. Additionally, both an electric field and the energetic disorder (Section 4.2.3) as well as the influence of the Coulomb potential (Section 4.2.4) induced by other charges in the cell contribute to the local energy levels.

Altogether, these four influences make up the overall energy landscape that electrons and holes experience and are the determining factor to calculate the hopping transition rate.

In contrast to the photoactive layer nodes, sites representing electrodes act as charge reservoirs. The occupation of every single site at $m_i^z = 0$ and $m_i^z = M_z$ is seen to be always one, mimicking the metal character of the anode and the cathode. If a charge carrier is injected from an electrode node into the photoactive layer, then the occupation of the electrode node should be empty. But since metals can be seen as a continuum of fully occupied and delocalized electronic states below the Fermi energy, the empty state is assumed to get refilled immediately. The energy levels of the contact nodes are equal to the Fermi energy of the respective metal, i.e. the cathode work function $\phi_{cathode}$ and the anode work function ϕ_{anode}. The energy difference between the Fermi level and the energy levels of the adjacent organic nodes is the determining quantity for the charge injection at the metal-organic contact and the reverse extraction process.

4.2.2. Morphology generation

Bulk-heterojunction

After the grid is set up and the node positions are fixed, the distribution of donor and acceptor sites must be assigned to the grid. The morphology of a BHJ is an intertwined phase separation of donor and acceptor molecules with subsequent "percolation pathways" within the respective phases [120]. In studies by Ma et al. [72] and Li et al. [71], it has been shown that the nanoscale morphology of a P3HT:PCBM blend can be influenced by a thermal annealing process and that a coarser morphology leads to both an increased

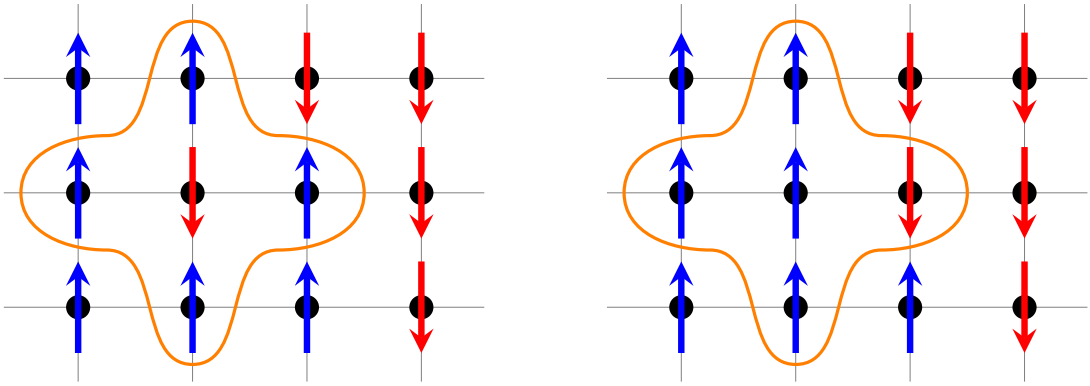

Figure 4.2. – Illustration of the spin-exchange algorithm. The magnetic interaction energy with a defined set of neighbors determines the likelihood for the exchange.

fill factor and short circuit current, and, thus, a higher overall efficiency. To be able to control the intermixing in the simulation, a model based on the Kawasaki spin-exchange algorithm [145] is used [121]. The algorithm allows for an efficient way to reproduce the BHJ morphology.

In the spin-exchange algorithm, compare Figure 4.2, the donor and acceptor materials are interpreted as spins, pointing up or down. They are initially randomly distributed over the entire photoactive layer with equal probability of pointing up or down. Then, two *non-equal spins* are chosen at random and the magnetic interaction energy with their surroundings is calculated according to the Ising model [106], where only first and second neighbors are considered. The second nearest neighbor interaction energy is weighted by a factor $\frac{1}{\sqrt{2}}$ to account for their larger distance. The magnetic interaction energy of a spin s_i with its neighbors s_j without an external magnetic field is

$$\varepsilon_i = -J \sum_j (s_i \, s_j - 1) \,, \tag{4.1}$$

where J is the interaction energy and the summation index j ranges over all first and second neighbors. The spins can take on values of $+1$ (up) or -1 (down). The interaction energy is chosen to be $J = 0.5\, k_B T$, where $k_B T$ is the thermal energy. This value, together with $k_B T = 26\,\text{meV}$, was found to reproduce the BHJ effectively in terms of calculation time. Periodic boundary conditions for the interaction are applied in x- and y-direction to make sure that there is a continuous transition in the material distribution from one face of the periodic lattice box to the next. Then, an attempt is made to swap the neighboring spins and the energy of the new configuration is recalculated. A swap is actually executed with a probability given by the Boltzmann factor for a canonical ensemble

$$P(\Delta\varepsilon) = \frac{\exp\left(-\frac{\Delta\varepsilon}{k_B T}\right)}{1 + \exp\left(-\frac{\Delta\varepsilon}{k_B T}\right)}, \tag{4.2}$$

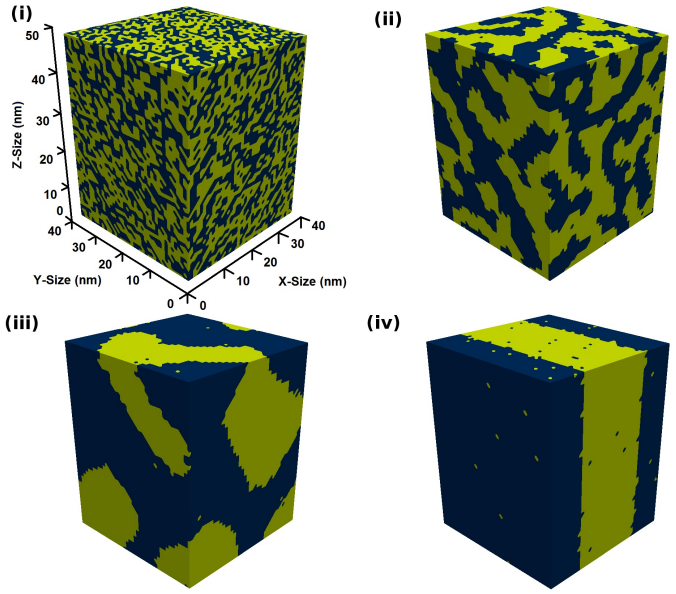

Figure 4.3. – Morphology generation of a BHJ by a spin-exchange algorithm allows control of cluster size: (i) initial random distribution, (ii) weak clustering, (iii) strong clustering and (iv) equilibrium configuration. Figure reprinted from [38]. ©2014 IEEE.

where $\Delta\varepsilon = \varepsilon_{i'} - \varepsilon_i$ is the energy difference between two (swapped) configurations ε_i (initial) and $\varepsilon_{i'}$ (final). Note that the overall number of spins pointing upwards or downwards does not change during a spin exchange. The number of acceptor and donor sites does not change, they only get redistributed.

Subsequent iterations of exchanges lead to the relaxation of the system to a lower energy and a less intermixed state. The number of swaps is counted in terms of Monte Carlo Steps (MCs) in the literature [121], where one MC equals the number of sites in the cell, i.e. 1 MC $= M_x \times M_y \times M_z$. The cluster size of the phase mixing can be roughly estimated by $d = 3V/A$, where V is the total volume and A the interface area. The algorithm allows to control the generated device morphology. As the result of the spin exchange, a 3D view of the various BHJs that can be generated this way is illustrated exemplarily in Figure 4.3. The corresponding MCs range from 0 (random distribution) to 10^6 (very ordered) and yield cluster sizes of 1.9 nm, 6.3 nm, 15.9 nm and 28.3 nm, respectively. The latter case is the equilibrium state of the spin-exchange and results in an almost perfect segregation of the two phases. This configuration is not suitable for a BHJ but is meant to illustrate the algorithm. The morphologies generated this way can be used to mimic the distribution of donor and acceptor material in a BHJ on the discrete lattice.

With this algorithm it is possible that there remain single material sites embedded into the opposite material as can be observed from Figure 4.3. These sites are removed

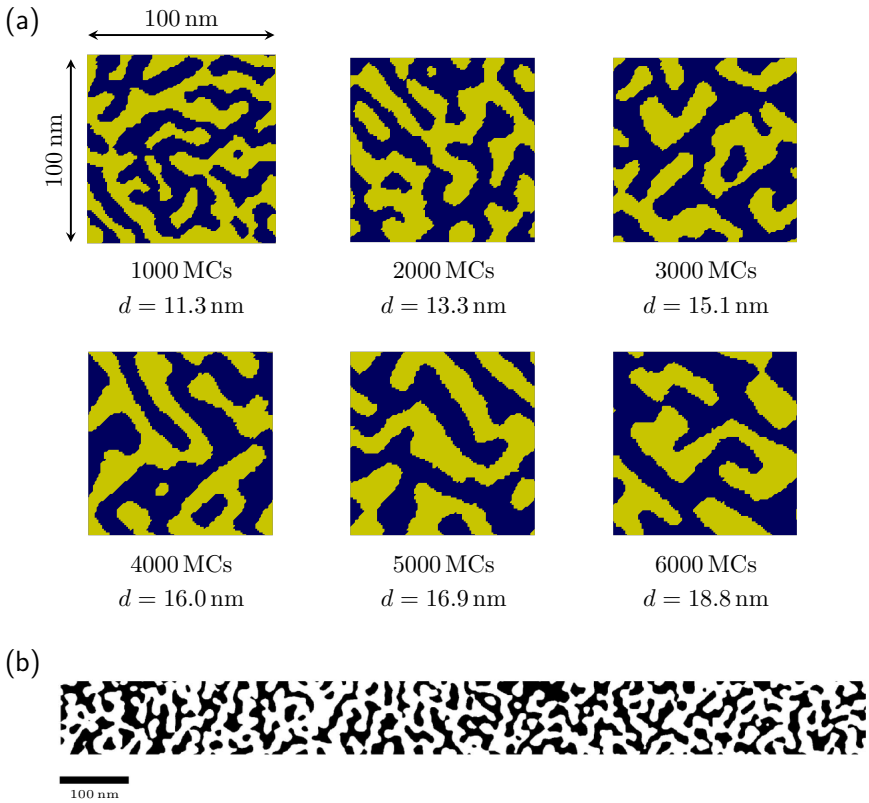

Figure 4.4. – Adjusting cluster size with the spin exchange algorithm (a) to match the morphology of an annealed P3HT:PCBM blend as observed by TEM (b). (b) is reprinted with permission from J. S. Moon, J. K. Lee, S. Cho, J. Byun, and A. J. Heeger, "'Columnlike' Structure of the Cross-Sectional Morphology of Bulk Heterojunction Materials", *Nano Letters*, vol. 9, no. 1, pp. 230–4, 2009. ©2009 American Chemical Society.

from the distribution because it is not possible to control their number and distribution due to the randomness of the generation process.

In a study about the morphology of a P3HT:PCBM blend [146], Moon et al. used a Focused Ion Beam (FIB) to cut out a slice of a standard blend as used in their experiments. They examined the cross section of the slice with a Transmission Electron Microscopy (TEM) to get insight into the cluster sizes of the respective phases. Figure 4.4 shows a comparison of the TEM image of the real blend and the distributions obtained with the spin exchange algorithm for a various number of MCs. Slices through the generated virtual morphology are $100\,\mathrm{nm} \times 100\,\mathrm{nm}$ wide. The TEM image shows a $1.15\,\mu\mathrm{m} \times 100\,\mathrm{nm}$ wide section from the experimentally observed morphology after a binary filter was applied for better distinction of the phases. As can be seen, at around 5000 MCs, a reasonably accurate representation of the real blend can be obtained by the virtual model. This

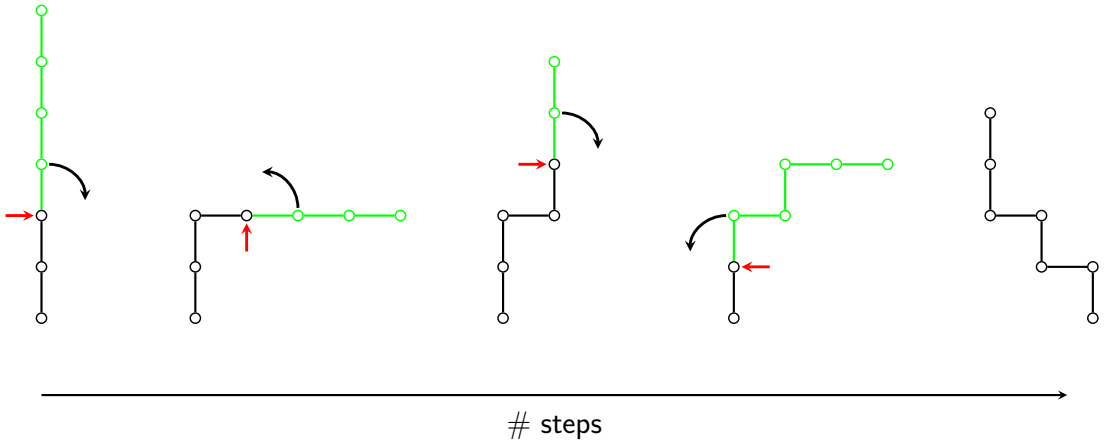

Figure 4.5. – Pivot algorithm for polymer chain generation illustrated in 2D and for a chain length of $N = 7$ and the first 4 steps. The red arrow points to the pivot site. The black arrow indicates the direction of rotation around which the sites before or after the pivot site (marked green) are rotated.

corresponds to an average cluster size of $d \approx 17\,\text{nm}$. For the blend simulations later on, the algorithm is used with this cluster size, unless stated otherwise.

Polymer chain generation

Next to the BHJ generation, in which the donor and acceptor regions are connected bulk regions, it is also possible to explicitly generate polymer chains. A simple model to generate polymer chains is the Pivot algorithm [147]. The Pivot algorithm is a Metropolis Monte Carlo algorithm to construct a polymer chain on a regular lattice by a Self-Avoiding Walk (SAW). The implementation of the algorithm was adapted from [148] and works as follows: at first, the length of the polymer chains to be generated is defined as $L = N \cdot l$, where N is the number of monomers and l is the lattice constant. In our model, we assume all polymers to have the same length. The length can alternatively be drawn from a certain distribution individually for each polymer chain. Furthermore, the number of pivot steps (kinks) to apply is specified as n. The number of kinks executed is initially set to $k = 0$. The algorithm starts with a linear chain of length N. Then, the sequence illustrated in Figure 4.5 is applied:

1. Pick a random 'pivot' site from the chain (red arrow).
2. Pick a direction to modify: either the sites before the pivot or after.
3. Apply a 90° rotation around the pivot site to all sites of the selected chain part (black arrow). This rotation can be in either direction by equal chance.
4. Check if the chain is touching itself (self-avoidance). If yes, undo the rotation. If no, keep the rotation.

5. Increment number of steps performed and terminate if $k = n$.

Depending on the dimension, the rotation in step 3 can occur in a plane (2D) or in space (3D). With increasing number of steps n, the chains will cluster to a more confined region.

4.2.3. Energy distribution

The energy level assigned to each node reproduces the potential landscape experienced by particles in the photoactive layer. There are four terms contributing to the local potential energy at node i:

$$E_i^{HOMO} = E_i^{0,HOMO} + E_i^F + E_i^\sigma + E_i^C \qquad \text{(for holes)} \tag{4.3}$$

$$E_i^{LUMO} = E_i^{0,LUMO} + E_i^F + E_i^\sigma + E_i^C \qquad \text{(for electrons)} \tag{4.4}$$

where E_i^0 is the MO energy of the respective material, E_i^F is the electric field, E_i^σ the energetic disorder and E_i^C the Coulomb potential – each at node i. While the first three contributions (MO energy, electric field and energetic disorder) are considered to be fixed for each simulation run, the Coulomb interaction is dynamically updated during each simulation step to account for the motion of charges and their mutual interaction. The implementation of each of the four terms E_i^0, E_i^F, E_i^σ and E_i^C is explained in the following sections. Alongside the explanations, a typical distribution of the four contributions to LUMO and HOMO energy levels is depicted in Figure 4.6 and Figure 4.7, respectively. From these illustrations it is evident that the potential landscape in spatially and energetically disordered materials, and hence the charge transport, is tremendously complex. The consideration of single-particle effects on such disordered structures is virtually impossible to describe by continuum models – which is where the kMC method shows its potential.

Molecular orbital energies

The first energy term E_i^0 in Equations (4.3) and (4.4) is associated with the MO energy of the material at node i. Depending on the node material, HOMO and LUMO energy levels have to be considered accordingly. If node i is an acceptor material, E_i^0 gets the HOMO and LUMO energy level of the acceptor, E_A^{HOMO} and E_A^{LUMO}, assigned in two designated variables. Vice versa, if node i is a donor site, E_i^0 gets the HOMO and LUMO energy level of the donor, E_D^{HOMO} and E_D^{LUMO}, assigned. Thus,

$$E_i^{0,HOMO} = \begin{cases} E_A^{HOMO} & \text{if } i \text{ acceptor site} \\ E_D^{HOMO} & \text{if } i \text{ donor site} \end{cases} \tag{4.5}$$

$$E_i^{0,LUMO} = \begin{cases} E_A^{LUMO} & \text{if } i \text{ acceptor site} \\ E_D^{LUMO} & \text{if } i \text{ donor site.} \end{cases} \tag{4.6}$$

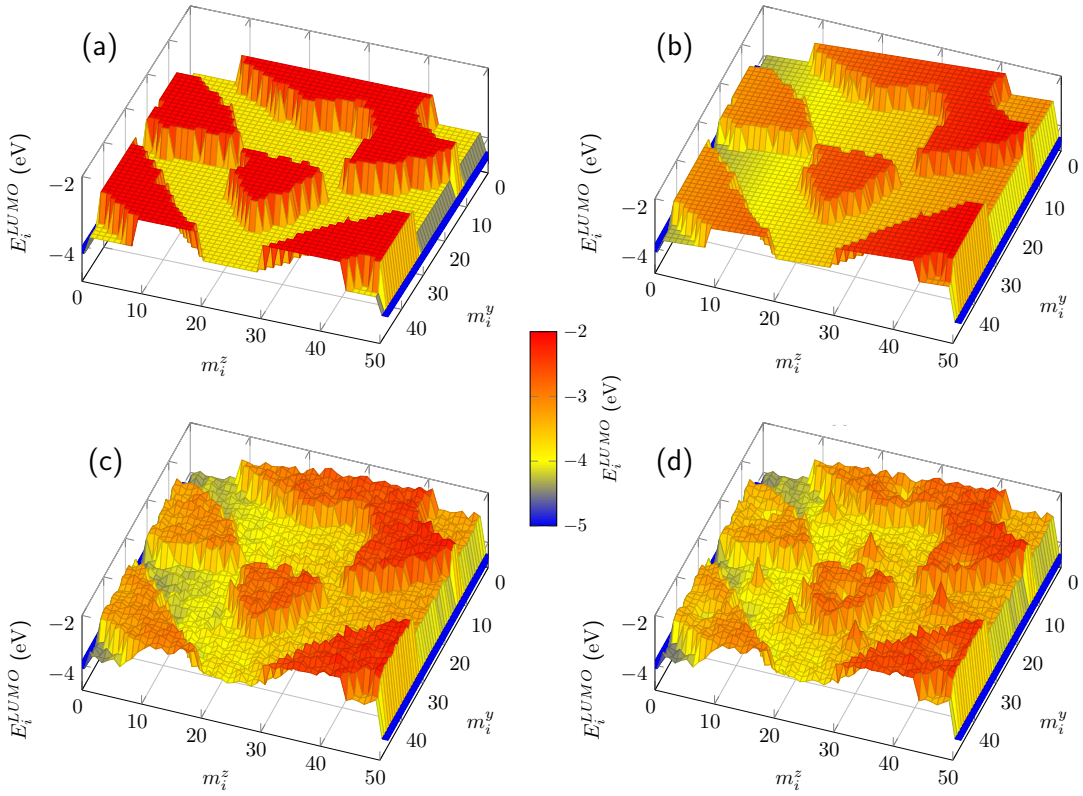

Figure 4.6. – Energy distribution of LUMO levels, affecting electrons, with: (a) distribution of donor and acceptor materials, (b) with electric field and contact work-function difference, (c) with energetic disorder, and (d) with the influence of charge carriers in the system.

This results in two different energetic distributions for electrons and holes. Electrons are transported in the LUMO levels and holes in the HOMO levels. Therefore, when considering an electron movement only the LUMO energy states are considered and vice versa the HOMO levels for holes. Figure 4.6a and Figure 4.7a show an example for the constant energetic distributions for $E_i^{0,HOMO}$ and $E_i^{0,LUMO}$ of a slice through a blend as generated by this setup. The intermixing of donor and acceptor sites with their respective MO levels and the periodic boundary condition in y-direction can be observed. Subsequent pathways within the respective phases act as possible percolation pathways for the charge carriers to be transported through the bulk. A large energy barrier between the different materials restricts them to stay in one phase, namely the acceptor for electrons and the donor for holes. Simultaneously, these interfaces offer the energy necessary to separate an exciton into free charge carriers. Cathode and anode nodes are at $m_i^z = 0$ and $m_i^z = M_z$, respectively.

Electric field contribution

The second term in Equations (4.3) and (4.4), E_i^F, reflects the internal distribution of the electric field induced by the contacts. It is assumed that the potential difference between cathode and anode drops linearly across the organic layer, justified for low charge carrier densities [149], in a direction perpendicular to the electrode surfaces. The total potential energy drop from $m_i^z = 0$ to $m_i^z = M_z$ consists of the contribution of the electrode work function difference $\Delta\phi = \phi_{anode} - \phi_{cathode}$ and the potential energy drop across the external load eU_{ext}. Electrode work functions are defined as negative, $\phi_{anode} < 0,\ \phi_{cathode} < 0$. Thus, the energy of every node at constant m_i^z (all nodes in planes parallel to the electrodes) is modified by

$$E_i^F = \frac{m_i^z}{M_z}\,(eU_{ext} - \Delta\phi). \tag{4.7}$$

For no external potential drop (short-circuit condition), the influence of the electric field is determined only by the work functions of the electrodes. Usually, in OSCs, the anode material has a larger (negative) work function so that $\Delta\phi < 0$. Both HOMO and LUMO level get tilted upwards in energy as m_i^z increases and the driving force acts towards the cathode for electrons and towards the anode for holes (reverse current).

The modification of the node energies over the photoactive layer under the influence of different work functions and $U_{ext} = 0$ (short-circuit) condition is shown in Figure 4.6b for the LUMO level and in Figure 4.7b for the HOMO level. The electric field acts as driving force for charge carriers to the electrodes. Electrons tend to move downwards the "LUMO surface" in order to relax in energy. Vice versa, holes relax in energy when they hop upwards the HOMO. In order to extract power from the device, solar cells are operated in a configuration in which electrons are driven to the bottom contact, defining the cathode, and holes are driven to the top contact, defining the anode.

A reverse bias condition ($U_{ext} < 0$) is conceptually similar to the short-circuit condition, i.e. electrons tend to percolate towards the bottom (cathode) contact, and hole toward the top (anode) contact. The only difference is that the slope of the electric field contribution $(eU_{ext} - \Delta\phi)/M_z$ is steeper, and hence the driving force stronger. For large U_{ext} in negative direction, this setup corresponds to a photo-diode. Such a setup can also be simulated by the model but is not done within this work. Power is dissipated in this regime.

By applying a forward bias $U_{ext} > 0$, the energy landscape tilts downwards and eventually reaches flat band conditions ($eU_{ext} - \Delta\phi = 0 \Rightarrow E_i^F = 0\ \forall i$, similar to Figure 4.6a and Figure 4.7a). At flat band conditions, no net driving force induced by E_i^F to either electrode acts on particles. For even larger voltages, a driving force acts in forward current direction. In forward bias condition, the slope of the energy levels has turned the other way around and more electrons become collected at the anode and holes at the cathode than the other way around. Forwards bias, however, is not relevant for solar cell operation as no power is extracted from the cell in this condition but only dissipation occurs.

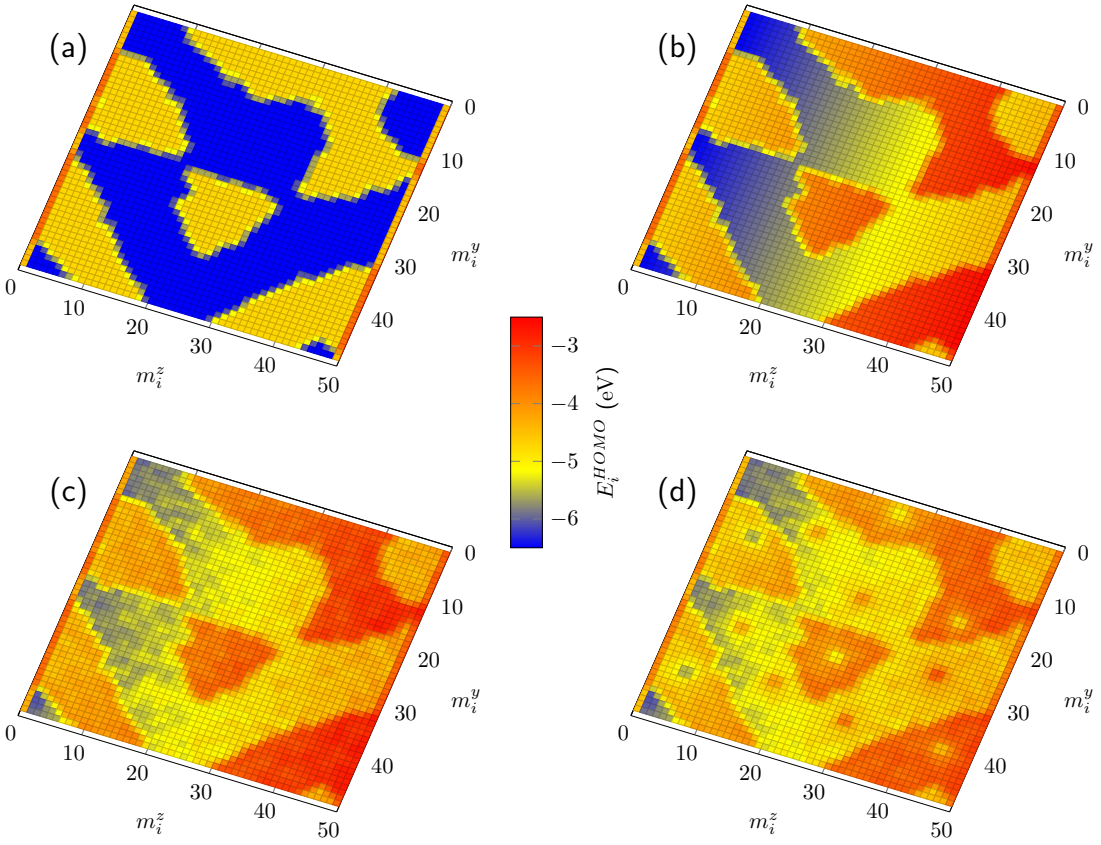

Figure 4.7. – Energy distribution of HOMO levels, affecting holes, with: (a) distribution of donor and acceptor materials, (b) with electric field and contact work-function difference, (c) with energetic disorder, and (d) with the influence of charge carriers in the system.

In the model, it is assumed that the potential energy of the cathode stays the same for any applied voltage and only the anode and photoactive layer nodes energies get shifted. The cathode work function acts as reference potential. This can be justified by the fact that only energy differences between two nodes $E_{ij} = E_j - E_i$ are relevant for the calculation of any transition rate (cf. Section 4.3) and it is of no importance how large the absolute values are. Nodes at $m_i^z = M_z$, which correspond to the energy levels of the anode, are shifted by $E^F_{m_i^z=M_z} = eU_{ext} - \Delta\phi$. The anode energy level relative to the cathode is then

$$\phi_{anode} + E^F_{m_i^z=M_z} = \phi_{anode} + eU_{ext} - \Delta\phi = eU_{ext} + \phi_{cathode}. \tag{4.8}$$

This way, for the equilibrium state $U_{ext} = 0 \Rightarrow E^F_{m_i^z=M_z} = \phi_{cathode}$, anode and cathode have the same energy level, namely the equilibrium Fermi energy of the entire device.

During a simulation run, the external bias can be varied to obtain the current-voltage

characteristics of the solar cell. For every voltage, the influence of E_i^F has to be recalculated and added to the HOMO/LUMO levels E_i^0. Apart from the Coulomb forces, which vary during each time step of the simulation, $E_i^0 + E_i^F + E_i^\sigma$ is calculated once per setup process and remains fixed throughout one simulation run for constant voltage.

Energetic disorder

The third term in Equations (4.3) and (4.4), E_i^σ, accounts for the energetic disorder of the organic semiconductors. Due to the lack of a periodic spatial arrangement of disordered materials, the concept of a band structure and its physical description of delocalized states forming electronic bands with a parabolic DOS does not apply. Disordered semiconductors can therefore only be described by a DOS by which the localized states are distributed.

One should generally distinguish between the intrinsic DOS, i.e. the distribution of states around the MO levels of the pure material, broadened by structural disorder, and the DOS of (deep) trap states. For the intrinsic DOS, an uncorrelated Gaussian distribution of localized states (Gaussian Density of States (GDOS)) was introduced by Bässler [56] and is nowadays widely adapted to model charge transport in disordered organic semiconductors, especially by kMC simulations. A correlation, i.e. smoothing of the uncorrelated disorder and its effect on charge transport have been investigated [116] but are not considered here.

For pure films of organic semiconductors, a GDOS (intrinsic) with an exponential low energy tail (trap states) has been extracted by Kelvin probe force microscopy e.g. in [150], [151]. In OSCs, the shape of the DOS for trap states is controversial. Statements that the GDOS can be suitable to describe intrinsic and trap states [58], [152] as well as arguments in favor of a pure exponential DOS can be found [153].

In terms of modelling transport in organic disordered materials, Baranovskii has extensively compared the applicability of a (pure) exponential DOS and a (pure) GDOS in his reviews [57], [154]. The conclusion of his comparison is that when the charge mobility in an organic semiconductor is dependent on the charge carrier concentration at low concentrations, as it was measured in commonly studied polymers such as P3HT, an exponential DOS can be ruled out and the DOS must be close to a Gaussian [155]. Based on these arguments, and since we do not explicitly introduce traps, we employ the GDOS model without additional extensions in the bandgap.

The energetic disorder E_i^σ can be chosen separately for donor and acceptor sites

$$E_i^\sigma = \begin{cases} E_A^\sigma & \text{if } i \text{ acceptor site,} \\ E_D^\sigma & \text{if } i \text{ donor site.} \end{cases} \tag{4.9}$$

where E_A^σ is the contribution of energetic disorder to node i at an acceptor site and E_D^σ is the contribution at a donor site. The energetic disorder affects HOMO and LUMO levels in Equations (4.3) and (4.4) equally.

The value of E_i^σ is, for each node and for donor and acceptor sites independently,

drawn by a Gaussian distribution of the form

$$g(E) = \begin{cases} \dfrac{N}{\sqrt{2\pi\sigma_A^2}} \exp\left(-\dfrac{(E-E_i^0)^2}{2\sigma_A^2}\right) & \text{if } i \text{ acceptor site,} \\ \dfrac{N}{\sqrt{2\pi\sigma_D^2}} \exp\left(-\dfrac{(E-E_i^0)^2}{2\sigma_D^2}\right) & \text{if } i \text{ donor site.} \end{cases} \tag{4.10}$$

where $N = l^{-3}$ is the available site density, E_i^0 is the MO energy level of site i, and σ_A and σ_D are the standard deviations of the distribution in acceptor and donor material, respectively. The standard deviation is commonly labeled as the *energetic disorder*. Unless stated otherwise, we will use one common value of energetic disorder σ for both donor and acceptor sites, i.e. $\sigma = \sigma_A = \sigma_D$. Values around $\sigma = 70\,\text{meV}$ have been found for materials established in OSCs such as P3HT:PCBM [156]–[158].

An illustration of the potential landscape for charges with the influence of a GDOS (on top of $E_i^0 + E_i^F$) is represented in Figure 4.6c for electrons and in Figure 4.7c for holes, respectively.

4.2.4. Treatment of Coulomb interaction

During a simulation run, charge carriers are constantly in motion and modify the local Coulomb potential acting on each node point at every time step. The last term in Equations (4.3) and (4.4) must therefore be updated during the simulation run with every charge carrier hopping to another node. The local modification of the potential energy with electrons and holes in the system is depicted in Figure 4.6d for electrons and in Figure 4.7d for holes at a snapshot in time. The particles induce local spikes in potential energy due to their Coulomb attraction/repulsion.

Since organic materials have a relatively low dielectric constant ($\varepsilon_r \approx 3-5$), Coulomb forces are not well screened and act on much larger distances than in inorganic semiconductors like silicon. Thus, the interaction between charged particles is expected to have a larger influence on transport and recombination in organic solar cells than in inorganic solar cells.

Most of the former kMC models [121], [122], [124] use a cutoff radius for the range in which charges are influenced by the Coulomb potential of other charges around them in order to save computation time. Casalegno et al. [118] addressed this problem because no studies on the justification for the use of a cutoff, especially in low ε_r materials, existed. Their model is based on a full-range treatment of Coulomb interactions with image charges induced in the electrodes and consideration of interactions across the periodic simulation box, with only little additional computational effort at runtime. In this work, the full range model is adapted to preserve accuracy and is described in this section, following the implementation of Casalegno et al. [118]

Method of image charges

Charge carriers within the photoactive layer are located in between two metallic surfaces. As known from basic electrostatics, a particle with charge q next to a bulk metallic conductor induces a non-negative surface charge to account for the boundary conditions (vanishing electric field in metals) at the interface between the metal and the material the charge resides in. To calculate the electrostatic energy of this setup, it is a common approach to use the method of image charges [159], [160]. In this method, the conductor is replaced by a charge of opposite sign $q' = -q$, located at a position exactly mirrored to the original charge q with regard to the metallic surface. This imaginary setup fulfills the boundary conditions of the real system. It allows to calculate the electrostatic energy of a point charge next to a conductor, simply as interaction between two point charges, the real and the mirrored one, but without the existence of the conductor.

To apply the method of image charges to a solar cell setup, Casalegno et al. used a setup as shown in Figure 4.8a. Particles located in the region from $-\frac{Z}{2}$ to $+\frac{Z}{2}$ (organic layer) induce image charges in the electrodes. The electrodes are represented as half spaces from $-\frac{Z}{2}$ to $-\infty$ and $+\frac{Z}{2}$ to $+\infty$. An image charge in one electrode, in turn, induces itself another image charge inside the opposite electrode. Continuing this pattern periodically, the relative position of mirrored charges can be reduced to a single unit cell of height $2Z$. As a concrete example, let a hole with charge $+q$ be located at $-\frac{Z}{2} < z_0 < +\frac{Z}{2}$. The first order image charges have an opposite charge $-q$. They are induced in the lower electrode at $z_{-1} = -Z - z_0$ and at $z_{+1} = +Z - z_0$ in the upper electrode, respectively. Mirroring z_{-1} at the upper electrode interface yields again a positive charge at z_{+2} and, vice versa, z_{+1} induces z_{-2}. Without loss of generality, a box of height $2Z$ containing the initial charge and the first mirror charge in the upper electrode can be defined as periodically reoccurring in z-direction. This periodic box represents the unit element for the treatment of Coulomb interaction including all mirror charges.

The Ewald sum

To determine whether a particle at a node i experiences a driving force due to electrostatic interaction with other charges, all possible interactions must be considered. One has to take into account the Coulomb interaction with other charges in the original simulation box, the periodically mirrored charges in the electrodes (z-direction), and the periodic replicas in neighboring cells in x- and y-direction. In general, the electrostatic potential at node i is calculated by

$$U_i = \frac{1}{4\pi\varepsilon_r\varepsilon_0} \sum_{\bar{n}} \sum_{j=1}^{2N}{}' \frac{q_j}{|\bar{r}_{ij} + \bar{n}|}. \tag{4.11}$$

Here, the first sum over $\bar{n}$ corresponds to the periodically reoccurring unit boxes in x-, y- and z-direction with $\bar{n} = (n_x X,\, n_y Y,\, 2n_z Z)$ where $n_{x,y,z} = 0, \pm 1, \pm 2, \ldots$. The second sum includes all charged particles q_j in box $\bar{n}$ interacting with i at a distance r_{ij} between

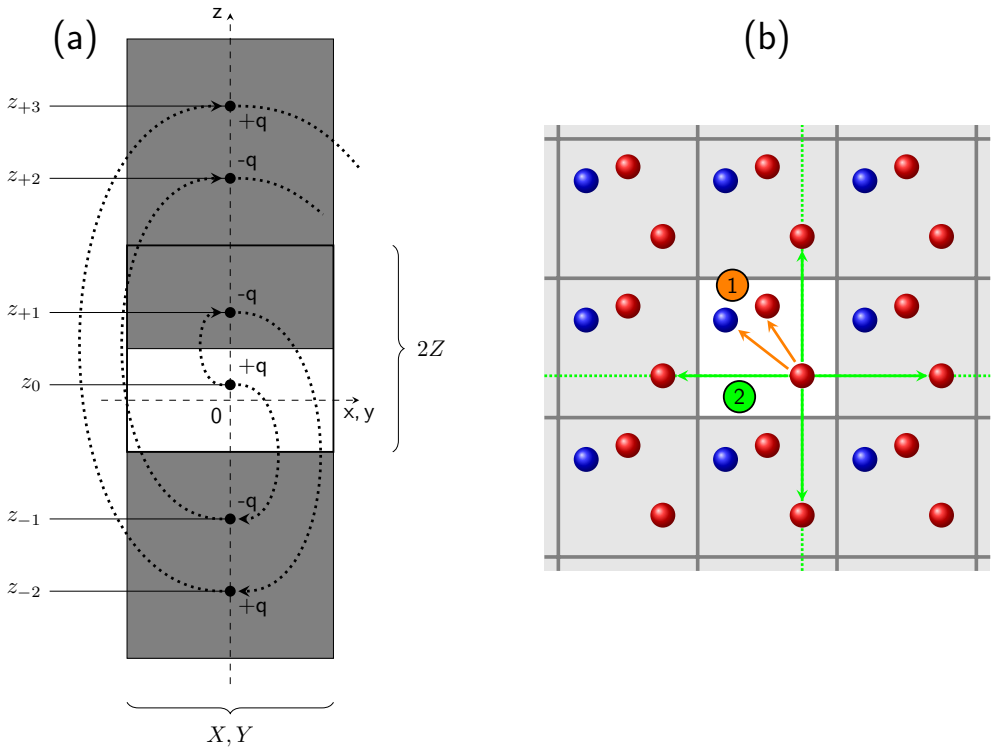

Figure 4.8. – Charges inside the photoactive layer induce mirror charges in the electrodes by a periodic pattern (a). Exploiting the pattern and considering periodic boundary conditions in x- and y-direction (b), the Coulomb interaction calculation can be calculated by the evaluation of the Ewald sum in a periodic simulation box of size $X \times Y \times 2Z$. (a) adapted (replicated) from [118].

node i and a particle at j. The inner summation index j ranges over N real particles and N first order mirror charges in box $\bar{n}$. The periodicity of the unit boxes is completely considered in $\bar{n}$. All image charges are included by considering only the first order image charge in the $2Z$ box and calculating the sum over the n_z indices. Duplicated charges in simulation box replicas in x- and y-direction enter the interaction potential by summation over n_x and n_y (Figure 4.8b). Self-interaction of the particle at i must be omitted, which is indicated by the prime $'$.

To determine whether it is favorable for a particle to hop from node i to j in terms of electrostatic energy, the difference $\Delta E_{ij}^C = \frac{1}{2}q(U_j - U_i)$ has to be calculated. It would be possible to consider the local Coulomb energy by adding an energy term $E_i^C = \frac{1}{2}qU_i$ to every single node as indicated in Equations (4.3) and (4.4) in analogy to the initial setup process for the MO levels and the electric field. However, U_i would have to be recalculated for every single node in every kMC step to update the constantly changing Coulomb forces. A more efficient treatment is to calculate U_i at runtime and only for those nodes a particle can hop to. This way, a sufficient amount of processing time can

be saved.

The evaluation of Equation (4.11) for a multi-particle system is complicated. A direct evaluation is computationally not feasible. A common approach is to consider only the next neighbor's boxes in the calculation or even only the particles residing in a certain cutoff radius around a charge. However, an exact evaluation can be obtained by making use of the Ewald sum [141], an approach that is commonly used in MD. According to [161], [162] the sum is conditionally convergent, meaning that the result depends on the order of summation. If chosen appropriately the sum converges to its limit value but only very slowly [163]. By separation into two specifically chosen sub-sums, a fast convergence of both sub sums can be achieved. The fundamental idea behind the Ewald summation is to separate the Coulomb interactions into short range and long range interactions. While the component for short range interactions is calculated best in real space coordinates, the long range part converges quickly in the reciprocal space. The full derivation is beyond the scope of this thesis and can be found in [107], [163]. According to [161] the final expression is

$$U_i = \frac{1}{4\pi\varepsilon_r\varepsilon_0}\left[\sum_{\bar{n}}\sum_{j=1}^{2N}{}' q_j \frac{\operatorname{erfc}(\alpha|\bar{r}_{ij}+\bar{n}|)}{|\bar{r}_{ij}+\bar{n}|} + \frac{4\pi}{V_{\mathrm{sb}}}\sum_{\bar{k}\neq\bar{0}}\sum_{j=1}^{2N}\frac{q_j}{|\bar{k}|^2}\exp\left(-\frac{|\bar{k}|^2}{4\alpha^2}\right)\cos(\bar{k}\cdot\bar{r}_{ij}) - q_j\frac{2\alpha}{\sqrt{\pi}}\right]. \tag{4.12}$$

Here, erfc(..) is the complementary error function[1], α is the so called splitting parameter, $\bar{k}$ the lattice vector in reciprocal space and $V_{sb} = 2XYZ$ the volume of the simulation box. The first term corresponds to the sum in real space, the second is the sum in k-space, and the third term is a self-potential term.

According to [161], α shifts the ratio between real and reciprocal space contributions to the sum. By setting $\alpha = 2^{1/6}\sqrt{\pi}\ {V_{sb}}^{1/3}$, the evaluation in real space can be executed within the boundaries of two periodic boxes without loss of accuracy. This makes it possible to reduce the number of possible interactions to a finite number and to implement the full Coulomb treatment efficiently into the model.

Implementation

Calculating the Coulomb potential for every charged particle at simulation runtime after Equation (4.12) in every kMC step would lead to an unfeasible amount of computational effort. By a restatement of Equation (4.11), it is possible to outsource a sufficient amount of calculations to the initial setup process before the dynamic kMC part begins. Taking

$$U_i = \sum_{j=1}^{2N} q_j\left[\frac{1}{4\pi\varepsilon_r\varepsilon_0}\sum_{\bar{n}}{}'\frac{1}{|\bar{r}_{ij}+\bar{n}|}\right], \tag{4.13}$$

[1] complementary error function $\operatorname{erfc}(t) = \frac{2}{\pi}\int_x^\infty e^{-t^2}dt$

the evaluation can be separated in the inner part, which represents the interaction of one single particle j with all its images in different image boxes $\bar{n}$, and the outer part, which considers the total number of different particles in the unit box. As stated above, it is sufficient to evaluate the Ewald sum for two neighboring periodic simulation boxes in the real space because the long range interactions are effectively calculated in the k-space summation. Since the number of nodes in these is restricted, the number of interactions with their images is also restricted and the term inside the square brackets can only take on a finite number of values. Exploiting the fact that the system is set up on a discrete grid, the distances between two distinct particles are:

$$\begin{aligned}\bar{r}_{ij} &= (\ (m_j^x - m_i^x)\, l,\ (m_j^y - m_i^y)\, l,\ (m_j^z - m_i^z)\, l\ ) \\ &= (m_{ij}^x\, l,\ m_{ij}^y\, l,\ m_{ij}^z\, l)\end{aligned} \tag{4.14}$$

For two neighboring simulation boxes in each direction, the node indices are restricted to integer values in the ranges $m_{ij}^x \in [-M_x, M_x]$, $m_{ij}^y \in [-M_y, M_y]$, and $m_{ij}^z \in [-2M_z, 2M_z]$. By defining a pair potential function as

$$U^{pair}(m_{ij}^x, m_{ij}^y, m_{ij}^z) = \frac{1}{4\pi\varepsilon_r\varepsilon_0} {\sum_{\bar{n}}}' \frac{1}{|\bar{r}_{ij} + \bar{n}|}, \tag{4.15}$$

that can only take on a discrete set of constant values depending only on the distance of two distinct charge carriers, it is possible to pre-calculate these values and store them in the memory prior to runtime. During runtime, the only evaluations that have to be made are

$$U_i = \sum_{j=1}^{2N} q_j\, U^{pair}(m_{ij}^x, m_{ij}^y, m_{ij}^z), \tag{4.16}$$

where the values for U^{pair} are stored in the memory and can easily be read out, passing U^{pair} the distance between two nodes i and j with a set of the three integers $\{m_{ij}\}$.

The initial setup of U^{pair} still has to be calculated by the Ewald sum, whose inner part reads after reformulation:

$$\begin{aligned}U^{pair}(m_{ij}^x, m_{ij}^y, m_{ij}^z) = \frac{1}{4\pi\varepsilon_r\varepsilon_0} \Bigg(&{\sum_{\bar{n}}}' \frac{\operatorname{erfc}(\alpha|\bar{r}_{ij} + \bar{n}|)}{|\bar{r}_{ij} + \bar{n}|} \\ &+ \frac{4\pi}{V_{sb}} \sum_{\bar{k}\neq\bar{0}} \frac{1}{|\bar{k}|^2} \exp\left(-\frac{|\bar{k}|^2}{4\alpha^2}\right) \cos(\bar{k}\cdot\bar{r}_{ij}) \Bigg).\end{aligned} \tag{4.17}$$

The third term in Equation (4.12), the self-potential term, is omitted because it vanishes when a difference between two potentials is calculated by $\Delta E_{ij}^C = \frac{1}{2} q(U_j - U_i)$.

In summary, the Coulomb energy calculation comprises a full treatment of electrostatic forces with interaction over periodic boundaries in x- and y-direction and mirror charge effects in the electrodes (z-direction) are implemented after Casalegno et al. [118]. A reformulation of the total electrostatic energy by the Ewald sum is taken into account

to optimize the demand on processing time. This allows to make use of (i) the specific periodic boundary conditions applied, and (ii) the discrete nature of the lattice, in order to outsource the interactions of a single particle with its images in the electrodes and replicas in other periodic simulation boxes. These interactions are calculated via Equation (4.17) before kMC runtime and stored in the memory as pair potentials. During runtime, interactions between distinct particles is calculated via Equation (4.16), where the values for the pair potentials can simply be read from the memory, and the final contribution to the last term in the potential landscape is calculated by $\Delta E_{ij}^{C} = \frac{1}{2}q(U_j - U_i)$.

4.3. Implementation of processes

After the initial system setup, the kMC loop is entered (see flowchart in Figure 3.5). Depending on the current system state, the transition rate values determine the probability for the steps in the dynamic evolution of the system. Each process is described either by a physical model or takes on values extracted from experimental measurements. In this section it is described by which model the individual rates are implemented or what measurement values are used for the magnitude of the rates.

The implemented processes are:

1. exciton generation (exg)
2. exciton diffusion by hopping (exh)
3. exciton separation (exs)
4. exciton decay (exd)
5. electron and hole hopping (elh, hoh)
6. electron-hole recombination (ehr)
7. electron and hole injection from electrodes (eli, hoi)
8. electron and hole collection at electrodes (elc, hoc)

In Figure 4.9, an overview on the events and their chain of dependencies on processes necessary for their activation is given. For example, at the beginning of a simulation only two processes are enabled, namely the exciton generation and the injection of electrons or holes from the electrodes. It is obvious that no exciton diffusion or charge carrier hopping should occur if there are currently no excitons or charge carriers present in the photoactive layer. Thus, all other rates must be zero to disable the corresponding processes. Physically forbidden processes are deactivated by setting the corresponding rate to zero. In the same logical manner each process activation is considered. Periodic boundary conditions in the planar dimensions are implemented for exciton hopping, exciton separation, charge carrier hopping and recombination. While charge carriers can be injected and collected at the bottom and top contacts, excitons are confined to the simulation box.

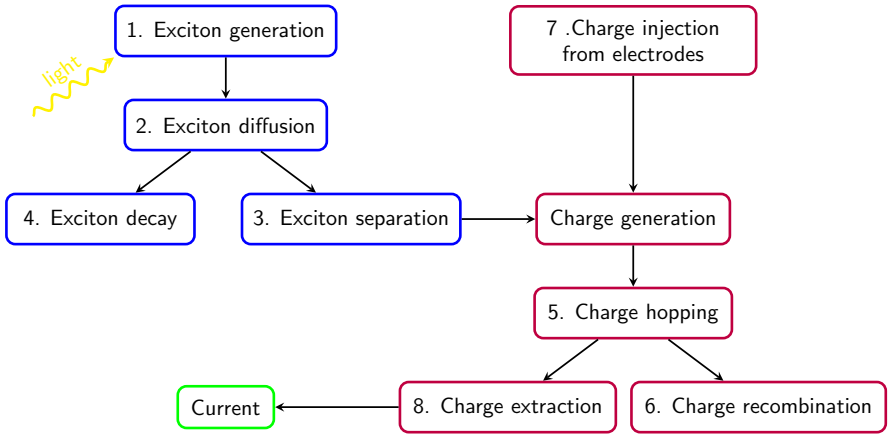

Figure 4.9. – Schematic representation of process activation. At the beginning of a simulation, either light induced exciton generation or charge injection from the electrodes can occur. If excitons and charge carriers are present, their respective processes for motion, recombination, and removal become activated. Finally, if charge carriers get collected at an electrode they contribute to an external current.

To adapt the derived models to real devices, specific input parameters must be taken from experimental data. It is not possible by the kMC method to derive material parameters per se, because it is not an ab-initio method based on fundamental physical laws. The focus is directed towards parameter values for the benchmark device comprised of P3HT:PCBM because it is the most extensively studied composition regarding polymer based compositions. Nevertheless, the derivations are applicable in the same manner for other compositions, considered that equivalent data is available for those materials.

Alongside the explanation of the processes (1)-(8) throughout this section, an illustration of the respective process behavior on the simulation grid is depicted in Figure 4.10; in Figure 4.10a for the excitonic processes and in Figure 4.10b for the charge processes.

4.3.1. Exciton generation

Upon illumination, excitons are generated in the photoactive layer. We describe the exciton generation by a generation profile $G(x_i, y_i, z_i)$ in units of $\mathrm{nm}^{-3}\,\mathrm{s}^{-1}$ to count the number of excitons created per unit time and volume at node i. Two models for the exciton generation are implemented:

- a constant generation over the entire active layer and
- a Transfer Matrix Method (TMM) generation profile.

It shall be explicitly noted at this point that for all simulations the TMM model is used. Both the constant generation and the TMM model are an approximation to cover the optical effects leading to the absorption of photons and generation of excitons. For a

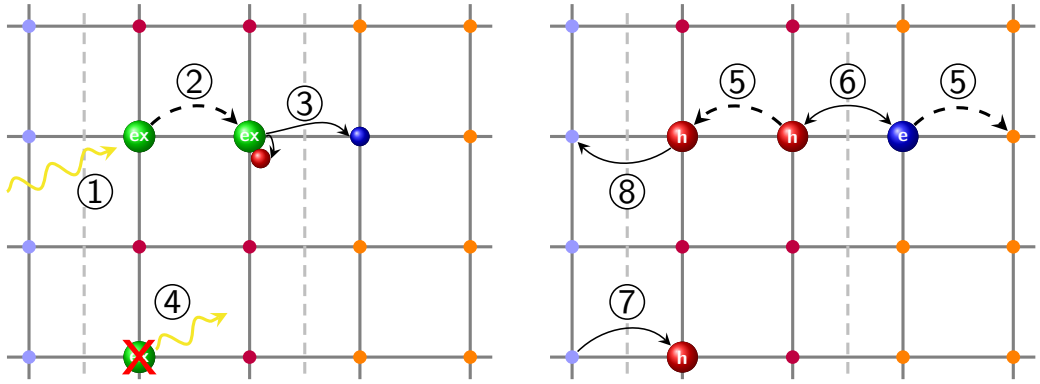

(a) Exciton processes **(b)** Charge processes

Figure 4.10. – Geometrical illustration of implemented processes for excitons (a) and charge carriers (b) on the simulation grid. The right broken line represent the heterojunction between donor (left, purple) and acceptor (right, orange) nodes at which excitons are separated and electron and hole can recombine. The left broken line indicates the interface between a contact (left, light blue) and the donor material (right, purple) at which charges can be injected or collected.

sophisticated treatment of the optical effects, a full 3D solution of the Maxwell equations [160] would be most desirable to calculate the local $G(x_i, y_i, z_i)$. However, this approach is not straightforward: solving the Maxwell equations on an intertwined geometrical structure such as a BHJ is exceedingly complex. One must rely on numerical methods, such as the Finite Element Method (FEM) on a discretized representation of the blend. A method to generate a discrete mesh on which the equations can be solved without convergence problems does not yet exist. While our group is working on such a structure (see refs. [164], [165]), this approach is not covered here. In this study, the mentioned simplified exciton generation models are used and they are assumed to contain all optical effects. We have furthermore investigated the influence of different generation profiles on the performance of BHJ OSCs and found little influence on the results (cf. Appendix A.1). It is therefore argued that the TMM model is sufficient to describe the exciton generation.

In the case of constant generation, a fixed generation rate a_{exg} in units of $\mathrm{nm}^{-3}\,\mathrm{s}^{-1}$ is chosen. For a lattice constant of 1 nm, a_{exg} represents precisely the exciton generation rate per single node in the layer, i.e.

$$G(x_i, y_i, z_i) = a_{exg} \quad \forall i. \tag{4.18}$$

The generation rate is assumed to be constant regardless of the node materials, i.e. exciton generation happens with equal probability in donor and acceptor material. Since there is no information about the external illumination strength in the constant generation model, a_{exg} needs to be adapted to the illumination spectrum, i.e. $100\,\mathrm{mW\,cm}^{-2}$ in standard conditions, or needs to be fitted to experimental results. For a given incident power, a_{exg}

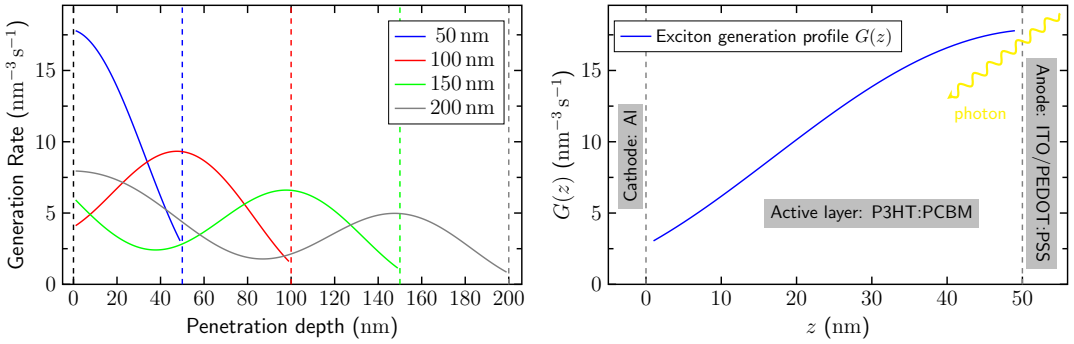

(a) Generation profile for different active layer thicknesses

(b) $G(z)$ as used in the 50 nm simulations. Contacts and incident light are indicated

Figure 4.11. – Exciton generation profiles $G(z)$ obtained from [166] by TMM for different active layer thicknesses. (b) is adapted from [33]. ©2016 IEEE.

can easily be estimated under the assumption that each incident photon has the same energy, creates one electron-hole pair, and that all charges are collected.

The TMM model is a more sophisticated model that allows to calculate the generation profile in dependency of the external illumination spectrum and utilizes the specific complex refraction indices $\bar{n} = n + i\kappa$ of the materials in the active layer, where n is the refractive index and κ is the extinction coefficient. It also considers interference effects that arise from reflection of light at the contacts and lead to a standing wave in the active layer. We use a TMM model in one dimension based on the work of Burkhard et al. [166]. Following this model, the exciton generation rate is determined with respect to the penetration depth z,

$$G(x_i, y_i, z_i) = G(z_i) \tag{4.19}$$

and is considered to have the same value for all nodes in each plane perpendicular to the contacts, irrespective of the material. With the effective refractory indices of a P3HT:PCBM blend, $\bar{n}_{\text{P3HT:PCBM}}$, also taken from [166], and for a device structure ITO/PEDOT:PSS/ P3HT:PCBM/Al the generation profiles obtained under 1 sun (AM1.5) illumination (cf. Figure 2.1) are shown in Figure 4.11a for several different active layer thicknesses ranging from 50 nm-200 nm. For most of the simulations a 50 nm structure will be used. The generation profile $G(z)$ as used in the 50 nm simulations is depicted in Figure 4.11b, together with the contacts and the incident light. Further information on the TMM model and its application to organic thin-films can be found in [32], [167], [168].

Each exciton generated in the simulation box has individual properties assigned that represent its current state and can be used for evaluation:

- Exciton position
- Exciton diffusion rate in ±x, ±y, ±z direction

- Exciton decay rate
- Exciton separation rate in ±x, ±y, ±z direction

4.3.2. Exciton diffusion

Because electron and hole are strongly bound to each other in an excitonic state, they are spatially localized and can therefore be considered as a neutral particle that is not affected by the influence of an internal electric field. This gives rise to the assumption that excitons diffuse randomly through the organic material. In analogy to a 3D random walk, commonly used for Brownian motion, the exciton diffusion can be described by a diffusion coefficient

$$D = \frac{L^2}{6T} \tag{4.20}$$

with L and T being the average diffusion length and lifetime, respectively, of an exciton before it decays. These values correspond to the average distance L a neutral particle diffuses from the originating location after a Brownian random walk for a time interval of T. Experimental measurements show that $L \approx 10\,\mathrm{nm}$ and $T \approx 500\,\mathrm{ps}$ [6] for excitons in BHJs, yielding a diffusion constant of $D = 3.3 \times 10^{-2}\,\mathrm{nm^2\,ps^{-1}}$. Further, the hopping rate is calculated as the inverse of the mean time interval for a hopping process τ_{hop} from one node to another where only next neighbor hopping is considered ($l = 1\,\mathrm{nm}$),

$$a_{exh} = \frac{1}{\tau_{hop}} = \frac{6D}{l^2}. \tag{4.21}$$

According to this model, an average exciton hopping rate of $a_{exh} = 2 \times 10^{11}\,\mathrm{s^{-1}}$ is obtained.

4.3.3. Exciton decay

An exciton decays radiatively after its average lifetime of $T \approx 500\,\mathrm{ps}$ if it has not reached a donor/acceptor heterojunction to become separated in this time. The decay rate can therefore be expressed as the inverse of the lifetime

$$a_{exd} = \frac{1}{T}. \tag{4.22}$$

With $T = 500\,\mathrm{ps}$ from above, $a_{exd} = (500\,\mathrm{ps})^{-1} = 2 \times 10^{9}\,\mathrm{s^{-1}}$. The decay rate is considered to be a cumulative rate for all exciton decay channels and constant for every exciton. Exciton decay is considered to be definite, i.e. after decay has occurred the excitation energy is lost and cannot contribute to any other process anymore.

4.3.4. Exciton separation

A study about the separation has shown that the charge transfer process happens extremely fast [69], [169], [170], i.e. on timescales of $\tau_{sep} \approx 50\,\mathrm{fs}$. The exciton separation

rate is defined as the inverse of the separation time

$$a_{exs} = \frac{1}{\tau_{sep}}. \tag{4.23}$$

Thus, a separation rate of $a_{exs} = \tau_{sep}^{-1} = 2 \times 10^{13}\,\mathrm{s}^{-1}$ is used. Because the rate is large compared to the order of magnitude of all other rates, separation is the dominant process to be executed in case excitons reside at an interface.

Depending on whether the exciton resided in a donor or acceptor material when separation occurs, charge transfer is treated in the opposite manner: in case the exciton was on a donor, an electron transfer to the acceptor is performed and the hole remains in the donor. Vice versa, in case the exciton was on an acceptor, a hole transfer to the donor is performed and the electron remains in the acceptor.

4.3.5. Charge carrier hopping

Charge carriers move under the influence of the internal energy distribution as assigned to the nodes in Section 4.2.3. The hopping process of a charge carrier at node i to node j is described by the Miller-Abrahams formula [63],

$$a_{i\to j} = a_{0,i} \cdot \exp(-2\gamma_i\, r_{ij}) \begin{cases} \exp\left(-\frac{\Delta E_{ij}}{k_B T}\right) & \text{for} \quad \Delta E_{ij} > 0 \\ 1 & \text{for} \quad \Delta E_{ij} \leq 0 \end{cases} \tag{4.24}$$

This equation forms the fundamental basis for the dynamic behavior of all charged particles in the solar cell and its terms and parameters need particular explanation.

The prefactor $a_{0,i}$ represents the so called attempt-to-hop frequency at node i and originates from the interaction of charges carrier from the interactions with phonons. The value of $a_{0,i}$, in units of s^{-1}, is of the order of typical phonon frequencies. $a_{0,i}$ can be set separately for electrons and holes and depends on the material at node i, i.e. different hopping prefactors for donor and acceptor can be chosen. From an energetic point of view, $a_{0,i} \cdot \exp(-2\gamma_i r_{ij})$ is the rate by which a particle hops from one localized state to another under isoenergetic site conditions $\Delta E_{ij} = 0$, as suggested by [121]. It can be derived in close analogy to the random walk treatment of excitons. With the Einstein-Smoluchowksi relation for charged particles [171], [172], the diffusion coefficient reads

$$D = \frac{\mu \cdot k_B T}{e}, \tag{4.25}$$

where electrons and holes have to be treated differently with their respective mobility μ_e and μ_h. The mobilities enter the model by experimental measurements. It needs to be mentioned that the validity of the Einstein relation in Equation (4.25) may not be fulfilled in general in organic semiconductors. There is however evidence that in particular for small electric fields as applied in OSCs, the relation is valid [33]. More on the validity of the Einstein relation in BHJs can be found in the results in Chapter 5.3.2.

Substituting D in Equation (4.21) and considering $\Delta E_{ij} = 0$ in Equation (4.24), one obtains for next neighbor hopping ($r_{ij} = l$):

$$a_{0,i} = \frac{6\mu k_B T}{e \cdot l^2} e^{2\gamma_i l}. \tag{4.26}$$

Exact mobility values for organic materials are hard to determine and depend on many factors such as the grade of disorder and purity. Some typical values are of the order of $10^{-3}\,\mathrm{cm^2\,V^{-1}\,s^{-1}}$ for electrons and $10^{-4}\,\mathrm{cm^2\,V^{-1}\,s^{-1}}$ for holes in a P3HT:PCBM blend [173], [174]. With $\mu_e = 3.7 \times 10^{-3}\,\mathrm{cm^2\,V^{-1}\,s^{-1}}$ and $\mu_h = 7.1 \times 10^{-4}\,\mathrm{cm^2\,V^{-1}\,s^{-1}}$, different attempt-to-hop frequencies for electrons and holes are obtained: $a_{0,elh} = 3 \times 10^{12}\,\mathrm{s^{-1}}$ and $a_{0,hoh} = 6 \times 10^{11}\,\mathrm{s^{-1}}$. As mentioned, these values can vary in a wide range for different materials, morphologies, processing conditions, etc. For the scope of this work, electrons only reside in the acceptor material and holes in the donor material due to the large offset in MO energies between donor and acceptor. We therefore consider only one electron hopping prefactor $a_{0,elh}$ and one hole hopping prefactor $a_{0,hoh}$.

The second factor accounts for the tunneling character of the hopping process from one localized state to another. γ_i is the inverse localization radius (in $\mathrm{nm^{-1}}$) of the material at node i and originates from the overlap integral between neighboring wave functions. It can be chosen separately for donor and acceptor materials. Here, it is set to a fixed value of $\gamma = \gamma_i = 2\,\mathrm{nm^{-1}}$ according to [118], [121] and similar to $1.7\,\mathrm{nm^{-1}}$ which was observed in [61]. The localization constant is a complex function of the spatial arrangement of the atomic orbitals and its exact prediction requires a full quantum mechanical treatment. This is beyond the scope of the mesoscopic kMC method which is why γ is considered as a constant here. r_{ij} is the distance between the two nodes i and j. If only next neighbor hopping is considered, r_{ij} is always equal to the lattice constant l.

The last factor is of major importance for the dynamical evolution. Its influence can be imagined as a thermal activation process. The differences in the single node energy levels $\Delta E_{ij} = E_j - E_i = \Delta E_{ij}^0 + \Delta E_{ij}^F + \Delta E_{ij}^\sigma + \Delta E_{ij}^C$ enter the model here, as derived in Section 4.2.3. The contributions from the first three terms $\Delta E_{ij}^0 + \Delta E_{ij}^F + \Delta E_{ij}^\sigma$ are assigned to the local node sites. For the Coulomb interaction energy of a charge carrier at node i with all other real, image and replica (in neighboring simulation boxes) particles, the previously stored pair potentials can be read out from the local memory and are used to calculate U_i from Equation (4.16). Then, the third energy term is calculated by $\Delta E_{ij}^C = \frac{1}{2} q(U_j - U_i)$. Because ΔE_{ij} is evaluated for every charge carrier in every kMC step and for every direction a particle is allowed to hop, the calculation of hopping rates is one of the computationally most demanding processes in the simulation. This holds especially true for a large number of charge carriers, i.e. high charge densities.

If the energy of a particle can be lowered by a transition from $i \to j$, the last factor is independent of the exact energy difference and set to 1. On the contrary, if an energy barrier has to be surmounted for a transition, its rate drops exponentially with the magnitude of the barrier $\Delta E_{ij} > 0$.

After exciton separation or charge injection, electrons or holes are introduced to the

simulation box. In analogy to the excitons, both electrons and holes have the following information assigned for each charge carrier individually that can be used for further evaluation:

- Position
- Hopping rate in $\pm x$, $\pm y$, $\pm z$ directions
- Recombination rate (only for electrons, see below)
- Collection rate
- Origin (which exciton, cathode or anode)

4.3.6. Charge carrier recombination

Charge recombination represents one of the major loss mechanisms in OSCs. In case two oppositely charged particles are located on adjacent sites (with a distance of 1 nm), they can recombine with a recombination rate a_{ehr}. It represents the rate at which *direct* recombination of a bound electron-hole pair takes place.

One should generally distinguish between different types of recombination in organic solar cells. In case recombination takes place between an electron and a hole that originated from the same exciton, recombination is termed *geminate* recombination. On the other hand, in case the two charges originated either from two different excitons, or one of the charges stems from injection from a contact, recombination is *non-geminate*. Since the origin of each charge is tracked, these recombination channels are easily distinguishable in the kMC model. One value for a_{ehr} is used for the direct recombination, independently of whether they originate from the same exciton (geminate recombination) or from a different source (non-geminate recombination). Figure 4.12 depicts an illustration of the different recombination processes.

In experiments it is hard to determine the origin of charges and a spatial resolution of where exactly recombination took place is difficult to achieve. Recombination is therefore often described by effective recombination models of the form

$$R = k \cdot np \tag{4.27}$$

where R is the volume recombination rate (in $\mathrm{cm}^{-3}\,\mathrm{s}^{-1}$), k is a model-specific recombination parameter (in $\mathrm{cm}^3\,\mathrm{s}^{-1}$), and n and p are the electron and hole charge densities (in cm^3). One of the most widely used recombination models for OSCs, the Langevin model [175], is given for

$$k = \frac{e}{\varepsilon_0 \varepsilon_r}(\mu_e + \mu_h) \tag{4.28}$$

where ε_r is the permittivity of the material and μ_e, μ_h are the electron and hole mobilities. However, large deviations from the Langevin model have been observed in OSCs [176], [177]. The Langevin model is not generally applicable to spatially and energetically disordered BHJs since it was derived for homogeneous materials and does not include

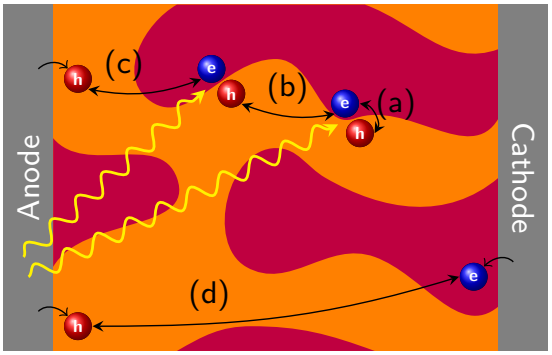

Figure 4.12. – Definition of different recombination processes: (a) geminate recombination of a charge pair. (b)-(d) non-geminate recombination between charges of (b) different charge pairs, (c) an optically generated charge and an injected charge, and (d) two injected charges.

any information about the blend geometry. More on the validity of the Langevin model and its deviations will be investigated and discussed in the results in Chapters 5 to 7.

If a neutral system is assumed, $n = p$ and Equation (4.27) reads $R = k \cdot n^2$, a typical expression used to describe (bimolecular) recombination. The exponent of the charge density can be generalized to classify recombination in terms of the recombination order δ in an effective recombination across the entire device with

$$R = k \cdot n^{\delta} \tag{4.29}$$

With δ, different recombination orders can be classified: for $\delta = 1$ recombination is *monomolecular* because it is only dependent on the density of one type of particle; this is the case if e.g. one type of charge is trapped in a defect and recombination is limited by another type of charge approaching the trap, or for the recombination of bound electron-hole pairs. For $\delta = 2$ recombination is *bimolecular* because it depends on the product of two charge densities; in this case two types of charges must find each other in order to recombine. Even higher recombination orders can exist (e.g. $\delta = 3$, Auger recombination) but are not considered here.

The relation between the direct recombination rate a_{ehr} and the volume recombination rate R is difficult to establish. We can however, derive the volume recombination rate R from the kMC simulations and compare to experiments, which will be shown in Chapter 8.

In case the charges of a charge pair have successfully managed to separate from each other, it is unlikely for them to find their geminate partner again. Therefore, separated charges may only recombine non-geminately when they find a distinct oppositely charged partner. The latter is equal to the definition of bimolecular recombination. We can therefore approximately compare non-geminate with bimolecular recombination. Monomolecular recombination contains geminate recombination and recombination by immobilized charges by local valleys in the energetic disorder. Throughout this thesis,

we will refer to geminate and non-geminate recombination because the kMC model is able to extract these quantities and they provide for a more detailed insight into the recombination processes.

a_{ehr} is defined as the inverse of the recombination time τ_{rec},

$$a_{ehr} = \frac{1}{\tau_{rec}}, \tag{4.30}$$

where τ_{rec} is either directly extracted from experiments, or is obtained from fits of device models to measurements.

An kMC study on recombination was done by Marsh et al. [122] who have set the recombination rate to $a_{rec} = 5 \times 10^5\,\mathrm{s}^{-1}$, to achieve a good agreement with measured results. However, they stated that the rate can vary by several orders of magnitude depending on the materials and the exact molecular interaction at the interface. Fits to j-U characteristics have been achieved with recombination rates between $10^4\,\mathrm{s}^{-1}$-$10^6\,\mathrm{s}^{-1}$ [178], [179].

Also in terms of measurements, τ_{rec} and concomitantly a_{ehr} can vary over large ranges. Values between in the range of µs and sub-µs have been reported for bimolecular recombination, while recombination investigated by Transient Absorption Spectroscopy (TAS) measurements was found to vary between $10^7\,\mathrm{s}^{-1}$-$10^9\,\mathrm{s}^{-1}$ and even down to sub-ns by CT lifetime measurements [81], [131], [180]–[184].

Summing up, due to large uncertainties in the value for the recombination rate, values in the range of $a_{ehr} = 10^4\,\mathrm{s}^{-1}$-$10^{10}\,\mathrm{s}^{-1}$ are used, where the exact values are stated when used.

It shall be noted that we do not explicitly introduce trap states in addition to the distribution of the density of states around the MO energy levels. Although charges will relax in local minima of the density of states during the simulation, recombination within such a state is generally not considered as trap-assisted recombination. All recombination in this model is therefore direct recombination and no trap-assisted recombination is considered.

When a recombination event occurs, both contributing charges are removed and excitation energy is lost ultimately.

4.3.7. Collection at electrodes

In order to extract a current, the collection rate of electrons and holes at nodes adjacent to the electrodes ($m_z^i = 1$ and $m_z^i = M_z - 1$) is enabled. The collection process is treated in analogy to charge carrier hopping with $\Delta E_{ij} \leq 0$. This yields $a_{col} = a_0 \cdot \exp(-2\gamma r_{ij})$. For a fixed $r_{ij} = l$ and γ, the collection rates are reduced to a constant rate. The collection rates can separately be set for electrons at the bottom and top contact, $a_{elc,bot}$ and $a_{elc,top}$, as well as for holes at the bottom and top contact, $a_{hoc,bot}$ and $a_{hoc,top}$ to reflect the quality of the contact with respect to the collection of a particular charge. Here, we use the same values at the bottom and top contact for electron collection $a_{elc} = a_{hoc} = 10^{10}\,\mathrm{s}^{-1}$, following previous kMC models [118].

After a collection process the corresponding particle is removed from the photoactive layer and contributes to the photo-current extracted from the cell.

4.3.8. Injection from electrodes

To be able to simulate full j-U characteristics of a solar cell, the dark current, i.e. the injection of charges from the contacts, must be considered. A model based on thermionic injection of charge carriers from the electrodes into the adjacent organic materials according to Wolf et al. [123] is used. This is fundamentally a charge hopping process from the Fermi energy level of the electrode into the HOMO/LUMO level of the organic material. In the applied model the influence of the charge under its own image induced in the electrode is considered, which reduces the injection barrier. This is in addition to the already considered influences of the morphology, an applied electric field and the energetic disorder on the local energy level in the adjacent organic layer. These factors determine the energy that has to be surmounted from metal into the organic layer, the local injection barrier. The local injection barriers are the determining factors for the dark current of a solar cell.

When the morphology of the photoactive layer has been created in the setup process, a random distribution of clustered donor and acceptor areas is adjacent to the electrode nodes. Because donor and acceptor level usually have a large deviation in MO energies of several hundred meV, the injection rate into a donor material differs strongly from the injection rate into an acceptor. Electrons are usually injected in the acceptor LUMO because of the lower energy barrier from electrode to acceptor LUMO than donor LUMO. Vice versa, hole injection takes place with great probability into a donor HOMO. To calculate the injection rates, there are four distinct injection processes that have to be considered:

- electron injection from cathode (bottom) into adjacent LUMO ($a_{eli,bot}$)
- hole injection from cathode (bottom) into adjacent HOMO ($a_{hoi,bot}$)
- electron injection from anode (top) into adjacent LUMO ($a_{eli,top}$)
- hole injection from anode (top) into adjacent HOMO ($a_{hoi,top}$)

The rate for each of these processes is, in analogy to hopping, calculated by the Miller-Abrahams equation. The total injection rate for each of the processes, separately, is calculated by

$$a_{inj} = \sum_n a_{0,n} \exp\left(-2\gamma l\right) \exp\left(-\frac{E_b^{(n)} - \frac{e^2}{16\pi\varepsilon_r\varepsilon_0\, l}}{k_B T}\right), \tag{4.31}$$

where $E_b^{(n)} = E_n - \phi$ is the injection barrier from the electrode node at $m_z^n = 0$ (with $\phi = \phi_{cathode}$) into the adjacent organic node $m_z^n = 1$ for injection at the cathode or the barrier from the anode at $m_z^n = M_z$ (with $\phi = \phi_{anode}$) into $m_z^n = M_z - 1$ for anodic injection. The summation index n ranges over the entire metal-organic contact area,

i.e. for all nodes $[0, M_x - 1] \times [0, M_y - 1]$. The term $\frac{e^2}{16\pi\varepsilon_r\varepsilon_0 l}$ accounts for the reduction of the barrier due to an induced mirror charge [123]. The prefactor $a_{0,n}$ can be chosen individually for electrons and holes, injection from the cathode or anode, and injection into donor and acceptor, in each combination.

For example, consider injection of electrons at the cathode. At every single electrode node $n \in [0, M_x - 1] \times [0, M_y - 1] \times [0]$, the energy barrier is determined by $E_b^n = E_{m_z^n=1}^{LUMO} - \phi_{cathode} - \frac{e^2}{16\pi\varepsilon_r\varepsilon_0 l}$. Whether the adjacent organic material is of donor or acceptor character is already defined by the energy levels of $E_{m_z^n=1}^{LUMO}$, and so is the influence of the electric field and the disorder. Iterating over all junction nodes and summing up the rates after Equation (4.31) yields the total electron injection rate at the cathode $a_{eli,bot}$. Proceeding in the same manner for all processes mentioned above, the four different total injection rates are stored.

An important effect to be mentioned arises from the combination of charge injection and charge collection at the metal organic interface. After a charge carrier has been injected, it resides at a node next to the electrode. Thus, its collection rate is enabled and a recently injected charge carrier can immediately be extracted from the device again. For low injection barriers and low driving electric fields as for example at open-circuit condition, these subsequent injection and recollection processes dominate the simulation and are computationally expensive. This is known as the "small-barrier" problem in the recent kMC literature [143], [185] and restricts kMC models with the sort of injection treatment described here from simulating configurations where the injection barrier is smaller than approximately 0.2 eV, ohmic, or even negative (no barrier at all).

The injection model considers the static energy distribution in the active layer to determine the injection rates, but does not consider the dynamical fluctuations induced by charges in the system. Updating the calculation of injection rates and considering specific nodes for the injection process (instead of randomly picking a node) considering the internal electrostatic potential should be done for a more sophisticated contact model. However, doing so in every simulation step is computationally not feasible, and approximations must be made in order to achieve a tradeoff between simulation time and physical accuracy. We consider the implementation described above as a good tradeoff for OSCs.

4.4. Simulation input parameters

To summarize all input parameters, the system setup parameters are listed in Table 4.1 and the input rate values are listed in Table 4.2. If different values than indicated in these tables are used, then it is explicitly stated in the text.

Table 4.1. – System setup parameters.

Parameter	Symbol	Value	Reference
Nodes x direction	M_x	50	-
Nodes y direction	M_y	50	-
Nodes z direction	M_z	50	-
Lattice constant	l	1 nm	-
Localization constant	γ	$2\,\mathrm{nm}^{-1}$	[61], [118], [121]
Relative permittivity	ε_r	3 to 5	[65]
Energetic disorder	σ	0 meV-100 meV	[156]–[158]
Work function cathode	$\phi_{cathode}$	−4.3 eV	[65], [186]
Work function anode	ϕ_{anode}	−4.95 eV	[65], [187]
PCBM (acceptor) HOMO level	E_A^{HOMO}	−6.0 eV	[65], [188]
PCBM (acceptor) LUMO level	E_A^{LUMO}	−3.8 eV	[65], [187]
P3HT (donor) HOMO level	E_D^{HOMO}	−5.2 eV	[189]
P3HT (donor) LUMO level	E_D^{LUMO}	−3.0 eV	[190]
Thermal energy (temperature)	E_{th} (T)	25.7 meV (298 K)	-
Monte Carlo steps	MCs	5000	[146]
Cluster size	d	≈ 15 nm	[146]
External voltage range	U_{ext}	0.0 to 0.8 V	-
Simulation time	t_{stop}	1 ms-10 ms	-

Table 4.2. – Transition rate values.

Process	Symbol	Rate value	Reference
Exciton generation	a_{exg}	Generation profile $G(z)$	[166]
Exciton hopping	a_{exh}	$2 \times 10^{11}\,\mathrm{s}^{-1}$	[6]
Exciton decay	a_{exd}	$2 \times 10^{9}\,\mathrm{s}^{-1}$	[6]
Exciton separation	a_{exs}	$2 \times 10^{13}\,\mathrm{s}^{-1}$	[69], [169]
Electron hopping prefactor	a_{elh}	$3 \times 10^{12}\,\mathrm{s}^{-1}$	[173], [174]
Hole hopping prefactor	a_{hoh}	$6 \times 10^{11}\,\mathrm{s}^{-1}$	[173], [174]
Electron hole recombination	a_{ehr}	$10^{4}\,\mathrm{s}^{-1}$-$10^{10}\,\mathrm{s}^{-1}$	[81], [122], [178]–[184]
Electron collection prefactor	a_{elc}	$10^{10}\,\mathrm{s}^{-1}$	-
Hole collection prefactor	a_{hoc}	$10^{10}\,\mathrm{s}^{-1}$	-
Electron injection prefactor	a_{eli}	Thermionic injection	[123]
Hole injection prefactor	a_{hoi}	Thermionic injection	[123]

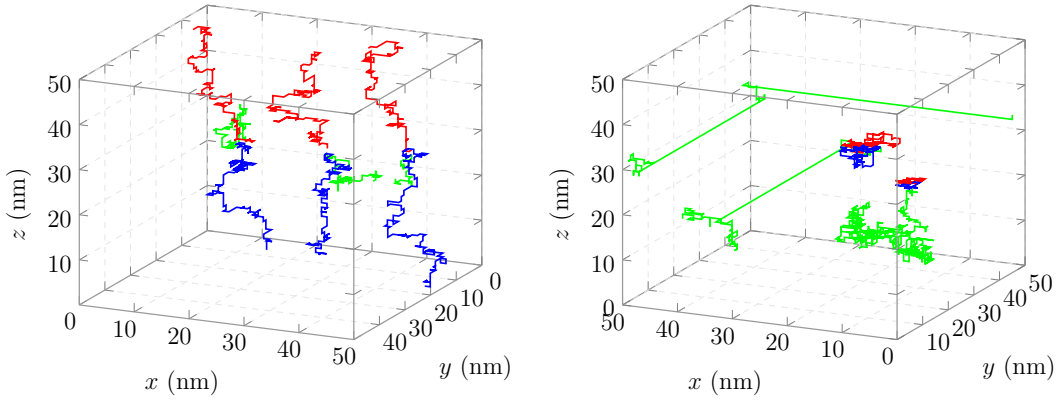

(a) Charge collection **(b)** Charge recombination/exciton decay

Figure 4.13. – Illustration of particle trajectories for photocurrent generation (a) and loss mechanisms (b). Excitons (green) diffuse randomly after their generation and get separated into electron (blue) and hole (red) at a heterojunction. Charges can then be transported and collected at the electrodes (a) and contribute to a photocurrent or recombine (b), in which case the excitation is lost. The long pathways from one face of the box to the opposite face indicate the periodic boundary conditions.

4.5. Evaluation details

4.5.1. Particle trajectories

To highlight the particular advantage of a kMC model to track the transport pathway of individual particles through the photoactive layer, an exemplary extract of the processes responsible for current generation and recombination, as recorded at runtime, is shown in Figure 4.13. Positions and time information of individual particles from their generation to their removal can be stored during runtime and utilized for further processing afterwards, as described for the most relevant quantities in the following sections.

The sequence of processes for photocurrent generation is shown in Figure 4.13a. At first, an exciton (green) is created somewhere inside the photoactive layer by absorption of an incident photon based on the exciton generation model. The exciton then diffuses through the material by hopping from node to neighboring node with equal probability, according to the random walk treatment. As soon as it meets a donor acceptor interface, the separation rate gets activated. The electron (blue) is placed in the acceptor material and the hole (red) in the donor material. The generated charge carriers then move in their respective material phases under the influence of the energy distribution. The data in Figure 4.13a was taken from a cell in reverse bias condition where the electric field is directed as such that the electron is driven to the cathode at the bottom ($z = 0$) and the hole to the anode at the top ($z = 50$). After the charge carriers have been collected they are removed from the layer and contribute to an external current.

The implemented loss processes due to exciton decay and electron-hole recombination are depicted in Figure 4.13b. If a generated exciton does not reach a donor acceptor interface within its average hopping length, it decays and is removed from the simulation box.

In the upper half of the simulation box the pathway of a decaying exciton is shown. After generation and a certain amount of hopping events from node to node, an exciton decay transition is chosen by the algorithm and the exciton vanishes. Note the periodic boundary conditions on the hopping path: a particle at the boundaries of the simulation box making an attempt to hop over the edge gets re-entered on the opposite side to continue its path. This is indicated by the long green pathways from one face of the periodic simulation box to the opposite side.

In the lower half of the simulation box two excitons are separated at an interface and generate an electron-hole pair. The depicted simulation was executed at a bias around the open-circuit voltage, i.e. the driving force on the charge carriers induced by the internal electric field is small in this configuration and the predominant force between electrons and holes is Coulomb interaction. Attempts to become spatially separated from each other are suppressed and the charges stay close to each other on their hopping pathways. This increases the probability for them to recombine because the corresponding rate is always activated when two charges reside at nodes next to each other. If they recombine, they are removed from the layer and cannot contribute to an external current anymore.

4.5.2. Charge mobilities

With the trajectory information for all charges, we have the information about location of origin $\vec{x}_s$ and destination $\vec{x}_e$ of all charges as well as time of origin t_s and time of death t_e. Together with the internal electric field $F = E^F_{i=M_z}/(e \cdot M_z \cdot l) = \Delta\phi/(e \cdot M_z \cdot l)$, the effective charge mobility of a single charge carrier through the morphology can be evaluated by

$$\mu = \frac{v}{F} = \frac{|\vec{x}_e - \vec{x}_s|}{|t_e - t_s| \cdot F}. \tag{4.32}$$

Averaging over a large number of charges then yields a mean value for the charge mobility in the operating solar cell.

4.5.3. Charge carrier densities

To determine the local particle densities for electrons, n_e or n, and holes, n_h or p, we use the average occupancy by electrons and holes, separately, of each node i. By tracking the occupation $X^{(i)}_k \in \{0, 1\}$ at node i for each time step τ_k during the absolute simulation time $T = \sum_k \tau_k$, the densities are defined by

$$\left\langle n_{e/h} \right\rangle^{(i)} = \frac{1}{l^3 \cdot T} \sum_k X^{(i)}_k \cdot \tau_k \tag{4.33}$$

where l is the lattice constant. The maximum density is limited by the site density $l^{-3} = 10^{21}\,\mathrm{cm}^{-3}$ in case of $l = 1\,\mathrm{nm}$ if a site is occupied by a charge during the entire simulation time T.

4.5.4. Charge pair displacement

With the position and time information of electrons and holes, $\vec{r}_e(t_k)$ and $\vec{r}_h(t_k)$, the time-dependent displacement $d(t_k)$ of an electron-hole pair after exciton separation can be described by a discrete time-series:

$$d(t_k) = |\vec{r}_e(t_k) - \vec{r}_h(t_k)|\,, \tag{4.34}$$

where $d(t_k)$ needs to be updated every time step k in which a charge of the charge pair moves. A simple average over different $d(t)$ is not appropriate to statistically evaluate the pair displacement due to the different timescales and different outcomes a pair might end up (collection, geminate and non-geminate recombination and combinations). A more appropriate evaluation technique is described in Chapter 7.

4.5.5. Counter-based evaluation

Each event that takes place has a designated counter variable that is incremented every time the event occurs. After a simulation run has been completed, the counters can be used to calculate characteristic quantities. Counter variables are implemented for the number of

- excitons generated N_{exg},
- excitons decayed N_{exd},
- excitons separated N_{exs},
- charge carriers originating from exciton separation and recombining N_{ehr},
- geminate recombination events N_{gr},
- non-geminate recombination events N_{ngr},
- electrons and holes injected from the electrodes $N_{hoi}^{cathode}$, N_{hoi}^{anode}, $N_{eli}^{cathode}$, N_{eli}^{anode},
- electrons and holes collected at the electrodes $N_{elc}^{cathode}$, N_{elc}^{anode}, $N_{hoc}^{cathode}$, N_{hoc}^{anode}.

From these counters, the following quantities can be derived:

Exciton separation efficiency: The ratio of excitons successfully separated into charge carriers can be expressed as

$$\eta_{exs} = \frac{N_{exs}}{N_{exg}} \tag{4.35}$$

The loss of excitons by decay is the complementary process,

$$\eta_{exd} = \frac{N_{exd}}{N_{exg}} = 1 - \eta_{exs} \tag{4.36}$$

because excitons either get separated or they decay ($N_{exg} = N_{exs} + N_{exd}$).

Total charge carrier recombination: Only charges originating from a separated exciton are considered for the total recombination ratio. They are set in relation to the total number of charge carriers that can possibly be generated from exciton separation, where one electron and one hole emerge from one exciton:

$$\eta_{ehr} = \frac{N_{ehr}}{2\,N_{exg}} \tag{4.37}$$

This quantity represents the loss of optically generated charges. It contains both geminate and non-geminate (only between charges from different excitons, no injected charges) recombination events.

Geminate and nongeminate recombination: Furthermore, we count the number of geminate and non-geminate recombination events, N_{gr} and N_{ngr}, respectively. With these, we can evaluate the relative geminate recombination ratio as the ratio of geminate recombination events with respect to the total number of recombination events

$$\eta_{gr} = \frac{N_{gr}}{N_{gr} + N_{ngr}}. \tag{4.38}$$

as well as the relative non-geminate recombination ratio as the ratio of non-geminate recombination events with respect to the total number of recombination events

$$\eta_{ngr} = \frac{N_{ngr}}{N_{gr} + N_{ngr}}. \tag{4.39}$$

These allow for further investigation about how much geminate/non-geminate recombination actually takes place with respect to the overall recombination. It needs to be noted that N_{ngr} can also contain charges that originate from injection from the contacts.

Current density: The current density is the net charge that is passing the organic/electrode contact per electrode area and unit time. The current density is evaluated at the bottom and top contact, separately. Negative charges count oppositely to positive charges and injected charges count oppositely to collected charges. Thus for the cathode the current density leaving the cell is

$$j = 10^{17} \cdot \frac{-e(N_{elc}^{cathode} - N_{eli}^{cathode} + N_{hoi}^{cathode} - N_{hoc}^{cathode})}{A\,t_{stop}} \tag{4.40}$$

where $A = l^2\,M_x M_y$ is the electrode area in nm^2 and t_{stop} the simulation time in s. The dimensionless prefactor allows to express the current density in units of $\mathrm{mA\,cm^{-2}}$. Vice versa for the anode current density. In a steady state, the top and bottom current are equal.

4.5.6. Local Coulomb potential

The evaluation of the local Coulomb potential $\phi_C^{(i)}$ was performed by a block-averaging technique as described by Casalegno et al. [118]. After every pre-defined time block Δt_{block}, the Coulomb potential induced on node i by all charge particles currently in the simulation cell, i.e. at nodes j and with charge $q_j = \pm e$, is calculated for the time block k by

$$\phi_{block,k}^{(i)} = \sum_{j=1}^{2N} q_j \, U^{pair}(m_{ij}^x, m_{ij}^y, m_{ij}^z) \tag{4.41}$$

in analogy to the treatment of Coulomb interaction from Section 4.2.4. Then, the arithmetic mean of all time blocks gives the average electric potential at node i:

$$\phi_C^{(i)} = \frac{1}{N_{blocks}} \sum_{k=1}^{N_{blocks}} \phi_{block,k}^{(i)} \tag{4.42}$$

where N_{blocks} is the number of time blocks for which the potential was evaluated. For example, when choosing a block time interval of $\Delta t_{block} = 10^{-5}\,\mathrm{s}$, for a total simulation time of $T = 10\,\mathrm{ms}$ a total of $N_{blocks} = \frac{T}{\Delta t_{block}} = 1000$ time blocks are averaged to obtain ϕ_C. The smaller the block time interval is chosen, the larger the computational effort to calculate ϕ_C but the more representable its value, and vice versa. This technique is only used for visualization purposes of the local potential induced by charges.

5. Investigation of Blend Effects in Bulk-Heterojunction Organic Solar Cells

The intermixing of donor and acceptor materials in the active layer of BHJ OSCs leads to a complex morphology. Many processes such as the dissociation of excitons, charge dynamics, and charge recombination are based on the morphology, in particular on the interface between the two materials. To enhance the solar cell performance that is mainly based on these processes, two different modeling techniques are established today. In Drift-Diffusion (DD) simulations, the common assumption is to reduce the morphology including all interfaces to an effective material. On the contrary, kMC simulations offer a method to investigate organic solar cells considering a realistic blend morphology. We establish a common basis between the real blend kMC simulations and DD simulations with an Effective Medium Approximation (EMA) and compare the two models. Our results show that in the effective medium, the absence of local interface effects such as an explicit treatment of the short-ranged Coulomb interaction of charges across an interface lead to a fundamentally different charge density profile across the active layer. We show that it is not possible to capture the morphological effects by an EMA-based model. We provide hints that the effective medium approach might not be sufficient to treat the internal effects induced by the blend morphology.

The content of this chapter is adapted, with permission, from T. Albes, P. Lugli, and A. Gagliardi, "Investigation of the Blend Morphology in Bulk-Heterojunction Organic Solar Cells", *IEEE Transactions on Nanotechnology*, vol. 15, no. 2, pp. 281–288, 2016.

5.1. Background

The concept of an intermixed BHJ [69] between organic donor and acceptor materials forms the basis for OSCs with the currently highest reported PCEs [16]. The BHJ allows to handle both the separation of photo-generated excitons and the successive charge transport efficiently, while maintaining a simple fabrication process.

The fabrication of BHJ active layers is usually performed by spin-coating of the donor and acceptor blend from solution with a successive thermal annealing process to improve the clustering of identical materials [71]. As a consequence and due to the resulting intermixed morphology, the interface area between the donor and acceptor phases has a complex geometry. The interface is the region where photo-generated excitations are separated and charges originate. On the other hand, these are also the regions where charge recombination takes place. The BHJ interface is therefore directly related to loss processes.

One established way to model organic solar cells is to solve the DD equations. They offer an approach at a macroscopic continuum level, low computational effort, and with good fits to experimental data [178], [191]. A common approximation used in DD simulations is the EMA [136], [144], [153], [178], [192]–[195], i.e. the reduction of the 3D donor:acceptor morphology to a single effective medium with intermediate properties. In an EMA model, all interface effects between the donor/acceptor boundaries, such as exciton splitting and electron-hole recombination, are assumed to be bulk processes and evenly distributed across the photoactive layer. Therefore, neither are the real exciton dynamics considered, i.e. an absorbed photon directly generates an electron-hole pair, nor is the actual transport of charges through the complex blend treated in an EMA-DD model. This affects for example the dynamics of charges after their separation at an interface under the influence of Coulomb interaction. These disadvantages of the 1D EMA model have been pointed out by Li et al. [196] and need to be addressed.

For this purpose, lattice-based kMC simulations offer a suitable tool to investigate the processes in BHJ solar cells [38], [124]. A schematic comparison of the real blend morphology and the EMA is shown in Figure 5.1. In contrast to an effective medium DD model, the interface effects exciton dissociation and the charge recombination can explicitly be treated in a kMC model. Also, charge transport through the complex pathways is taken into account by a hopping model between localized states, which cannot explicitly be considered on a local scale in an effective medium.

We compare the results from DD simulations in 1D with the EMA approach to kMC simulations incorporating the 3D blend geometry to investigate whether an EMA with a bulk treatment for interface processes can be considered a realistic approximation. To our knowledge, a direct comparison between full-device kMC and DD simulations has not been performed yet. Only a loose multiscale approach has been reported [197] where certain parameters (e.g. charge mobility, exciton separation ratio) are extracted from kMC simulations and plugged into the DD model. The comparison to a full kMC simulation is the aim of this study.

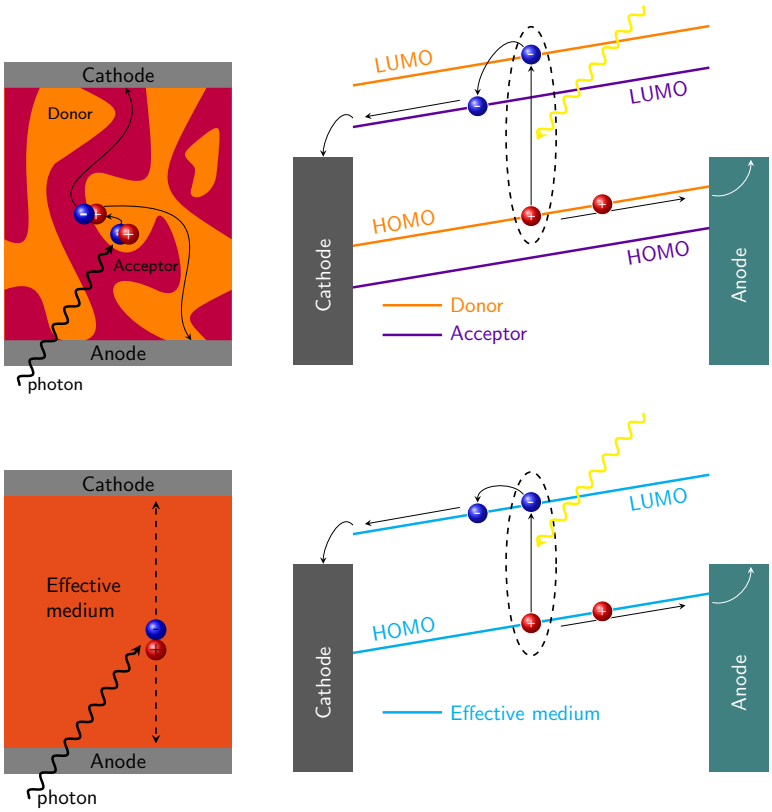

Figure 5.1. – Real blend (top) vs. EMA (bottom). In the EMA, the BHJ blend is treated as an effective medium with properties intermediate between the two materials.

In Section 5.2 the DD model is briefly described and the specific differences between the kMC and DD model are highlighted. Section 5.3 shows the comparison of the EMA and the real blend simulations and a discussion about the validity of the EMA.

5.2. Model specifics

The DD model and the kMC model need to be based on the same parameters to be able to decide whether the EMA with its bulk models is a valid approximation or if important effects cannot be captured without the real blend morphology. We set up each model to simulate a 50 nm thick OSC comprised of the established device structure ITO/PEDOT:PSS/P3HT:PCBM/Al under a standard illumination condition of 1000 $\mathrm{W\,m^{-2}}$. ITO/PEDOT:PSS acts as transparent anode and is on the illuminated side of the cell. P3HT:PCBM is the intermixed active layer, and Al is the cathode.

5.2.1. Drift-Diffusion model

The DD method solved on finite elements is a common technique for semiclassical modelling of semiconductor devices. The model for the OSC treated here has been implemented within the TiberCAD simulation tool [198], [199] in 1D.

The solar cell model consists of the 1D active layer representing the region where generation, transport, and recombination take place. At the boundaries, cathode and anode are located and are used to inject and collect charges. The EMA is used for the active layer, i.e. a virtual semiconductor with the HOMO level of the donor and the LUMO level of the acceptor acts as an effective medium.

The complete equation system coupled to the Poisson and continuity equations is:

$$\nabla \cdot (\varepsilon_r \nabla \varphi) = e\,(n - p - N^+ + N^-) = -\rho \tag{5.1}$$

$$\nabla \cdot j_n = \nabla \cdot (\mu_n n \nabla \phi_n) = -R + G \tag{5.2}$$

$$\nabla \cdot j_p = \nabla \cdot (\mu_p p \nabla \phi_p) = R - G \tag{5.3}$$

where ε_r is the dielectric constant of the material, φ the electric potential, n and p are the electron and hole densities of mobile charges, μ_n and μ_h are the electron and hole mobilities, and N^+ and N^- are the densities of a general static charge distribution, i.e. trap states. No trap states are considered in this model. The last two equations are the continuity equations for the electron and hole currents, proportional to the gradients of their electro-chemical potentials ϕ and their mobilities μ, respectively. R and G are the recombination and generation rates, respectively.

Recombination is described by the Langevin model, in which R is proportional to the mobilities of electrons and holes:

$$R_{Langevin} = C \cdot \frac{\mu_n + \mu_p}{\varepsilon_0 \varepsilon_r} \cdot (np - n_0 p_0) \tag{5.4}$$

here, C is a prefactor to correct morphological effects that lead to deviations from the ideal Langevin law. The densities n_0 and p_0 are the electron and hole densities in equilibrium.

For the energetic structure in the organic materials a Gaussian DOS is assumed. This is a common approach for all simulations of disordered organic semiconductors [124], [199] and is based on the work of Bässler [56]. Due to the irregular structure of small organic molecules and polymers, each molecule and/or monomer of a polymer acts as a single charge transport site, a localized state. The dynamics of charges is based on phonon assisted hopping between localized states. The conduction band is centered at the LUMO level, while the valence band is centered at the HOMO level. Hence the GDOS can be written as:

$$g(E, \sigma) dE = \frac{N_0}{\sigma \sqrt{2\pi}} \exp\left(-\frac{1}{2} \frac{E - E_{C,V}}{\sigma^2}\right) dE \tag{5.5}$$

where N_0 is the site density of the localized states, E_C and E_V are the LUMO and HOMO centers, respectively, and σ is magnitude of the energetic disorder.

In analytic derivations of hopping transport mobilities in disordered materials, for rather small values of energetic disorder, the mobility is constant with respect to the electric field [154], [200]. Nevertheless, mobility is strongly dependent on the disorder σ. We used a constant mobility model in the DD simulations, for an additional justification see the mobility extraction part in Section 5.3.2.

With 50 nm, the active layer is so thin that interference effects from the incident light waves with the reflected waves at the electrode have to be taken into account. To capture this feature and to consider the different absorption spectra of donor and acceptor materials, photo-generation is adopted using the TMM as described in Section 4.3.1 for a P3HT:PCBM blend. The TMM can be used to calculate the exciton generation profile through the active layer under an AM1.5 illumination spectrum. The profile obtained from these calculations and used in both models is depicted in Figure 4.11b and is used in both the DD and the kMC model.

The boundaries between the active layer and the electrodes are treated as Schottky contacts. At the boundaries, charges can be injected from the electrodes into the active layer or become extracted from the active layer at the contacts. Injection considers an image charge potential lowering, while the collection is modelled after a model by Scott and Malliaras [201], both as implemented in [199].

5.2.2. Kinetic Monte Carlo model

The implementation of the kMC model described in Chapter 4 is used for a $50 \times 50 \times 50\,\mathrm{nm}^3$ cell with a BHJ morphology of 15.7 nm cluster size.

The recombination rate was fixed at $a_{ehr} = 5 \times 10^5\,\mathrm{s}^{-1}$ after [122]. The simulations were run for 10 ms, where a steady state was reached after approximately 1 ms. All quantities extracted are based on a steady state condition and we compare the equilibrium results. The DD model only yields results in an equilibrium state.

5.2.3. Establishing a common basis

In order to compare the two models a common basis has to be established. Table 5.1 depicts a list of the simulation parameters used for both models. Unmentioned parameters used in the kMC model are taken as listed in Table 4.1 and Table 4.2. The differences between the DD and the kMC model are: 1D vs. 3D; the morphology itself (EMA vs. real blend); the treatment of Coulomb interaction (Poisson equation vs. Ewald sum); the recombination model (bulk Langevin vs. interface); exciton splitting (uniform vs. interface); and charge transport (implicitly given by the morphology; in the EMA the effects of the morphology are contained in the effective mobility). Therefore, a comparison of the results will highlight mainly morphology related differences.

The use of the EMA and a DD model reduces the computational demand significantly.

Table 5.1. – Parameters equal in both models.

Parameter	Value
Active layer thickness	50 nm
Exciton generation profile	$G(z)$ (Figure 4.11b)
Cathode (Al) work function	−4.3 eV
Anode (ITO/PEDOT:PSS) work function	−4.95 eV
Acceptor (PCBM) LUMO	−3.8 eV
Donor (P3HT) HOMO	−5.17 eV
Temperature	298 K
Dielectric constant	3.5
Gaussian energetic disorder	10 meV, 65 meV
Localized state density	10^{21} cm^{-3}

Since the spatial 3D structure of the blend does not need to be considered, a 1D representation of the solar cell is sufficient. The electrostatic potential obtained by the solution of the Poisson equation is therefore only dependent on a 1D charge distribution. In comparison to the Ewald sum solution in 3D in the kMC model, there are no periodic boundary conditions perpendicular to the light incidence to be considered. A second special feature of the Ewald model is the treatment of mirror charges induced in the electrodes.

Another difference is the treatment of charge recombination. The Langevin recombination model is a bulk model, i.e. recombination can take place everywhere in the active layer, with a spatial dependency on the local charge densities, see Equation (5.4). These in turn are not depending on the morphology because there is no morphology implemented. Recombination in the kMC model is explicitly controlled by the blend morphology. The condition for recombination is that oppositely charged particles are located on nodes next to each other which is only possible at a donor/acceptor interface. When this condition is fulfilled, the recombination is controlled by a constant rate. This rate is dependent on molecular properties of P3HT and PCBM. Higher interface charge densities also lead to higher recombination. The effect of the blend on recombination is often fitted into the prefactor C of the Langevin recombination model.

Since excitons are not explicitly treated in the DD model, we renormalized the results by the exciton separation ratio that we observe with the kMC model. There, for the cluster size of 15.7 nm, about 95 % of the excitons are successfully separated, i.e. a loss of 5 % is observed. The current and charge densities of the DD model are therefore multiplied by this factor of 0.95.

The differences in charge mobilities between the models are discussed in the results section below. At first we tried to use the mobilities as fitting parameter to adapt the DD simulations to the kMC results. In a later step, we extracted the mobilities of charges

through the kMC blend, their 'effective mobility', and plugged it into the DD model to contain the blend effect in the DD simulations. The so obtained results of the 1D DD model with the blend mobilities from kMC are then compared to the kMC model itself in more detail, i.e. by comparing their internal charge density distribution.

In all results, we show the data for one low-disorder case (10 meV) and a medium-disorder case (65 meV). Since the kMC model is computationally expensive with higher values of energetic disorder, no higher values than 65 meV are shown here. These two cases allow us to observe how effect of the disorder influences the results in the two different models, especially in relation to the charge densities and how the charge transport is influenced by the disorder for different electric fields.

5.3. Results and discussion

5.3.1. Mobility fit

The aim of the comparison is to keep as many parameters of both models equal as possible and to see whether it is theoretically possible to achieve similar results by neglecting the morphology and putting all blend information in the remaining fitting parameters. We took the kMC model as reference for the DD model. Only the prefactor in the Langevin recombination model and the mobilities for electrons and holes in the DD model are taken as fitting parameters. The closest fit to the kMC model that could be achieved is depicted in Figure 5.2 for two different values of energetic disorder. The Langevin recombination prefactor was found to be $C = 5$. The mobilities obtained from the fit are $\mu_e^{10meV} = 5 \times 10^{-5}\,\mathrm{cm^2\,V^{-1}\,s^{-1}}$ and $\mu_h^{10meV} = 1 \times 10^{-5}\,\mathrm{cm^2\,V^{-1}\,s^{-1}}$ for the 10 meV case. For the 65 meV case $\mu_e^{65meV} = 1 \times 10^{-4}\,\mathrm{cm^2\,V^{-1}\,s^{-1}}$ and $\mu_h^{65meV} = 5 \times 10^{-4}\,\mathrm{cm^2\,V^{-1}\,s^{-1}}$ are obtained.

In recent studies of BHJ OSCs, the Langevin prefactor is known to be well below $C = 1$ [202]. This correction factor is assumed to be due to the fact that recombination may not be described by a bulk model such as the simple Langevin model. The Langevin model is overestimating the recombination rate because recombination processes only take place at donor-acceptor interfaces while the derivation of the model assumes a continuous medium. Therefore, the recombination rate in the DD model to fit the kMC results is artificially higher than what is expected. This is a first hint for the incompatibility of the models.

In a P3HT:PCBM blend, experimental measurements show that the electron mobility is usually higher than the hole mobility [71], [203], depending on the parameters of the thermal annealing process. While in the 10 meV case the hole mobility had to be chosen lower than the electron mobility to achieve a reasonable fit, the reverse was necessary in the 65 meV case. A disorder of 65 meV is more in the range of the real value for the disorder. Therefore, the parameters that had to be used for the fit appear to be artificial and in no good agreement with the experimentally observed values.

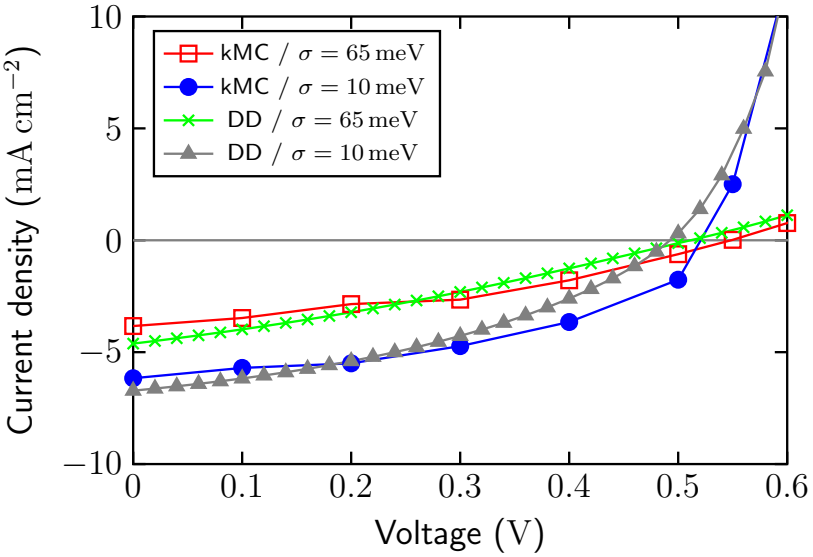

Figure 5.2. – Comparison of EMA and real blend j-U characteristics. Here, the mobilities and the Langevin recombination prefactor in the DD model have been fitted in order to match the kMC results.

5.3.2. Mobility extraction

In a next step, to confirm that the kMC simulations lead to a better representation of the internal working principles of the BHJ cell, we extracted the effective mobility of electrons and holes through the blend. Since the internal electric field induced by the work function difference and the applied bias is small in OSCs ($\lesssim 10^4\,\mathrm{V\,cm^{-1}}$) under operation condition, the evaluation of the mobility as the relationship between the velocity of a particle through the blend and the (small) electric field might not be accurate because the driving force is very small and the particle dynamics could be diffusion controlled [154]. We therefore not only evaluate the drift mobility, but also the diffusion coefficient $D = \frac{\langle z^2 \rangle}{2t}$ as the mean square deviation of the position of a particle with respect to its origin $\langle z^2 \rangle$ and time t. This quantity can be set into relation with the drift mobility by the Einstein relation. It shall be noted that the validity of the Einstein relation $\mu = \frac{e}{k_B T} \cdot D$ in OSCs is still under discussion. But for the case of low electric fields and energetic disorders below about 150 meV, it was shown to be valid by theoretical studies [154], [200]. The results of the evaluation are shown in Figure 5.3.

For both cases of energetic disorder, respectively, the mobilities obtained by the drift- and the diffusion-evaluations are of the same order of magnitude, implying the validity of the Einstein relation. Moreover, the mobilities are only slightly dependent of the electric field and can therefore be considered as constant, justifying the use of a constant mobility in the DD model. A field-independent mobility has been found in organic materials at small electric fields [56], [154] such as applied in OSCs, which coincides with our results,

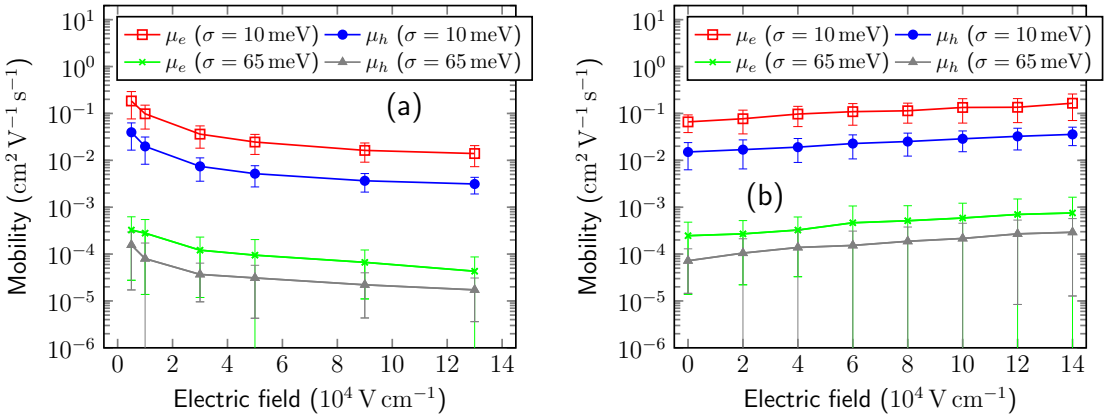

Figure 5.3. – Evaluation of the effective mobility of charges through the BHJ morphology. (a) Evaluation based on drift induced by the electric field. (b) Diffusion mobility based on the mean square displacement of charges with respect to their origin. The error bars show the standard deviation over 1000 evaluated particles each.

while for larger fields a Poole-Frenkel law of the form $\mu(E) \propto \exp(-\sqrt{E/E_0})$ applies.

As it can be seen, both mobilities drop by orders of magnitude when the disorder is increased from 10 meV to 65 meV. The low disorder simulations show electron mobilities of approximately $\mu_e^{10meV} = 1.1 \times 10^{-1}\,\mathrm{cm^2\,V^{-1}\,s^{-1}}$ and $\mu_h^{10meV} = 2.5 \times 10^{-2}\,\mathrm{cm^2\,V^{-1}\,s^{-1}}$. At 65 meV, $\mu_e^{65meV} = 1.4 \times 10^{-4}\,\mathrm{cm^2\,V^{-1}\,s^{-1}}$ and $\mu_h^{65meV} = 4.6 \times 10^{-5}\,\mathrm{cm^2\,V^{-1}\,s^{-1}}$ are obtained. The values achieved here can be compared to experimental measurements of the mobility because it includes the pathway of charges through the intermixed structure. For the latter, realistic (i.e. comparable to what is observed in experiments) values in a P3HT:PCBM system are obtained by the kMC simulations. Also electrons are more mobile in PCBM than holes in P3HT.

5.3.3. Re-fit with extracted mobilities

With the mobility results from the previous evaluation, the DD-EMA simulations are repeated. This time, the information about the blend should be correctly included in the mobility values for electrons and holes. All other parameters are kept the same. The new EMA j-U characteristics with the kMC results for both cases of disorder are shown in Figure 5.4. With just a change in the mobilities the previous agreement is lost. All critical quantities, short-circuit current, open-circuit voltage and fill factor do not match the kMC results anymore.

With the only remaining parameter, the prefactor of Langevin recombination, it was not possible to achieve a fit. Thus, we could not find a way to match the 1D DD EMA and the 3D kMC real blend models. This means that the effects specific to the morphology, i.e. the interface effects and the charge dynamics, could not be included in bulk models and parameters in the here presented manner.

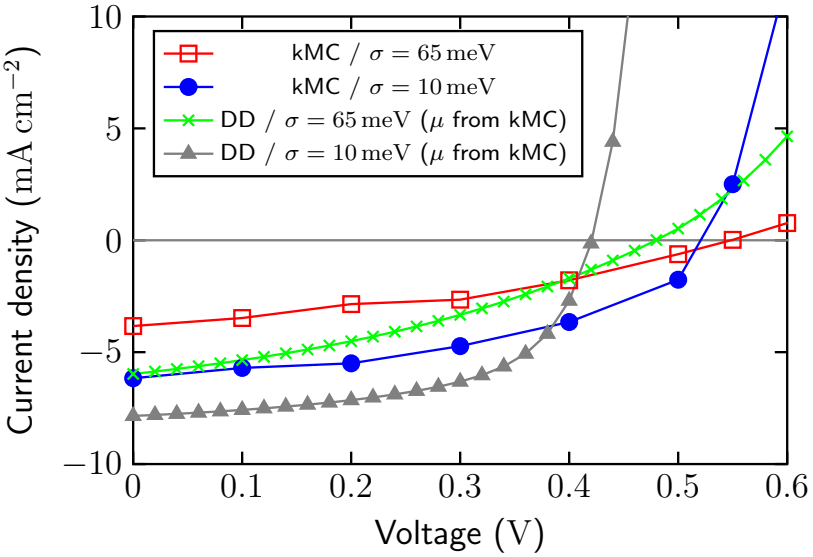

Figure 5.4. – Comparison of EMA and real blend j-U characteristics *with* effective blend mobilities extracted from the kMC simulations. For both values of the energetic disorder the results differ noticeably in open-circuit voltage, short-circuit current as well as in the fill factor.

5.3.4. Charge density evaluation

To take a closer look at why the results are different, Figure 5.5 shows the charge densities along the z-direction of the active layer for both cases of energetic disorder and both models. For the 3D kMC simulations these are the averaged densities for electrons and holes, respectively, per 2D slice along the z-direction.

The predominant difference between the DD and the kMC model is the separation of positive and negative charges. The electron and hole densities in the real blend kMC model are similar in most layers. This indicates that electrons and holes, after they have been created by exciton separation at a donor-acceptor interface, stay together and are located very close to each other leading to equal densities throughout the active layer. The local Coulomb interaction induced by the electron-hole pair on each other is therefore stronger than the electric field to separate the pair. The electron and hole densities only differ near the contacts, where the electron density is increased near the cathode and hole density near the anode. This is attributed for one to the injection of charges from the contact: the injection barrier is much lower for holes at the anode and for electrons at the cathode, and hence lead to more charge injection. Furthermore, in the low disorder case, charge collection is slower than charge transport to the contact, which leads to a further pile-up of charges. The average charge density across all layers at 10 meV disorder is $n = 1.34 \times 10^{16}\,\mathrm{cm}^{-3}$ for electrons and $p = 1.83 \times 10^{16}\,\mathrm{cm}^{-3}$ for holes. Increasing the disorder to 65 meV, the densities increase slightly to $n = 2.45 \times 10^{16}\,\mathrm{cm}^{-3}$

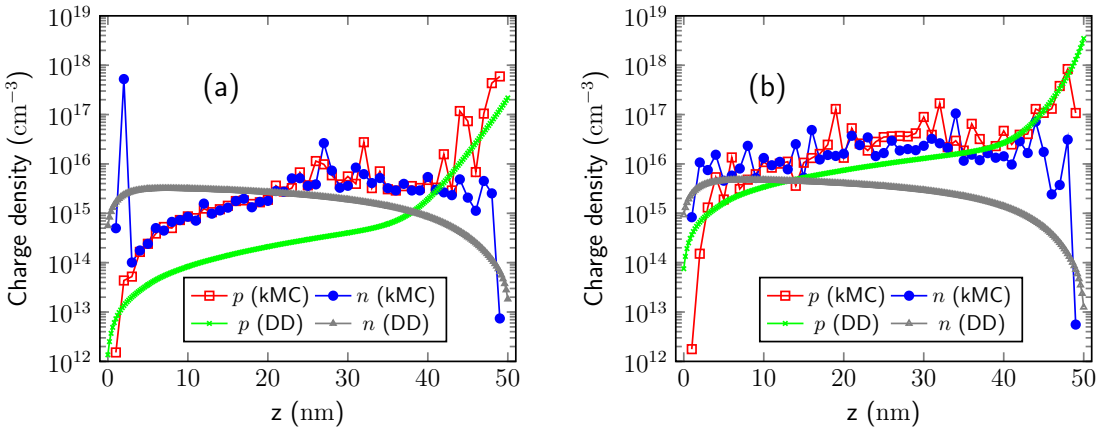

Figure 5.5. – Comparison of the average charge densities per slice along the z-direction for 10 meV (a) and 65 meV (b) of disorder for both the DD and the kMC model. All results are at short-circuit condition.

and $p = 7.50 \times 10^{16}\,\mathrm{cm}^{-3}$. These are commonly assumed values in organic solar cells [203]. Higher disorder is the reason for decreased charge mobility due to trapping in deep states of the Gaussian disorder. The trapping of charges leads to an increased charge density, both positive and negative, inside the active layer. Since hole mobility is lower than electron mobility, the increase is stronger for p than for n.

The result of the DD simulations with the same system setup is also shown in Figure 5.5. The densities in the EMA show a different behavior. Electron and hole densities are not equal throughout the layer but rather seem being influenced strongly by the electric field across the active layer. Holes are pushed towards the anode and electrons towards the cathode, i.e. an internal charge separation takes place. This is fundamentally different to the kMC results where opposite charges stay clustered together and the electron and hole are still Coulomb bound in a region around the interface where they have been created. However, it is impossible for the EMA model to show this effect because it is purely morphological/interface effect. Therefore, the global electric field dominates here over the effects of the local one. Increased electron density at the cathode and increased hole density at the anode can also be observed in the EMA model, i.e. the injection processes are comparable. The general trend is the same for the 65 meV simulations although the effect of charge separation seems to be lower, i.e. influence of the disorder on the charge density distribution has grown.

5.4. Conclusion

We compared DD and kMC simulations of an organic solar cell comprised of a P3HT:PCBM blend as the active layer. In the DD simulations the blend is modeled as a 1D effective material while the kMC method includes the realistic blend morphology in 3D. We ex-

tracted mobilities containing the charge dynamics through the blend by the kMC model. These mobilities were plugged in the DD model to represent the blend information. The j-U characteristics of the two models showed no good agreement in terms of short-circuit current, open-circuit voltage and fill-factor. Investigating the charge density distribution across the active layer shows that local (interface) effects are hidden with the EMA and that it is not possible to put morphological effects in the mobility and the recombination prefactor of the Langevin recombination in a 1D DD model. In the DD model, the lack of morphology leads to charge separation and the formation of an imbalance between positive and negative charge throughout the layer. In the real 3D blend simulations, opposite charges stick together at an interface for most of their lifetime and no global charge separation can be observed. These are blend effects that cannot be captured by the EMA. Due to the close distance of electrons and holes, more recombination takes place, reducing the short-circuit current and lowering the performance in comparison to less recombination in the DD model due to charge separation. Thus, the results can raise doubt on the physical accuracy of the EMA for OSCs which possess both a low dielectric constant, due to which local Coulomb effects play a major role, and a complex geometrical structure, such as in a BHJ configuration.

6. Influence of Permittivity and Energetic Disorder on the Spatial Charge Carrier Distribution in Organic Bulk-Heterojunction Solar Cells

In BHJ OSCs the low permittivity in combination with the spatial and energetic disorder of the organic materials leads to a complex behavior of charge carriers within the active layer. Charges originate in the form of bound electron-hole pairs from exciton separation at the heterojunction interface. The successive interplay between mutual Coulomb interaction and the transport through the disordered organic can lead to insufficient separation from the interface, increased interface densities with respect to the bulk regions and, hence, affect recombination. To further understand the mechanisms of recombination, insight into the explicit spatial distribution of charge carriers within the blend is crucial. We performed kMC simulations on a BHJ OSC to assess the effect of Coulomb interaction and energetic disorder on the three-dimensional spatial distribution of charge carriers and highlight the correlation to both geminate and non-geminate recombination. We show that for materials with low permittivity and large energetic disorder the charge distribution is strongly inhomogeneous with accumulation along the heterojunction interface. In such cases recombination is not limited by recombination partners finding each other but rather an interface controlled process where geminate recombination dominates over nongeminate recombination.

The content of this chapter is adapted from T. Albes and A. Gagliardi, "Influence of Permittivity and Energetic Disorder on the Spatial Charge Carrier Distribution and Recombination in Organic Bulk-Heterojunctions", *Physical Chemistry Chemical Physics*, vol. 19, no. 31, pp. 20 974–20 983, 2017, with permission from the PCCP Owner Societies.

6.1. Background

In BHJs, after the charge transfer at the donor/acceptor heterojunction, the electron resides in the acceptor material and the hole in the donor material. In this intermediate state, the geminate charges can still feel their mutual Coulomb attraction (controlled by the ε_r), up to a separation distance of about the Coulomb radius $r_C = 14 - 19\,\mathrm{nm}$ for $\varepsilon_r = 3 - 4$, and see an energetically disordered landscape in their respective phase (controlled by σ). Both Coulomb attraction and energetic disorder hinder the electron and hole from separating from each other and the interplay between ε_r and σ is expected to have a big impact on the spatial Charge Carrier Distribution (CCD) and, in turn, recombination. The crucial question arising is: are charges rather concentrated along the heterojunction interface or can they be considered free within their respective phase? In the former case the photogeneration process is controlled by the size and the properties of the heterojunction, in the latter case it might be sufficient to reduce the BHJ to effective bulk models. The longer opposite charges stick together in a bound state at the interface (i.e. the larger the interface charge density) the more likely it is for them to undergo geminate recombination. If they have managed to overcome their mutual influence (by the support of thermal fluctuation or an electric field) they can, on their pathway towards the contacts, meet a charge originating from a different exciton and recombine, in which case the recombination is considered nongeminate.

Techniques like TEM can be used to determine the structural morphology of BHJs and estimate the grade of intermixing and typical cluster sizes [146]. However, the spatial resolution of location-dependent physical quantities such as the CCD or recombination channels is challenging to obtain during device operation [204]. Quantities extracted by experimental techniques such as photo-Charge Extraction by Linearly Increasing Voltage (p-CELIV) [205], Impedance Spectroscopy (IS) [206] or transistor methods [207] are mostly bulk/average quantities because they assume a homogeneous distribution, reducing the BHJ to a single effective medium and hiding all blend/interface effects within them.

While there are OSC systems with a charge separation yield approaching unity [208], recombination remains a limiting factor in others [209], [210] and the question under which conditions charge separation or accumulation are dominating needs further investigation.

The reason for efficient charge separation is an actively discussed topic, and especially the theory about hot CT states [211] has gained popular interest. The theory describes a long-range charge transfer process using excess energy of the photon. However, there has been evidence that the separation probability does only weakly depend on excess energy of the incident photon [212]–[214]. Forcing the charge pair to have an initial separation distance of up to several tens of nanometers willingly suppresses geminate recombination. This method was used within kMC simulations to specifically study nongeminate recombination on its own [215]. Suppressing nongeminate recombination is inappropriate to compare the relationship between geminate and nongeminate recombination. We do therefore not consider an initial long-ranged charge pair splitting in this study.

After separation has occurred, the Langevin model [175] is most widely used to describe nongeminate recombination. The Langevin model is of the form $R = (q\,\mu_e\mu_h)/\varepsilon_r \cdot np$, where n, p are the (mean) electron and hole charge densities and μ_e, μ_h their (mean) mobilities. It describes a bimolecular process where recombination is limited by the chance of charges finding each other within their Coulomb radius r_C, after which the actual recombination process is inevitable and happens instantaneously. All charge pairs generated within $r_C = 14 - 19\,\mathrm{nm}$ would therefore be condemned to recombine. The Langevin model was derived for free charges in homogeneous, low mobility materials to describe nongeminate bimolecular recombination. In organic BHJs charges cannot generally be considered free due to their confinement to their respective phase. Even within the respective phase the CCD is not necessarily uniform due to the initial charge generation at the heterojunction, mutual Coulomb interaction and energetic disorder. Deviations from Langevin behavior due to spatial separation have been reported in polymer:fullerene blends [176], [177]. For charges accumulated at the interface the limitation of recombination being based on charges finding each other is not given anymore. They are already in vicinity of each other and recombination is a monomolecular (instead of a bimolecular) process based on the CT state density and its actual (geminate) recombination rate.

In order to consider the spatial variations of charge densities, models with a representation of the 3D blend are needed. Continuum models in combination with 1D effective medium descriptions for the BHJ are established to simulate OSCs [33], [195], especially due to their low computational demand. However, extending the blend geometry to 3D, continuum models often suffer from convergence issues and studies are scarce [216], [217].

The kMC method is the most suitable simulation technique to model processes in disordered OSCs as it allows to implement an approximation of the 3D blend morphology and explicitly evaluate the spatially resolved CCD in the BHJ.

In this study we use a kMC model of a BHJ OSC to show the effect of permittivity in combination with the energetic disorder on the 3D resolved charge density distribution within the cell and its correlation to recombination. For data evaluation, we explicitly distinguish between interface and bulk charge densities as well as geminate and nongeminate recombination which allows us to quantify the absolute values and the ratio of the interface/bulk densities and geminate/nongeminate recombination.

6.2. Model specifics

The implementation of the kMC model described in Chapter 4 is used for a $50\times50\times50\,\mathrm{nm}^3$ cell with a BHJ morphology of 13.7 nm cluster size. The cluster size in combination with the exciton diffusion rate used yields an exciton separation efficiency of $95\,\% \pm 0.5\,\%$ throughout all simulations and can be considered constant. In this way, we make sure that the exciton separation efficiency does not influence the electrical part which is the focus of this study.

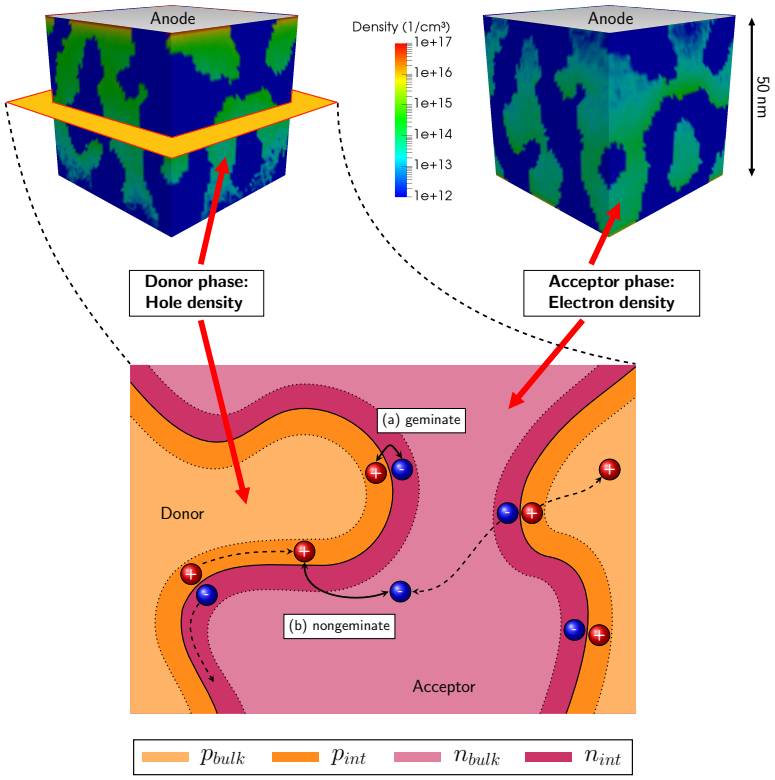

Figure 6.1. – (top) Illustration of the 3D electron and hole charge density distribution in the BHJ. (bottom) Definition of interface densities (electron n_{int}, hole p_{int}) and bulk charge densities (electron n_{bulk}, hole p_{bulk}) as well as geminate (a) and nongeminate (b) recombination events.

Comparing the magnitude of the four contributions to charge transport in Equation (4.2.3), the MO offset between donor and acceptor is usually large ($\gtrapprox 600\,\mathrm{meV}$) so that electrons and holes are confined to the acceptor and donor phase, respectively, at all times. The influence of E^F is small on local scales with $\approx 10\,\mathrm{meV\,nm^{-1}}$ compared to the disorder, usually in the range of 70 meV, and the Coulomb interaction with E^C up to more than 400 meV for two charges within a distance of 1 nm at $\varepsilon_r = 3.5$. Disorder and Coulomb interaction are therefore expected to have the dominating influence on charge dynamics on close scales.

Interface nodes are classified as all nodes within a distance of 1 nm to a heterojunction. Bulk region are all regions further away from a heterojunction. We define the arithmetic mean of all interface nodes in the donor as the hole interface density p_{int}, and vice versa n_{int} as the electron interface density in the acceptor. The bulk densities p_{bulk} and n_{bulk} are defined in analogy for the nodes in the bulk regions. A typical result for the charge density distribution as obtained by the kMC simulations and an illustration of the

definition of the interface and bulk densities for both electrons and holes are depicted in Fig. 6.1. The immediate regions near the contacts are not included in the density evaluation in order not to distort the results by space charge effects induced by charge injection from the contacts.

All simulations are performed at short-circuit condition ($U_{ext} = 0$) and the overall simulation time was $T = 10\,\text{ms}$ where equilibrium was reached after approximately 1 ms, determined by a steady current extracted from the contacts. For the analysis presented here, the values of energetic disorder were chosen to be 42 meV, 71 meV and 99 meV.[1] For convenience, we will refer to them as 40 meV, 70 meV and 100 meV, respectively, throughout this study. An overview of the remaining parameters used in the simulations is listed in Table 4.1 and Table 4.2.

6.3. Results and discussion

6.3.1. Charge accumulation and operation regimes

At first, we investigate the effect of energetic disorder σ and the strength of Coulomb interaction controlled by ε_r on the spatial distribution of charges within the active layer.

Figure 6.2 pictures the CCD of electrons and holes across a slice though the center of the active layer for both lower and higher permittivity (3 and 5) and for different values of the energetic disorder ranging from 40 meV to 100 meV (Figure 6.2a–c). Figure 6.2d shows the corresponding charge density scale and an illustration on how the density relates to the Gaussian disorder centered around the MO level E^0 of acceptor or donor, respectively. While for small disorder the distribution is relatively smooth and almost uniform within the respective phases, spatial fluctuations in the CCD become much more evident with increasing energetic disorder. With rising disorder there are an increasing number of sites with either deep or high energy levels around the MO level. These tail states shape the potential landscape charges experience and directly influence the CCD. Deep levels act as local trapping sites in which charges can get stuck repeatedly. Thus, these sites can show drastically increased charge densities (shown in red). High levels have elevated energy levels and appear as hills for charges that are unlikely to be occupied, therefore decreasing the density at those sites (shown in blue). A disorder of 100 meV can make the CCD fluctuate locally by several orders of magnitude around the average charge density in the phases. In addition, also the permittivity leads to an inhomogeneity in CCDs: for low permittivity charges appear to be located rather at the interface than in the bulk regions. This effect is more evident for larger energetic disorder. Especially

[1] In [34], the values used for the Gaussian energetic disorder σ were stated as 0 meV, 30 meV, 50 meV and 70 meV. Due to a mistake in the implementation, these values need to be rescaled by a factor of $\sqrt{2}$ and correspond to 42.4 meV, 70.7 meV, and 99.0 meV, respectively. In the content presented here, the disorder has been re-labeled accordingly in the text and the figures. The overall implications of interface accumulation at large disorder in combination with a low permittivity as well as the conclusions drawn do not change. See also [218].

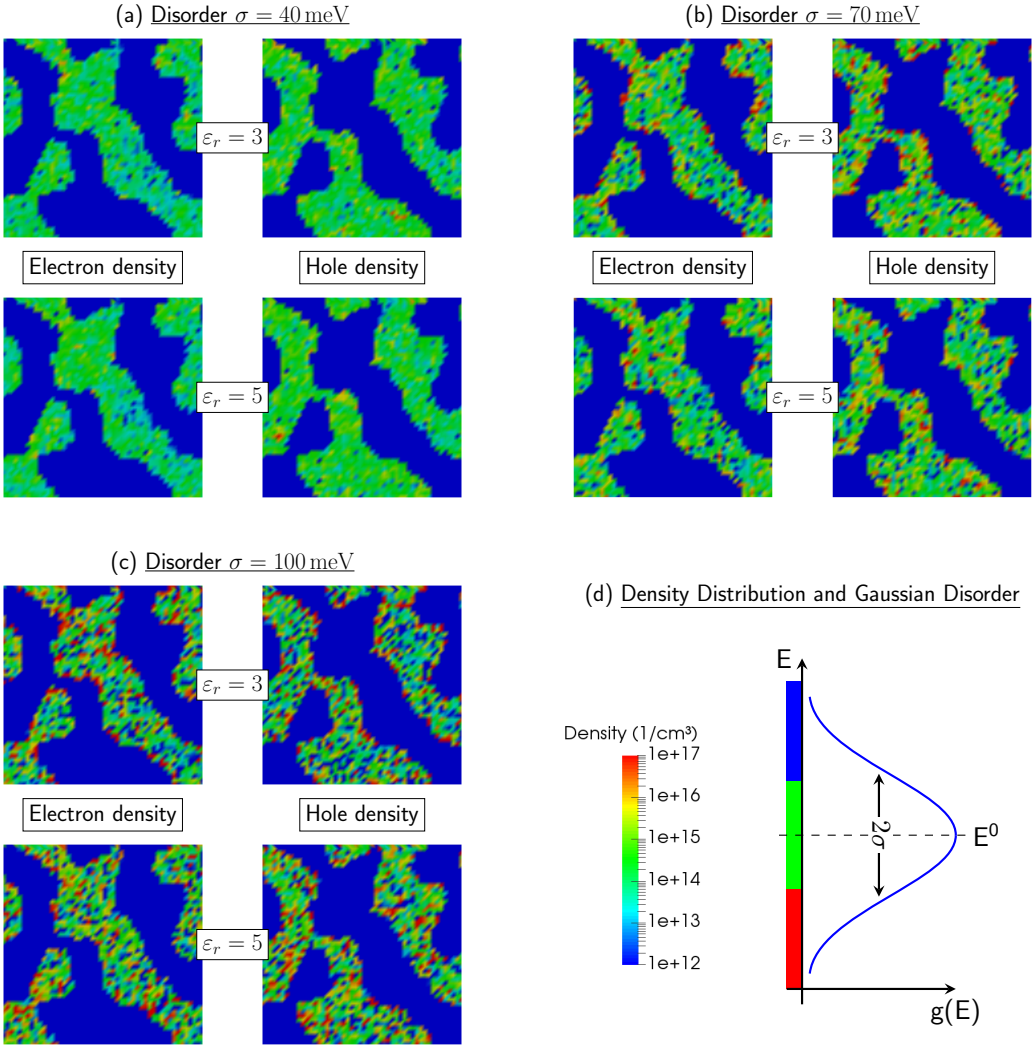

Figure 6.2. – Electron and hole charge density distributions along a slice through the morphology for different values of energetic disorder ranging from 40 meV (a) via 70 meV (b) to 100 meV (c). All density maps are shown for two cases of permittivity ($\varepsilon = 3$ and $\varepsilon = 5$), respectively. In (d), the corresponding density scale and the relationship of energy levels within the Gaussian distribution and the charge density is shown.

for higher values of disorder, the exact behavior of the CCD is rather unclear from the raw data. In order to decide if and under which conditions charges accumulate near the interface an analysis setting the interface and bulk densities into relation is needed.

The ratio between interface charge densities and the bulk densities for holes, p_{int}/p_{bulk}, and for electrons, n_{int}/n_{bulk}, is illustrated in Figure 6.3 for a parameter set of $\sigma = 0$, 40, 70, and 100 meV and $\varepsilon_r = 3$, 3.5, 4, 5 and the artificial case of ∞. It gives an indication

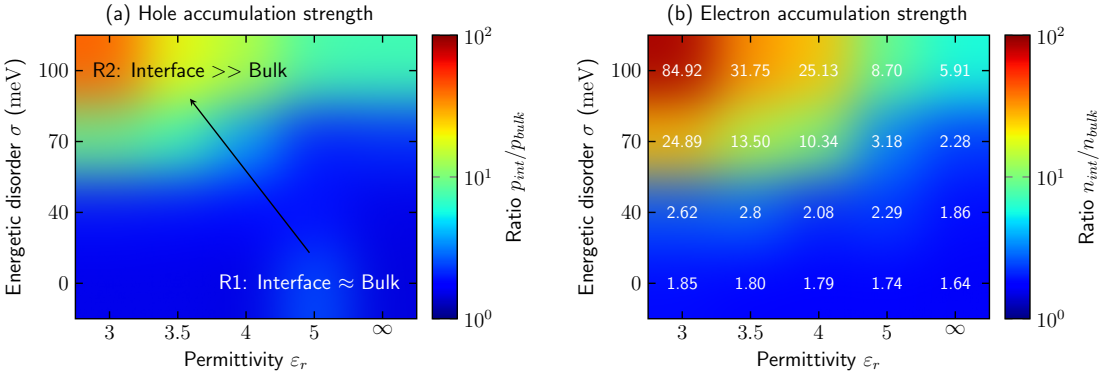

Figure 6.3. – Ratio of interface to bulk charge densities of (a) holes and (b) electrons for different parameter sets of energetic disorder and permittivity (σ, ε_r). High values indicate an inhomogeneous charge distribution with accumulation of charges at the heterojunction interface while a value of 1 represents homogeneous charge distributions of electrons in the acceptor and holes in the donor, respectively. The artificial case of $\varepsilon_r = \infty$ (no Coulomb interaction) is added to be able to interpret the effect of disorder alone.

whether charge carriers accumulate near the heterojunction interface or if they are rather distributed homogeneously within their respective phases. After Equation (4.33) the interface and bulk densities are in direct correlation to the average time a charge spends at the interface or in the bulk regions, respectively. The recombination rate is fixed with a value of $a_{ehr} = 5 \times 10^4\,\mathrm{s}^{-1}$ for these simulations.

It is clearly visible from Figure 6.3 that the combination of disorder and permittivity is controlling where charges are located. For no disorder the interface density is almost identical to the bulk density, only a slight increase up to a factor of $n_{int}/n_{bulk} \approx p_{int}/p_{bulk} \approx 2$ can be observed, attributed to the fact that charges are initially generated in the interface regions. After generation they can quickly move away from the interface because they experience a flat energetic landscape due to the missing disorder. The disorder generally has a negative effect on charge transport because charges tend to get stuck in deep tails and are less likely to overcome hills of the distribution. In the no-disorder-regime, Coulomb interaction only plays a minor role and affects accumulation only slightly. The larger the energetic disorder, the larger not only the overall magnitude of the accumulation but also the influence of permittivity grows. Since the permittivity controls the strength of the electrostatic interaction, it directly affects the efficiency of electron/hole pairs to overcome the mutual attraction and move from the interface region into the respective bulk regions. While at ($\sigma = 0\,\mathrm{meV}$, $\varepsilon_r = 5$) the ratio is around 2, it increases up to $n_{int}/n_{bulk} \approx 85$ for electrons and up to $p_{int}/p_{bulk} \approx 41$ for holes at ($\sigma = 100\,\mathrm{meV}$, $\varepsilon_r = 3$) indicating that most of the charges in the cell remain in the interface region for the largest part of their lifetime.

The operation principle can therefore roughly be classified into two different regimes: R1 (low σ, high ε_r) and R2 (high σ, low ε_r). In R1 charge transport is good and Coulomb interaction weak, we can observe a homogeneous CCD without regions of accumulation. This regime can be attributed to highly organized, well screening materials. R2 applies to materials with substantial energetic disorder and weak screening of electrostatic interaction. In this regime, the CCD within the BHJ is inhomogeneous with a large accumulation of charges at the heterojunction interface. The interplay between σ and ε_r is controlling where charges are located and can shift the operation regime from bulk to interface dominated.

The artificial case of no Coulomb interaction was added to the data to show the influence of increasing energetic disorder independently of the influence of electrostatic interaction. While accumulation is sensitive to increasing disorder, only the combination of bad charge transport and mutual interaction drastically increases interface accumulation.

It needs to be mentioned that in case the permittivity exceeds $\varepsilon_r \gtrapprox 9$ excitons have negligible binding energy and are thermally dissociated into free charges [86], [87], [178]. This effect is not implemented in our simulations but needs to be considered in the interpretation. It would render the exciton separation efficiency to be 100 %. Compared to the weakly fluctuating exciton separation efficiency of $95\,\% \pm 0.5\,\%$ in all our simulations, one could expect a minor difference in the results as more charges should have been created than they actually were in our model.

Values for the energetic disorder are around 70 meV for established material combinations used in polymer:fullerene blends formed from P3HT and PCBM [156]–[158]. Depending on the crystallinity and purity of the materials, the disorder can vary around this commonly assumed value. Higher values than 100 meV of disorder lead to an extensively large computational demand of the kMC model. To maintain a feasible amount of simulation time we restricted our analysis to $\sigma \leq 100\,\text{meV}$. Interpolating the trend of charge accumulation strength, in case of an energetic disorder larger than 100 meV the effect of accumulation will only be pronounced stronger. The permittivity of organic materials is mostly assumed to be around 3.5. For permittivity the choice of our parameter variation from 3 to 5 is meant to provide a sensitivity analysis to show how already slight changes can affect the charge location drastically.

The accumulation effect qualitatively holds true for both electron and hole distribution although the effect is more pronounced for electrons than for holes. To have a more detailed look at the absolute values of the charge densities, Figure 6.4 illustrates the absolute interface and bulk densities face to face for an energetic disorder of 100 meV. At $\varepsilon_r = 3$, the interface densities with $n_{int} = 1.07 \times 10^{18}\,\text{cm}^{-3}$ and $p_{int} = 1.28 \times 10^{18}\,\text{cm}^{-3}$ are by the previously mentioned factors, 85 and 41 respectively, larger than the bulk densities of $n_{bulk} = 1.26 \times 10^{16}\,\text{cm}^{-3}$ and $p_{bulk} = 3.13 \times 10^{16}\,\text{cm}^{-3}$. The total charge density in the active layer is therefore mainly made up by charges at the interface.

With increasing permittivity, n_{int} and p_{int} drop while the bulk densities rise. By increasing the permittivity only slightly to $\varepsilon_r = 5$, the interface densities drop to

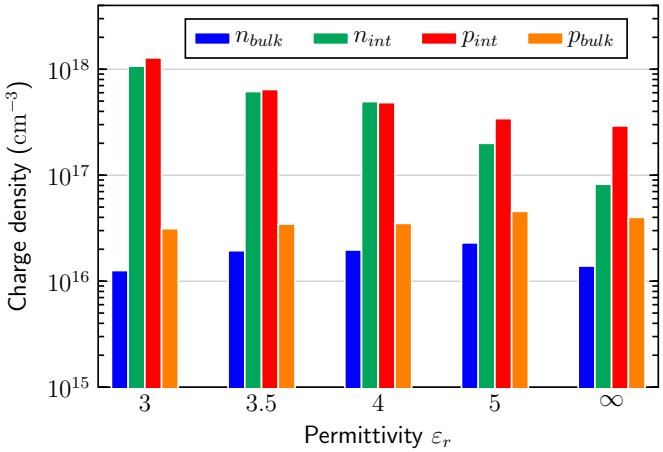

Figure 6.4. – Absolute values of interface and bulk charge densities of electrons and holes at energetic disorder $\sigma = 100\,\text{meV}$ for different values of permittivity ε_r. For each ε_r, the inner two bars show the interface densities and the outer two bars the bulk densities.

$n_{int} = 2.00 \times 10^{17}\,\text{cm}^{-3}$ and $p_{int} = 3.42 \times 10^{17}\,\text{cm}^{-3}$ and the bulk densities increase to $n_{bulk} = 2.30 \times 10^{16}\,\text{cm}^{-3}$ and $p_{bulk} = 4.56 \times 10^{16}\,\text{cm}^{-3}$. Charges are not drawn to the interface as strong, they are moving away from the interface into the bulk regions more quickly, and the distribution inclines towards a more homogeneous distribution. But even in the case of no Coulomb interaction they are not fully equal induced by the bad transport due to the disorder. The generally higher hole densities are a result of the lower hole hopping mobility compared to the electrons we assumed. This means holes are slower and need more time to move both away from the interface and also spend more time in the bulk regions resulting in higher average densities. These results show that the permittivity has a strong effect on charge location and that even slight modifications can drastically change the distribution.

6.3.2. Influence on recombination

Independently of whether opposite charges in a pair stem from the same or from a different origin, the longer they spend time in vicinity of each other the higher the chance for them to undergo recombination. Therefore, and because opposite charges can only meet at the interface, a correlation between the interface charge accumulation and recombination is expected. Recombination occurs with the rate a_{ehr} and is dependent on many factors, e.g. the molecular species of the donor and acceptor materials and their arrangement along the heterojunction. The kMC model cannot make predictions about such properties, and therefore about the magnitude of a_{ehr}, and its value is still under debate. Fitting current j-U characteristics to measurements yielded values in the range of $10^4\,\text{s}^{-1}$ to $10^6\,\text{s}^{-1}$ [178], [179], while TAS measurements concluded a recombination

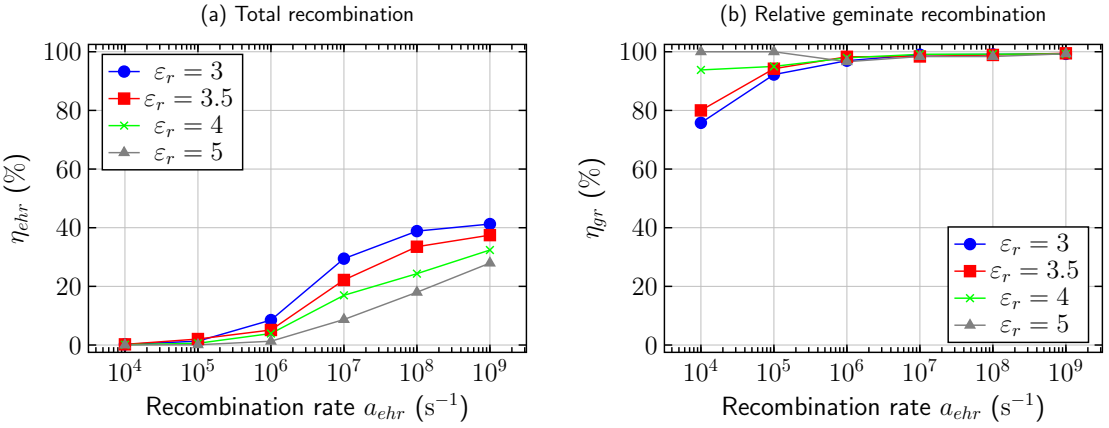

Figure 6.5. – Amount of total recombination η_{ehr} (a) and the corresponding relative part of geminate recombination η_{gr} (b), both shown vs. recombination constant a_{ehr} at different values of ε_r and at an energetic disorder of 70 meV. A value of $\eta_{ehr} = 100\,\%$ means that all charges generated by exciton splitting undergo recombination. A value of $\eta_{gr} = 100\,\%$ means that from all recombination events, every single one is geminate and none are nongeminate. All recombination that is not geminate is nongeminate recombination.

rate in the range of $a_{ehr} = 10^7\,s^{-1}$ up to $10^9\,s^{-1}$ [131], [181], [183], [219]. In previous kMC models the most commonly used values are around $5 \times 10^5\,s^{-1}$ as in [142]. Due to the uncertainty in recombination rate and the sensitivity of the accumulation effect with respect to small changes in permittivity shown above, we analyzed the amount of recombination with respect to a variation of a_{ehr} many orders of magnitude from $10^4\,s^{-1}$ to $10^9\,s^{-1}$ and ε_r ranging between 3 and 5, inducing different accumulation strengths.

In order to show the influence of permittivity at a realistic disorder of 70 meV, Figure 6.5 shows the total recombination η_{ehr} and the ratio of geminate recombination with respect to the total recombination η_{gr} in dependence of the recombination rate a_{ehr}, varied between $10^4\,s^{-1}$ and $10^9\,s^{-1}$, for different permittivities. From Figure 6.5a it can be observed that both a lower permittivity as well as a higher recombination constant increase the total recombination. At a low recombination of $10^4\,s^{-1}$, there is only little recombination observable: η_{ehr} ranges between 0.24 % at $\varepsilon_r = 3$ and 0.02 % at $\varepsilon_r = 5$. Increasing a_{ehr} to $10^7\,s^{-1}$, i.e. 100 ns of recombination time, η_{ehr} drastically increases to 29.45 % for $\varepsilon_r = 3$ and can be lowered by more than a third down to 8.7 % when increasing the permittivity to 5. At very high recombination rates of $10^9\,s^{-1}$ ($\tau_{rec} = 1$ ns), the total recombination further increases to 41.25 % at $\varepsilon_r = 3$ and 27.94 % at $\varepsilon_r = 5$. The fact that a_{ehr} is varied by several orders of magnitude and ε_r only between values of 3 and 5, and yet the changes in overall recombination are of comparable magnitude, highlights the drastic influence of ε_r on charge recombination.

When the average time two charges spend next to each other approaches the range of

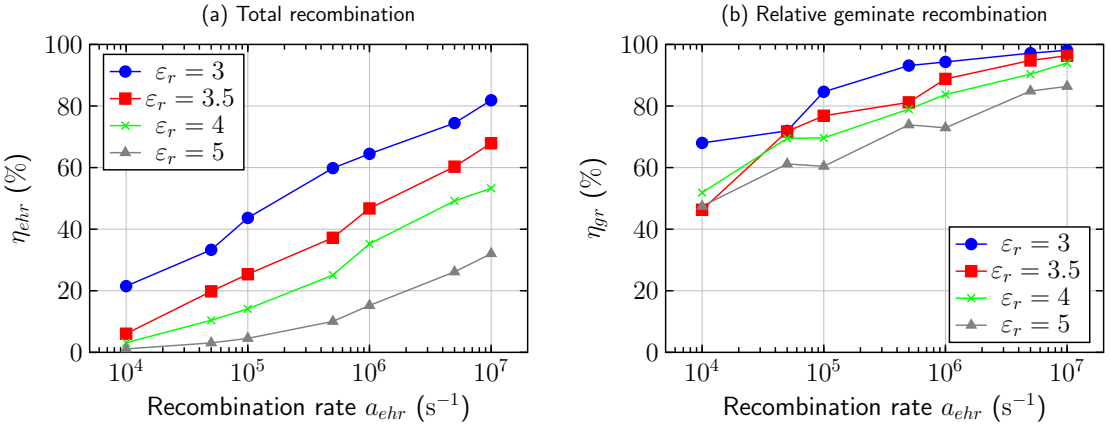

Figure 6.6. – Amount of total recombination η_{ehr} (a) and the corresponding relative part of geminate recombination η_{gr} (b), both shown vs. recombination constant a_{ehr} at different values of ε_r at an energetic disorder of 100 meV.

the average recombination time $\tau_{rec} = (a_{ehr})^{-1}$, recombination is starting to occur. The interface charge density is a measure for the time charges spend in the interface regions. In Langevin theory, the actual recombination process is independent of the rate of the actual recombination process and is considered instant. However, if charges are mostly confined to the interface regions due to bad transport and mutual Coulomb interaction, the influence of the bimolecular part (i.e. the recombination partners finding each other) is reduced, as they have already found each other or have never been separated, and the actual recombination rate cannot be neglected. For the case of interface accumulation, the strong dependency of the recombination rate is obvious from the results and it increases with higher accumulation, for instance induced by lower permittivity. This is in accordance with theoretical and experimental studies of increasing permittivity to reduce recombination [87], [88], [90], [92].

Figure 6.5b shows the amount of geminate recombination with respect to the total recombination η_{gr}. For recombination rates larger than $10^6\,s^{-1}$, almost all recombination is geminate. For lower a_{ehr}, η_{gr} slightly reduces, but the majority of recombination remains geminate. It has to be noted that at very low recombination rates the overall recombination is next to negligible and prevents a meaningful interpretation of the ratio between geminate and nongeminate recombination. It can be concluded that without an additional mechanism to support charge separation, and only based on the influence of Coulomb interaction and Gaussian disorder, geminate recombination cannot be neglected as a major loss pathway in BHJs, as stated in e.g. [220].

In order to show the sensitivity of the recombination to the energetic disorder, Figure 6.6 shows η_{ehr} and η_{gr} at a large energetic disorder of $\sigma = 100$ meV, for a recombination rate a_{ehr} between $10^4\,s^{-1}$ and $10^7\,s^{-1}$. While the general trend remains similar, the overall recombination is strongly increased (Figure 6.6a). The influence of only small

Table 6.1. – Effect of permittivity and disorder on short-circuit current density j_{sc} (in $\mathrm{mA\,cm^{-2}}$) at $a_{ehr} = 10^7\,\mathrm{s^{-1}}$.

	ε_r				
σ	3	3.5	4	5	∞
100 meV	0.95	2.08	3.24	5.18	8.08
70 meV	5.08	5.72	6.15	6.85	8.10
40 meV	7.45	7.51	7.54	7.69	8.13
0 meV	7.47	7.51	7.66	7.86	8.35

changes in ε_r on overall recombination is drastic: for a slow recombination process with $a_{ehr} = 10^4\,\mathrm{s^{-1}}$, the total recombination increases from 1.12 % at $\varepsilon_r = 5$ to 21.5 % at $\varepsilon_r = 3$. Here, the biggest change occurs when changing ε_r from 3 to only 3.5, where η_{ehr} changes from 6.05 % to 21.5 % and highlights the sensitivity of recombination to the dielectric screening strength at a large disorder. With higher recombination rate the relative influence of ε_r drops, however the absolute number of photogenerated charge carriers recombining is very high. At $a_{ehr} = 10^7\,\mathrm{s^{-1}}$, the recombination varies between 81.87 % and 32.05 % for permittivity changing from 3 to 5. The corresponding amount of geminate recombination η_{gr} is shown in Figure 6.6b The general trend is similar to the overall recombination, i.e. geminate recombination increases with higher a_{ehr} as well as with lower ε_r. At $a_{ehr} = 10^7\,\mathrm{s^{-1}}$, between 86.4 % and 98.1 % of recombination is geminate and only a marginal part of recombination is nongeminate. Slower recombination reduces the ratio of geminate recombination to as low as 47 % at low $a_{ehr} = 10^4\,\mathrm{s^{-1}}$ and high $\varepsilon_r = 5$, because it is easier for charge pairs to separate from each other before they reach the critical recombination time.

It can be concluded that the overall recombination is very sensitive to both permittivity and disorder and that the dominant recombination mechanisms as predicted by the model is geminate recombination. If it were possible tuning the permittivity and disorder, recombination could be strongly suppressed even for large recombination rates.

A particularly interesting result is observed for no Coulomb interaction ($\varepsilon_r = \infty$) as well as for no disorder, independently of one another: here, no recombination at all is observed (data not shown). In these cases the average time a charge pair stays at the heterojunction is small and does not interfere with the average recombination time τ_{rec}, i.e. separation is much faster than recombination. Therefore no recombination occurs in this regime and interface accumulation can seems to be a requirement for recombination to occur.

Finally, to link the effect of σ and ε_r to the performance of the cell, Table 6.1 shows the short-circuit current density at $a_{ehr} = 10^7\,\mathrm{s^{-1}}$. In accordance to the discussion about recombination there is an anti-correlation of interface accumulation strength and j_{sc}. Larger accumulation leads to more recombination and, in turn, recombination reduces

the current reaching the contacts, i.e. j_{sc}. While disorder and permittivity separately have an influence on j_{sc}, only the combination of both dramatically influences the current. No disorder and perfect screening lead to perfect charge collection efficiency without recombination and $j_{sc} = 8.35\,\mathrm{mA\,cm^{-2}}$. The influence of ε_r is particularly evident for $\sigma = 100\,\mathrm{meV}$ and the increased recombination due to low Coulomb screening reduces the short-circuit current down to $0.95\,\mathrm{mA\,cm^{-2}}$ at $\varepsilon_r = 3$.

6.4. Conclusion

The kMC method allows to investigate the 3D CCD and recombination events in complex morphologies such as BHJs, otherwise challenging to assess by experiments and scarcely modeled by DD models. We set up a kMC model with particular focus on Coulomb interaction and showed that the two key differences of disordered organic with respect to inorganic semiconductors, energetic disorder and permittivity, strongly affect the charge carrier distribution in BHJs which, in turn, have a direct influence on the losses by recombination. The CCD can be classified into two regimes:

- A low permittivity in combination with a high disorder leads to a strongly inhomogeneous CCD with accumulation of charges along the interface. In this case charge pair separation is inefficient due to strong mutual Coulomb interaction and bad transport though the disordered landscape. As a result, recombination is an interface-controlled process with strong dependence on the recombination rate a_{ehr}. Geminate recombination clearly dominates over nongeminate recombination and cannot be neglected as major loss mechanism.
- On the contrary, a high permittivity and a low disorder lead to a homogeneous distribution of charges within their phases. In this case the overall recombination ratio is strongly reduced because charge pairs can separate faster than the average recombination time. Furthermore, the ratio of geminate recombination reduces and slightly shifts towards nongeminate recombination, however in the light of a low overall recombination.

The accumulation effect and its influence on recombination are very sensitive on both permittivity as well as energetic disorder. Even slight changes can shift the operation away from the an accumulation regime with high recombination losses towards a more homogeneous CCD regime with lower recombination and therefore support other studies where increasing the permittivity was stated as the route towards high-efficiency BHJ OSCs.

7. Charge Pair Separation Dynamics in Organic Bulk-Heterojunction Solar Cells

Charge pair separation in organic BHJ solar cells is a complex interplay between numerous factors such as the spatial geometry of the blend, the distribution of energetic disorder, the electric field, thermal fluctuations, and the mutual electron-hole Coulomb attraction. Insufficient separation from the interface and concomitant charge pair recombination is a main limitation in improving the power conversion efficiency of organic BHJ solar cells and requires in-depth understanding of the time scales involved. We investigate the time-dependent evolution of mutual electron-hole pair distances separating from the heterojunction interface by using a 3D kMC model of a BHJ OSC. We find large fluctuations in separation times, in particular in dependence of the energetic disorder and the permittivity of the organic materials. At commonly observed values of energetic disorder, already slight modifications of the permittivity can drastically influence the charge separation time and even outweigh orders of magnitude of geminate recombination rates, hence help to suppress geminate recombination. Thus, our results strongly support the recent trend of developing high-permittivity organic materials for solar cell applications.

The content of this chapter is adapted, with permission, from T. Albes and A. Gagliardi, "Charge Pair Separation Dynamics in Organic Bulk-Heterojunction Solar Cells", *Advanced Theory and Simulations*, vol. 1, no. 7, p. 1 800 032, 2018.

7.1. Background

Charge generation in BHJ OSCs takes place at the donor/acceptor interface: after the dissociation of an exciton into electron and hole, the electron-hole pair remains in a state bound across the heterojunction interface. The electron and hole must first separate against their mutual attraction and away from the BHJ interface, before they can be transported to the contacts and contribute to a photocurrent.

Both partners of the Charge Pair (CP) feel the mutual Coulomb interaction and see a disordered landscape, spatially due to BHJ morphology and energetically due to the energetic disorder. Separation of the CP is driven by thermal fluctuations and an eventual electric field. In case of insufficient separation, the CP pair can recombine geminately reducing the photocurrent. It is therefore evident that the entire charge separation process in organic BHJs is a complex interplay between Coulomb interaction, spatial and energetic disorder, thermal fluctuations, diffusion, and the electric field.

Recent studies state that the dynamics of CP separation, in particular the timescales involved, still lack understanding and that a deeper insight is of utmost importance [221], [222]. In some systems, almost all photo-generated charges can separate from the heterojunction [208], in others large losses by recombination can be observed [209], [210]. No general understanding exists to predict the requirements on efficient charge separation [223].

Direct investigation of the time-dependent evolution of single charge pairs is challenging and the explicit charge separation dynamics have only scarcely been studied. For instance, Vithanage et al. have shown by the time-resolved electric field-induced second harmonic method that (thermally activated) diffusion is dominating CP separation at close scales [224], while this dominance weakens at farther separation distance in favor of drift. For an analytic description of the dynamics the OB model is often applied [83], [84]. However, it does not include the spatial variations of energetic disorder or local electrostatic effects [79], [85], [131]. Furthermore, models based on continuum approaches are not sufficient to describe the spatial and energetic disorder [33], as well as the impact of Coulomb correlation [225], especially when time-dependent processes are to be investigated. A complementary approach from a thermodynamic point of view has shown that entropy in combination with disorder is sufficient for charge separation for even strongly localized and thermalized charge carriers, but the need for more kinetic approaches is also stated herein [226].

The kMC method is a powerful simulation technique to model the time-dependent behavior of physical systems. A specific advantage of the kMC method is that it allows to include explicit particle-particle interactions and that it gives direct access to the charge trajectories which can be used to determine the time-dependent displacement of the electron and the hole of a CP.

A pathway for highly-efficient OSCs was given by Koster et al. [87], who suggested to increase the permittivity of the organic materials used within OSCs in order decrease the mutual attraction of CPs and enhance their separation. This strategy has not gained

much attention until recently, but is now actively studied: increasing the permittivity was shown to be very beneficial for OSC device performance by many groups [27], [28], [82], [88]–[92], [227]–[230]. In addition, pristine organic materials with low energetic disorder can support separation dynamics: a low disorder leads to a more ballistic transport and more efficient separation [221], [222]. Typical values for the energetic disorder range from 100 meV in blends formed from P3HT and PCBM blend, down to 40 meV [221], [231], [232].

Also charge recombination in organic BHJs takes place at the donor/acceptor interface. Independently of whether a CP fails to separate from the interface and thus recombines geminately or whether two charges from distinct excitons find each other at the interface and recombine non-geminately, the actual recombination process of a CP occurs with a monomolecular rate a_{ehr} of the CT state. The recombination rate for bound CPs is under active discussion and expected to depend on many factors such as interfacial properties of the materials, i.e. their molecular orientation [233]. The kMC method takes the recombination rate as an input parameter which needs to be derived from underlying models or measurements. Fits to j-U curves yielded recombination rates of $10^4\,\mathrm{s}^{-1}$ to $10^6\,\mathrm{s}^{-1}$ [178], [179], while measurements found it to be in the range of $a_{ehr} = 10^7\,\mathrm{s}^{-1}$, up to $10^9\,\mathrm{s}^{-1}$ [131], [180], [183], [219]. The recombination time as the inverse of a_{ehr} is competing with the time that charges need to separate from each other and decides whether successful separation or recombination takes place. The Langevin recombination model [175] is the most common way to describe recombination in OSCs: it assumes that once two charges are within the Coulomb radius, they inevitably recombine. However, deviations from Langevin have been observed which are most likely attributed to the fact that the model was derived for homogeneous materials, and that it does not consider the motion of single CP dynamics but is rather based on a continuum approach. In reality, the explicit CP dynamics needs to be considered: if separation time is of the order or larger than the average pair-recombination time, recombination is more likely to occur. Here we put our focus on geminate recombination only, since it is directly linked to the CP separation dynamics. Improving the CP separation, e.g. by the enhancement of mobility, has direct consequences on geminate recombination and hence the performance of OSCs [181], [234]. Non-geminate recombination as the alternative recombination channel has been studied thoroughly both by simulations and experiments [138], [202], [215] and is not considered here.

We have already shown in a previous study by kMC simulations that both a large disorder and low permittivity lead to increased interface charge density and, in turn, larger recombination [34]. However, the explicit time-dependent evolution of large sets of CPs and their separation times have not been extracted and a link to the current research on the effect of permittivity on CP separation times, as well as the relation of separation times to CP recombination times, is missing.

In this study, we employ kMC simulations for BHJ OSCs and investigate the time-dependent evolution of electron-hole pair separation under the influence of various

Table 7.1. – Comparison of different energetic contributions to the overall energy change ΔE on charges on local nm scale.

	ΔE^0	ΔE^F	ΔE^σ	ΔE^C	$k_B T$
ΔE/nm in meV nm^{-1}	≈700	≈13	≈70	$\lesssim$411	≈26

permittivities and values of energetic disorder. Due to the statistical nature of hopping transport, CP separation can follow very different distributions. We evaluate a large dataset of electron-hole pairs and classify times after which the majority of charges have separated or recombined. We show the sensitivity of charge separation to the strength of the Coulomb interaction and the energetic disorder and extract absolute times. These absolute times are put into relation to the charge mobilities, as the dominating material property for charge transport, and the CP recombination strength as the controlling factor for geminate CP recombination.

7.2. Model specifics and evaluation details

The implementation of the kMC model described in Chapter 4 is used for a $50\times50\times50\,\mathrm{nm}^3$ cell with a BHJ morphology of 15 nm cluster size. Here, we only investigate the dynamical evolution of CPs that originate from the same exciton.

Once an exciton is dissociated into electron and hole, the offset in donor/acceptor MO levels of typically several hundreds of meV prevents electrons to move back from the acceptor to the donor and vice versa for holes, i.e. positive and negative charges are confined within their respective phases. Besides the dominant MO offset, charges move under the influence of electric field, the energetic disorder, the mutual Coulomb interaction between themselves and their geminate partner and the electrostatic surroundings. A comparison of the typical energetic contributions that charges of a bound electron-hole pair feel on the local scale after they have been generated from an exciton and are closely (1 nm) apart from each other is listed in Table 7.1. It is evident that the influence of energetic disorder and Coulomb interaction prevails over the influence of the electric field as well as the thermal energy on the local scale. It shall be noted that the contribution of the electric field is largest in short-circuit condition (as considered in this study) and decreases the closer the applied bias approaches the open-circuit voltage. The electric field and the thermal fluctuations must act as the driving forces for charge pair separation because Coulomb interaction prevents charge pair separation and the energetic disorder is a spatially random contribution that can either support or hinder separation, depending on the local distribution. The separation process therefore is mainly dominated by the interplay between E^σ and E^C. We therefore focus on analyzing the effects of disorder and permittivity on charge separation dynamics.

For the CP separation analysis, we define $d(t)$ as the (Euclidean) distance between the electron and the hole of a single charge pair originating from an exciton with respect to

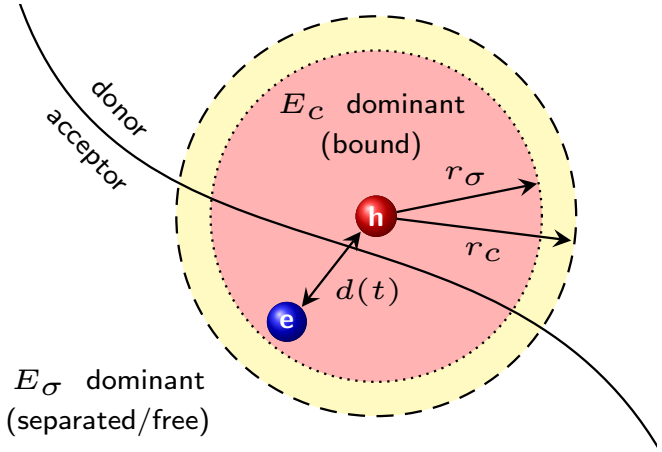

Figure 7.1. – Electron-hole separation distance $d(t)$ after charge transfer. The separation time t_{sep} with $d(t_{\text{sep}}) = r_c$ defines the transition from bound state to separated state, where r_c is the Coulomb radius defined by $E^C(t_{sep}) = k_B T$ (outer dashed radius). The disorder time t_{dis} with $d(t_{dis}) = r_\sigma$ marks the transition between Coulomb interaction and energetic disorder being the dominant influence on charge pair dynamics, where r_σ is the disorder radius defined by $E^C(r_\sigma) = \sigma$ (inner dotted radius).

its time of origin (exciton dissociation). Figure 7.1 illustrates the CP distance and the following definitions required for the data evaluation. CP separation is often defined by the Coulomb radius r_c, which is the distance after which the attractive force between the mutual partners becomes indistinguishable from thermal fluctuations, i.e. $E^C(r_c) = k_B T$. With the definition of Coulomb energy

$$E^C(r) = \frac{e^2}{4\pi\varepsilon_0\varepsilon_r r}, \tag{7.1}$$

the Coulomb radius reads explicitly

$$r_c = \frac{e^2}{4\pi\varepsilon_0\varepsilon_r k_B T}. \tag{7.2}$$

We define the separation time t_{sep} as the time at which two charges of a geminate pair have reached the Coulomb radius $d(t_{sep}) = r_c$. In case a bound pair does re-form and overcome the radius multiple times, the last time after which definite separation occurs is chosen as separation time. As long as the charges of a CP are located within this radius, $d(t) < r_c$, they can be considered a bound pair; once they have managed to overcome this radius (for the final time), i.e. $d(t) > r_c \; \forall t$, the CP is considered as separated.

The strength of the Coulomb interaction drops with the CP distance and after only a couple of nm, the effect of the energetic disorder can dominate over the Coulomb energy. We therefore define a disorder radius r_σ as the radius at which the influence of energetic

Table 7.2. – Overview of disorder radii r_σ ($E^C(r_\sigma) = \sigma$) for different combinations of energetic disorder and permittivity. For comparison, the Coulomb separation radii r_c ($E^C(r_c) = k_BT$) at room temperature are listed for different values of permittivity.

	ε_r			
r	3	3.5	4	5
r_σ ($\sigma = 99\,\mathrm{meV}$)	4.8 nm	4.1 nm	3.6 nm	2.9 nm
r_σ ($\sigma = 71\,\mathrm{meV}$)	6.9 nm	5.9 nm	5.1 nm	4.1 nm
r_σ ($\sigma = 42\,\mathrm{meV}$)	12.0 nm	10.1 nm	9.0 nm	7.2 nm
r_c ($k_BT = 26\,\mathrm{meV}$)	18.5 nm	15.8 nm	13.8 nm	11.1 nm

disorder equals the electrostatic interaction energy $E^C(r_\sigma) = \sigma$:

$$r_\sigma = \frac{e^2}{4\pi\varepsilon_0\varepsilon_r\sigma}. \tag{7.3}$$

In analogy to the separation time, a disorder time t_{dis} is introduced as the time at which the Coulomb energy equals the energetic disorder, i.e. $d(t_{dis}) = r_\sigma$. Similarly to the separation, the last time step after which the CP distance exceeds the disorder radius definitively, $d(t) > r_\sigma\ \forall t$, is picked as the disorder time in case of multiple crossings of r_σ.

In this study, we consider values for the energetic disorder of 42 meV, 71 meV and 99 meV.[1] For convenience, we will refer to them as 40 meV, 70 meV and 100 meV, respectively. All calculations have been performed with the exact values. Table 7.2 presents an overview of the disorder and Coulomb radii for the different permittivities considered, $\varepsilon_r = 3 - 5$. At room temperature ($k_BT = 26\,\mathrm{meV}$) and for the investigated values of energetic disorder ($\sigma = 40\,\mathrm{meV} - 100\,\mathrm{meV}$), the disorder radius is always smaller than the Coulomb radius, i.e. disorder time is reached before separation time. The charge separation dynamics of one individual CP can therefore be divided into the following timeline (see Figure 7.2a for an illustration of a typical evolution of $d(t)$ for no disorder as well as 100 meV of disorder):

At generation electron and hole are put on adjacent nodes, therefore $d(t = 0) = 1\,\mathrm{nm}$ for every pair. They then move under the influence of the local potential Equation (4.24) by the thermally activated hopping after Equation (4.2.3). Until the charge pair reaches the disorder radius r_σ (for no disorder, the disorder radius is not defined), i.e. during the disorder time t_{dis}, the attractive Coulomb force is the dominant influence, controlled

[1] In [35], the values used for the Gaussian energetic disorder σ were stated as 0 meV, 30 meV, 50 meV and 70 meV. Due to a mistake in the implementation, these values need to be rescaled by a factor of $\sqrt{2}$ and correspond to 42.4 meV, 70.7 meV, and 99.0 meV, respectively. The content presented here shows the re-calculated results with the correct values of disorder. Except for a slight shift of the disorder and interim times the results do not change. The disorder has been re-labeled accordingly in the text and the figures. The overall implications of slow charge pair separation at large disorder and low permittivity as well as the conclusions drawn do not change. See also [235].

by the permittivity ε_r. Eventually, after further successful separation, the charge pair can reach the Coulomb radius r_c at t_{sep}. We define the time between separation and disorder time as the interim time $t_{int} = t_{sep} - t_{dis}$. During t_{int}, charge separation is an interplay between Coulomb attraction and the influence on energetic disorder, with energetic disorder dominating however. When $d(t)$ has surpassed r_c, the influence of Coulomb attraction is indistinguishable from thermal fluctuations and does not influence the pair anymore, it can be considered as separated. We define the lifetime t_{life} of a pair as the time after which the first of the two geminate partners has been removed from the cell, either by collection at a contact or by recombination with a different charge (non-geminate recombination). The time between the lifetime and the separation time is classified as transport time $t_{trans} = t_{life} - t_{sep}$. By definition and for the investigated parameters, these times always occur in the order as discussed: $0 \rightarrow t_{dis} \rightarrow t_{sep} \rightarrow t_{life}$.

We analyze $d(t)$ for all charge pairs generated by exciton separation under standard operation of the solar cell in a steady state, which corresponds to a minimum of 11 000 pairs for each parameter set. We neglect very long living pairs, i.e. the largest 5 % lifetimes are removed from the evaluation. Those charges are found to be stuck in local minima of the disorder. Ultimately, a charge pair can evolve in the following scenarios:

(1) both charges of a pair are collected;

(2) one charge is collected, the other recombines non-geminately;

(3) both charges recombine non-geminately;

(4) the pair recombines geminately.

Furthermore, (1)-(3) can occur before or after charge separation, while in (4) the pair never manages to separate. We focus our analysis on (1) and (4). Therefore, the collection of charge pair distances is split into two datasets:

(i) one set for charge pairs that manage to separate definitively, where both charges are collected at the contacts and contribute to the photocurrent and

(ii) the complementary dataset with the charges pairs that do not manage to separate and therefore eventually recombine geminately.

The former dataset (i) is used to evaluate the separation dynamics (Section 7.3.1) and the charge carrier mobility (Section 7.3.3), while the latter (ii) is used to study geminate recombination (Section 7.3.4). The remaining charge pairs, where at least one partner recombines non-geminately, are not considered in the evaluation because a common basis needs to be established in order to achieve a meaningful comparison.

The processing steps applied to the dataset (i) are illustrated in Figure 7.2 for $\varepsilon_r = 3.5$, $\sigma = 0\,\mathrm{meV}$ (1, left column) as well as $\sigma = 100\,\mathrm{meV}$ (2, right column) at $a_{ehr} = 10^5\,\mathrm{s}^{-1}$. Figure 7.2a depicts the typical evolution of the pair distance in time including the definitions for disorder-, separation-, and lifetime. Figure 7.2b shows the distribution those times for a total of 9247 (0 meV) or 4980 (100 meV) resp. (collected) charge pairs. It can be seen that they follow different distributions which is a result of the various

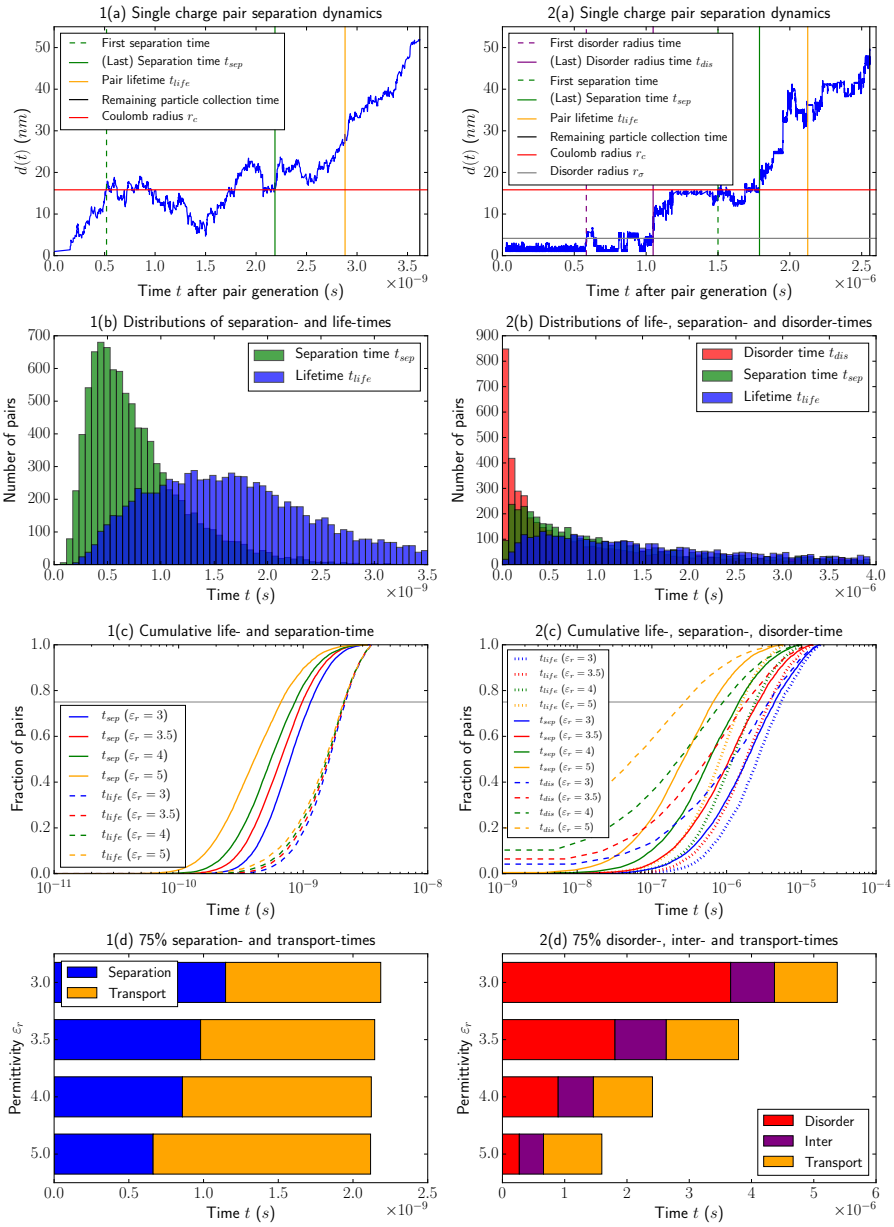

Figure 7.2. – Illustration of the evaluation steps of charge pair separation dynamics for $\sigma = 0\,\text{meV}$ (1, left column) and $\sigma = 100\,\text{meV}$ (2, right column) at $\varepsilon_r = 3.5$. (a) Typical evolution of $d(t)$ for a charge pair. The threshold radii r_c (red, horizontal), r_σ (gray, horizontal) and the corresponding times t_{sep} (purple, vertical), t_{dis} (green, vertical) as well as the pair lifetime (orange, vertical) are indicated. (b) Distributions of t_{dis}, t_{sep}, and t_{life} of all pairs in this dataset. (c) Cumulative distributions of (b) with 75 % threshold (horizontal line). (d) Threshold values from (c) in comparison for different permittivities, including the interim- (between disorder and separation) and the transport (between separation and lifetime) times.

influences on different length scales. In order to quantify and compare these times we investigate the cumulative distributions with respect to the time after pair origin, which are shown in Figure 7.2c for different permittivities. The plot shows the fraction of pairs having reached r_σ, r_c and their lifetime after time t after their origin. Thus, the fraction of pairs ranges from 0 being no charges having reached the respective time to 1 meaning all charge pairs have reached those times. With the 75 % threshold we define the 75 %-times $t_{dis}^{75\,\%}$, $t_{sep}^{75\,\%}$ and $t_{life}^{75\,\%}$, at which time three quarters of all charge pairs have reached said condition. Systematically, $t_{int}^{75\,\%} = t_{sep}^{75\,\%} - t_{dis}^{75\,\%}$ and $t_{trans}^{75\,\%} = t_{life}^{75\,\%} - t_{sep}^{75\,\%}$ are defined. An overview of all 75 % times defined for this dataset is shown in Figure 7.2d extracted from Figure 7.2c for several permittivities. This evaluation allows to quantify and compare the complex distribution of charge pair separation times. In the following results, only the 75 % threshold times will be compared.

The evaluation of the recombination distribution (ii) is performed in the same manner as for the collected charge pairs to obtain a recombination time $t_{gr}^{75\,\%}$, after which 75 % of charges in the recombination dataset have recombined geminately.

7.3. Results and discussion

At first, we analyze the interplay of energetic disorder and permittivity on the charge pair timelines and charge mobilities. For this analysis the charge recombination rate was fixed at $a_{ehr} = 10^5\,\mathrm{s}^{-1}$, sufficiently low to have a large number of charges separating in order to have a good statistics. We then fix the energetic disorder to 100 meV, an upper limit for the value observed in well-studied systems such as P3HT:PCBM, and study the effect of recombination rate, by varying a_{ehr} by several orders of magnitude ($a_{ehr} = 10^4\,\mathrm{s}^{-1} - 10^7\,\mathrm{s}^{-1}$), in combination with the permittivity on geminate recombination times. Charge pair separation and mobility studies are based on the same dataset (i) (all particles collected), while the recombination study is based on a different dataset (ii) (only geminate recombination, i.e. all charges that did neither surpass r_σ nor r_c). All times presented and compared here are the 75 % times defined in the previous section.

7.3.1. Charge pair separation dynamics: absolute times

The absolute times are presented in Figure 7.3 for combinations of $\sigma = 0\,\mathrm{meV} - 100\,\mathrm{meV}$ and $\varepsilon_r = 3 - 5$, with an illustration of the characteristic timeline. Note that no disorder and interim times are shown for t_{dis} and t_{int} because the disorder radius is not defined for $\sigma = 0\,\mathrm{meV}$ after Equation (7.3).

A first observation is that all times can vary over a large range from below ns to above µs and are strongly dependent on the energetic disorder, whereas a considerable dependence on the permittivity exists for the disorder-, separation-, and lifetime at large σ. During the disorder time $\Delta E^C > \Delta E^\sigma$, therefore the influence of Coulomb attraction dominates over disorder. At a small disorder of 40 meV, r_{dis} is reached very fast with a disorder time of the order of ns. Changing the permittivity from 3 to 5 leads to a

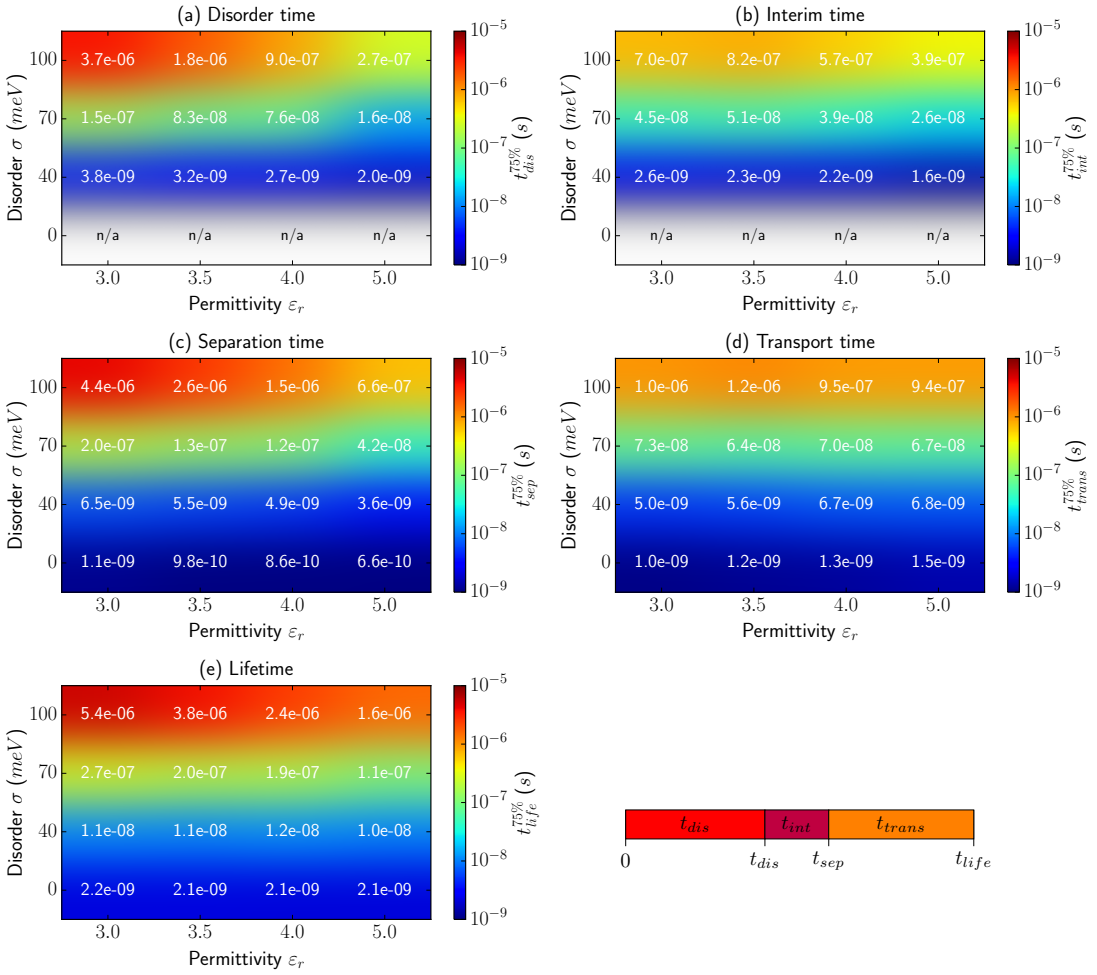

Figure 7.3. – Absolute values for characteristic times: Absolute values for characteristic times: (a) disorder-, (b) interim-, (c) separation-, (d) transport-, and (e) lifetime in dependence on disorder and permittivity. At $\sigma = 0\,\text{meV}$, the disorder- and interim time are not defined. The timeline of a charge pair with the characteristic times is schematically illustrated on the bottom right.

2-fold decrease of disorder time. Here, the overall charge motion is not strongly affected by the disorder because the disorder is roughly in the range of the thermal fluctuations. Separation can therefore occur relatively fast and the effect of Coulomb attraction is low. At $\sigma = 100\,\text{meV}$ however, charge motion is more strongly affected by the local energetic fluctuations which renders the effective charge motion to be slower. This makes the effect of mutual attraction more pronounced: reaching t_{dis} takes $3.7 \times 10^{-6}\,\text{s}$ at $\varepsilon_r = 3$ and decreases by roughly one order of magnitude to $2.7 \times 10^{-7}\,\text{s}$ at $\varepsilon_r = 5$. The disorder time is the most decisive point in time when it comes to the question whether a charge pair

manages to successfully separate, and hence leading to collection, or whether it will never overcome the disorder radius in which case it will most likely recombine geminately. t_{dis} is the upper limit in time that needs to be compared to a competing recombination time, since t_{dis} is the time during which the geminate charges are nearby and have the change of recombining. A ten-fold increase in t_{dis}, as observed for a change in permittivity from 3 to 5, should therefore have considerable influence on suppressing geminate charge pair recombination. The absolute times will be linked in the recombination section.

After the disorder time, t_{int} marks the interplay between disorder and Coulomb attraction until full charge separation occurs. However, already at this stage, the effect of permittivity is small: between $\varepsilon_r = 3$ and $\varepsilon_r = 5$, the interim time less than halves for all values of disorder, but the strong influence of disorder remains. The combination of disorder time and interim time constitute the separation time. Since t_{int} is almost independent of the permittivity, it is mostly a constant offset on top of t_{dis} and t_{sep} is mainly made up by the behavior of t_{dis}. This is reflected in the distribution of t_{sep}: for no disorder, t_{sep} is very small with values between $6.6 \times 10^{-10}\,\mathrm{s} - 1.1 \times 10^{-9}\,\mathrm{s}$ when ε_r is reduced from 5 to 3. The separation time, just like the disorder time, increases by orders of magnitude with increasing disorder due to worsened charge transport. At $\sigma = 100\,\mathrm{meV}$, the effect of Coulomb interaction is evident also for t_{sep}, and separation time varies between $6.6 \times 10^{-7}\,\mathrm{s} - 4.4 \times 10^{-6}\,\mathrm{s}$.

After t_{sep}, the strength of mutual Coulomb interaction is not distinguishable from thermal fluctuations. Therefore the transport time t_{trans} is independent of permittivity and solely determined by the energetic disorder. It changes by three orders of magnitude from $10^{-9}\,\mathrm{s}$ at $\sigma = 0\,\mathrm{meV}$ to $10^{-6}\,\mathrm{s}$ at $\sigma = 100\,\mathrm{meV}$, with almost no influence of ε_r. During this stage of the separation process, the charges act as if they are transported through a disordered semiconductor alone. The transport time will be related to the charge mobility in Section 7.3.3.

The overall lifetime as the sum of disorder-, interim-, and transport time therefore follows a similar behavior as the disorder time. Charge pairs live about 2 ns without disorder and independently of the influence of ε_r, and the lifetime gradually increases with σ to the µs regime at 100 meV, with a moderate dependence on permittivity. While the overall lifetime of charges is not particularly relevant for the overall separation process, slower charge lifetimes lead to higher overall charge densities in the solar cell and might affect non-geminate recombination which is not discussed here.

The influence of the disorder therefore affects the separation process over the entire lifetime, In contrast, the influence of permittivity drops with larger separation distance and is most relevant on smaller distances up to the Coulomb radius and irrelevant afterwards. This insight into the absolute times allows is particularly interesting to compare the separation process to opposing processes such as recombination.

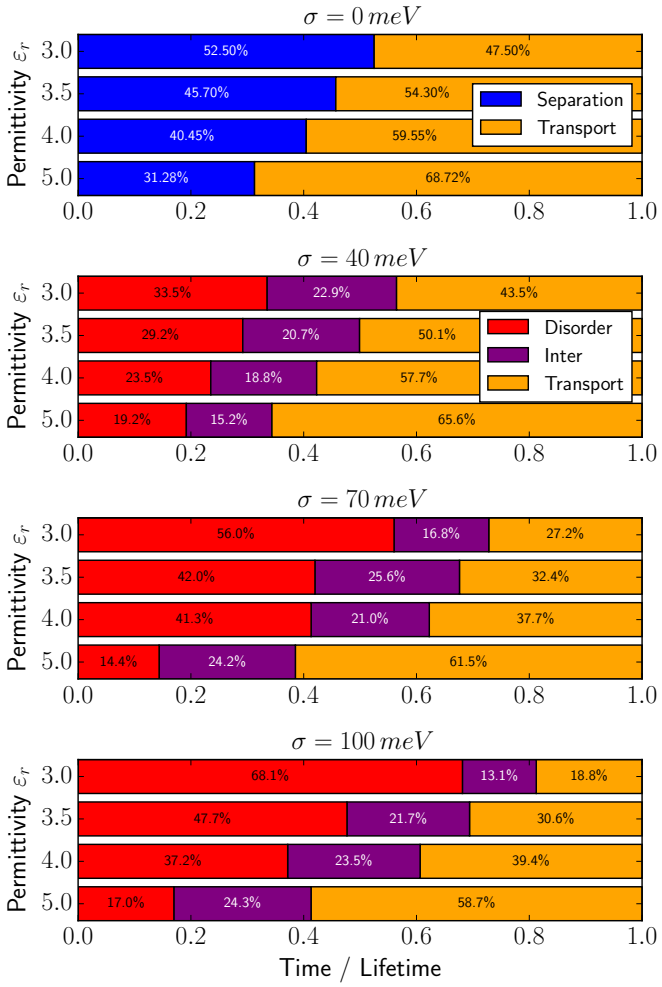

Figure 7.4. – Relative values for characteristic times normalized to the respective lifetime for the investigated values of disorder and permittivity. For no disorder (top), the disorder time is not defined, therefore only separation (blue) and transport times (orange) are shown. For finite disorders, the first bar represents the disorder time (red), the middle bar is the interim time (purple) and the last bar the transport time (orange). The ratio of each time with respect to the lifetime is indicated in the bars in percent.

7.3.2. Charge pair separation dynamics: relative times

In order to get a better understanding of the relative interplay between disorder-, separation- and transport time independently of their absolute lifetime, Figure 7.4 shows the characteristic times (t_{dis}, t_{sep}, t_{int}, t_{trans}) normalized to their respective lifetime t_{life}. For all cases of disorder, the permittivity has a considerable influence on the relative times. At $\sigma = 0\,\mathrm{meV}$, t_{sep} reduces from approximately half of the lifetime to around one

third when increasing epsilon from 3 to 5. For a finite disorder, a similar trend can be observed for t_{sep}. Here, t_{sep} consists of the contributions of t_{dis} and t_{int}; the relative interim time is not strongly affected by permittivity at lower disorders, but the influence increases with σ. The effect of the permittivity occurs as a shift between disorder- and transport-time.

At $\sigma = 100\,\mathrm{meV}$ and for a permittivity of $\varepsilon_r = 3$, the charge pairs spend 68.1 % of their lifetime just to overcome the disorder radius of $r_{dis} = 4.8\,\mathrm{nm}$. It takes 13.1 % of the lifetime more to reach the Coulomb radius $r_c = 18.5\,\mathrm{nm}$ after which they are considered to be free of mutual influence. During a remaining 18.8 % of the lifetime electron and hole are transported though the disordered landscape to the contacts. Increasing the permittivity only to 5, the distribution changes drastically: the disorder radius is reached after around 17.0 % of the overall lifetime, and another 24.3 % are required to overcome the Coulomb radius, which is $r_c = 11.1\,\mathrm{nm}$ at this permittivity. The last 58.7 % of lifetime is spent on transport in this case. This highlights how already a small increase in permittivity can drastically improve the charge separation efficiency.

7.3.3. Relation of transport to mobility

Based on Equation (4.32) we evaluate the mobility for all collected electrons and holes, individually, and calculate the average mobilities as the arithmetic means over the entire dataset for the investigated parameter sets. Figure 7.5 shows the obtained electron (solid lines) and hole (dashed lines) mobilities. The mobility is found to be strongly dependent on the energetic disorder: the electron mobility decreases by around three orders of magnitude from $\mu_e^{0\,\mathrm{meV}} = 1.6 \times 10^{-2}\,\mathrm{cm^2\,V^{-1}\,s^{-1}}$ to $\mu_e^{100\,\mathrm{meV}} = 1.3 \times 10^{-5}\,\mathrm{cm^2\,V^{-1}\,s^{-1}}$ (at $\varepsilon_r = 3$) and $\mu_e^{100\,\mathrm{meV}} = 3.5 \times 10^{-5}\,\mathrm{cm^2\,V^{-1}\,s^{-1}}$ (at $\varepsilon_r = 5$); similarly, the hole mobility decreases from $\mu_h^{0\,\mathrm{meV}} = 3.2 \times 10^{-3}\,\mathrm{cm^2\,V^{-1}\,s^{-1}}$ to $\mu_h^{100\,\mathrm{meV}} = 5.2 \times 10^{-6}\,\mathrm{cm^2\,V^{-1}\,s^{-1}}$ (at $\varepsilon_r = 3$) and $\mu_h^{100\,\mathrm{meV}} = 8.5 \times 10^{-6}\,\mathrm{cm^2\,V^{-1}\,s^{-1}}$ (at $\varepsilon_r = 5$). A large disorder leads to a highly inhomogeneous energy landscape that charges move in. They repeatedly get stuck in local minima of the disorder which slows them down and decreases the mobility. The permittivity and hence the strength of the Coulomb attraction shows an influence only at large disorder, at low disorder no influence of ε_r on μ can be observed. This is because the disorder is present over the entire charge lifetime, while the Coulomb attraction influences charge mobility considerably in the first t_{dis} after generation as was shown previously. A slow separation gives the charges more time to re-approach each other and explains the slight increase in mobility with permittivity as the effect of Coulomb interaction decreases with ε_r.

The definition of charge mobilities $\mu = v/F$ considers the velocity v of a charge only under the influence of an applied electric field F and no other confounding quantities. During the charge separation process, especially during $t < t_{dis}$, charges are affected by the mutual attraction – thus lowering the average velocity with respect to the electric field. Once charges are free of mutual interaction, i.e. after t_{sep}, the remaining time until their final collection, t_{trans}, must correlate to the charge velocity unaffected by

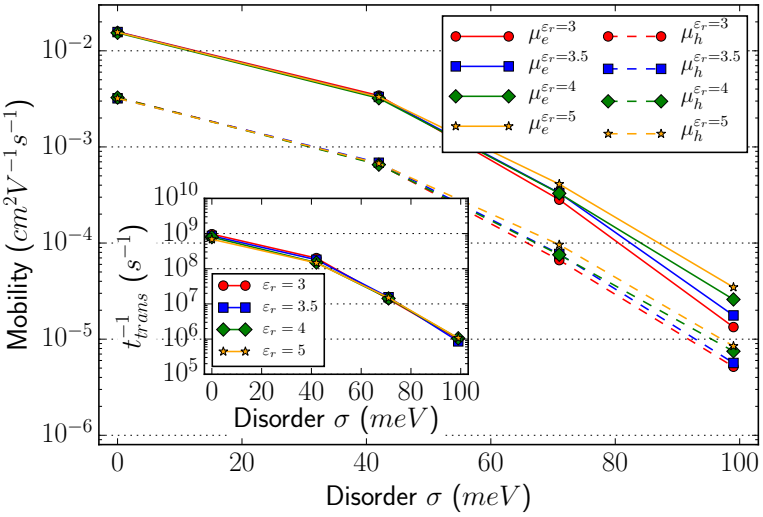

Figure 7.5. – Electron (solid lines) and hole (dashed lines) mobilities vs. energetic disorder for different permittivities. The inset shows the inverse transport time of the charge pair statistics for the same parameters.

charge pair interaction, while the mobility evaluation from above includes the dynamics of the separation process. Comparing these allows to investigate the differences between transport and separation. The inset in Figure 7.5 shows the inverse transport time t_{trans}^{-1}. The trend closely resembles that of charge mobilities, i.e. the decrease with disorder by the same orders of magnitude, but no influence of the permittivity can be seen. The difference observed at large disorder, where μ increases with ε_r is attributed to the fact that the evaluation of the mobility includes the separation process and the slower separation at lower ε_r. We can therefore conclude that the effective mobility of charges is slightly affected by the permittivity, while after separation charge transport is independent of permittivity.

7.3.4. Relation of separation to geminate recombination

At the end of their lifetime, charge pairs that do not manage to separate will recombine geminately. Charge separation times and mobilities are obtained from the dataset with all charges fully separating, i.e. not recombining. We will now compare only recombining charges, which have never managed to overcome the disorder radius. The amount of recombination of charges from a pair (geminate) and the absolute times after which they recombine are evaluated with respect to the permittivity and the charge pair recombination rate at fixed values for disorder of 100 meV. We only evaluate pure geminate recombination here as we are focusing on the explicit separation of a pair.

Figure 7.6 shows the recombination time $t_{gr}^{75\,\%}$ after which three quarters of all charges in this set have recombined in dependence of ε_r and a_{ehr}. The recombination time $t_{gr}^{75\,\%}$

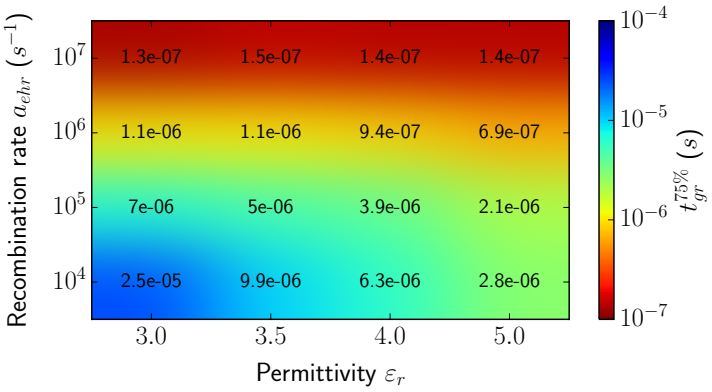

Figure 7.6. – Effective geminate recombination time $t_{gr}^{75\,\%}$ for combinations of permittivity and recombination rate.

is, at large recombination rates $10^7\,\mathrm{s}^{-1}$, found to be independent of permittivity with a recombination time of $\approx 1.4 \times 10^{-7}\,\mathrm{s}$. The lower the recombination rates, the more does the permittivity affect $t_{rec}^{75\,\%}$. In order to explain this behavior one must compare the average time charges need to separate, which we classify by t_{dis}, and the average time for geminate recombination of a CP, the inverse recombination rate a_{ehr}^{-1}. It needs to be noted that the evaluation of the disorder time is based on the charge set in which all charges have managed to separate, while the recombination times are based on the CP set in which no CP has managed to separate. Therefore the comparison between disorder time and recombination time represents an estimation and is aimed to reveal tendencies.

Previously we extracted $t_{dis} \approx 3.7 \times 10^{-6}\,\mathrm{s} - 2.7 \times 10^{-7}\,\mathrm{s}$ for a disorder of $\sigma = 100\,\mathrm{meV}$ and for ε_r varying from 3 to 5. At large $a_{ehr} = 10^{-7}\,\mathrm{s}$, we therefore have $t_{dis} \gtrsim a_{ehr}^{-1} = 10^{-7}\,\mathrm{s}$. The time needed for charges to overcome the disorder radius is larger than a_{ehr}^{-1}. The charges remain longer nearby each other than the average time after which CP recombination occurs, i.e. recombination occurs faster than separation. In this case, charge recombination is controlled by the recombination rate itself, meaning $t_{gr} \approx a_{ehr}^{-1}$. This is reflected in the results for t_{gr} in Figure 7.6: the actual recombination time $t_{gr} \approx 1.4 \times 10^{-7}\,\mathrm{s}$ is just slightly slower than $a_{ehr}^{-1} = 10^{-7}\,\mathrm{s}$. The recombination time also independent of ε_r, because for all permittivities slower disorder times that the inverse recombination rate ($t_{dis} > a_{ehr}^{-1}$) are observed.

As we lower the recombination rate to $a_{ehr} = 10^4\,\mathrm{s}^{-1}$, now t_{dis} is faster than the inverse recombination rate, i.e. $t_{dis} < a_{ehr}^{-1} = 10^{-4}\,\mathrm{s}$. This means that CP separation is faster than the geminate recombination rate acts. In contrast to large a_{ehr}, where slow separation gives enough time for the nearby charges to recombine, the recombination time is now not purely controlled by the recombination rate itself but it depends on the separation time, which in turn is controlled by the permittivity. The difference between $\varepsilon_r = 3 - 5$ leads to t_{gr} decreasing by roughly one order of magnitude from $2.5 \times 10^{-5}\,\mathrm{s}$ to $2.8 \times 10^{-6}\,\mathrm{s}$. The faster CP separation occurs (at larger permittivity), the less time

remains for recombination to occur and those charges which do recombine, must do so faster than the CP separates. On the contrary, the slower CP separation occurs (at smaller permittivity), the more time the CP has to recombine before separation occurs, This means the longer the disorder time is, the closer t_{gr} is to a_{ehr}^{-1}. In this scenario: for small permittivities the recombination time (2.5×10^{-5} s) is closer to the inverse recombination rate (10^{-4} s) than for larger permittivities ($t_{gr} = 2.8 \times 10^{-6}$ s) with $a_{ehr}^{-1} = 10^{-7}$ s.

The results lead to the following picture about geminate recombination: the recombination times are either recombination rate controlled (insufficient separation with respect to recombination) in the case of large (with respect to separation/disorder time) recombination rates or permittivity controlled (separation controlled by ε_r) in the case of slow recombination rates.

7.4. Conclusion

The kMC method is a suitable tool to access the time-dependent separation process of electron-hole pairs in spatially and energetically disordered BHJs during operation. Using a 3D kMC simulation model of a BHJ solar cell we investigated the charge pair separation dynamics under the influence of energetic disorder and in particular the mutual Coulomb interaction of the electron-hole pair, controlled by the permittivity, as well as the geminate recombination rate of the bound electron-hole pair. Both separation- and recombination times were extracted over a large set of exciton-generated charge pairs.

We find that the energetic disorder strongly affects the charge separation dynamics over their entire lifetime, while the Coulomb interaction dominates on local scales and during the initial time of separation. The (disorder) radius after which the disorder is larger than the Coulomb attraction is found to be a more meaningful definition to classify charge separation in organic materials than the Coulomb radius. Once charges are separated by more than the disorder radius, the influence of Coulomb attraction does not considerably affect transport anymore. The amount of geminate recombination is a results of a combination between large recombination rate and low permittivity (i.e. low disorder/separation times); however, for realistic values of energetic disorder, even small increases in permittivity can suppress orders of magnitude of geminate recombination. Hence, improving the permittivity provides a pathway to suppress charge pair recombination.

In conclusion, the recent pathway of utilizing high-ε_r organic materials for more effective charge separation is strongly supported by our results. Additionally, low-disorder materials are highly beneficial for a fast charge separation. Both routes should be pursued in order to support efficient charge separation in BHJ OSCs.

8. The Origin of Photocurrent in Fullerene-Based Solar Cells

Fullerene-based organic solar cells with only a minute amount of donor show a substantial photocurrent while maintaining a large open-circuit voltage. At low concentrations the donor is fully dispersed within the fullerene and no percolation pathways of holes towards the anode exist; this morphology is in contrast to BHJ donor:acceptor blends where percolative pathways for both electrons and holes are present within their respective transport phases. Therefore, the question arises how holes contribute to the photocurrent. Here we demonstrate that the photocurrent is readily explained by photo-generated holes transferring back to the fullerene matrix due to Coulomb repulsion and the fullerene acting as an ambipolar conductor for both electrons and holes. The two critical parameters controlling this process are the values of the HOMO level difference between the donor and the acceptor and of the recombination strength, both are found to agree between experimental measurements and kinetic Monte Carlo simulations. We provide evidence that the HOMO level difference between donor and acceptor is smaller in a dilute donor configuration. Successive percolation pathways towards the contacts – the reason for introducing the BHJ configuration – are not an absolute requirement to obtain substantial photocurrents in OSCs.

The content of this chapter is adapted with permission from T. Albes, L. Xu, J. Wang, J. W. P. Hsu, and A. Gagliardi, "Origin of Photocurrent in Fullerene-Based Solar Cells", *The Journal of Physical Chemistry C*, vol. 122, no. 27, pp. 15 140–15 148, 2018.

8.1. Background

The ratio by which a solar cell can convert an incident radiative power P_γ to electrical power defines the PCE, $\eta = j_{sc} \cdot A_c \cdot U_{oc} \cdot FF \,/\, P_\gamma$, which increases with the short-circuit current density j_{sc}, the open-circuit voltage U_{oc} and the fill factor FF of the cell with surface area A_c. Enhancing these device parameters by e.g. proper material choice [9] or morphology control [71], [236] has led to a steady increase of PCEs in OSCs. The highest efficiency OSC devices currently are based on a BHJ [75], comprised of a donor:acceptor blend, with PCEs surpassing 13 % [16]. In BHJs, material choice and blend morphology influence both j_{sc} and U_{oc}. Donors with lower bandgap allow to utilize a larger part of the solar spectrum and hence increase the j_{sc}, but at the same time reduce the difference in quasi-Fermi levels of electrons and holes, and therefore limit U_{oc}. This is why in BHJs j_{sc} and U_{oc} often behave inversely proportional to changes in donor bandgap, and tuning them for optimum performance presents an intrinsic tradeoff [237]–[239].

Recently, an emerging OSC system has gained attention that seems to circumvent the tradeoff between j_{sc} and U_{oc}. Fullerene-based OSCs, also called dilute-donor OSCs [240], contain only a small amount of donor material embedded in the fullerene matrix and show substantial j_{sc} while maintaining a high U_{oc}, with the highest reported PCE already reaching 8.1 % [241]. The high U_{oc} in these systems is assumed to be a result of a Schottky barrier forming at the fullerene/anode contact [242] or a reduction in recombination of free charge carriers [243]. Large U_{oc} were first observed in pure C_{60} devices [244] and shortly afterwards the introduction of even small donor amounts showed a striking increase in j_{sc} [240]. The observation of a substantial short-circuit current in dilute donor systems is not restricted to a single material system: a multifold increase of j_{sc} can be observed in devices based on a variety of fullerene-based acceptors, such as phenyl-C61-butyric acid methyl ester ($PC_{61}BM$) and phenyl-C71-butyric acid methyl ester ($PC_{71}BM$), with donor materials as used in well-studied in BHJ OSCs, such as the polymers P3HT, Tetraphenyldibenzoperiflanthene (DBP) or 1,1-bis-(4-bis(4-methyl-phenyl)-amino-phenyl)-cyclohexane (TAPC) [76]–[78], [240]; see Figure 8.1. For a pure fullerene-based device without donor material, the PCE, especially the j_{sc}, is low. Adding minute amounts of donor (a few wt.%) results in an increase in j_{sc} and can substantially improve the device performance. The observed behavior holds true as long as the amount of donor is small enough; above a certain donor concentration U_{oc} drops, and the device behaves increasingly like a standard BHJ. Further studies on the influences on U_{oc} [243], j_{sc} [77] and stability [245] were recently performed in order to gain a better understanding of the working principle of dilute-donor cells.

Despite good performances, the detailed origin of photocurrent in fullerene-based solar cells still lacks understanding: how do holes transport to the anode when donor molecules are unlikely to form a percolative pathway at low concentrations? The general working principle of OSCs consists of the key steps absorption, exciton splitting at a donor/acceptor heterojunction and transport of charges towards the contacts. In BHJs, the percolative donor domains provide transport paths for photo-generated holes and

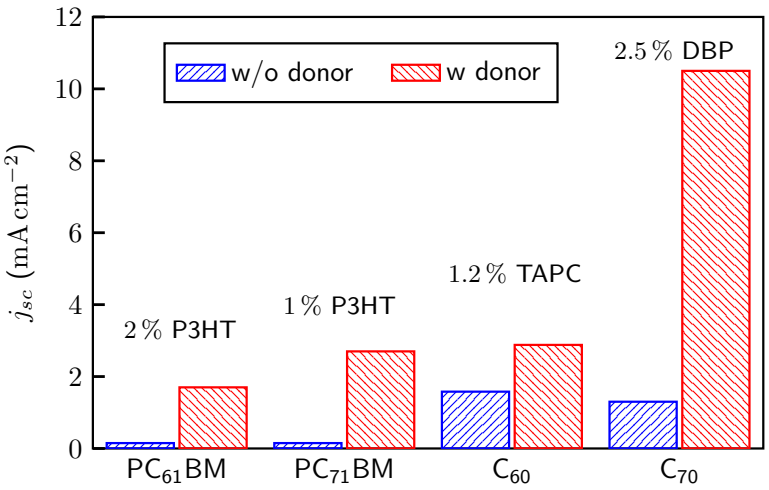

Figure 8.1. – Comparison of increased short-circuit current in different fullerene-based OSC systems with very low donor concentration. Donor materials: P3HT, TAPC, DBP. Data from [76]–[78], [240].

the acceptor domains for electrons. Percolation pathways within the respective material phases towards the contacts lead to the photocurrent (Figure 8.2a). In fullerene-based OSCs with only minute amounts of donor, light absorption mainly takes place in the fullerene. This is evident from absorption spectra of fullerene-based OSCs, where the absorption spectra of cells with donor concentrations below 30 wt.% are similar to that of pure $PC_{71}BM$ [36]. The typical vibronic features of P3HT are missing in the absorption spectra which is an indication for a fully disperse arrangement of the P3HT chains in the fullerene matrix. If agglomerates of P3HT were formed, it would likely crystallize which would show absorption peaks in the spectra. We therefore assume that the polymer chains are most likely fully dispersed within the fullerene matrix.

After light absorption, the generated excitons need to dissociate to obtain free charges. A field-assisted mechanism to split excitons within the fullerene has been discussed but was concluded to not be sufficient for efficient charge separation in fullerene-based solar cells [242]. In an experimental study [77], charge photo-generation is shown to arise from exciton diffusion to donor/acceptor interfaces; similarly to BHJs, the offset of HOMO levels between donor and acceptor then induces the transfer of holes from fullerene to donor and vice versa for electrons.

Due to the low concentration of only a few wt.% and the dispersion in the fullerene, the donor polymer chains are likely to be entirely enclosed by fullerenes, i.e. without percolation pathways to the anode (Figure 8.2b). During exciton separation, holes are transferred from the fullerene to the donor. The donor regions enclosed within the fullerene phase act as confining regions for holes (Figure 8.2c) because the HOMO energy level of the donor E^D_{HOMO} lies shallower than the HOMO energy level of the acceptor

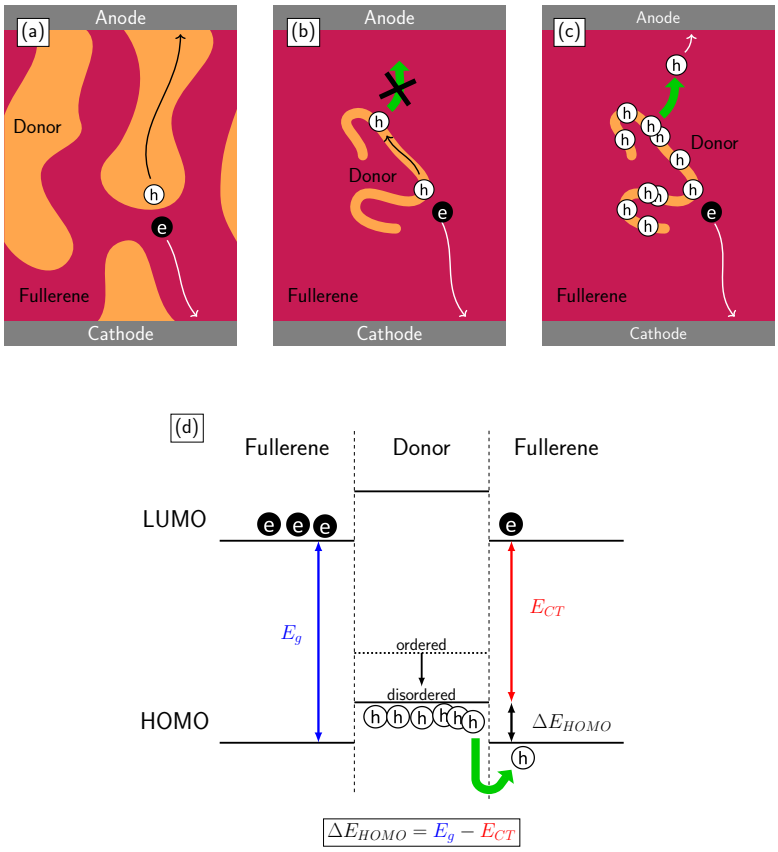

Figure 8.2. – Scheme of BHJ (a) vs. dilute donor device configuration (b). In BHJs, the donor acts as hole conductor and the acceptor as electron conductor. In dilute donor systems, pathways for holes towards the contact may not be available and holes can accumulate on the polymer chains. The hole-escape effect is illustrated in (c) and the corresponding energetics are shown in (d).

E^A_{HOMO}. We hypothesize that holes must transfer back to the fullerene matrix in order to extract a photocurrent and both electron and hole transport must occur in the fullerene material. Hence, holes need to surmount the HOMO level offset

$$\Delta E_{HOMO} = \left| E^D_{HOMO} - E^A_{HOMO} \right| \tag{8.1}$$

as depicted in Figure 8.2d in order to leave the donor regions and contribute to the experimentally observed photocurrent. The origin of how holes can gain the required escape-energy to be transferred back to the fullerene phase is examined here.

It has recently been stated that percolation pathways within the donor are not necessarily a requirement in order to obtain a photo-current in donor/acceptor systems by Melianas et al. [246]. They show that for dilutions of less than 4 wt.%-7 wt.% no continuous pathways exist within the donor and that the donor forms a fully discontinuous

network, further supporting the assumption of a fully disperse morphology. For such concentrations they propose a hole transport mechanism by long-range tunneling between donor molecules, where the average tunneling distance is up to 4 nm. For donor concentrations below 4 wt.% however, in particular at 1 wt.% and below, tunneling between donors was shown to be hindered. An additional mechanism of tunneling from the donor into the acceptor is not shown for donor concentrations of 1 wt.% and below. Furthermore, a substantial photo-current is observable even in systems with donor concentrations as low as 0.1 wt.% [36]. In such cases, a different mechanism must be responsible for hole transport.

In this joint experimental and numerical study, we propose an alternative mechanism for the origin of hole current at very low donor concentrations that relies on hole-escape from the isolated polymer chains into the fullerene material due to a lowering of the HOMO energy barrier between donor and acceptor supported by Coulomb repulsion of holes confined on the donor. We show that charge transport of holes towards the contacts takes place in the fullerene instead of in the donor as it is the working principle in BHJs. Using kMC simulations we show that a hole back-transfer is enabled by the combination of (a) a reduction of ΔE_{HOMO} between donor and fullerene and (b) the Coulomb repulsion energy arising due to accumulation of holes in the donor domains (Figure 8.2 c-d). By varying ΔE_{HOMO} and the electron-hole pair recombination rates, we study the hole-escape current as well as the charge density distribution and the recombination current in a dilute-donor OSC system. Realistic values for ΔE_{HOMO} and the recombination current for a dilute-donor cell comprised of $PC_{71}BM$ with minute amounts of P3HT are extracted by External Quantum Efficiency (EQE) measurements and IS analysis, respectively. The experimental results are compared to the simulation results and act as showcase to illustrate how the presented model explains photocurrent generation in fullerene-based solar cells.

8.2. Methods

8.2.1. Model specifics

In order to test if and under which conditions it is possible for holes to undergo a back-transfer from donor regions to the fullerene phase and reach the anode, we set up a kMC model of a fullerene-based solar cell with a low donor concentration. Our model system is a slab of fullerene molecules ($PC_{71}BM$) with volume $V = 50 \times 50 \times 50\,\mathrm{nm}^3 = 1.25 \times 10^{-16}\,\mathrm{cm}^3$ in between two contacts. Embedded into the fullerene matrix, we distribute the donor material (P3HT) in form of 64 polymer chains with fixed length of $L = 33\,\mathrm{nm}$ each. The polymers are generated by a SAW described in Section 4.2.2. The algorithms is executed until 100 successful kinks have been performed. Furthermore, distinct chains do not touch each other in order to represent the discontinuous polymer chain network. Each polymer chain spreads along 33 sites with volume $1\,\mathrm{nm}^3$, i.e. each polymer occupies a volume of $33\,\mathrm{nm}^3$. The total polymer volume is therefore

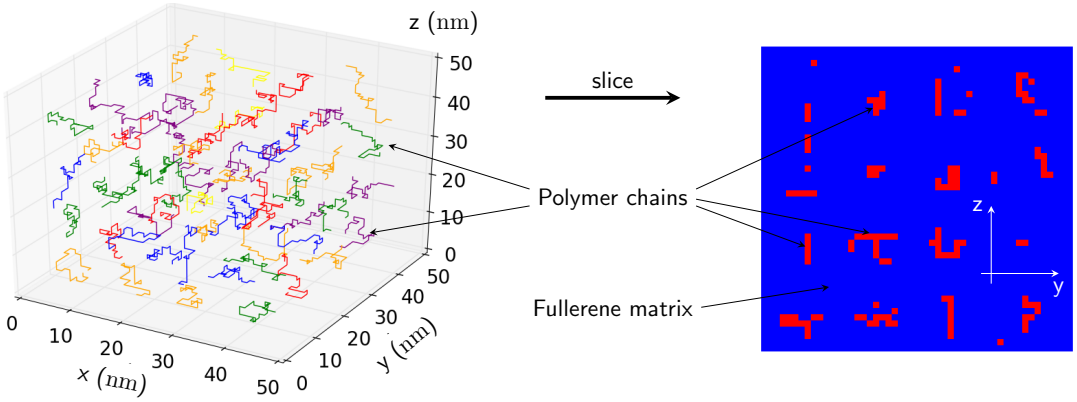

Figure 8.3. – Polymer chain distribution in the kMC model (left). A slice through the morphology (right) is used to illustrate the charge density distributions and the potential distribution on the polymer chains.

$64 \times 33\,\mathrm{nm}^3 = 2112\,\mathrm{nm}^3$. In relation to the volume of the simulation box this leads to a polymer content of $2112\,\mathrm{nm}^3/50\,\mathrm{nm}^3 = 1.69\,\mathrm{vol.\%}$. Considering the molecular weight of P3HT and $PC_{71}BM$, this corresponds to 1.2 wt.% of donor in the active layer. The surface area of the polymer/fullerene heterojunction is $A_{hj} = 7898\,\mathrm{nm}^2$, which is used to calculate the escape- and recombination current density. An illustration of the distribution of polymers is shown in Figure 8.3. Although we do not know the exact shape of the donor polymer chains in experiments, we use the above mentioned results from the absorption spectra as justification for a fully disordered morphology. ΔE_{HOMO} can explicitly be tuned in the model by setting the value of E^D_{HOMO} while keeping the fullerene HOMO fixed. In P3HT:PCBM BHJs the HOMO is usually around $-5.2\,\mathrm{eV}$, yielding a HOMO level offset of 0.8 eV. For the fullerene-based simulations, the HOMO level offset is varied between 0.1 eV and 0.8 eV by varying the donor HOMO between $-5.2\,\mathrm{eV}$ and $-5.9\,\mathrm{eV}$ in 0.1 eV steps. No external potential is applied, i.e. the system is in short-circuit condition with only the contact work-function difference as the internal electric field. The energetic disorder is assumed as $\sigma = 30\,\mathrm{meV}$.

In order to quantify the amount of holes leaving the donor region, we store the net number of holes leaving the donor regions N_h (with charge $q = +e$) and, by dividing through the surface area A_{hj} of the heterojunction between donor regions and surrounding acceptor material as well as the simulation time t_{sim}, define the net hole-escape current density by

$$j^h_{esc} = \frac{q \cdot N_h}{A_{hj} \cdot t_{sim}} \tag{8.2}$$

The number of geminate and non-geminate recombination events, N_{gr} and N_{ngr} (as defined in Section 4.3.6), allows to explicitly calculate the recombination current density at the donor/acceptor interface. Once a charge pair is separated by more than the Coulomb radius the charges are considered free and it is unlikely for them to find their

geminate partner again. Hence in most cases, charge recombination after separation (i.e. recombination between free charges) is considered to be non-geminate. The timescale of geminate recombination is ranging from hundreds of picoseconds up to $\approx 100\,\mathrm{ns}$ [81], [131], [180]–[184]. In accordance to these measurements, we choose the value for a_{ehr} used in the kMC simulations to range between $10^7\,\mathrm{s}^{-1}$ and $10^{10}\,\mathrm{s}^{-1}$. We evaluate the non-geminate recombination current density

$$j_{rec}^{ngr} = \frac{q \cdot N_{ngr}}{A_{hj} \cdot t_{sim}}. \tag{8.3}$$

as well as the total recombination ratio η_{ehr} defined in Section 4.5. Similarly, we determine the volume recombination rate in the entire system, normalized to the volume of the simulation cell V, based on non-geminate recombination

$$R = \frac{N_{ngr}}{t_{sim} \cdot V}. \tag{8.4}$$

The quantities j_{esc}^{h} and R obtained from the kMC simulations will be compared with the corresponding experimentally obtained values in the last section. Apart from the j_{rec} and R we evaluate spatially resolved local charge densities for holes in the donor n_h and for electrons in the acceptor n_e as well as the local electric potential ϕ_C in short-circuit condition.

8.2.2. Experimental details

In order to determine whether the barrier between donor and acceptor material can be decreased in dilute donor systems and the assumption for the kMC model is justified, fullerene-based OSC with a low donor content of 1 wt.% in a $PC_{71}BM$ matrix were fabricated and characterized by Liang Xu and Julia W.P. Hsu from the Department of Materials Science and Engineering, University of Texas at Dallas, Texas, United States. The solar cells are comprised of a ITO/PEDOT:PSS/active layer/Ca/Al structure. Further details on the fabrication process and the experimental methods can be found in [36], [77].

8.3. Results and discussion

8.3.1. The origin of hole-escape

First, we illustrate the effect of different ΔE_{HOMO} on the distribution of electrons and holes as well as the local Coulomb potential throughout the active layer. Figure 8.4 depicts the results for a selection of three different values of ΔE_{HOMO}: (a) 0.8 eV, (b) 0.4 eV, and (c) 0.2 eV. A full set of densities and Coulomb potential distribution is shown in Figure A.2 and A.3. For this illustration the recombination rate was fixed at $a_{ehr} = 10^9\,\mathrm{s}^{-1}$.

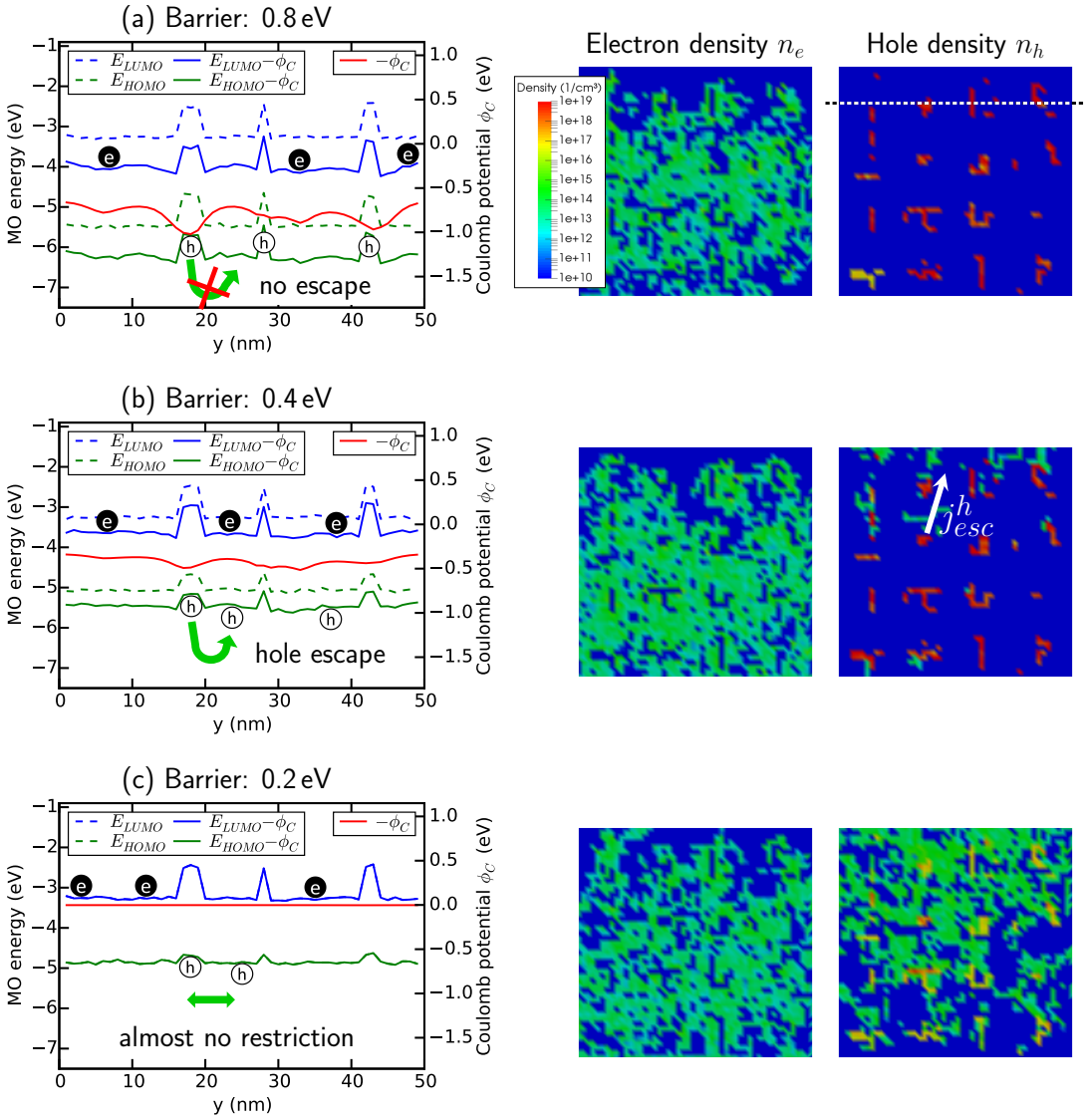

Figure 8.4. – MO energy distribution, electric potential and charge densities across isolated donor domains for HOMO level offsets of (a) 0.8 eV, (b) 0.4 eV, and (c) 0.2 eV. The left part shows the HOMO and LUMO energy distribution along a straight line though the donor region (line indicated on the right), without the influence of the electrostatic potential ϕ_C due to the accumulation (dashed lines) and including the potential (solid lines). The typical behavior of electrons and holes, in particular the trapping in and escape from the donor phase, is schematically visualized. The right panel shows electron and hole densities, where n_e is depicted on the left, and n_h on the right hand side, respectively.

For typical barriers between donor/acceptor HOMO levels as observed in BHJs of 0.8 eV [247]–[249] as shown in (a), holes stay confined to the isolated polymer chains and large hole densities up to $n_h \approx 10^{20}\,\mathrm{cm}^{-3}$ build up because there is no possibility for holes to leave the donor regions. As a result, ϕ_C within the confined region is positive and reaches values up to +1 eV locally, shifting E^D_{HOMO} downwards in energy and decreasing the effective barrier that holes need to surmount in order to perform a transition into the fullerene phase. However, the barrier is too high in order for hole-escape to occur. No finite hole density is observed in the fullerene phase. In contrast to holes, electrons do show percolation pathways within the fullerene matrix. The negatively charged particles move under the influence of the (positively) charged donor islands and the potential drop induced by the contact work functions. It can be observed that the electron density is distributed more or less evenly within the fullerene phase, i.e. the electrons can move from chain to chain and to the contacts and are not confined. However, in the steady state only a negligible short-circuit current is obtained because there is no flow of holes towards the contacts which prevents the solar cell from working. The strongly positively charged donor regions act as recombination centers for the electrons and all generated electrons recombine with holes confined on donor regions. Recombination can take place either with holes from the polymer chain on which the exciton was separated or with a hole from another chain.

Upon lowering the barrier to 0.4 eV as shown in (b), a similarly high n_h builds up within the donor regions; only in this case a finite n_h also appears in the acceptor matrix. The formation of pathways of holes leaving the polymer chains and percolating towards the anode can be observed. A Coulomb potential of up to +0.5 eV in the regions around the polymer is obtained. In this case, Coulomb repulsion can provide a sufficient amount of energy for holes to surmount the barrier. This means some holes are able to escape the donor and can be transported to the anode via the fullerene phase. The fullerene is then an ambipolar charge conductor and transports both electrons and holes to their respective contacts; in contrast, charge transport in BHJ is spatially separated into acceptor as the conductor for electrons and donor as the conductor for holes.

For a small barrier of 0.2 eV, a lower $n_h \approx 10^{17}\,\mathrm{cm}^{-3}$ indicates reduced confinement; almost all holes are able to transfer unrestrictedly into the acceptor. Once in the fullerene region, charges are subject to the dominating internal electric field and are driven to the respective contacts. Due to a strongly reduced Coulomb potential on the donor regions, also the amount of recombination is reduced. Charge pairs can separate faster which leads to an increased photocurrent. It has to be noted that a sufficiently large difference in ΔE_{HOMO} is needed to provide the necessary driving force to dissociate the excitons. The influence of barrier height on exciton separation is not included in our model, excitons are always separated with a fixed rate. However, there is evidence that charge transfer can take place even at very small HOMO level offsets [250].

Ultimately, all charges that are generated either reach the contacts, and contribute to the short-circuit current $I_{sc} = j_{sc} \cdot A_c$, with A_c the conctact area, or recombine at the

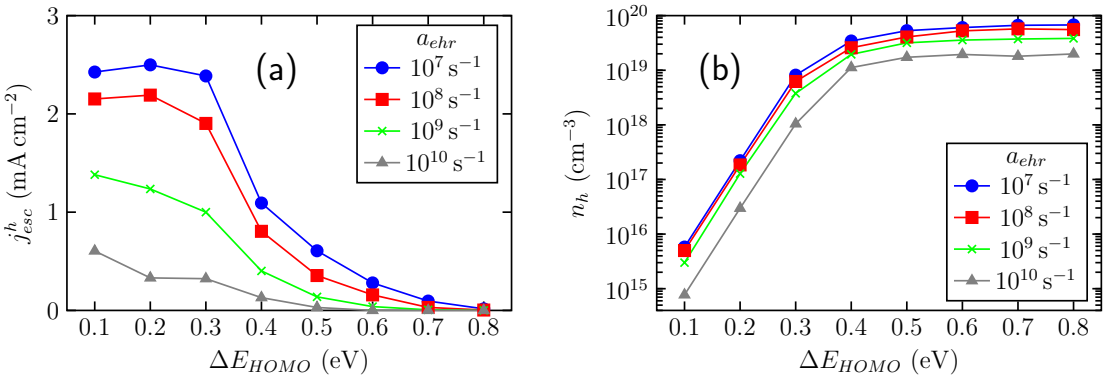

Figure 8.5. – Hole-escape current density j^h_{esc} (a) and equilibrium hole density on the donor n_h (b) as a function of the HOMO level offset ΔE_{HOMO} for various values of the recombination rate a_{ehr}.

heterojunction interface and contribute to the recombination current $I_{rec} = j_{rec} \cdot A_{hj}$, with A_{hj} the heterojunction interface area. In an idealized case of no recombination, the highest possible I_{sc} is equal to the net hole escape current $I^h_{esc} = j^h_{esc} \cdot A_{hj}$. A finite a_{ehr}, next to ΔE_{HOMO}, is expected to affect n_h because recombination reduces the average time holes spend in the donor domain. Implicitly, n_h determines ϕ_C (i.e. the repulsion energy) and, in combination with ΔE_{HOMO}, controls j^h_{esc}. Figure 8.5 shows the interplay of ΔE_{HOMO} and a_{ehr} on j^h_{esc} (Figure 8.5a) and on n_h (Figure 8.5b). The barriers were varied in a range from deliberately too small values of 0.1 eV up to values realistic in BHJs of 0.8 eV to cover a wide parameter range.

The transition between hole escape and hole confinement upon changes in ΔE_{HOMO} can be observed in Figure 8.5 for different values of a_{ehr}. The barrier must be lowered to values of $\Delta E^{th}_{HOMO} \approx 0.3 - 0.4\,\text{eV}$ in order for holes to leave the donor and to achieve a substantial j^h_{esc}. There is also a large dependence of j^h_{esc} on a_{ehr}: at lower a_{ehr} the threshold in ΔE_{HOMO} to observe a back-transfer increases. For large a_{ehr}, holes recombine with surrounding electrons before they can escape the donor. In the hole-escape regime with a low barrier and low a_{ehr}, j^h_{esc} approaches a maximum of $j^h_{esc} \approx 2.5\,\text{mA cm}^{-2}$. Translated to the absolute current through the donor/acceptor heterojunction $I^h_{esc} = j^h_{esc} \cdot A_{hj}$ this current approaches $I^h_{esc} = 2 \times 10^{-13}\,\text{A}$. No recombination leads to the largest achievable current due to photo-generation with the generation profile used in the simulations, and matches the absolute current through the contact interface A_c, $I_{sc} = j_{sc} \cdot A_c = 1.9 \times 10^{-13}\,\text{A}$ (with $j_{sc} = 7.5\,\text{mA cm}^{-2}$). The resulting short-circuit current for the same set of parameters is shown in Figure 8.6. Hence, all photo-generated holes can escape the donor and reach the anode to contribute to the short-circuit current.

Investigating the equilibrium hole density profile in Figure 8.5b, one can observe a general trend of an exponentially increasing hole density as the barrier is increased until a saturation is reached for large barriers. n_h ranges from $10^{15}\,\text{cm}^{-3}$ up to around $10^{20}\,\text{cm}^{-3}$

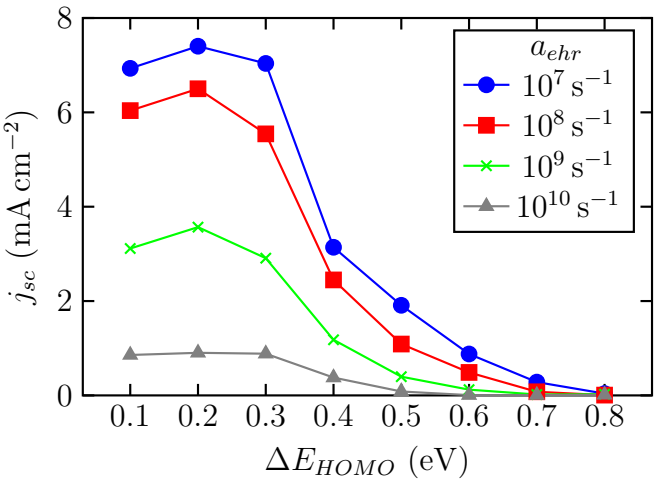

Figure 8.6. – Short-circuit current density vs. HOMO level offset for various recombination rates a_{ehr}.

when ΔE_{HOMO} is changed from 0.1 eV to 0.8 eV, but is only slightly dependent on a_{ehr}. In the regime where no hole escape takes place, the confined charges can recombine with electrons surrounding the donor, thus lowering the density for larger a_{ehr}. Upon lowering the barrier, holes are able to escape leading to decreased equilibrium hole density down to 10^{15} cm^{-3}. At large barriers the charge density is very high and holes stack up on the polymer and cannot back transfer to the fullerene. At a certain point, no excitons can be split anymore because there are no free sites for holes to be transferred onto the donor. The equilibrium state of this configuration is a strongly positively charged polymer with electrons surrounding them and all generated excitons are lost.

In the steady state, all charges that do not reach the contacts must recombine. The recombination current must therefore behave inversely proportional to the short-circuit current (Figure 8.6). Figure 8.7 depicts the influence of ΔE_{HOMO} on the total ratio of photo-generated charges recombining η_{ehr} (Figure 8.7a) as well as on j^h_{rec} (Figure 8.7) for various values of a_{ehr}. The same transition at barrier values around $\Delta E^{th}_{HOMO} \approx 0.3-0.4$ eV and a strong dependence on a_{ehr} can be seen (Figure 8.7a): for barriers smaller or equal to 0.2 eV, η_{ehr} is on a plateau determined by a_{ehr}. For large $a_{ehr} = 10^{10}$ s^{-1}, even at small barriers around $\eta_{ehr} = 87\,\%$ of a photo generated charges recombine. For low $a_{ehr} = 10^7$ s^{-1}, almost no recombination (η_{ehr} less than 2 %) at all is observable because holes can pass the small barrier faster than recombination can occur. Above a ΔE_{HOMO} of 0.3 eV, η_{ehr} starts to surge and for increasing barriers almost all photo-generated charges recombine, corresponding to a vanishing escape-current. The larger a_{ehr}, the faster the maximum recombination is reached: at the critical barrier of 0.3 eV a low $a_{ehr} = 10^7$ s^{-1} leads to $\eta_{ehr} = 3.4\,\%$ of all generated charges recombining, while for $a_{ehr} = 10^{10}$ s^{-1} already $\eta_{ehr} = 86.3\,\%$ of all charges recombine. η_{ehr} includes both

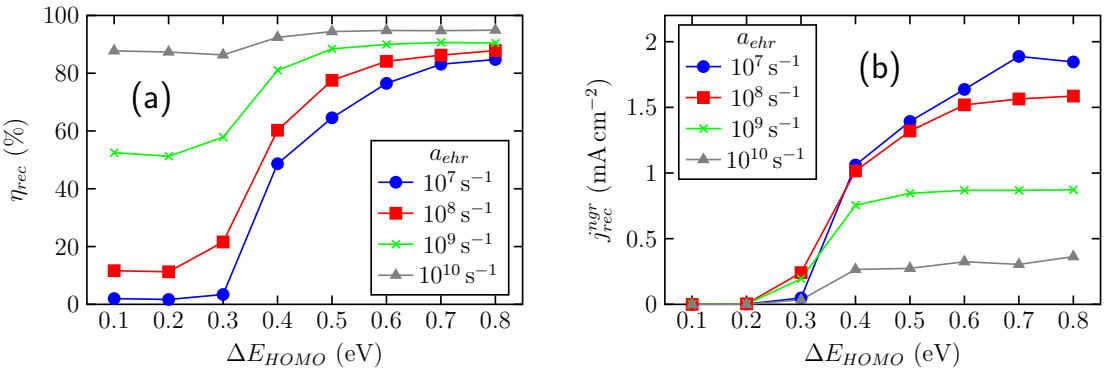

Figure 8.7. – Overall recombination ratio η_{ehr} (a) and non-geminate recombination current j_{rec}^{ngr} (b) as a function of the HOMO level offset ΔE_{HOMO} for various values of the recombination rate a_{ehr}.

geminate and non-geminate recombination. In order to compare to the experimental measurements from IS, we are interested in the non-geminate recombination current only (Figure 8.7b). j_{rec}^{ngr} also reflects the strong increase in recombination with ΔE_{HOMO} and shows a maximum of $j_{rec}^{ngr} = 1.9\,\mathrm{mA\,cm^{-2}}$ for large barriers, thus approaches the maximum achievable photo-current in the escape-regime. At $\Delta E_{HOMO} = 0.3\,\mathrm{eV}$, j_{rec}^{ngr} ranges between $0.035\,\mathrm{mA\,cm^{-2}}$ and $0.241\,\mathrm{mA\,cm^{-2}}$. Interestingly, with larger a_{ehr} the amount of non-geminate recombination is found to decrease. A larger a_{ehr} increases the amount of geminate recombination in the initial charge separation process. The more charges recombine geminately, the less charges can separate and are therefore available for non-geminate recombination. However, as previously discussed, the overall recombination ratio increases drastically with a_{ehr}. Therefore, the absolute amount of recombination increases but the relative amount of non-geminate recombination shifts in favor of geminate recombination.

In this model, we assume a fully dispersed configuration of the donor polymer chains in the acceptor phase. The distribution affects many properties such as the MO levels, charge separation, transport, as well as recombination. The exact morphology is not easily accessible, however there is evidence for dispersion based on the missing peaks for crystallic features in the absorption spectra. Full dispersion is an extreme case and in reality there might occur some clustering of the polymer chains, i.e. by π-π stacking of the sidechains. For the sake of generality we have also considered the other extreme case, namely a full clustering of the polymer chains to small spherical bubbles. A visualization of the morphology and the results for an analogous evaluation of this configuration are shown in Figure 8.8 and yield qualitatively the same results: also here the effect of hole-escape, as well as a substantial photocurrent, can be observed upon barrier lowering and due to charge accumulation. We can therefore conclude that the effect occurs independently of the detailed shape of the molecular arrangement. Larger clusters are however unlikely because they would show crystalline features in the absorption.

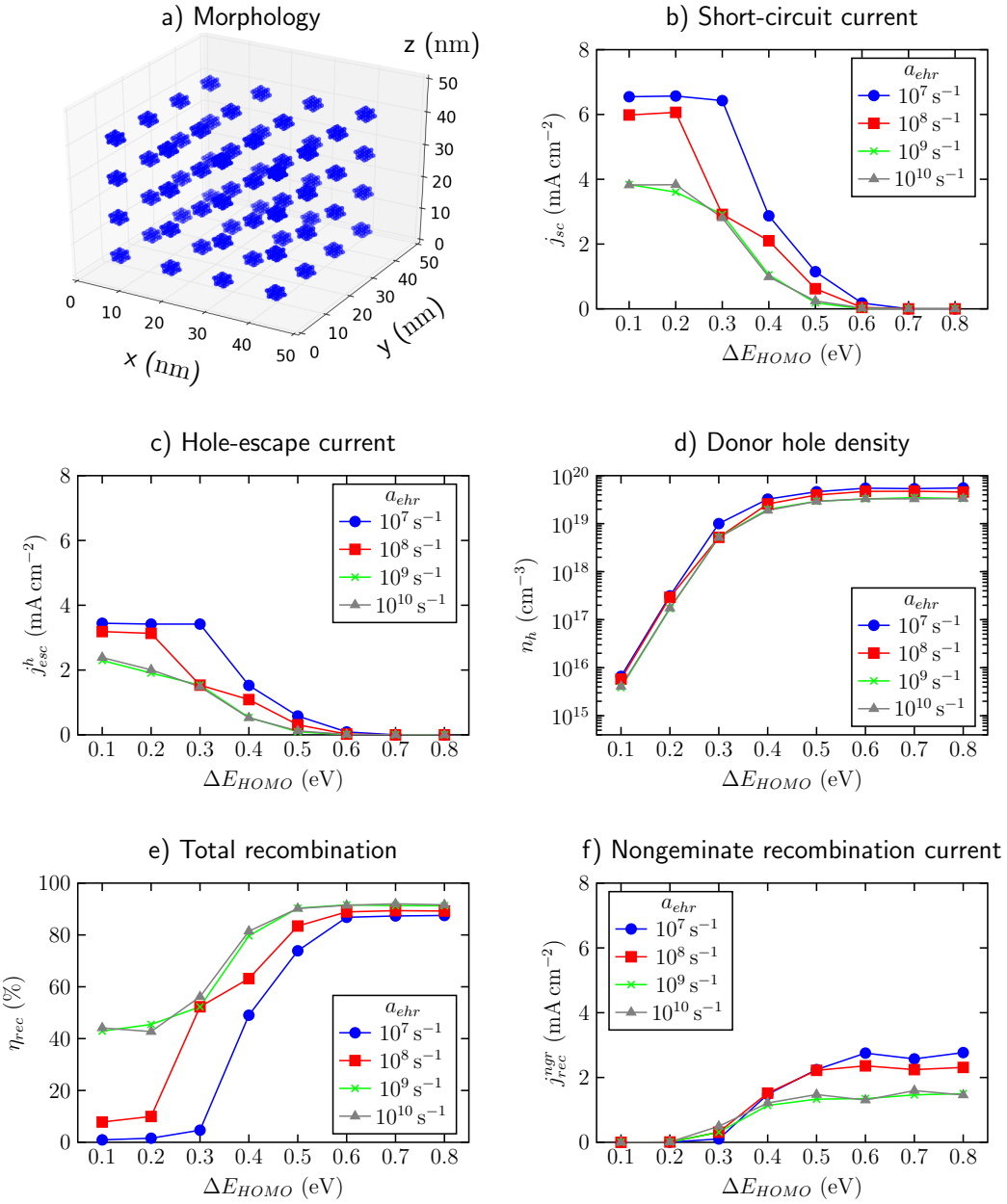

Figure 8.8. – Evaluation of hole-escape effect for fully clustered polymer chains as depicted in (a). Short-circuit current density j_{sc} (b), hole-escape current density j^h_{esc} (c), hole density in the donor phase n_h (d), the total recombination ratio η_{rec} (e), and the nongeminate recombination current density j^{ngr}_{rec} (f) are shown. This morphology is the opposite extreme case to completely dispersed polymer chains and yields qualitatively the same results.

8.3.2. Energy barrier lowering

As shown in Figure 8.2d, ΔE_{HOMO} can be determined as the difference between the bandgap energy of the fullerene $E_{g,PCBM}$ and the energy of the CT state energy (E_{CT}),

$$\Delta E_{HOMO} = E_{g,PCBM} - E_{CT}. \tag{8.5}$$

In order to determine ΔE_{HOMO} from experiments, the bandgap energy $E_{g,PCBM}$ and the CT state energy E_{CT} can be extracted from EQE spectra. Details about the extraction can be found in [36], [77]. The EQE measurements yield $E_{g,PCBM} = 1.75\,\text{eV}$ for $PC_{71}BM$, which agrees with literature values [251]. E_{CT} can be obtained from the EQE spectra by a Gaussian fitting of the spectra below the bandgap energy. A value of $E_{CT} = 1.45\,\text{eV}$ was found for various different (low) donor concentrations. This yields a HOMO level offset of $\Delta E_{HOMO} = 1.75\,\text{eV} - 1.45\,\text{eV} = 0.3\,\text{eV}$. Such an offset is considerably lower than what is generally reported in BHJ cells, i.e. values between 0.8 eV-1.0 eV.

The difference in HOMO energy levels between a BHJ and a dilute donor configuration can be explained by the morphological difference in the two configurations. In a dilute donor configuration, the vibronic features at 570 nm and 610 nm, which are attributed to an ordered P3HT arrangement, are absent in the absorption spectra [36]. The spectra of the fullerene-based systems with low donor content closely resemble those of $PC_{71}M$ alone, from which we conclude that the P3HT is in a fully disperse configuration, i.e. the PCBM acts as a good solvent for the P3HT polymer chains. The HOMO level of the disperse P3HT is found to be 0.3 eV deeper than in a BHJ configuration, therefore resulting in a lower ΔE_{HOMO}, in accordance with e.g. [252], [253]. The difference in HOMO energy levels between ordered and disordered P3HT is also indicated in Figure 8.2d.

Furthermore, at the donor/acceptor interface, the MOs of the P3HT and the PCBM overlap and interact with each other. This can lead to a significant broadening of the interfacial MOs. We can determine the reorganization energy λ from Marcus theory by determining the width of a Gaussian fit to the EQE spectra [254], [255]. For our fullerene-based systems, the reorganization energy is found to be $0.35 \pm 0.05\,\text{eV}$. λ represents the full width at half maximum of the DOS at the donor/acceptor interface in a disperse donor configuration. This can be an indication that the local ΔE_{HOMO} at the donor/acceptor interface can even be lower, and is meant as a supporting result to justify the lower ΔE_{HOMO} down to $\approx 0.3\,\text{eV}$ in fullerene-based systems.

8.3.3. Comparison of model and measurements

We compare the experimentally determined values for j_{rec} and R with the corresponding values extracted from the kMC simulations. All recombination currents and rates compared here are based on non-geminate recombination exclusively. Experimentally we calculate the recombination current density by $j_{rec}^{exp} = eLn/\tau$, where e is the magnitude of the elementary charge, L is the active layer thickness, n is the carrier density, and τ is the carrier recombination time. The quantities n and τ are obtained from IS analysis

[36], [77]. $R_{exp} = V \cdot n/\tau$ is normalized with the volume of the simulation cell. With $\Delta E_{HOMO} = 0.3\,\text{eV}$, as was determined to be a realistic case, and at $a_{ehr} = 10^9\,\text{s}^{-1}$, the kMC simulations yield $j_{rec}^{sim} = 0.195\,\text{mA}\,\text{cm}^{-2}$ and $R_{sim} = 9.6 \times 10^4\,\text{s}^{-1}$. The donor concentration in the simulation is 1.2 wt.%, which we compare to measurements obtained from cells with 1 wt.% donor concentration. Experimentally, it is determined $j_{rec}^{exp} = 0.056\,\text{mA}\,\text{cm}^{-2}$ and $R_{exp} = 6.3 \times 10^3\,\text{s}^{-1}$. The measured recombination current agrees with what is obtained by the simulations within a factor of 3-4, giving validation to our proposed hole back transfer model to explain photocurrent generation in these dilute-donor OSC system. Furthermore, the short circuit currents (cf. Figure 8.6) match well with $j_{sc}^{sim} = 2.9\,\text{mA}\,\text{cm}^{-2}$ and $j_{sc}^{exp} = 2.5\,\text{mA}\,\text{cm}^{-2}$ and show that the device performance can be reproduced by the model. We attribute the differences in recombination to the unknown details of the geometry of the donor aggregates, which largely impacts charge separation and recombination. Additionally, the exact value for a_{ehr} is under active investigation; for reduced a_{ehr} of e.g. $a_{ehr} = 10^7\,\text{s}^{-1}$ we obtain a recombination current of $j_{rec}^{sim} = 0.049\,\text{mA}\,\text{cm}^{-2}$ and a volume recombination rate of $R_{sim} = 2.4 \times 10^4\,\text{s}^{-1}$ which coincides well with what is obtained experimentally. We therefore argue that this simplified model produces values in good agreement with those obtained experimentally.

8.4. Conclusion

In conclusion, we provide a model explaining the high photocurrent reported for fullerene-based solar cells. First, we performed kMC simulations on a fullerene-based device with polymer chains as donor material in low concentration embedded in a fully dispersed configuration. We varied ΔE_{HOMO} and a_{ehr} and investigated the transport processes related to holes, in particular the hole current from the isolated donor domains to the anode. The results show that a hole back-transfer from isolated donor domains can occur, thus providing an explanation of the so far not yet understood origin of hole-photocurrent in this system. We further identify threshold values of the HOMO level offset of around $\Delta E_{HOMO} = 0.3\,\text{eV}$ for this process to occur. These barrier heights induce critical hole densities in the donor phase of $n_h^{th} \approx 10^{19}\,\text{cm}^{-3}$, which provide a Coulomb repulsion force large enough for holes to overcome the barrier and transfer to the fullerene phase. The amount of j_{esc}^h and concomitantly the resulting photocurrent is strongly dependent on a_{ehr}, but hole back-transfer was shown to be possible for all a_{ehr} considered between $10^7\,\text{s}^{-1}$ and $10^{10}\,\text{s}^{-1}$. After hole-transfer, the fullerene matrix acts as an ambipolar charge transport layer for both electrons and holes towards the contacts. Furthermore, we experimentally showed with the EQE measurements of $PC_{71}BM$ based devices containing small amounts of P3HT that ΔE_{HOMO} between fullerene and donor phase is low, $\approx 0.3\,\text{eV}$, in contrast to commonly reported offsets of 0.8 eV in BHJs, due to the highly disordered morphology of P3HT in the fullerene-based OSCs. The barrier height extracted from the measurements fits well with the critical barrier predicted to enable hole-escape by the simulations and hence supports this theory. Finally, we compare

the measured and simulated recombination, which are consistent between experiment and model for $\Delta E_{HOMO} \approx 0.3\,\mathrm{eV}$ and a_{ehr} of $10^9\,\mathrm{s}^{-1}$. Our model represents a new mechanism, alternative to e.g. that of Melianas et al. [246], to explain the origin of photocurrent in fullerene-based systems with low concentrations of donor material, by which the hole transport takes place in the fullerene instead of the donor. The mechanism of hole-escape renders the possibility that percolation pathways within the donor might not be necessary to obtain efficiently operating organic solar cell devices.

9. Summary and Conclusion

In this thesis, a 3D kMC model for OSCs was presented and used to provide insight into the mechanisms controlling the photo-current generation and recombination in the active layer. The model is capable of simulating full solar cell devices while considering effects on the nm/sub-ps scale. The event- and particle-based kMC method is particularly suited to describe the hopping transport between localized states in energetically disordered organic semiconductors and allows to incorporate the active layer morphology of OSCs on a nanometer scale, such as a BHJ geometry or the distribution of individual polymer chains.

The physical processes controlling the behavior of particles in OSCs are transferred into rate equations fitting for the kMC algorithm, which then allows to directly simulate the time-dependent evolution of the solar cell during operation. By tracing the origin, the pathways and the recombination of excitons and charge carriers, both spatially and in time, macroscopic figures of merit of the solar cell can be evaluated and linked to the underlying microscopic behavior of the particles.

The low permittivity of organic materials and the concomitant generation of charges via an intermediate, strongly localized charge transfer state makes the treatment of electrostatic interactions in OSCs particularly relevant. A specific advantage of the presented model over established implementations is the utilization of an Ewald summation which makes it possible to consider both the short-ranged and the long-ranged Coulomb interactions between all individual charges; this allows to account for effects arising from direct particle-particle interactions while at the same time considering the influence of long-ranged space-charge effects in the device.

At first, it is shown that effective medium models are not sufficient to capture the morphological effects of BHJs with large energetic disorder and low permittivity. A 1D DD model based on an EMA was compared to the 3D kMC model. A common basis of the two models was established and it was not possible to achieve agreement between them. The reduction of a BHJ to an effective medium hides processes at the donor/acceptor heterojunction which was elucidated by the charge carrier distribution: the DD model shows a polarization of the device as negative and positive charges are separated throughout the entire active layer while in the kMC simulations positive and negative charges are confined at the heterojunction interface as a result of the weak screening of electrostatic interactions. With this, the necessity of a 3D kMC model including the heterojunction interface, the local energetic disorder as well as direct particle-particle interactions is highlighted.

Following this, the charge behavior at the heterojunction was investigated in more

detail. It is shown that a low permittivity and a large disorder lead to a strongly inhomogeneous charge distribution throughout the active layer and that in such cases charges are mostly confined along the BHJ interface. The charge accumulation is quantified and it is shown that it strongly correlates to recombination, with geminate recombination clearly dominating over nongeminate recombination. In a next step, we analyze the time-resolved charge pair separation process and quantify the different phases of separation by characteristic times. The initial phase of charge separation is found to be strongly dependent on the permittivity. The charge separation times are put into relation to recombination times. At common values of energetic disorder, it is shown that even small increases in permittivity can suppress orders of magnitude of recombination rates. Hence, the results strongly support the recent trend of developing high-permittivity organic semiconductors for efficient OSC devices.

At last, a novel active layer morphology, a dilute donor configuration, is investigated. In these devices, the donor is only present in very small amounts and does not form percolation pathways (for holes) towards the contact. Thus, the mechanism of how holes can contribute to the photocurrent was not understood well. The performed kMC simulations provide an explanation for the working mechanism of such devices, in accordance with experimental measurements. Due to confinement on isolated donor molecules, holes accumulate on these. After a certain threshold in density, the Coulomb repulsion leads to a transfer of holes to the acceptor. The transfer is supported by a lower energy barrier between donor and acceptor in disperse systems (than in BHJs), which was supported by EQE measurements. After hole-transfer, the acceptor is the ambipolar conductor for both electrons and holes, in contrast to the working principle of BHJ cells, where holes are transported only in the donor phase. This study elucidates the flexibility of the kMC model and highlights its power to gain new physical insight into the mechanisms governing the operation functionality of OSCs.

Altogether, the kMC model has shown to be a powerful tool to gain a deeper understanding of the internal processes in OSCs, such as the spatially resolved charge carrier distributions or the time-resolved single-particle dynamics, which are otherwise challenging to access by experimental techniques or continuum-based models. A comprehensive picture of the different steps involved in the process of photo-current generation could be obtained and the underlying origins of loss mechanisms identified. The proposed explanation of the working principle of a novel system, in combination with the agreement between model and experiment, highlight the advantage of the kMC method in the design and optimization of next-generation OSCs.

A. Appendix

A.1. Generation profiles

We compared three different generation profiles in order to investigate the effect on the current density generated at different biases for two different active layer thicknesses, see Figure A.1. A constant generation, a profile based on the TMM, and an artificially defined profile, in which all excitons are generated close to one contact. The total generation $G_{\mathrm{tot}} = \int G(z)dz$ was kept the same for all three profiles. It can be observed that for both thicknesses, no particular difference between the constant and the TMM profile in the current can be observed. Only for the artificial profile with a strong localization near the bottom contact (cathode), a slight change in the current can be seen. The current is reduced in this case, which is a result of the difficulty for holes to reach the top contact (anode). All holes need to be transported though the entire active layer morphology, which increases losses by recombination and thus reduces the current. The analysis is meant to justify the TMM method in comparison to a full solution of the Maxwell equations because it shows that the exact origin of excitons does not have a tremendous influence on the solar cell performance.

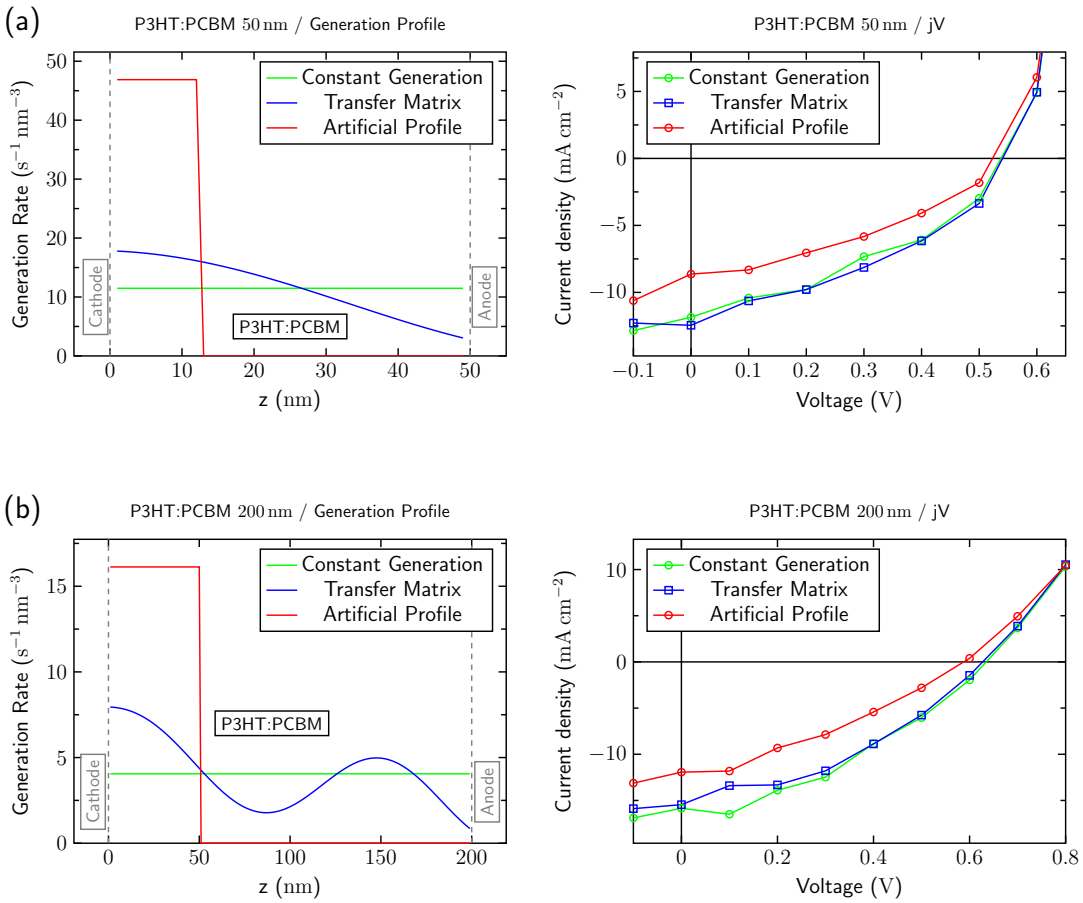

Figure A.1. – Comparison of different generation profiles on solar cell characteristics. (a) 50 nm and (b) 200 nm active layer. The artificial (red) profile was tested as an extreme case to see the differences to a constant and a TMM profile.

A.2. Densities and potential in fullerene-based solar cells

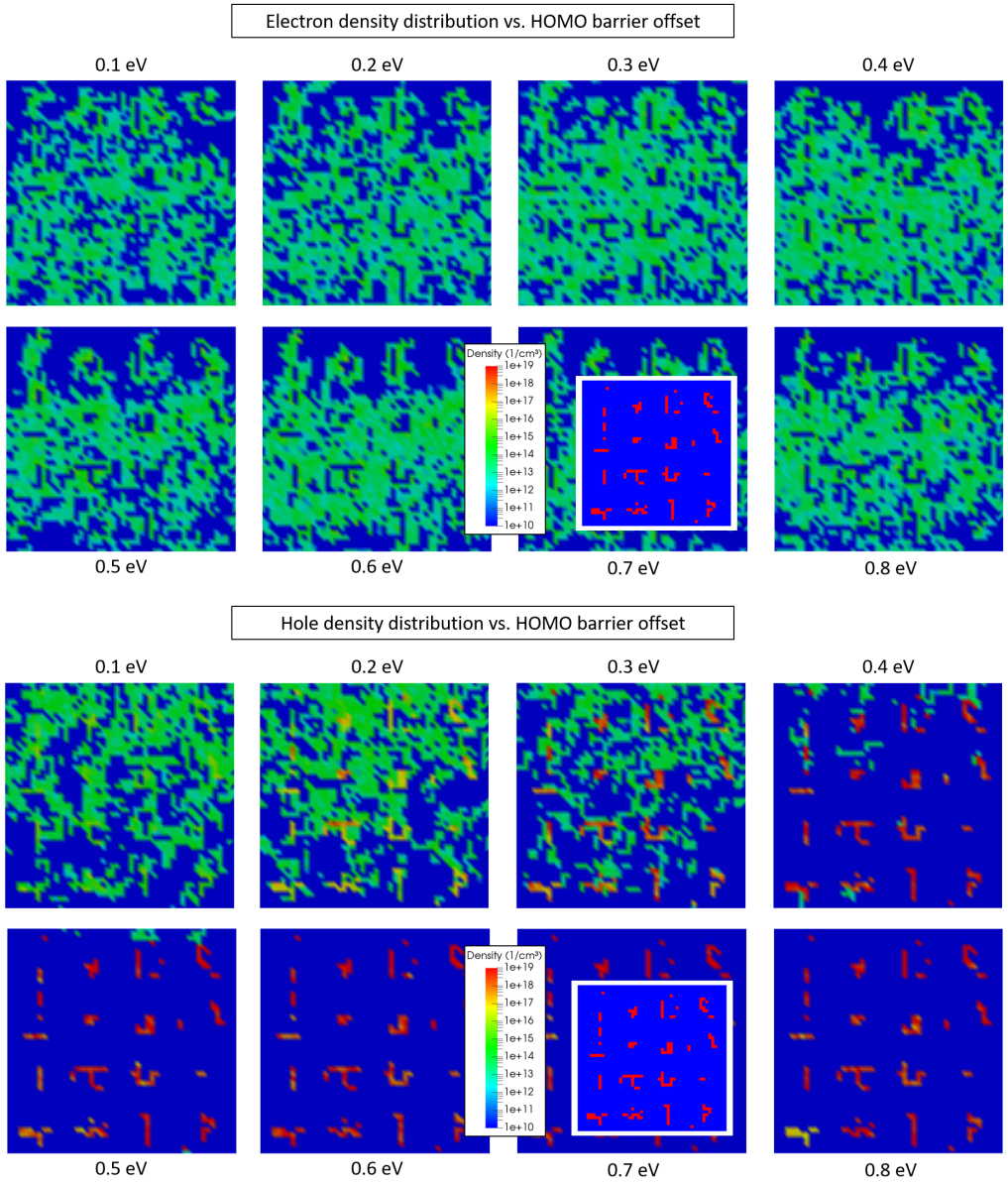

Figure A.2. – Full set of electron (top) and hole (bottom) densities vs. donor-acceptor HOMO level difference in dilute donor configuration. The inset shows the polymer chain configuration in the considered slice through the active layer.

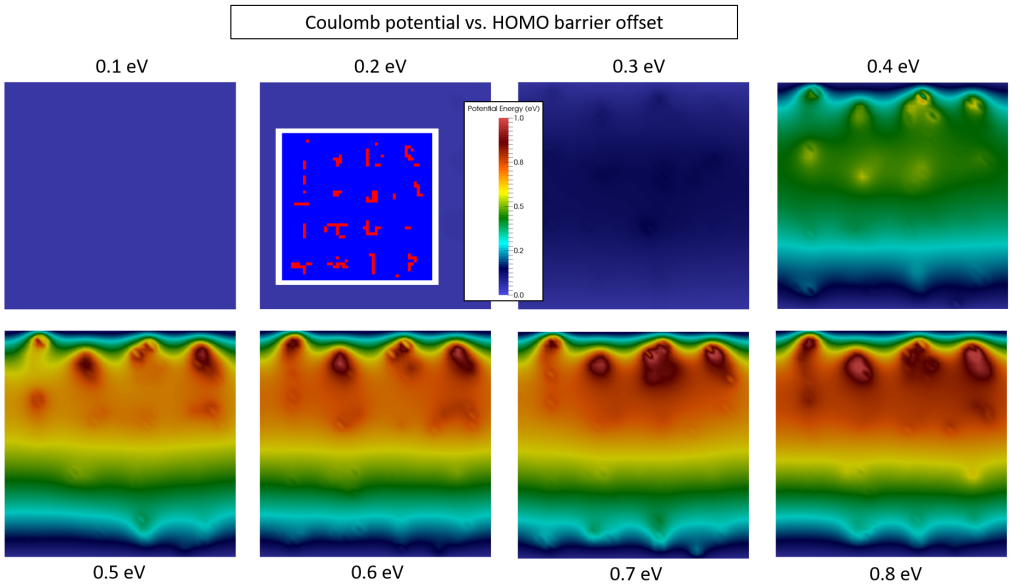

Figure A.3. – Full set of electrostatic potential distribution vs. donor-acceptor HOMO level difference in dilute donor configuration. The inset shows the polymer chain configuration in the considered slice through the active layer.

List of Figures

1.1. Organic solar cell record efficiencies 2

2.1. Solar spectrum 10
2.2. Generic solar cell working principle 11
2.3. Output characteristics of a solar cell with figures of merit 13
2.4. Wave function overlap forming (anti-) bonding states 19
2.5. Formation of hybrid orbitals in carbon 20
2.6. Overlap of p_z orbitals 21
2.7. Structural disorder leads to energetic disorder 22
2.8. Hopping transport between localized states 24
2.9. Working principle of an organic solar cell 27

3.1. Classification of the kMC method 35
3.2. Infrequent events and state-to-state transitions 37
3.3. Illustration of probability density function interpretation 39
3.4. Drawing a discrete transition by a continuous random variable 43
3.5. Flowchart of a general kinetic Monte Carlo algorithm 46

4.1. Grid representation of the solar cell 50
4.2. Spin-exchange illustration 53
4.3. Cluster size control by spin-exchange algorithm 54
4.4. Adjusting cluster size to experimental measurements 55
4.5. Pivot algorithm 56
4.6. Energy distribution of LUMO levels 58
4.7. Energy distribution of HOMO levels 60
4.8. Mirror and replica charges in the Ewald sum 64
4.9. Rate activation dependency 68
4.10. Illustration of implemented processes 69
4.11. Exciton generation profiles 70
4.12. Definition of recombination events 75
4.13. Particle trajectories 80

5.1. Real blend vs. effective medium 87
5.2. Mobility fit 92
5.3. Mobility extraction 93
5.4. Comparison effective medium and real blend currents 94

5.5. Comparison of charge densities 95

6.1. Definition interface densities 100
6.2. Electron and hole charge density distributions along a slice 102
6.3. Ratio of interface to bulk densities 103
6.4. Absolute densities 105
6.5. Total and geminate recombination 106
6.6. Total and geminate recombination 107

7.1. Disorder and Coulomb radius 115
7.2. Illustration of charge pair separation evaluation 118
7.3. Absolute values for characteristic times 120
7.4. Relative values for characteristic times normalized 122
7.5. Electron and hole mobilities vs. disorder and permittivity 124
7.6. Effective recombination time 125

8.1. Comparison of increased short-circuit current 129
8.2. BHJ vs. dilute donor configuration 130
8.3. Polymer chain distribution 132
8.4. Densities and energetics in a dilute donor configuration 134
8.5. Escape current density 136
8.6. Short-circuit current dilute donor 137
8.7. Total and non-geminate recombination 138
8.8. Spherical clusters: current, density, recombination 139

A.1. Comparison of generation profiles 146
A.2. Charge densities in a dilute donor system 147
A.3. Electric potential in a dilute donor system 148

List of Tables

4.1. System setup parameters 79
4.2. Transition rate values 79

5.1. Common parameters 90

6.1. Effect of permittivity and disorder on short-circuit current 108

7.1. Comparison of energetic contributions 114
7.2. Overview of Coulomb and disorder radii 116

Bibliography

[1] P. Würfel and U. Würfel, *Physics of Solar Cells: From Basic Principles to Advanced Concepts*. New York: Wiley, 2016.

[2] Energy Information Administration (EIA), *Key World Energy Statistics*, `https://www.iea.org/publications/freepublications/publication/KeyWorld2017.pdf`, [Online; accessed 11-May-2018], 2018.

[3] ——, *Solar Energy Perspectives: Executive Summary*, `http://www.iea.org/Textbase/npsum/solar2011SUM.pdf`, [Online; accessed 11-May-2018], 2011.

[4] M. A. Green, Y. Hishikawa, E. D. Dunlop, D. H. Levi, J. Hohl-Ebinger, M. Yoshita, and A. W. Ho-Baillie, "Solar Cell Efficiency Tables (Version 53)", *Progress in Photovoltaics: Research and Applications*, vol. 27, no. 1, pp. 3–12, 2019.

[5] L. Dou, J. You, Z. Hong, Z. Xu, G. Li, R. A. Street, and Y. Yang, "25th Anniversary Article: A Decade of Organic/Polymeric Photovoltaic Research", *Advanced Materials*, vol. 25, no. 46, pp. 6642–6671, 2013.

[6] S. Günes, H. Neugebauer, and N. S. Sariciftci, "Conjugated Polymer-Based Organic Solar Cells", *Chemical Reviews*, vol. 107, no. 4, pp. 1324–38, 2007.

[7] G. Dennler, M. C. Scharber, and C. J. Brabec, "Polymer-Fullerene Bulk-Heterojunction Solar Cells", *Advanced Materials*, vol. 21, no. 13, p. 1323, 2009.

[8] C. Deibel and V. Dyakonov, "Polymer–Fullerene Bulk Heterojunction Solar Cells", *Reports on Progress in Physics*, vol. 73, no. 9, p. 096 401, 2010.

[9] L. Lu, T. Zheng, Q. Wu, A. M. Schneider, D. Zhao, and L. Yu, "Recent Advances in Bulk Heterojunction Polymer Solar Cells", *Chemical Reviews*, vol. 115, no. 23, p. 12 666, 2015.

[10] R. Søndergaard, M. Hösel, D. Angmo, T. T. Larsen-Olsen, and F. C. Krebs, "Roll-to-Roll Fabrication of Polymer Solar Cells", *Materials Today*, vol. 15, no. 1, pp. 36–49, 2012.

[11] Y.-J. Heo, Y.-S. Jung, K. Hwang, J.-E. Kim, J.-S. Yeo, S. Lee, Y.-J. Jeon, D. Lee, and D.-Y. Kim, "Small-Molecule Organic Photovoltaic Modules Fabricated via Halogen-Free Solvent System with Roll-to-Roll Compatible Scalable Printing Method", *ACS Applied Materials & Interfaces*, vol. 9, no. 45, pp. 39 519–39 525, 2017.

[12] J. Kalowekamo and E. Baker, "Estimating the Manufacturing Cost of Purely Organic Solar Cells", *Solar Energy*, vol. 83, no. 8, pp. 1224–1231, 2009.

[13] N. Espinosa, M. Hösel, D. Angmo, and F. C. Krebs, "Solar Cells with One-Day Energy Payback for the Factories of the Future", *Energy & Environmental Science*, vol. 5, no. 1, pp. 5117–5132, 2012.

[14] S. Lizin, S. Van Passel, E. De Schepper, W. Maes, L. Lutsen, J. Manca, and D. Vanderzande, "Life Cycle Analyses of Organic Photovoltaics: A Review", *Energy & Environmental Science*, vol. 6, no. 11, pp. 3136–3149, 2013.

[15] J. Zhao, Y. Li, G. Yang, K. Jiang, H. Lin, H. Ade, W. Ma, and H. Yan, "Efficient Organic Solar Cells Processed from Hydrocarbon Solvents", *Nature Energy*, vol. 1, p. 15 027, 2016.

[16] W. Zhao, S. Li, H. Yao, S. Zhang, Y. Zhang, B. Yang, and J. Hou, "Molecular Optimization Enables over 13% Efficiency in Organic Solar Cells", *Journal of the American Chemical Society*, vol. 139, no. 21, p. 7148, 2017.

[17] S. Holliday, Y. Li, and C. Luscombe, "Recent Advances in High Performance Donor-Acceptor Polymers for Organic Photovoltaics", *Progress in Polymer Science*, vol. 70, pp. 34–51, 2017.

[18] S. Zhang, Y. Qin, J. Zhu, and J. Hou, "Over 14% Efficiency in Polymer Solar Cells Enabled by a Chlorinated Polymer Donor", *Advanced Materials*, p. 1 800 868, 2018.

[19] J. Zhang, L. Zhu, and Z. Wei, "Toward Over 15% Power Conversion Efficiency for Organic Solar Cells: Current Status and Perspectives", *Small Methods*, vol. 1, no. 12, p. 1 700 258, 2017.

[20] J. Yuan, Y. Zhang, L. Zhou, G. Zhang, H.-L. Yip, T.-K. Lau, X. Lu, C. Zhu, H. Peng, P. A. Johnson, M. Leclerc, Y. Cao, J. Ulanski, Y. Li, and Z. Yingping, "Single-Junction Organic Solar Cell with over 15% Efficiency Using Fused-Ring Acceptor with Electron-Deficient Core", *Joule*, vol. 3, no. 4, pp. 1140–1151, 2019.

[21] X. Che, Y. Li, Y. Qu, and S. R. Forrest, "High Fabrication Yield Organic Tandem Photovoltaics Combining Vacuum- and Solution-Processed Subcells with 15% Efficiency", *Nature Energy*, vol. 3, pp. 422–427, 2018.

[22] N. C. Giebink, G. P. Wiederrecht, M. R. Wasielewski, and S. R. Forrest, "Thermodynamic Efficiency Limit of Excitonic Solar Cells", *Physical Review B*, vol. 83, no. 19, p. 195 326, 2011.

[23] C. K. Chiang, C. R. Fincher, Y. W. Park, A. J. Heeger, H. Shirakawa, E. J. Louis, S. C. Gau, and A. G. MacDiarmid, "Electrical Conductivity in Doped Polyacetylene", *Physical Review Letters*, vol. 39, no. 17, pp. 1098–1101, 1977.

[24] Y.-J. Cheng, S.-H. Yang, and C.-S. Hsu, "Synthesis of Conjugated Polymers for Organic Solar Cell Applications", *Chemical Reviews*, vol. 109, no. 11, pp. 5868–5923, 2009.

[25] B.-G. Kim, X. Ma, C. Chen, Y. Ie, E. W. Coir, H. Hashemi, Y. Aso, P. F. Green, J. Kieffer, and J. Kim, "Energy Level Modulation of HOMO, LUMO, and Band-Gap in Conjugated Polymers for Organic Photovoltaic Applications", *Advanced Functional Materials*, vol. 23, no. 4, pp. 439–445, 2013.

[26] F. Bureš, "Fundamental Aspects of Property Tuning in Push–Pull Molecules", *RSC Advances*, vol. 4, no. 102, pp. 58 826–58 851, 2014.

[27] J. Brebels, J. V. Manca, L. Lutsen, D. Vanderzande, and W. Maes, "High Dielectric Constant Conjugated Materials for Organic Photovoltaics", *Journal of Materials Chemistry A*, vol. 5, no. 46, p. 24 037, 2017.

[28] P. Boufflet, G. Bovo, L. Occhi, H.-K. Yuan, Z. Fei, Y. Han, T. D. Anthopoulos, P. N. Stavrinou, and M. Heeney, "The Influence of Backbone Fluorination on the Dielectric Constant of Conjugated Polythiophenes", *Advanced Electronic Materials*, p. 1 700 375, 2017.

[29] S. Reineke, M. Thomschke, B. Lüssem, and K. Leo, "White Organic Light-Emitting Diodes: Status and Perspective", *Reviews of Modern Physics*, vol. 85, no. 3, p. 1245, 2013.

[30] H. Sirringhaus, "25th Anniversary Article: Organic Field-Effect Transistors: The Path Beyond Amorphous Silicon", *Advanced Materials*, vol. 26, no. 9, pp. 1319–1335, 2014.

[31] B. Russ, A. Glaudell, J. J. Urban, M. L. Chabinyc, and R. A. Segalman, "Organic Thermoelectric Materials for Energy Harvesting and Temperature Control", *Nature Reviews Materials*, vol. 1, p. 16 050, 2016.

[32] M. Auf der Maur, T. Albes, and A. Gagliardi, "Thin-Film Solar Cells", in *Handbook of Optoelectronic Device Modeling and Simulation: Lasers, Modulators, Photodetectors, Solar Cells, and Numerical Methods*, J. Piprek, Ed., Taylor & Francis, Boca Raton, Sep. 2017.

[33] T. Albes, P. Lugli, and A. Gagliardi, "Investigation of the Blend Morphology in Bulk-Heterojunction Organic Solar Cells", *IEEE Transactions on Nanotechnology*, vol. 15, no. 2, pp. 281–288, 2016.

[34] T. Albes and A. Gagliardi, "Influence of Permittivity and Energetic Disorder on the Spatial Charge Carrier Distribution and Recombination in Organic Bulk-Heterojunctions", *Physical Chemistry Chemical Physics*, vol. 19, no. 31, pp. 20 974–20 983, 2017.

[35] ——, "Charge Pair Separation Dynamics in Organic Bulk-Heterojunction Solar Cells", *Advanced Theory and Simulations*, vol. 1, no. 7, p. 1 800 032, 2018.

[36] T. Albes, L. Xu, J. Wang, J. W. P. Hsu, and A. Gagliardi, "Origin of Photocurrent in Fullerene-Based Solar Cells", *The Journal of Physical Chemistry C*, vol. 122, no. 27, pp. 15 140–15 148, 2018.

[37] T. Albes, "Kinetic Monte Carlo Modelling of Bulk-Heterojunction Organic Solar Cells", Diplomarbeit, Department of Physics, Technical University of Munich, Munich, Germany, 2014.

[38] T. Albes, B. Popescu, D. Popescu, M. Loch, F. Arca, and P. Lugli, "Kinetic Monte Carlo Modeling of Low-Bandgap Polymer Solar Cells", in *40th IEEE Photovoltaic Specialist Conference (PVSC)*, Denver, CO, USA, 2014, pp. 0057–0062.

[39] T. Albes, B. Popescu, D. Popescu, F. Arca, and P. Lugli, "Optimization of Organic Solar Cells by kinetic Monte Carlo Simulations", in *14th IEEE International Conference on Nanotechnology (IEEE-NANO)*, Toronto, ON, Canada, 2014, pp. 1023–1028.

[40] E. Becquerel, "Mémoire sur les effets électriques produits sous l'influence des rayons solaires", *Comptes rendus hebdomadaires des séances de l'Académie des Sciences*, vol. 9, pp. 561–567, 1839.

[41] A. Einstein, "Über einen die Erzeugung und Verwandlung des Lichtes betreffenden heuristischen Gesichtspunkt", *Annalen der Physik*, vol. 322, no. 6, pp. 132–148, 1905.

[42] W. Shockley and H. J. Queisser, "Detailed Balance Limit of Efficiency of p-n Junction Solar Cells", *Journal of Applied Physics*, vol. 32, no. 3, pp. 510–519, 1961.

[43] T. Kirchartz, K. Taretto, and U. Rau, "Efficiency Limits of Organic Bulk Heterojunction Solar Cells", *The Journal of Physical Chemistry C*, vol. 113, no. 41, pp. 17 958–17 966, 2009.

[44] C. E. Fritts, "On a New Form of Selenium Cell, and Some Electrical Discoveries Made by Its Use", *American Journal of Science*, no. 156, pp. 465–472, 1883.

[45] D. M. Chapin, C. S. Fuller, and G. L. Pearson, "A New Silicon p-n Junction Photocell for Converting Solar Radiation into Electrical Power", *Journal of Applied Physics*, vol. 25, no. 5, pp. 676–677, 1954.

[46] Fraunhofer Institute for Solar Energy Systems (ISE), *Photovoltaics Report*, `http://webcitation.org/6qWF4v37d`, [Online; accessed 14-May-2018], 2018.

[47] M. A. Green, Y. Hishikawa, E. D. Dunlop, D. H. Levi, J. Hohl-Ebinger, and A. W. Ho-Baillie, "Solar cell Efficiency Tables (Version 51)", *Progress in Photovoltaics: Research and Applications*, vol. 26, no. 1, pp. 3–12, 2018.

[48] A. Richter, M. Hermle, and S. W. Glunz, "Reassessment of the Limiting Efficiency for Crystalline Silicon Solar Cells", *IEEE Journal of Photovoltaics*, vol. 3, no. 4, pp. 1184–1191, 2013.

[49] B. O'regan and M. Grätzel, "A Low-Cost, High-Efficiency Solar Cell Based on Dye-Sensitized Colloidal TiO_2 Films", *Nature*, vol. 353, no. 6346, p. 737, 1991.

[50] U. Bach, D. Lupo, P. Comte, J. Moser, F. Weissörtel, J. Salbeck, H. Spreitzer, and M. Grätzel, "Solid-State Dye-Sensitized Mesoporous TiO_2 Solar Cells with High Photon-to-Electron Conversion Efficiencies", *Nature*, vol. 395, no. 6702, p. 583, 1998.

[51] A. Kojima, K. Teshima, Y. Shirai, and T. Miyasaka, "Organometal Halide Perovskites as Visible-Light Sensitizers for Photovoltaic Cells", *Journal of the American Chemical Society*, vol. 131, no. 17, pp. 6050–6051, 2009.

[52] G. E. Eperon, V. M. Burlakov, P. Docampo, A. Goriely, and H. J. Snaith, "Morphological Control for High Performance, Solution-Processed Planar Heterojunction Perovskite Solar Cells", *Advanced Functional Materials*, vol. 24, no. 1, pp. 151–157,

[53] W. S. Yang, J. H. Noh, N. J. Jeon, Y. C. Kim, S. Ryu, J. Seo, and S. I. Seok, "High-Performance Photovoltaic Perovskite Layers Fabricated Through Intramolecular Exchange", *Science*, vol. 348, no. 6240, pp. 1234–1237, 2015.

[54] C. E. Swenberg and M. Pope, *Electronic Processes in Organic Crystals and Polymers*. Oxford University Press, 1999.

[55] W. Brütting, *Physics of Organic Semiconductors*. John Wiley & Sons, 2006.

[56] H. Bässler, "Charge Transport in Disordered Organic Photoconductors: A Monte Carlo Simulation Study", *Physica Status Solidi B*, vol. 175, no. 1, p. 15, 1993.

[57] A. Nenashev, J. Oelerich, and S. Baranovskii, "Theoretical Tools for the Description of Charge Transport in Disordered Organic Semiconductors", *Journal of Physics: Condensed Matter*, vol. 27, no. 9, p. 093 201, 2015.

[58] G. Garcia-Belmonte, P. P. Boix, J. Bisquert, M. Sessolo, and H. J. Bolink, "Simultaneous Determination of Carrier Lifetime and Electron Density-of-States in P3HT:PCBM Organic Solar Cells Under Illumination by Impedance Spectroscopy", *Solar Energy Materials and Solar Cells*, vol. 94, no. 2, pp. 366–375, 2010.

[59] A. J. Heeger, "Nobel Lecture: Semiconducting and Metallic Polymers: The Fourth Generation of Polymeric Materials", *Reviews of Modern Physics*, vol. 73, no. 3, pp. 681–700, 2001.

[60] O. Rubel, S. Baranovskii, P. Thomas, and S. Yamasaki, "Concentration Dependence of the Hopping Mobility in Disordered Organic Solids", *Physical Review B*, vol. 69, no. 1, p. 014 206, 2004.

[61] W. Roelofs, S. Mathijssen, R. Janssen, D. de Leeuw, and M. Kemerink, "Accurate Description of Charge Transport in Organic Field Effect Transistors Using an Experimentally Extracted Density of States", *Physical Review B*, vol. 85, no. 8, p. 085 202, 2012.

[62] N. Tessler, Y. Preezant, N. Rappaport, and Y. Roichman, "Charge Transport in Disordered Organic Materials and Its Relevance to Thin-Film Devices: A Tutorial Review", *Advanced Materials*, vol. 21, no. 27, pp. 2741–2761, 2009.

[63] A. Miller and E. Abrahams, "Impurity Conduction at Low Concentrations", *Physical Review*, vol. 120, no. 3, p. 745, 1960.

[64] R. A. Marcus and N. Sutin, "Electron Transfers in Chemistry and Biology", *Biochimica et Biophysica Acta, Reviews on Bioenergetics*, vol. 811, no. 3, pp. 265–322, 1985.

[65] C. Brabec, U. Scherf, and V. Dyakonov, *Organic Photovoltaics: Materials, Device Physics, and Manufacturing Technologies*. John Wiley & Sons, 2014.

[66] S. M. Sze and K. K. Ng, *Physics of Semiconductor Devices*. John Wiley & Sons, 2006.

[67] G. Li, R. Zhu, and Y. Yang, "Polymer Solar Cells", *Nature Photonics*, vol. 6, no. 3, p. 153, 2012.

[68] T. M. Clarke and J. R. Durrant, "Charge Photogeneration in Organic Solar Cells", *Chemical Reviews*, vol. 110, no. 11, p. 6736, 2010.

[69] N. S. Sariciftci, L. Smilowitz, A. J. Heeger, and F. Wudl, "Photoinduced Electron Transfer from a Conducting Polymer to Buckminsterfullerene", *Science*, vol. 258, no. 5087, pp. 1474–1476, 1992.

[70] C. Yan, S. Barlow, Z. Wang, H. Yan, A. K.-Y. Jen, S. R. Marder, and X. Zhan, "Non-Fullerene Acceptors for Organic Solar Cells", *Nature Reviews Materials*, vol. 3, p. 18 003, 2018.

[71] G. Li, V. Shrotriya, J. Huang, Y. Yao, T. Moriarty, K. Emery, and Y. Yang, "High-Efficiency Solution Processable Polymer Photovoltaic Cells by Self-Organization of Polymer Blends", *Nature Materials*, vol. 4, no. 11, pp. 864–868, 2005.

[72] W. Ma, C. Yang, X. Gong, K. Lee, and A. J. Heeger, "Thermally Stable, Efficient Polymer Solar Cells with Nanoscale Control of the Interpenetrating Network Morphology", *Advanced Functional Materials*, vol. 15, no. 10, pp. 1617–1622, 2005.

[73] H. Spanggaard and F. C. Krebs, "A Brief History of the Development of Organic and Polymeric Photovoltaics", *Solar Energy Materials and Solar Cells*, vol. 83, no. 2-3, pp. 125–146, 2004.

[74] C. W. Tang, "Two-Layer Organic Photovoltaic Cell", *Applied Physics Letters*, vol. 48, no. 2, pp. 183–185, 1986.

[75] G. Yu, J. Gao, J. C. Hummelen, F. Wudl, and A. J. Heeger, "Polymer Photovoltaic Cells: Enhanced Efficiencies Via a Network of Internal Donor-Acceptor Heterojunctions", *Science*, vol. 270, no. 5243, pp. 1789–1790, 1995.

[76] Y.-Q. Zheng, W. J. Potscavage Jr, T. Komino, M. Hirade, J. Adachi, and C. Adachi, "Highly Efficient Bulk Heterojunction Photovoltaic Cells Based on C70 and Tetraphenyldibenzoperiflanthene", *Applied Physics Letters*, vol. 102, no. 14, p. 60, 2013.

[77] L. Xu, J. Wang, M. d. A. Villa, T. B. Daunis, Y.-J. Lee, A. V. Malko, and J. W. Hsu, "Quantitative Analyses of Competing Photocurrent Generation Mechanisms in Fullerene-Based Organic Photovoltaics", *The Journal of Physical Chemistry C*, vol. 120, no. 30, pp. 16 470–16 477, 2016.

[78] B. Yang, F. Guo, Y. Yuan, Z. Xiao, Y. Lu, Q. Dong, and J. Huang, "Solution-Processed Fullerene-Based Organic Schottky Junction Devices for Large-Open-Circuit-Voltage Organic Solar Cells", *Advanced Materials*, vol. 25, no. 4, pp. 572–577, 2013.

[79] F. Gao and O. Inganas, "Charge Generation in Polymer-Fullerene Bulk-Heterojunction Solar Cells", *Physical Chemistry Chemical Physics*, vol. 16, no. 38, pp. 20 291–20 304, 2014.

[80] P. Deotare, W. Chang, E. Hontz, D. Congreve, L. Shi, P. Reusswig, B. Modtland, M. Bahlke, C. Lee, A. Willard, V. Bulović, T. Van Voorhis, and M. A. Baldo, "Nanoscale Transport of Charge-Transfer States in Organic Donor-Acceptor Blends", *Nature Materials*, vol. 14, no. 11, pp. 1130–1134, 2015.

[81] I. A. Howard, R. Mauer, M. Meister, and F. Laquai, "Effect of Morphology on Ultrafast Free Carrier Generation in Polythiophene:Fullerene Organic Solar Cells", *Journal of the American Chemical Society*, vol. 132, no. 42, pp. 14 866–14 876, 2010.

[82] T. M. Burke, S. Sweetnam, K. Vandewal, and M. D. McGehee, "Beyond Langevin Recombination: How Equilibrium Between Free Carriers and Charge Transfer States Determines the Open-Circuit Voltage of Organic Solar Cells", *Advanced Energy Materials*, vol. 5, no. 11, p. 1 500 123, 2015.

[83] L. Onsager, "Initial Recombination of Ions", *Physical Review*, vol. 54, no. 8, p. 554, 1938.

[84] C. L. Braun, "Electric Field Assisted Dissociation of Charge Transfer States as a Mechanism of Photocarrier Production", *The Journal of Chemical Physics*, vol. 80, no. 9, pp. 4157–4161, 1984.

[85] M. L. Jones, B. Chakrabarti, and C. Groves, "Monte Carlo Simulation of Geminate Pair Recombination Dynamics in Organic Photovoltaic Devices: Multi-Exponential, Field-Dependent Kinetics and Its Interpretation", *The Journal of Physical Chemistry C*, vol. 118, no. 1, pp. 85–91, 2014.

[86] M. Scharber and N. Sariciftci, "Efficiency of Bulk-Heterojunction Organic Solar Cells", *Progress in Polymer Science*, vol. 38, no. 12, pp. 1929–1940, 2013.

[87] L. J. Koster, S. E. Shaheen, and J. C. Hummelen, "Pathways to a New Efficiency Regime for Organic Solar Cells", *Advanced Energy Materials*, vol. 2, no. 10, p. 1246, 2012.

[88] N. Cho, C. W. Schlenker, K. M. Knesting, P. Koelsch, H.-L. Yip, D. S. Ginger, and A. K.-Y. Jen, "High-Dielectric Constant Side-Chain Polymers Show Reduced Non-Geminate Recombination in Heterojunction Solar Cells", *Advanced Energy Materials*, vol. 4, no. 10, 2014.

[89] S. Y. Leblebici, T. L. Chen, P. Olalde-Velasco, W. Yang, and B. Ma, "Reducing Exciton Binding Energy by Increasing Thin Film Permittivity: An Effective Approach to Enhance Exciton Separation Efficiency in Organic Solar Cells", *ACS Applied Materials & Interfaces*, vol. 5, no. 20, pp. 10 105–10 110, 2013.

[90] G. Zhang, T. M. Clarke, and A. J. Mozer, "Bimolecular Recombination in a Low Bandgap Polymer:PCBM Blend Solar Cell with a High Dielectric Constant", *The Journal of Physical Chemistry C*, vol. 120, no. 13, pp. 7033–7043, 2016.

[91] S. Chen, S.-W. Tsang, T.-H. Lai, J. R. Reynolds, and F. So, "Dielectric Effect on the Photovoltage Loss in Organic Photovoltaic Cells", *Advanced Materials*, vol. 26, no. 35, pp. 6125–6131, 2014.

[92] S. Torabi, F. Jahani, I. Van Severen, C. Kanimozhi, S. Patil, R. W. Havenith, R. C. Chiechi, L. Lutsen, D. J. Vanderzande, T. J. Cleij, J. C. Hummelen, and J. A. Koster, "Strategy for Enhancing the Dielectric Constant of Organic Semiconductors Without Sacrificing Charge Carrier Mobility and Solubility", *Advanced Functional Materials*, vol. 25, no. 1, pp. 150–157, 2015.

[93] N. Metropolis, *From Cardinals to Chaos: Reflection on the Life and Legacy of Stanislaw Ulam*, N. G. Cooper, Ed. CUP Archive, 1989, p. 125.

[94] H. L. Anderson, "Scientific Uses of the MANIAC", *Journal of Statistical Physics*, vol. 43, no. 5-6, pp. 731–748, 1986.

[95] N. Metropolis, A. W. Rosenbluth, M. N. Rosenbluth, A. H. Teller, and E. Teller, "Equation of State Calculations by Fast Computing Machines", *The Journal of Chemical Physics*, vol. 21, no. 6, p. 1087, 1953.

[96] R. Rhodes, *Making of the Atomic Bomb*. Simon and Schuster, 2012.

[97] G. P. Lepage, "A New Algorithm for Adaptive Multidimensional Integration", *Journal of Computational Physics*, vol. 27, no. 2, pp. 192–203, 1978.

[98] J. R. Beeler (Jr.), "Displacement Spikes in Cubic Metals. I. α-Iron, Copper, and Tungsten", *Physical Review*, vol. 150, no. 2, p. 470, 1966.

[99] E. S. Hood, B. H. Toby, and W. H. Weinberg, "Precursor-Mediated Molecular Chemisorption and Thermal Desorption: The Interrelationships Among Energetics, Kinetics, and Adsorbate Lattice Structure", *Physical Review Letters*, vol. 55, no. 22, p. 2437, 1985.

[100] A. B. Bortz, M. H. Kalos, and J. L. Lebowitz, "A New Algorithm for Monte Carlo Simulation of Ising Spin Systems", *Journal of Computational Physics*, vol. 17, no. 1, pp. 10–18, 1975.

[101] Z. Li and H. A. Scheraga, "Monte Carlo-Minimization Approach to the Multiple-Minima Problem in Protein Folding", *Proceedings of the National Academy of Sciences*, vol. 84, no. 19, pp. 6611–6615, 1987.

[102] C. Jacoboni and P. Lugli, *The Monte Carlo Method for Semiconductor Device Simulation*. Springer Vienna, 1989.

[103] G. Jegert, A. Kersch, W. Weinreich, U. Schroder, and P. Lugli, "Modeling of Leakage Currents in High-κ Dielectrics: Three-Dimensional Approach via kinetic Monte Carlo", *Applied Physics Letters*, vol. 96, no. 6, pp. 062 113–062 113, 2010.

[104] D. T. Gillespie, "A General Method for Numerically Simulating the Stochastic Time Evolution of Coupled Chemical Reactions", *Journal of Computational Physics*, vol. 22, no. 4, pp. 403–434, 1976.

[105] ——, "Exact Stochastic Simulation of Coupled Chemical Reactions", *The Journal of Physical Chemistry*, vol. 81, no. 25, pp. 2340–2361, 1977.

[106] E. Ising, "Beitrag zur Theorie des Ferromagnetismus", *Zeitschrift für Physik A: Hadrons and Nuclei*, vol. 31, no. 1, pp. 253–258, 1925.

[107] D. Frenkel and B. Smit, *Understanding Molecular Simulation: From Algorithms to Applications*, 2nd ed. Academic Press, 2001, vol. 1.

[108] A. F. Voter, "Introduction to the Kinetic Monte Carlo Method", *Radiation Effects*, vol. 235, pp. 1–23, 2005.

[109] J. R. Norris, *Markov Chains*, 2008. Cambridge University Press, 1998.

[110] F. Schwabl, *Statistical Mechanics*. Springer, 2006.

[111] J. H. Gibbs and P. D. Fleming III, "Stochastic Theory for Rate Constants of Chemical Reactions in Liquid Solution", *Journal of Statistical Physics*, vol. 12, no. 5, pp. 375–401, 1975.

[112] B. Ries and H. Bässler, "Monte Carlo Study of Dispersive Charge-Carrier Transport in Spatially Random Systems With and Without Energetic Disorder", *Physical Review B*, vol. 35, no. 5, p. 2295, 1987.

[113] P. Borsenberger, E. Magin, V. Auweraer, M. Der, and F. De Schryver, "The Role of Disorder on Charge Transport in Molecularly Doped Polymers and Related Materials", *Physica Status Solidi A: Applications and Materials Science*, vol. 140, no. 1, pp. 9–47, 1993.

[114] S. Baranovskii, I. Zvyagin, H. Cordes, S. Yamasaki, and P. Thomas, "Electronic Transport in Disordered Organic and Inorganic Semiconductors", *Journal of Non-Crystalline Solids*, vol. 299, pp. 416–419, 2002.

[115] C. Groves, "Simulating Charge Transport in Organic Semiconductors and Devices: A Review", *Reports on Progress in Physics*, vol. 80, no. 2, p. 026 502, 2016.

[116] W. Kaiser, T. Albes, and A. Gagliardi, "Charge Carrier Mobility of Disordered Organic Semiconductors With Correlated Energetic and Spatial Disorder", *Physical Chemistry Chemical Physics*, vol. 20, no. 13, pp. 8897–8908, 2018.

[117] P. Peumans and S. R. Forrest, "Separation of Geminate Charge-Pairs at Donor–Acceptor Interfaces in Disordered Solids", *Chemical Physics Letters*, vol. 398, no. 1-3, pp. 27–31, 2004.

[118] M. Casalegno, G. Raos, and R. Po, "Methodological Assessment of kinetic Monte Carlo Simulations of Organic Photovoltaic Devices: The Treatment of Electrostatic Interactions", *The Journal of Chemical Physics*, vol. 132, no. 9, p. 094 705, 2010.

[119] R. G. E. Kimber, E. N. Wright, S. E. J. O'Kane, A. B. Walker, and J. C. Blakesley, "Mesoscopic kinetic Monte Carlo Modeling of Organic Photovoltaic Device Characteristics", *Physical Review B*, vol. 86, no. 23, p. 235 206, 2012.

[120] P. Peumans, S. Uchida, and S. R. Forrest, "Efficient Bulk Heterojunction Photovoltaic Cells Using Small-Molecular-Weight Organic Thin Films", *Nature*, vol. 425, no. 6954, pp. 158–162, 2003.

[121] P. K. Watkins, A. B. Walker, and G. L. Verschoor, "Dynamical Monte Carlo Modelling of Organic Solar Cells: The Dependence of Internal Quantum Efficiency on Morphology", *Nano Letters*, vol. 5, no. 9, pp. 1814–8, 2005.

[122] A. Marsh, C. Groves, and N. C. Greenham, "A Microscopic Model for the Behavior of Nanostructured Organic Photovoltaic Devices", *Journal of Applied Physics*, vol. 101, no. 8, p. 083 509, 2007.

[123] U. Wolf, V. I. Arkhipov, and H. Bässler, "Current Injection From a Metal to a Disordered Hopping System. I. Monte Carlo Simulation", *Physical Review B*, vol. 59, no. 11, p. 7507, 1999.

[124] L. Meng, Y. Shang, Q. Li, Y. Li, X. Zhan, Z. Shuai, R. G. Kimber, and A. B. Walker, "Dynamic Monte Carlo Simulation for Highly Efficient Polymer Blend Photovoltaics", *The Journal of Physical Chemistry B*, vol. 114, no. 1, pp. 36–41, 2009.

[125] F. Yang and S. R. Forrest, "Photocurrent Generation in Nanostructured Organic Solar Cells", *ACS Nano*, vol. 2, no. 5, pp. 1022–1032, 2008.

[126] K. Feron, X. Zhou, W. Belcher, and P. Dastoor, "Exciton Transport in Organic Semiconductors: Förster Resonance Energy Transfer Compared With a Simple Random Walk", *Journal of Applied Physics*, vol. 111, no. 4, p. 044 510, 2012.

[127] I. Maqsood, L. D. Cundy, M. Biesecker, J.-H. Kimn, D. Johnson, R. Williams, and V. Bommisetty, "Monte Carlo Simulation of Förster Resonance Energy Transfer in 3D Nanoscale Organic Bulk Heterojunction Morphologies", *The Journal of Physical Chemistry C*, vol. 117, no. 41, pp. 21 086–21 095, 2013.

[128] C. Groves, L. Koster, and N. Greenham, "The Effect of Morphology Upon Mobility: Implications for Bulk Heterojunction Solar Cells With Nonuniform Blend Morphology", *Journal of Applied Physics*, vol. 105, no. 9, p. 094 510, 2009.

[129] M. C. Heiber, K. Kister, A. Baumann, V. Dyakonov, C. Deibel, and T.-Q. Nguyen, "Impact of Tortuosity on Charge-Carrier Transport in Organic Bulk Heterojunction Blends", *Physical Review Applied*, vol. 8, no. 5, p. 054 043, 2017.

[130] T. Offermans, S. C. Meskers, and R. A. Janssen, "Monte-Carlo Simulations of Geminate Electron–Hole Pair Dissociation in a Molecular Heterojunction: A Two-Step Dissociation Mechanism", *Chemical Physics*, vol. 308, no. 1-2, pp. 125–133, 2005.

[131] C. Deibel, T. Strobel, and V. Dyakonov, "Origin of the Efficient Polaron-Pair Dissociation in Polymer-Fullerene Blends", *Physical Review Letters*, vol. 103, no. 3, p. 036 402, 2009.

[132] M. C. Heiber and A. Dhinojwala, "Dynamic Monte Carlo Modeling of Exciton Dissociation in Organic Donor-Acceptor Solar Cells", *Journal of Chemical Physics*, vol. 137, no. 1, p. 014 903, 2012.

[133] H. van Eersel, R. A. Janssen, and M. Kemerink, "Mechanism for Efficient Photoinduced Charge Separation at Disordered Organic Heterointerfaces", *Advanced Functional Materials*, vol. 22, no. 13, pp. 2700–2708, 2012.

[134] C. Groves, R. Marsh, and N. C. Greenham, "Monte Carlo Modeling of Geminate Recombination in Polymer-Polymer Photovoltaic Devices", *The Journal of Chemical Physics*, vol. 129, no. 11, p. 114 903, 2008.

[135] C. Groves, J. C. Blakesley, and N. C. Greenham, "Effect of Charge Trapping on Geminate Recombination and Polymer Solar Cell Performance", *Nano Letters*, vol. 10, no. 3, pp. 1063–1069, 2010.

[136] J. Nelson, "Diffusion-Limited Recombination in Polymer-Fullerene Blends and Its Influence on Photocurrent Collection", *Physical Review B*, vol. 67, no. 15, p. 155 209, 2003.

[137] C. Groves and N. Greenham, "Bimolecular Recombination in Polymer Electronic Devices", *Physical Review B*, vol. 78, no. 15, p. 155 205, 2008.

[138] C. Göhler, A. Wagenpfahl, and C. Deibel, "Nongeminate Recombination in Organic Solar Cells", *Advanced Electronic Materials*, p. 1 700 505, 2018.

[139] C. Groves, "Developing Understanding of Organic Photovoltaic Devices: kinetic Monte Carlo Models of Geminate and Non-Geminate Recombination, Charge Transport and Charge Extraction", *Energy & Environmental Science*, vol. 6, no. 11, pp. 3202–3217, 2013.

[140] W. Kaiser, J. Popp, M. Rinderle, T. Albes, and A. Gagliardi, "Generalized Kinetic Monte Carlo Framework for Organic Electronics", *Algorithms*, vol. 11, no. 4, p. 37, 2018.

[141] P. P. Ewald, "Die Berechnung optischer und elektrostatischer Gitterpotentiale", *Annalen der Physik*, vol. 369, no. 3, pp. 253–287, 1921.

[142] C. Groves, R. G. Kimber, and A. B. Walker, "Simulation of Loss Mechanisms in Organic Solar Cells: A Description of the Mesoscopic Monte Carlo Technique and an Evaluation of the First Reaction Method", *The Journal of Chemical Physics*, vol. 133, no. 14, p. 144 110, 2010.

[143] M. Casalegno, A. Bernardi, and G. Raos, "Numerical Simulation of Photocurrent Generation in Bilayer Organic Solar Cells: Comparison of Master Equation and kinetic Monte Carlo Approaches", *The Journal of Chemical Physics*, vol. 139, no. 2, p. 024 706, 2013.

[144] W. Tress, "Device Physics of Organic Solar Cells", PhD thesis, 2011.

[145] M. Q. Zhang, "A Fast Vectorized Multispin Coding Algorithm for 3D Monte Carlo Simulations Using Kawasaki Spin-Exchange Dynamics", *Journal of Statistical Physics*, vol. 56, no. 5-6, pp. 939–950, 1989.

[146] J. S. Moon, J. K. Lee, S. Cho, J. Byun, and A. J. Heeger, "'Columnlike' Structure of the Cross-Sectional Morphology of Bulk Heterojunction Materials", *Nano Letters*, vol. 9, no. 1, pp. 230–4, 2009.

[147] N. Madras and A. D. Sokal, "The Pivot Algorithm: A Highly Efficient Monte Carlo Method for the Self-Avoiding Walk", *Journal of Statistical Physics*, vol. 50, no. 1-2, pp. 109–186, 1988.

[148] G. Shi, `https://gist.github.com/anyuzx/91ffa2ea98ceea1abba5f70cbc83b307`, [Online; accessed 19-January-2018], 2017.

[149] K. O. Sylvester-Hvid, S. Rettrup, and M. A. Ratner, "Two-Dimensional Model for Polymer-Based Photovoltaic Cells: Numerical Simulations of Morphology Effects", *The Journal of Physical Chemistry B*, vol. 108, no. 14, pp. 4296–4307, 2004.

[150] S. Yogev, E. Halpern, R. Matsubara, M. Nakamura, and Y. Rosenwaks, "Direct Measurement of Density of States in Pentacene Thin Film Transistors", *Physical Review B*, vol. 84, no. 16, p. 165 124, 2011.

[151] O. Tal, Y. Rosenwaks, Y. Preezant, N. Tessler, C. Chan, and A. Kahn, "Direct Determination of the Hole Density of States in Undoped and Doped Amorphous Organic Films With High Lateral Resolution", *Physical Review Letters*, vol. 95, no. 25, p. 256 405, 2005.

[152] H. Nicolai, M. Mandoc, and P. Blom, "Electron Traps in Semiconducting Polymers: Exponential Versus Gaussian Trap Distribution", *Physical Review B*, vol. 83, no. 19, p. 195 204, 2011.

[153] R. C. MacKenzie, T. Kirchartz, G. F. Dibb, and J. Nelson, "Modeling Nongeminate Recombination in P3HT:PCBM Solar Cells", *The Journal of Physical Chemistry C*, vol. 115, no. 19, pp. 9806–9813, 2011.

[154] S. Baranovskii, "Theoretical Description of Charge Transport in Disordered Organic Semiconductors", *Physica Status Solidi B*, vol. 251, no. 3, pp. 487–525, 2014.

[155] J. Oelerich, D. Huemmer, and S. Baranovskii, "How to Find Out the Density of States in Disordered Organic Semiconductors", *Physical Review Letters*, vol. 108, no. 22, p. 226 403, 2012.

[156] A. M. Ballantyne, L. Chen, J. Dane, T. Hammant, F. M. Braun, M. Heeney, W. Duffy, I. McCulloch, D. D. Bradley, and J. Nelson, "The Effect of Poly-(3-hexylthiophene) Molecular Weight on Charge Transport and the Performance of Polymer: Fullerene Solar Cells", *Advanced Functional Materials*, vol. 18, no. 16, pp. 2373–2380, 2008.

[157] N. R. Tummala, Z. Zheng, S. G. Aziz, V. Coropceanu, and J.-L. Brédas, "Static and Dynamic Energetic Disorders in the C_{60}, $PC_{61}BM$, C_{70}, and $PC_{71}BM$ Fullerenes", *The Journal of Physical Chemistry Letters*, vol. 6, no. 18, pp. 3657–3662, 2015.

[158] A. J. Mozer, N. S. Sariciftci, A. Pivrikas, R. Österbacka, G. Juška, L. Brassat, and H. Bässler, "Charge Carrier Mobility in Regioregular Poly (3-hexylthiophene) Probed by Transient Conductivity Techniques: A Comparative Study", *Physical Review B*, vol. 71, no. 3, p. 035 214, 2005.

[159] D. J. Griffiths, *Introduction to Electrodynamics*, 3rd. Addison Wesley, 1999.

[160] J. D. Jackson, *Classical Electrodynamics*, 3rd ed. Wiley, 1998.

[161] P. Gibbon and G. Sutmann, "Quantum Simulations of Complex Many-Body Systems: From Theory to Algorithms", *Lecture Notes, NIC Series (John von Neumann Institute for Computing, Julich)*, vol. Vol. 10, pp. 467–506, 2002.

[162] C. Holm, "Computational Soft Matter: From Synthetic Polymers to Proteins", *Lecture Notes, NIC Series (John von Neumann Institute for Computing, Julich)*, vol. Vol. 23, pp. 195–236, 2004.

[163] M. P. Allen and D. J. Tildesley, *Computer Simulation of Liquids*. Oxford University Press, 1989.

[164] A. Gagliardi, S. Wang, and T. Albes, "Simulation of Charge Carrier Mobility Unbalance in Organic Solar Cells", *Organic Electronics*, vol. 59, pp. 171–176, 2018.

[165] A. Gagliardi and A. Abate, "Mesoporous Electron Selective Contacts Enhance the Tolerance to Interfacial Ions Accumulation in Perovskite Solar Cells", *ACS Energy Letters*, 2017.

[166] G. F. Burkhard, E. T. Hoke, and M. D. McGehee, "Accounting for Interference, Scattering, and Electrode Absorption to Make Accurate Internal Quantum Efficiency Measurements in Organic and Other Thin Solar Cells", *Advanced Materials*, vol. 22, no. 30, p. 3293, 2010.

[167] P. Peumans, A. Yakimov, and S. R. Forrest, "Small Molecular Weight Organic Thin-Film Photodetectors and Solar Cells", *Journal of Applied Physics*, vol. 93, no. 7, pp. 3693–3723, 2003.

[168] L. A. Pettersson, L. S. Roman, and O. Inganäs, "Modeling Photocurrent Action Spectra of Photovoltaic Devices Based on Organic Thin Films", *Journal of Applied Physics*, vol. 86, no. 1, pp. 487–496, 1999.

[169] I.-W. Hwang, D. Moses, and A. J. Heeger, "Photoinduced Carrier Generation in P3HT/PCBM Bulk Heterojunction Materials", *The Journal of Physical Chemistry C*, vol. 112, no. 11, pp. 4350–4354, 2008.

[170] C. J. Brabec, N. S. Sariciftci, and J. C. Hummelen, "Plastic Solar Cells", *Advanced Functional Materials*, vol. 11, no. 1, pp. 15–26, 2001.

[171] A. Einstein, "Über die von der molekularkinetischen Theorie der Wärme geforderte Bewegung von in ruhenden Flüssigkeiten suspendierten Teilchen", *Annalen der Physik*, vol. 322, no. 8, pp. 549–560, 1905.

[172] M. von Smoluchowski, "Zur kinetischen Theorie der Brownschen Molekularbewegung und der Suspensionen", *Annalen der Physik*, vol. 326, no. 14, pp. 756–780, 1906.

[173] B. C. Thompson and J. M. Fréchet, "Polymer–Fullerene Composite Solar Cells", *Angewandte Chemie International Edition*, vol. 47, no. 1, pp. 58–77, 2008.

[174] E. von Hauff, V. Dyakonov, and J. Parisi, "Study of Field Effect Mobility in PCBM Films and P3HT:PCBM Blends", *Solar Energy Materials and Solar Cells*, vol. 87, no. 1, pp. 149–156, 2005.

[175] P. Langevin, "Recombinaison et mobilités des ions dans les gaz", *Annales de Chimie et de Physique*, vol. 28, no. 7, pp. 433–530, 1903.

[176] C. Deibel, A. Baumann, and V. Dyakonov, "Polaron Recombination in Pristine and Annealed Bulk Heterojunction Solar Cells", *Applied Physics Letters*, vol. 93, no. 16, p. 386, 2008.

[177] G. Juška, K. Arlauskas, J. Stuchlik, and R. Österbacka, "Non-Langevin Bimolecular Recombination in Low-Mobility Materials", *Journal of Non-Crystalline Solids*, vol. 352, no. 9, pp. 1167–1171, 2006.

[178] L. J. Koster, E. C. Smits, V. D. Mihailetchi, and P. W. Blom, "Device Model for the Operation of Polymer/Fullerene Bulk Heterojunction Solar Cells", *Physical Review B*, vol. 72, no. 8, p. 085 205, 2005.

[179] L. Koster, V. Mihailetchi, and P. Blom, "Bimolecular Recombination in Polymer/Fullerene Bulk Heterojunction Solar Cells", *Applied Physics Letters*, vol. 88, no. 5, p. 052 104, 2006.

[180] S. Meskers, P. van Hal, A. Spiering, J. Hummelen, A. Van der Meer, and R. Janssen, "Time-Resolved Infrared-Absorption Study of Photoinduced Charge Transfer in a Polythiophene-Methanofullerene Composite Film", *Physical Review B*, vol. 61, no. 15, p. 9917, 2000.

[181] S. De, T. Pascher, M. Maiti, K. G. Jespersen, T. Kesti, F. Zhang, O. Inganäs, A. Yartsev, and V. Sundström, "Geminate Charge Recombination in Alternating Polyfluorene Copolymer/Fullerene Blends", *Journal of the American Chemical Society*, vol. 129, no. 27, pp. 8466–8472, 2007.

[182] F. Etzold, I. A. Howard, R. Mauer, M. Meister, T.-D. Kim, K.-S. Lee, N. S. Baek, and F. Laquai, "Ultrafast Exciton Dissociation Followed by Nongeminate Charge Recombination in PCDTBT:PCBM Photovoltaic Blends", *Journal of the American Chemical Society*, vol. 133, no. 24, pp. 9469–9479, 2011.

[183] S. Shoaee, S. Subramaniyan, H. Xin, C. Keiderling, P. S. Tuladhar, F. Jamieson, S. A. Jenekhe, and J. R. Durrant, "Charge Photogeneration for a Series of Thiazolo-Thiazole Donor Polymers Blended with the Fullerene Electron Acceptors PCBM and ICBA", *Advanced Functional Materials*, vol. 23, no. 26, p. 3286, 2013.

[184] M. Gerhard, A. P. Arndt, M. Bilal, U. Lemmer, M. Koch, and I. A. Howard, "Field-Induced Exciton Dissociation in PTB7-Based Organic Solar Cells", *Physical Review B*, vol. 95, no. 19, p. 195 301, 2017.

[185] D. Kipp and V. Ganesan, "A kinetic Monte Carlo Model With Improved Charge Injection Model for the Photocurrent Characteristics of Organic Solar Cells", *Journal of Applied Physics*, vol. 113, no. 23, p. 234 502, 2013.

[186] M. Limpinsel, A. Wagenpfahl, M. Mingebach, C. Deibel, and V. Dyakonov, "Photocurrent in Bulk Heterojunction Solar Cells", *Physical Review B*, vol. 81, no. 8, p. 085 203, 2010.

[187] K. Yoshida, T. Oku, A. Suzuki, T. Akiyama, and Y. Yamasaki, "Fabrication and Characterization of PCBM:P3HT Bulk Heterojunction Solar Cells Doped with Germanium Phthalocyanine or Germanium Naphthalocyanine", *Materials Sciences and Applications*, vol. 4, p. 1, 2013.

[188] J. You, L. Dou, Z. Hong, G. Li, and Y. Yang, "Recent Trends in Polymer Tandem Solar Cells Research", *Progress in Polymer Science*, vol. 38, no. 12, pp. 1909–1928, 2013.

[189] J. Wu, G. Yue, Y. Xiao, J. Lin, M. Huang, Z. Lan, Q. Tang, Y. Huang, L. Fan, S. Yin, and T. Sato, "An Ultraviolet Responsive Hybrid Solar Cell Based on Titania/Poly (3-hexylthiophene)", *Scientific Reports*, vol. 3, 2013.

[190] H. T. Nicolai, M. Kuik, G.-J. A. Wetzelaer, B. de Boer, C. Campbell, C. Risko, J. Brédas, and P. W. Blom, "Unification of Trap-Limited Electron Transport in Semiconducting Polymers", *Nature Materials*, vol. 11, no. 10, pp. 882–887, 2012.

[191] A. Fallahpour, A. Gagliardi, D. Gentilini, A. Zampetti, F. Santoni, M. A. Der Maur, and A. Di Carlo, "Optoelectronic Simulation and Thickness Optimization of Energetically Disordered Organic Solar Cells", *Journal of Computational Electronics*, vol. 13, no. 4, pp. 933–942, 2014.

[192] Y. Shang, Q. Li, L. Meng, D. Wang, and Z. Shuai, "Device Simulation of Low-Band Gap Polymer Solar Cells: Influence of Electron-Hole Pair Dissociation and Decay Rates on Open-Circuit Voltage", *Applied Physics Letters*, vol. 97, no. 14, pp. 143 511–143 511, 2010.

[193] A. Wagenpfahl, D. Rauh, M. Binder, C. Deibel, and V. Dyakonov, "S-Shaped Current-Voltage Characteristics of Organic Solar Devices", *Physical Review B*, vol. 82, no. 11, p. 115 306, 2010.

[194] R. C. MacKenzie, C. G. Shuttle, M. L. Chabinyc, and J. Nelson, "Extracting Microscopic Device Parameters from Transient Photocurrent Measurements of P3HT:PCBM Solar Cells", *Advanced Energy Materials*, vol. 2, no. 6, pp. 662–669, 2012.

[195] A. Fallahpour, A. Gagliardi, F. Santoni, D. Gentilini, A. Zampetti, M. A. der Maur, and A. Di Carlo, "Modeling and Simulation of Energetically Disordered Organic Solar Cells", *Journal of Applied Physics*, vol. 116, no. 18, p. 184 502, 2014.

[196] G. Li, L. Liu, F. Wei, S. Xia, and X. Qian, "Recent Progress in Modeling, Simulation, and Optimization of Polymer Solar Cells", *IEEE Journal of Photovoltaics*, vol. 2, no. 3, pp. 320–340, 2012.

[197] F. Wei, L. Liu, L. Liu, and G. Li, "Multiscale Modeling and Simulation for Optimizing Polymer Bulk Heterojunction Solar Cells", *IEEE Journal of Photovoltaics*, vol. 3, no. 1, pp. 300–309, 2013.

[198] tiberlab S.r.l. (2018). TiberCAD - multiscale simulation, [Online]. Available: `http://www.tiberlab.com/` (visited on 04/18/2018).

[199] F. Santoni, A. Gagliardi, M. A. der Maur, and A. Di Carlo, "The Relevance of Correct Injection Model to Simulate Electrical Properties of Organic Semiconductors", *Organic Electronics*, vol. 15, no. 7, pp. 1557–1570, 2014.

[200] W. Pasveer, J. Cottaar, C. Tanase, R. Coehoorn, P. Bobbert, P. Blom, D. De Leeuw, and M. Michels, "Unified Description of Charge-Carrier Mobilities in Disordered Semiconducting Polymers", *Physical Review Letters*, vol. 94, no. 20, p. 206 601, 2005.

[201] J. C. Scott and G. G. Malliaras, "Charge Injection and Recombination at the Metal–Organic Interface", *Chemical Physics Letters*, vol. 299, no. 2, pp. 115–119, 1999.

[202] G. Lakhwani, A. Rao, and R. H. Friend, "Bimolecular Recombination in Organic Photovoltaics", *Annual Review of Physical Chemistry*, vol. 65, pp. 557–581, 2014.

[203] R. Mauer, M. Kastler, and F. Laquai, "The Impact of Polymer Regioregularity on Charge Transport and Efficiency of P3HT:PCBM Photovoltaic Devices", *Advanced Functional Materials*, vol. 20, no. 13, pp. 2085–2092, 2010.

[204] A. Foertig, A. Wagenpfahl, T. Gerbich, D. Cheyns, V. Dyakonov, and C. Deibel, "Nongeminate Recombination in Planar and Bulk Heterojunction Organic Solar Cells", *Advanced Energy Materials*, vol. 2, no. 12, pp. 1483–1489, 2012.

[205] A. Pivrikas, N. S. Sariciftci, G. Juška, and R. Österbacka, "A Review of Charge Transport and Recombination in Polymer/Fullerene Organic Solar Cells", *Progress in Photovoltaics*, vol. 15, no. 8, pp. 677–696, 2007.

[206] G. Garcia-Belmonte, A. Guerrero, and J. Bisquert, "Elucidating Operating Modes of Bulk-Heterojunction Solar Cells from Impedance Spectroscopy Analysis", *The Journal of Physical Chemistry Letters*, vol. 4, no. 6, pp. 877–886, 2013.

[207] H. Sirringhaus, P. Brown, R. Friend, M. M. Nielsen, K. Bechgaard, B. Langeveld-Voss, A. Spiering, R. A. Janssen, E. Meijer, P. Herwig, and D. M. de Leeuw, "Two-Dimensional Charge Transport in Self-Organized, High-Mobility Conjugated Polymers", *Nature*, vol. 401, no. 6754, pp. 685–688, 1999.

[208] S. H. Park, A. Roy, S. Beaupré, S. Cho, N. Coates, J. S. Moon, D. Moses, M. Leclerc, K. Lee, and A. J. Heeger, "Bulk Heterojunction Solar Cells With Internal Quantum Efficiency Approaching 100%", *Nature Photonics*, vol. 3, no. 5, pp. 297–302, 2009.

[209] P. C. Chow, S. Gélinas, A. Rao, and R. H. Friend, "Quantitative Bimolecular Recombination in Organic Photovoltaics Through Triplet Exciton Formation", *Journal of the American Chemical Society*, vol. 136, no. 9, pp. 3424–3429, 2014.

[210] S. Westenhoff, I. A. Howard, J. M. Hodgkiss, K. R. Kirov, H. A. Bronstein, C. K. Williams, N. C. Greenham, and R. H. Friend, "Charge Recombination in Organic Photovoltaic Devices With High Open-Circuit Voltages", *Journal of the American Chemical Society*, vol. 130, no. 41, pp. 13 653–13 658, 2008.

[211] A. A. Bakulin, A. Rao, V. G. Pavelyev, P. H. van Loosdrecht, M. S. Pshenichnikov, D. Niedzialek, J. Cornil, D. Beljonne, and R. H. Friend, "The Role of Driving Energy and Delocalized States for Charge Separation in Organic Semiconductors", *Science*, 2012.

[212] K. Vandewal, S. Albrecht, E. T. Hoke, K. R. Graham, J. Widmer, J. D. Douglas, M. Schubert, W. R. Mateker, J. T. Bloking, G. F. Burkhard, A. Sellinger, J. M. J. Fréchet, A. Amassian, M. K. Riede, M. D. McGehee, D. Neher, and A. Salleo, "Efficient Charge Generation by Relaxed Charge-Transfer States at Organic Interfaces", *Nature Materials*, vol. 13, no. 1, pp. 63–68, 2014.

[213] A. Zusan, K. Vandewal, B. Allendorf, N. H. Hansen, J. Pflaum, A. Salleo, V. Dyakonov, and C. Deibel, "The Crucial Influence of Fullerene Phases on Photogeneration in Organic Bulk Heterojunction Solar Cells", *Advanced Energy Materials*, vol. 4, no. 17, 2014.

[214] J. Lee, K. Vandewal, S. R. Yost, M. E. Bahlke, L. Goris, M. A. Baldo, J. V. Manca, and T. V. Voorhis, "Charge Transfer State Versus Hot Exciton Dissociation in Polymer–Fullerene Blended Solar Cells", *Journal of the American Chemical Society*, vol. 132, no. 34, pp. 11 878–11 880, 2010.

[215] M. C. Heiber, C. Baumbach, V. Dyakonov, and C. Deibel, "Encounter-Limited Charge-Carrier Recombination in Phase-Separated Organic Semiconductor Blends", *Physical Review Letters*, vol. 114, no. 13, p. 136 602, 2015.

[216] H. K. Kodali and B. Ganapathysubramanian, "A Computational Framework to Investigate Charge Transport in Heterogeneous Organic Photovoltaic Devices", *Computer Methods in Applied Mechanics and Engineering*, vol. 247, pp. 113–129, 2012.

[217] ——, "Computer Simulation of Heterogeneous Polymer Photovoltaic Devices", *Modelling and Simulation in Materials Science and Engineering*, vol. 20, no. 3, p. 035 015, 2012.

[218] T. Albes and A. Gagliardi, "Correction: Influence of Permittivity and Energetic Disorder on the Spatial Charge Carrier Distribution and Recombination in Organic Bulk-Heterojunctions", *Physical Chemistry Chemical Physics*, vol. 21, no. 21, pp. 11 488–11 490, 2019.

[219] I. A. Howard and F. Laquai, "Optical Probes of Charge Generation and Recombination in Bulk Heterojunction Organic Solar Cells", *Macromolecular Chemistry and Physics*, vol. 211, no. 19, pp. 2063–2070, 2010.

[220] T. M. Clarke, A. Ballantyne, S. Shoaee, Y. W. Soon, W. Duffy, M. Heeney, I. McCulloch, J. Nelson, and J. R. Durrant, "Analysis of Charge Photogeneration as a Key Determinant of Photocurrent Density in Polymer:Fullerene Solar Cells", *Advanced Materials*, vol. 22, no. 46, pp. 5287–5291, 2010.

[221] S. M. Menke, A. Cheminal, P. Conaghan, N. A. Ran, N. C. Greehnam, G. C. Bazan, T.-Q. Nguyen, A. Rao, and R. H. Friend, "Order Enables Efficient Electron-Hole Separation at an Organic Heterojunction With a Small Energy Loss", *Nature Communications*, vol. 9, no. 1, p. 277, 2018.

[222] Y. L. Lin, M. A. Fusella, and B. P. Rand, "The Impact of Local Morphology on Organic Donor/Acceptor Charge Transfer States", *Advanced Energy Materials*, p. 1 702 816, 2018.

[223] S. Baranovskii, M. Wiemer, A. Nenashev, F. Jansson, and F. Gebhard, "Calculating the Efficiency of Exciton Dissociation at the Interface Between a Conjugated Polymer and an Electron Acceptor", *Journal of Physical Chemistry Letters*, vol. 3, no. 9, pp. 1214–1221, 2012.

[224] D. A. Vithanage, A. Devižis, V. Abramavičius, Y. Infahsaeng, D. Abramavičius, R. MacKenzie, P. Keivanidis, A. Yartsev, D. Hertel, J. Nelson, V. Sundström, and V. Gulbinas, "Visualizing Charge Separation in Bulk Heterojunction Organic Solar Cells", *Nature Communications*, vol. 4, p. 2334, 2013.

[225] F. Liu, H. van Eersel, B. Xu, J. G. E. Wilbers, M. P. de Jong, W. G. van der Wiel, P. A. Bobbert, and R. Coehoorn, "Effect of Coulomb Correlation on Charge Transport in Disordered Organic Semiconductors", *Physical Review B*, vol. 96, p. 205 203, 20 2017.

[226] S. N. Hood and I. Kassal, "Entropy and Disorder Enable Charge Separation in Organic Solar Cells", *The Journal of Physical Chemistry Letters*, vol. 7, no. 22, pp. 4495–4500, 2016.

[227] X. Xu, Z. Li, J. Wang, B. Lin, W. Ma, Y. Xia, M. R. Andersson, R. A. Janssen, and E. Wang, "High-Performance All-Polymer Solar Cells Based on Fluorinated Naphthalene Diimide Acceptor Polymers with Fine-Tuned Crystallinity and Enhanced Dielectric Constants", *Nano Energy*, 2018.

[228] X. Liu, B. Xie, C. Duan, Z. Wang, B. Fan, K. Zhang, B. Lin, F. J. Colberts, W. Ma, R. A. Janssen, F. Huang, and Y. Cao, "A High Dielectric Constant Non-Fullerene Acceptor for Efficient Bulk-Heterojunction Organic Solar Cells", *Journal of Materials Chemistry A*, vol. 6, no. 2, p. 395, 2018.

[229] J. Brebels, E. Douvogianni, D. Devisscher, R. Thiruvallur Eachambadi, J. Manca, L. Lutsen, D. Vanderzande, J. C. Hummelen, and W. Maes, "An Effective Strategy to Enhance the Dielectric Constant of Organic Semiconductors - CPDTTPD-Based Low Bandgap Polymers Bearing Oligo(Ethylene Glycol) Side Chains", *Journal of Materials Chemistry C*, vol. 6, no. 3, pp. 500–511, 2018.

[230] F. Jahani, S. Torabi, R. C. Chiechi, L. J. A. Koster, and J. C. Hummelen, "Fullerene Derivatives With Increased Dielectric Constants", *Chemical Communications*, vol. 50, no. 73, p. 10 645, 2014.

[231] S. A. Hawks, G. Li, Y. Yang, and R. A. Street, "Band Tail Recombination in Polymer:Fullerene Organic Solar Cells", *Journal of Applied Physics*, vol. 116, no. 7, p. 074 503, 2014.

[232] R. Street, K. Song, J. Northrup, and S. Cowan, "Photoconductivity Measurements of the Electronic Structure of Organic Solar Cells", *Physical Review B*, vol. 83, no. 16, p. 165 207, 2011.

[233] K. R. Graham, C. Cabanetos, J. P. Jahnke, M. N. Idso, A. El Labban, G. O. Ngongang Ndjawa, T. Heumueller, K. Vandewal, A. Salleo, B. F. Chmelka, A. Amassian, P. M. Beaujuge, and M. D. McGehee, "Importance of the Donor:Fullerene Intermolecular Arrangement for High-Efficiency Organic Photovoltaics", *Journal of the American Chemical Society*, vol. 136, no. 27, p. 9608, 2014.

[234] T. M. Burke and M. D. McGehee, "How High Local Charge Carrier Mobility and an Energy Cascade in a Three-Phase Bulk Heterojunction Enable >90% Quantum Efficiency", *Advanced Materials*, vol. 26, no. 12, p. 1923, 2014.

[235] T. Albes and A. Gagliardi, "Correction: Charge Pair Separation Dynamics in Organic Bulk-Heterojunction Solar Cells", *Advanced Theory and Simulations*, p. 1 900 100, 2019.

[236] Y. Liu, J. Zhao, Z. Li, C. Mu, W. Ma, H. Hu, K. Jiang, H. Lin, H. Ade, and H. Yan, "Aggregation and Morphology Control Enables Multiple Cases of High-Efficiency Polymer Solar Cells", *Nature Communications*, vol. 5, p. 5293, 2014.

[237] P. W. Blom, V. D. Mihailetchi, L. J. A. Koster, and D. E. Markov, "Device Physics of Polymer:Fullerene Bulk Heterojunction Solar Cells", *Advanced Materials*, vol. 19, no. 12, pp. 1551–1566, 2007.

[238] Z. He, C. Zhong, X. Huang, W.-Y. Wong, H. Wu, L. Chen, S. Su, and Y. Cao, "Simultaneous Enhancement of Open-Circuit Voltage, Short-Circuit Current Density, and Fill Factor in Polymer Solar Cells", *Advanced Materials*, vol. 23, no. 40, pp. 4636–4643, 2011.

[239] R. A. Janssen and J. Nelson, "Factors Limiting Device Efficiency in Organic Photovoltaics", *Advanced Materials*, vol. 25, no. 13, pp. 1847–1858, 2013.

[240] M. Zhang, H. Wang, H. Tian, Y. Geng, C. Tang, *et al.*, "Bulk Heterojunction Photovoltaic Cells With Low Donor Concentration", *Advanced Materials*, vol. 23, no. 42, pp. 4960–4964, 2011.

[241] X. Xiao, K. J. Bergemann, J. D. Zimmerman, K. Lee, and S. R. Forrest, "Small-Molecule Planar-Mixed Heterojunction Photovoltaic Cells with Fullerene-Based Electron Filtering Buffers", *Advanced Energy Materials*, vol. 4, no. 7, 2014.

[242] S. Sutty, G. M. Williams, and H. Aziz, "Fullerene-Based Schottky-Junction Organic Solar Cells: A Brief Review", *Journal of Photonics for Energy*, vol. 4, no. 1, p. 040 999, 2014.

[243] K. Vandewal, J. Widmer, T. Heumueller, C. J. Brabec, M. D. McGehee, K. Leo, M. Riede, and A. Salleo, "Increased Open-Circuit Voltage of Organic Solar Cells by Reduced Donor-Acceptor Interface Area", *Advanced Materials*, vol. 26, no. 23, pp. 3839–3843, 2014.

[244] M. Zhang, Irfan, H. Ding, Y. Gao, and C. W. Tang, "Organic Schottky Barrier Photovoltaic Cells Based on MoO_x/C_{60}", *Applied Physics Letters*, vol. 96, no. 18, p. 87, 2010.

[245] B. Yang, Z. Xiao, and J. Huang, "Polymer Aggregation Correlated Transition from Schottky-Junction to Bulk Heterojunction Organic Solar Cells", *Applied Physics Letters*, vol. 104, no. 14, 54_1, 2014.

[246] A. Melianas, V. Pranculis, D. Spoltore, J. Benduhn, O. Inganäs, V. Gulbinas, K. Vandewal, and M. Kemerink, "Charge Transport in Pure and Mixed Phases in Organic Solar Cells", *Advanced Energy Materials*, vol. 7, no. 20, 2017.

[247] O. Solomeshch, Y. J. Yu, A. A. Goryunkov, L. N. Sidorov, R. F. Tuktarov, D. H. Choi, J.-I. Jin, and N. Tessler, "Ground-State Interaction and Electrical Doping of Fluorinated C_{60} in Conjugated Polymers", *Advanced Materials*, vol. 21, no. 44, pp. 4456–4460, 2009.

[248] J. Min, T. Ameri, R. Gresser, M. Lorenz-Rothe, D. Baran, A. Troeger, V. Sgobba, K. Leo, M. Riede, D. M. Guldi, and C. J. Brabec, "Two Similar Near-Infrared (IR) Absorbing Benzannulated AZA-bodipy Dyes as Near-IR Sensitizers for Ternary Solar Cells", *ACS applied Materials & Interfaces*, vol. 5, no. 12, pp. 5609–5616, 2013.

[249] J. Y. Kim, K. Lee, N. E. Coates, D. Moses, T.-Q. Nguyen, M. Dante, and A. J. Heeger, "Efficient Tandem Polymer Solar Cells Fabricated by All-Solution Processing", *Science*, vol. 317, no. 5835, pp. 222–225, 2007.

[250] N. A. Ran, J. A. Love, C. J. Takacs, A. Sadhanala, J. K. Beavers, S. D. Collins, Y. Huang, M. Wang, R. H. Friend, G. C. Bazan, and T.-Q. Nguyen, "Harvesting the Full Potential of Photons With Organic Solar Cells", *Advanced Materials*, vol. 28, no. 7, pp. 1482–1488, 2016.

[251] R. A. Street, S. A. Hawks, P. P. Khlyabich, G. Li, B. J. Schwartz, B. C. Thompson, and Y. Yang, "Electronic Structure and Transition Energies in Polymer–Fullerene Bulk Heterojunctions", *The Journal of Physical Chemistry C*, vol. 118, no. 38, pp. 21 873–21 883, 2014.

[252] J. Guo, H. Ohkita, H. Benten, and S. Ito, "Near-IR Femtosecond Transient Absorption Spectroscopy of Ultrafast Polaron and Triplet Exciton Formation in Polythiophene Films With Different Regioregularities", *Journal of the American Chemical Society*, vol. 131, no. 46, pp. 16 869–16 880, 2009.

[253] W. C. Tsoi, S. J. Spencer, L. Yang, A. M. Ballantyne, P. G. Nicholson, A. Turnbull, A. G. Shard, C. E. Murphy, D. D. Bradley, J. Nelson, and J.-S. Kim, "Effect of Crystallization on the Electronic Energy Levels and Thin Film Morphology of P3HT:PCBM Blends", *Macromolecules*, vol. 44, no. 8, pp. 2944–2952, 2011.

[254] R. Marcus, "Relation Between Charge Transfer Absorption and Fluorescence Spectra and the Inverted Region", *The Journal of Physical Chemistry*, vol. 93, no. 8, pp. 3078–3086, 1989.

[255] K. Vandewal, K. Tvingstedt, A. Gadisa, O. Inganäs, and J. V. Manca, "Relating the Open-Circuit Voltage to Interface Molecular Properties of Donor:Acceptor Bulk Heterojunction Solar Cells", *Physical Review B*, vol. 81, no. 12, p. 125 204, 2010.

Acronyms

BHJ Bulk-Heterojunction.

CCD Charge Carrier Distribution.

CIGS Copper Indium Gallium Selenide.

CP Charge Pair.

CT Charge Transfer.

DBP Tetraphenyldibenzoperiflanthene.

DD Drift-Diffusion.

DOS Density of States.

DSSC Dye-Sensitized Solar Cell.

EMA Effective Medium Approximation.

EQE External Quantum Efficiency.

FEM Finite Element Method.

FIB Focused Ion Beam.

FRM First Reaction Method.

GDOS Gaussian Density of States.

HOMO Highest Occupied Molecular Orbital.

IR Infra-Red.

IS Impedance Spectroscopy.

ITO Indium Tin Oxide.

j-U Current Density-Voltage.

kMC kinetic Monte Carlo.

LCAO Linear Combination of Atomic Orbitals.

LUMO Lowest Unoccupied Molecular Orbital.

MC Monte Carlo Step.

MD Molecular Dynamics.

MO Molecular Orbital.

MPP Maximum Power Point.

OB Onsager-Braun.

OSC Organic Solar Cell.

P3HT Poly(3-hexylthiophen-2,5-diyl).

PCBM Phenyl-C61/C71-butyric acid methyl ester.

PCE Power Conversion Efficiency.

p-CELIV photo-Charge Extraction by Linearly Increasing Voltage.

PDF Probability Density Function.

PEDOT:PSS Poly(3,4-ethylenedioxythiophene)-poly(styrenesulfonate).

SAW Self-Avoiding Walk.

TAPC 1,1-bis-(4-bis(4-methyl-phenyl)-amino-phenyl)-cyclohexane.

TAS Transient Absorption Spectroscopy.

TEM Transmission Electron Microscopy.

TF Thin-Film.

TMM Transfer Matrix Method.

UV Ultra-Violet.

Acknowledgment

First of all, I would like to express my gratitude to my supervisor Prof. Dr. Alessio Gagliardi. Thank you, Alessio, for giving me the opportunity to work on this topic and for providing me with an excellent working environment. Your door was always open for me when I had questions or needed help – be it related to simulations or about many, many other topics. I have grown and learned alot during the past years while establishing this workgroup together with you from scratch.

Further, I want to thank the other members of my examining committee: Prof. Dr. Müller-Buschbaum for co-examining and the chair Prof. Dr. Witzmann for filling in on such short notice!

I acknowledge the Nanosystems Initiative Munich (NIM) of the German Research Foundation (Deutsche Forschungsgemeinschaft, DFG) for funding my position.

Also, I would like to thank Prof. Dr. Paolo Lugli who supervised me during my diploma thesis, which laid the foundation for many different projects within our group including this thesis.

My sincere thanks to my colleague Waldemar Kaiser who supported me in basically everything. Through you I have experienced some life outside of the office again ;) Thank you for your valuable input, many interesting discussions and especially for critically proof-reading the code.

Thank you to the rest of the current and former group and institute members, in particular Prof. Dr. Markus Becherer, my mentor Prof. Dr. Christian Jirauschek, Barbara Asam, Dr. Benedikt Weiler, Petar Tzenov, Mohammed Darwish, Michael Haider, Marlon Rück, Michael Rinderle and Shengda Wang.

Many thanks to Dr. Alessandro Pecchia, Dr. Matthias Auf der Maur and Prof. Dr. Aldo di Carlo from the University of Rome 'Tor Vergata' for your help and support with TiberCAD, for our collaboration on the book chapter and for hosting me in Rome.

Special thanks to Prof. Dr. Julia W.P. Hsu and Dr. Liang Xu from the University of Texas at Dallas for fruitful discussions between experimentalists and theoreticians. Thank you for providing the experimental data for our collaboration and for proof-reading the manuscript.

Thanks alot to Thomas Kreitmair for thoroughly proof-reading the thesis and for personal guidance.

Lastly and most importantly: nothing can outweigh the unconditional support my parents and my brother have given me. All three of you have always been there for me, no matter what the circumstances. Without you, I would never have achieved what I have achieved so far. Thank you for everything.